NUSC Technical Document 8043
26 May 1988

(2)

AD-A197 282

Nearfield Acoustic Radiation From a Point-Excited Cylindrical Shell

Richard D. Vogelsong
Environmental and Tactical
Support Systems Department

Naval Underwater Systems Center
Newport, Rhode Island / New London, Connecticut

Preface

This study was prepared as a dissertation for the degree of Doctor of Philosophy in Acoustics from the Pennsylvania State University.

Reviewed and Approved: 26 May 1988

L. Solomon
Head: Environmental and Tactical
Support Systems Department

UNCLASSIFIED

SECURITY CLASSIFICATION OF THIS PAGE

REPORT DOCUMENTATION PAGE

1a. REPORT SECURITY CLASSIFICATION UNCLASSIFIED	1b. RESTRICTIVE MARKINGS
2a. SECURITY CLASSIFICATION AUTHORITY	3. DISTRIBUTION / AVAILABILITY OF REPORT Approved for public release; distribution is unlimited.
2b. DECLASSIFICATION / DOWNGRADING SCHEDULE	
4. PERFORMING ORGANIZATION REPORT NUMBER(S) NUSC TR 8043	5. MONITORING ORGANIZATION REPORT NUMBER(S)
6a. NAME OF PERFORMING ORGANIZATION Naval Underwater Systems Center 6b. OFFICE SYMBOL (If applicable) 3111	7a. NAME OF MONITORING ORGANIZATION
6c. ADDRESS (City, State, and ZIP Code) New London Laboratory New London, CT 06378	7b. ADDRESS (City, State, and ZIP Code)
8a. NAME OF FUNDING / SPONSORING ORGANIZATION 8b. OFFICE SYMBOL (If applicable)	9. PROCUREMENT INSTRUMENT IDENTIFICATION NUMBER
8c. ADDRESS (City, State, and ZIP Code)	10. SOURCE OF FUNDING NUMBERS PROGRAM ELEMENT NO. / PROJECT NO. / TASK NO. / WORK UNIT ACCESSION NO.

11. TITLE (Include Security Classification)
NEARFIELD ACOUSTIC RADIATION FROM A POINT-EXCITED CYLINDRICAL SHELL

12. PERSONAL AUTHOR(S) Vogelsong, Richard D.

13a. TYPE OF REPORT	13b. TIME COVERED	14. DATE OF REPORT (Year, Month, Day)	15. PAGE COUNT
Ph.D Thesis	FROM _____ TO _____	1988 May 16	222

16. SUPPLEMENTARY NOTATION

17 COSATI CODES			18. SUBJECT TERMS (Continue on reverse if necessary and identify by block number)
FIELD	GROUP	SUB-GROUP	
17	01		

19. ABSTRACT (Continue on reverse if necessary and identify by block number)

The surface force exerted by a dense medium such as water upon an elastic structure undergoing dynamic motion is often comparable to the inertial and damping forces found within the structure. Fluid loading may alter the structural response by strongly coupling the elastic and acoustic media. Any attempt to locally deform the structure may lead to a slowly decaying pressure field that excites the elastic structure further away. In this study, the acoustic nearfield and radial surface deformation of a cylindrical shell of infinite axial extent is examined. The shell is subject to external fluid loading and is excited by a radially acting, time harmonic point force. The shell is modeled using Flugge's thin shell theory.

Eigenfunction and integral transform methods are used to formulate the shell's radial deformation and the radiated acoustic pressure in terms of an infinite Fourier series of inverse transform integrals. The frequency spectra of the propagating and

20. DISTRIBUTION / AVAILABILITY OF ABSTRACT	21. ABSTRACT SECURITY CLASSIFICATION
☒ UNCLASSIFIED/UNLIMITED ☐ SAME AS RPT. ☐ OTIC USERS	UNCLASSIFIED
22a. NAME OF RESPONSIBLE INDIVIDUAL Richard D. Vogelsong	22b. TELEPHONE (Include Area Code) (203) 440-4979 22c. OFFICE SYMBOL 3111

DD FORM 1473, 84 MAR 83 APR edition may be used until exhausted. All other editions are obsolete.

SECURITY CLASSIFICATION OF THIS PAGE
UNCLASSIFIED

19. (Continued)

non-propagating modes of vibration are described. The propagating modes are compared to those of the shell in vacuo. For each circumferential mode, real singularities are shown to exist only at frequencies between a lower and an upper cutoff frequency. For fixed driving frequency, a limited number of circumferential modes will exhibit a real singularity.

The inverse transform integrals are solved by Cauchy's theorem. In the acoustic nearfield and at frequencies below the classical plate coincidence frequency, the solutions are shown to be dependent only upon the residue contribution of a single real singularity at each of a small number of modes. Strong acoustical coupling exists between the driving-point excitation and the acoustic nearfield. Above the coincidence frequency, the solutions are dominated by a branch line integral over subsonic axial wavenumbers that correctly exhibits the coincidence beaming effect. The acoustic coupling between the drive point and points outside this beaming region is weak. Predictions of the acoustic nearfield and the surface radial displacement are given over a wide frequency range.

TABLE OF CONTENTS

TABLE OF CONTENTS (Continued)

LIST OF TABLES

LIST OF FIGURES

LIST OF FIGURES (Continued)

LIST OF FIGURES (Continued)

LIST OF FIGURES (Continued)

LIST OF FIGURES (Continued)

LIST OF SYMBOLS

*	denotes complex conjugate
'	indicates the derivative of a function with respect to its argument
~	denotes a quantity that has been Fourier transformed into normalized axial wavenumber space using the transform pair given by Equations (2.17) and (2.18)
a	nondimensional outer radius of the cylindrical shell (normalized by R)
a_j	j^{th} coefficient of $D_{sn}(\xi)$, Equation (3.24)
$a_m(\xi)$	modal coefficients of the Fourier expansion of the spectral pressure, Equation (4.9)
A_n	modal coefficients, see Sections 5.3 and 5.7
b_j	j^{th} coefficient of $N_{sn}(\xi)$, Equation (3.24)
$b_1, b_2(\theta,x)$	total contribution of branch paths to $w(\theta,x)$, Equations (5.30) and (5.31)
$B_1, B_2(r,\theta,x)$	total contribution of branch paths to $p(r,\theta,x)$, Equation (5.9)
$B_{1n}, B_{2n}(r,x)$	integral coefficients of the Fourier series expansion of B_1 and B_2, Equations (5.10) and (5.17)
c	acoustic phase velocity of the fluid
c_p	low frequency phase velocity of compressional waves in a thin plate, $= [E/\rho_s(1-\mu^2)]^{1/2}$
C_b	longitudinal bar velocity
C_g	group velocity
C_G	normalized group velocity, $= C_g/c_p$
C_l	dilitational wave velocity of an infinite elastic solid
$C_n(r,x)$	modal residue contribution to the acoustic pressure of a symmetric pair of complex singularities, Equation (5.26)
C_R	Rayleigh wave velocity

LIST OF SYMBOLS (Continued)

C_s	shear wave velocity of an infinite elastic solid; also torsional wave velocity of a membrane cylindrical shell and solid circular rod
C_1, C_2	integration paths along a circular arc at infinity, see Figure 5.1
C_ϕ	phase velocity
C_Φ	normalized phase velocity, $= C_\phi / c_p$
D	normalized extensional rigidity of the shell, $= Eh/(1-\mu^2)$
$D_{sn}(\xi)$	normalized shell stiffness component, Equation (3.23a)
e	base of the Napierian logarithm, $= 2.718\cdots$
$e_{xx}, e_{\theta\theta}, e_{\theta x}$	cylindrical membrane strain components, Equation (2.8)
E	elastic modulus of shell material
$f_d(x,\theta,t)$	radial applied force distribution, Equation (3.16)
$[\tilde{F}]$	nondimensional spectral force matrix, Equation (3.18)
F_n	normailized modal force, $= \varepsilon_n F_r / 2\pi DR^2$
F_r	magnitude of the applied harmonic point force
$g_n(\xi)$	modal kernel of the inverse Fourier transform integral representation of $w(\theta,x)$, following Equation (5.28)
$G_n(\xi)$	modal kernel of the inverse Fourier transform integral representation of $p(r,\theta,x)$, Equation (5.2)
h	nondimensional cylindrical shell thickness (normalized by R)
$H_n^{(1)}, H_n(z)$	Hankel function of the first kind, $= J_n(z) + jY_n(z)$
$H_n^{(2)}(z)$	Hankel function of the second kind, $= J_n(z) - jY_n(z)$
$\bar{H}_{n+1/2}(z)$	half-order Struve function
I	normalized plate moment of inertia, $= \beta$
$[I]$	identity matrix
$I_n(z)$	modified Bessel function of the first kind
j	positive square root of -1

LIST OF SYMBOLS (Continued)

$J_n(z)$	Bessel function of the first kind
$k=k_r+jk_i$	nondimensional acoustic wavenumber, $= \omega R/c$
k_s	nondimensional effective structural wavenumber, $=[\xi^2+n^2]^{1/2}$
$K_n(z)$	modified Bessel function of the second kind
$[L]$	nondimensional differential operator matrix for the Flugge cylindrical shell equations with elements L_{ij}, Equation (2.12)
L_1	denotes the longitudinal branch of a fluid-loaded cylindrical shell in the complex ξ-plane
L_3	denotes the extensions of the real flexural branch of a fluid-loaded cylindrical shell into the complex ξ-plane at frequencies below the lower cutoff frequency and above the upper cutoff frequency
m	integer circumferential mode order number
$\tilde{m}_{ij}$	components of $\tilde{M}_{ij}$ defined by Equation (2.21)
$[M]$	nondimensional modal differential operator matrix for the Flugge cylindrical shell equations with elements M_{ij}, Equation (2.16)
$[\tilde{M}]$	nondimensional modal spectral operator matrix for the Flugge cylindrical shell equations with elements $\tilde{M}_{ij}$, Equation (2.21)
$[\tilde{M}_f]$	nondimensional spectral fluid reaction matrix, Equation (4.14)
n	integer circumferential mode order number
n_{max}	maximum mode order number at which real singularities exist for a fluid-loaded cylindrical shell, Equation (4.28)
N	modal truncation value of the Fourier series associated with the branch integral contributions $B_{1n}, B_{2n}, \simeq \gamma a+10$, see Figures 5.2 and 5.9
$N_{sn}(\xi)$	normalized shell stiffness component, Equation (3.23b)
$p(r,\theta,x,t)$	acoustic pressure field in the fluid
$p_a(\theta,x,t)$	acoustic loading on the cylindrical shell, $= p(r=a,\theta,x,t)$
p_{ref}	reference pressure, $= F_r/(2\pi R)^2$

LIST OF SYMBOLS (Continued)

$q=1,2,3$	indice associated with the branch nomenclature of a cylindrical shell in vacuo
$q_n(\xi)$	modal kernel of the integral of Equation (5.30)
$Q(r,\theta,\xi)$	kernel of the integral of Equation (5.16)
$Q_n(\xi)$	modal coefficients of $Q(r,\theta,\xi)$ and modal kernel of Equation (5.10) associated with $B_{2n}(r,x)$
r,θ,x	nondimensional cylindrical coordinates where both r and x have been normalized by R
$r_n(x)$	modal contribution of a real singularity to $res(\theta,x)$, equation (5.33)
$res(\theta,x)$	total residue contribution of real singularities to $w(\theta,x)$, Equation (5.32)
R	middle-surface radius of the cylindrical shell; also, in Chapter 5 designates path of integration along the real axial wavenumber axis, see Figure 5.1
$R_n(r,x)$	modal contribution of a real singularity to $Res(r,\theta,x)$, Equation (5.25)
$Res(\theta,x)$	total residue contribution of real singularities to $p(r,\theta,x)$, Equation (5.24)
s_j	j^{th} coefficient of the characteristic equation for a cylindrical shell in vacuo, Equation (3.5)
S	normalized plate shear deformation factor, $= 24I/\pi^2(1-\mu)$
t	time
$u,v,w(\theta,x,t)$	nondimensional axial, circumferential, and radial displacement of the shell's middle surface (normalized by R)
u_r,u_θ,u_x	nondimensional orthogonal displacement components at any point within the cylindrical shell (normalized by R)
$U_n,V_n,W_n(x)$	modal coefficients of the Fourier expansion of u,v, and w
w_{ref}	nondimensional reference displacement, $= p_{ref}/D$
$[\tilde{X}]$	nondimensional spectral displacement matrix
$X_{sn}(\xi)$	normalized spectral modal reactance of the shell, Equation (3.22)
$Y_n(z)$	Bessel function of the second kind

LIST OF SYMBOLS (Continued)

$Z_{an}(\gamma)$	normalized spectral modal acoustic radiation impedance, Equation (4.11)
$Z_{fn}(\gamma r)$	spectral modal specific acoustic impedance, Equation (4.10)
$Z_{sn}(\xi)$	shell spectral modal mechanical impedance, Equation (3.22)
β	normalized thickness-to-radius ratio,= $h^2/12$
$\gamma=\gamma_r+j\gamma_i$	nondimensional radial wavenumber (normalized by R), Equation (4.6)
$\bar{\gamma}$	magnitude of γ, used where phase has been explicitly shown
γ_o	general point in the first quadrant of the complex γ-plane
Γ_j	designates the j^{th} portion of the integration path along the branch line, see Figure 5.1
$\delta(z)$	Dirac delta function,= 1 for z=0 and zero otherwise
δ_{nm}	Kronecker delta function,= 1 for n=m and zero otherwise
Δ	coefficient,= $\rho\Omega^2/\rho_s h$, Equation (4.15)
ε_n	*Neumann* factor,= 1 for n=0 and 2 for n>0
$\varepsilon_{xx}, \varepsilon_{\theta\theta}, \varepsilon_{rr}$ $\varepsilon_{\theta x}, \varepsilon_{xr}, \varepsilon_{r\theta}$	strain components in the cylindrical shell, Equation (2.3)
$\kappa_{xx}, \kappa_{\theta\theta}$, $\kappa_{x\theta}, \kappa_{\theta x}$	curvature changes of the cylindrical shell's middle surface, Equation (2.9)
λ	eigenvalue
λ_{nq}	q^{th} eigenvalue of a cylindrical shell in vacuo at circumferential mode order number n
λ^c_{nq}	lower cutoff eigenvalue for the q^{th} branch of a cylindrical shell in vacuo at circumferential mode order number n
$[\tilde{\Lambda}]$	nondimensional spectral characteristic matrix
μ	Poisson's ratio of shell material
$\xi=\xi_r+j\xi_i$	nondimensional axial wavenumber (normalized by R)
ξ_j	denotes a point in the j^{th} quadrant on the top Riemann sheet of the complex ξ-plane
ρ	fluid mass density; Chapter 2 only, nondimensional radial component measured from R such that r=1+ρ

LIST OF SYMBOLS (Continued)

ρ_s	mass density of shell material
$\sigma_{xx}, \sigma_{\theta\theta}, \sigma_{\theta x}$	cylindrical shell stress components, Equation (2.10)
ϕ_c	coincidence angle, $= \sin^{-1} \sqrt{\Omega_c/\Omega}$
Ψ	principal angle of Equation (4.39) used to calculate n_{max}
ω	circular frequency
ω_c	classical plate coincidence frequency
ω_{ring}	ring frequency of a cylindrical membrane shell, $= c_p/R$
Ω	normalized frequency, $= \omega/\omega_{ring}$
Ω_c	normalized plate coincidence frequency, $= \beta^{-1/2}(c/c_p)^2$
Ω_{max}	normalized frequency at which n_{max} is attained, Equation (4.40)
Ω_{nq}	q^{th} natural frequency of a cylindrical shell in vacuo at circumferential mode order number n.
Ω_{nq}^c	lower cutoff frequency of the q^{th} branch of a cylindrical shell in vacuo at circumferential mode order number n
Ω_n^c	lower cutoff frequency of a fluid-loaded cylindrical shell at circumferential mode order number n
Ω_n^u	upper cutoff frequency of a fluid-loaded cylindrical shell at circumferential mode order number n
∇^2	Laplace operator
∇_R^2	normalized Laplace operator, $= R^{-2}\nabla^2$

ACKNOWLEDGMENTS

I would like to thank Dr. Sabih Hayek, thesis advisor, for his assistance, encouragement, and guidance during the course of this study. His energy and intellectual ardor have been both a stimulation and a source of aspiration. I would also like to express my appreciation to Dr. Alan Stuart who shared not only his office space but also his ideas on a wide range of topics. Appreciation is extended to Dr. Thomas Gabrielson and Dr. Courtney Burroughs for many helpful discussions. Further appreciation is extended to Dr. Jiri Tichy and to Dr. William Thompson, Jr., for serving on my doctoral committee.

I would like to thank Dr. Denos Gazis for his kind permission to reprint a portion of the material shown in Figures 3.19, 3.20, and 3.21 [Gazis (1959)]. Special appreciation is extended to the Applied Research Laboratory of The Pennsylvania State University for the use of its facilities during a portion of this research. I would also like to thank Joyce Scott and Catherin Osborn for their assistance in the preparation of the manuscript. Robert Wilkinson's assistance with the technical aspects of word processing a scientific manuscript is gratefully appreciated and acknowledged.

I would like to especially acknowledge the personal sacrifice, encouragement, and cooperation shown by my wife, Joyce Farman, during the many years over which this research has been pursued.

This research was partially supported by the Naval Underwater Systems Center. In particular, the interest and assistance of Dr. William Von Winkle, Dr. John Kingsbury, Dr. Charles Sherman, Dr. Ronald Radlinski, Larry Freeman, and George Carey is gratefully acknowledged.

Chapter 1

INTRODUCTION

1.1 Statement of the Problem

In this investigation the acoustic nearfield of a cylindrical shell of infinite axial extent will be examined. Fluid loading is considered external to the shell while the shell interior remains unloaded except for the application of a time harmonic point force acting in the radial direction. The behavior of the acoustic nearfield is of particular importance in the characterization of the self-noise of a sonar array attached to such a structure. The acoustical and structural behavior of this simple geometry can provide insight into the mechanisms by which energy is transported and the parameters that control these mechanisms. By use of Green's function techniques these results could be extended to include any type of distributed mechanical loading or non-harmonic excitation.

1.2 Historical Background

Gaseous loading usually has a negligible effect upon the dynamic response of a structure. Notable exceptions occur when the ambient medium is confined by rigid boundaries or when a nearly lossless structure is excited at one of its resonances. In contrast, the surface force exerted by a dense medium such as water is often comparable to the inertial and damping forces found in a metal structure undergoing dynamic motion. Fluid loading alters the structural response, thus creating a feedback loop that couples the elastic and acoustic media.

An early description of the behavior of acoustic radiation loading was given by Stokes (1868) where he discussed the transition from low to high frequency. As discussed by Crighton and Innes (1984), fluid loading is a non-local mechanism. Any attempt to locally deform a structure can lead to a slowly decaying pressure field that acts to excite the structure further away. The interaction between the ambient fluid and the structure has been a topic of considerable interest within the field of underwater acoustics from the time of Rayleigh.

During the past two decades considerable progress has been made in understanding how the ambient medium and the structure interact dynamically. This has been due to both the heightened interest in the subject among the Naval community and to the availability of high speed digital computers and efficient fast Fourier transform (FFT) algorithms. Researchers have commonly used four different methods to solve problems in which the fluid and structure are coupled. These are often called integral methods, the finite element method (FEM), the addition of a fluid virtual mass, and normal mode methods. Junger (1975) has presented an excellent historical review of techniques for solving radiation and scattering problems of submerged elastic structures. The particular approach chosen is often due to the geometry of the problem, the frequency regime of interest, the length scale of the structure, the type of results desired, computational considerations, or the personal preference of the investigator.

Integral methods formulate the desired results in terms of an integral equation. The complexity associated with solving the differential equation of motion of the system and its boundary conditions is replaced by the difficulty in performing a complicated integration. The integral contains information about the equation of motion, the boundary

conditions, and other dynamic specifications such as the behavior of the solution at large distances. For this reason, it is possible to derive general properties of the solution without an exact knowledge of its form. Usually asymptotic techniques are used to provide a solution in the farfield or high frequency limit. Numerical integration is often employed at intermediate ranges or frequencies. Integral transform techniques are a classical example of an integral method. Another example would be the use of the Helmholtz integral approach.

The finite element method (FEM) is a wholly numerical method that requires a digital computer. The FEM regards a system as a finite assemblage of discrete elastic elements where each element represents a continuous structure. Elements connect to their neighbors at discrete points, called nodes, at which the displacement and internal forces are required to be in balance. In this manner, complex systems with irregular geometries can be modeled as the sum of a large number of simple systems. The resultant governing equation of motion of the system and its boundary conditions are represented by matrix equations. The problem is characterized by a sequence of matrix manipulations. The power of the FEM lies with the complexity of the systems that can be analyzed. Unlike other methods, no requirement exists that boundaries represent constant coordinate surfaces. Perhaps the greatest disadvantage of the FEM is the long computer time required and the labor necessary in preparing the input data that characterizes the system. For acoustical problems, the FEM has been handicapped by difficulties in properly terminating the fluid model to represent energy propagating into the farfield. Recent advances have partially overcome this problem. Due to numerical considerations, the FEM remains essentially a low frequency method.

The virtual, effective, or equivalent mass method is an approximate method that attempts to characterize the fluid radiation loading upon a structure as an added mass (or impedance) term in the equation of motion. The concept of a virtual mass is used to quantify the fluid loading and therefore dynamically decouple the fluid and structure. Other methods would then be used to solve the problem. This is a lumped parameter approach that is generally accurate only for limiting values of some parameter like frequency. The difficulty is in accurately approximating the fluid impedance. Although the virtual mass is a property of the medium, it also depends upon the shape and volume of the vibrating structure. Perhaps the earliest example of the use of this method is Rayleigh's (1945) formulation in 1878 of the equation of motion of a piston in a rigid baffle that is radiating into an acoustic fluid. The piston is mounted on a spring. Rayleigh constructed an equivalent single degree of freedom system vibrating in vacuo that contained a larger mass and damping to account for the fluid.

An approximation that has recently gained some popularity is the doubly asymptotic approximation (DAA), as discussed by Geers (1978) and Geers and Felippa (1983). The DAA is asymptotically exact for both the low frequency, incompressible, inertial impedance and the high frequency, resistive, plane wave impedance. It effects a smooth transition in the intermediate frequency range. The DAA may also be expressed as a matrix of ordinary differential equations for application in discrete element analysis of complex structures. The method is also known as the matched asymptotic expansion, as described by Pierucci (1979). According to Junger (1984), the DAA does not correctly account for impedance curves that diverge or display a peak around the coincidence frequency.

The normal mode (or eigenfunction) method expresses the parameter of interest, such as the dynamic motion of the structure, in terms of a series expansion of the eigenfunctions of the system. The eigenfunctions represent solutions of the differential equations of motion for which the boundary conditions are satisfied. Slow convergence behavior of these series solutions often limit the practical application of the normal mode method. This method is suited for uniform or spatially periodic excitation that corresponds to discrete wavenumber spectra. A point force applied to a sphere or a line force exciting a cylinder are examples. Problems such as infinite plates or cylinders excited by a point force result in continuous wavenumber spectra and are therefore more compatible with integral transform methods.

This investigation employs integral transform methods to reduce the governing differential equations of motion to a set of algebraic equations in wavenumber space. Eigenfunction analysis is used to express the acoustic pressure in cylindrical coordinates in terms of a Fourier series of modal pressures over the discrete circumferential wavenumber spectra. For the acoustic nearfield, this spectra is shown to be finite. Each modal pressure is represented by an inverse Fourier integral over all of the real axial wavenumbers. The integrand is expressible in terms of both a spectral modal specific acoustic impedance that relates the radial surface velocity to the acoustic pressure and in terms of a spectral modal mechanical impedance of the shell vibrating in vacuo. Cauchy's theorem and integral formula are used to solve the integrals. The acoustic nearfield is represented as a residue contribution to the integral.

A recent report by Vogel and Feit (1980) also looks at the problem of a point-excited cylindrical shell immersed in a fluid. Although

the formulation was similar, they chose to solve the integrals numerically. However, Vogel and Feit are primarily interested in describing the vibrational response of the cylinder and do not calculate the acoustic nearfield. Much of their analysis deals with the driving point admittance (or velocity). A limited amount of velocity data around the cylinder circumference or along the cylinder axis is shown. Comparisons are made with a point-excited plate both with and without fluid loading. Vogel and Feit show that the greatest difference between the velocity response of a point-excited plate and cylinder occurs at low frequency and in the vicinity of the cylinder's ring frequency.

Liu and Tucker (1984a) have also investigated this problem. The formulation was again similar, and like Vogel and Feit, they also solve the integrals by numerical integration. Since Liu and Tucker were primarily interested in characterizing the power flow, they were only interested in the gross details of the fluid and structure dynamics. They decomposed the input power into a power radiated into the farfield and a "lost" power. This lost power was represented by energy propagating both down the elastic shell and in the acoustic nearfield. No detailed investigation of the acoustic nearfield was performed. The effect of structural damping upon the power flow into the acoustic farfield was investigated. They concluded that below the classical plate coincidence frequency radiated power is insensitive to an increase in structural damping. Above this frequency, the addition of structural damping only moderately reduces the radiated power. Comparisons were also made between the point-driven cylinder and both the line-driven plate and ring-driven cylinder. In a subsequent report, Liu and Tucker (1984b) investigated the effect the addition of a massless, compliant layer would have upon the radiated power. Two resonance frequencies are induced by

the addition of the layer. One defines an amplification region of radiation reduction (negative reduction) and the other defines a region with a low structural vibration level. In this second region the structural damping is enhanced by coating dissipation.

Asymptotic techniques are often used to solve the inverse transform integral. The farfield of the point-excited cylindrical shell has been studied by both Bleich (1954) and Junger and Feit (1972) using the method of steepest descents. A physical interpretation of this technique is that the pressure at a given point in the farfield is predominately associated with the structural wavenumber that matches the trace of the acoustic wavenumber on the radiating surface. High frequency asymptotic analysis of cylindrical shells has been primarily concerned with acoustic scattering using the Sommerfeld-Watson formulation. This method transforms the slowly converging Fourier series into an integral expression that is in turn expressible as a residue summation that rapidly converges. Reference is made to Horton et al. (1962), Doolittle and Uberall (1968), Junger and Feit (1972), Ugincius and Uberall (1968), and Uberall et al. (1977) as examples of this creeping wave solution. Since the infinite cylinder can be approximated by an infinite plate at high frequency, Feit's (1966, 1970) work would also be of interest.

Several simplifying approximations have been used by researchers in order to avoid solving the inverse transform integrals. One such assumption is to consider the exciting force to be independent of the coordinate that defines the axial direction of the cylinder. Effectively the degrees of freedom of the problem are reduced by one. This leads to a plane or two-dimensional problem commonly referred to as the line-excited problem. Examples are Junger (1952a, 1952b) and Junger and Feit

(1972). The acoustic field solution is expressed as an infinite summation over the circumferential modes.

Another assumption is that the excitation force is periodic with a specified axial wavelength. The solution is therefore applicable only for the wavelength chosen while, in reality, all wavelengths are permissible for a point-excited, infinite cylinder. Bleich and Baron (1954) and Baron and Bleich (1954) use this technique in their classic discussion and prediction of the natural frequencies and modes of an infinite cylindrical shell immersed in a fluid. They use the in vacuo modes as generalized coordinates in the formulation of the fluid-loaded velocity response of the shell. Kalolikhina (1958) also assumed periodic excitation, but restricted the analysis to the axisymmetric mode in his investigation of the farfield acoustic radiation.

If the infinitely long cylindrical shell contains rigid, periodic rib stiffeners, the inverse transform integral is reduced to a summation. This technique was used by Junger (1953, 1954) for both the radiation and scattering problem. However, if the ribs have a finite impedance, the regions between ribs can couple mechanically and the inverse transform integral formulation must be retained. Burroughs (1984) investigated the case of a doubly periodic set of elastic ring supports. The integrals were solved for the farfield by the method of steepest descents.

The true finite cylindrical shell problem can only be handled by surface integral techniques. Examples of the method are Cohen and Schwiekert (1963), Chertock (1964), Schenck (1968), and Copley (1968). Sandman (1976) investigated the fluid radiation loading due to a generalized velocity distribution on a finite cylinder with rigid end caps. Sandman's work represents a solution of the Helmholtz integral equation

by use of a Green's function. In this formulation, the discrete fluid loading matrix is often referred to as the influence coefficients.

By extending the finite shell with semi-infinite, rigid, cylindrical baffles, the problem becomes analytically tractable using eigenfunction techniques. Stephanishen (1978, 1982) used a combined Green's function and Fourier integral method to investigate the radiation loading and radiated power from a finite cylinder with a non-uniform velocity distribution. In the first of these papers, the general formulation is for the infinitely long elastic cylinder, however the cases evaluated all have a nonzero velocity distribution of finite length. In the second of these papers, Stephanishen expands the velocity field in terms of the in vacuo modes of the finite elastic shell. A similar technique was also used by Harari and Sandman (1976) in a study of the vibratory response of a three-layered cylindrical shell. Smith (1959) used lumped parameter assumptions to solve the finite cylinder with rigid ribs problem in terms of matrix equations in a manner that is somewhat analogous to the later development of the finite element method.

The introduction of FFT methods has been a powerful tool in the solution of radiation problems. The FFT algorithm has a tremendous computational advantage over other numerical integration schemes because of its speed. Recent papers by Stephanishen and Benjamin (1982) and by Williams and Maynard (1982) are an excellent discussion of the method using planar surfaces as examples. A subsequent paper by Stephanishen and Chen (1984) treats the infinite cylinder problem by FFT methods. The numerical examples presented are for a finite cylinder in an infinite baffle. The excitation is periodic in the axial direction. This work is particularly interesting because acoustic nearfield results are

presented. Below the coincidence frequency, edge effects due to the finite length of the cylindrical shell are shown to predominate.

Many of the methods for solving fluid-loaded cylinder problems and much of the insight into the dynamic interaction between the fluid and structure have come from investigations of the fluid-loaded plate problem. The structure has been idealized as a membrane, thin plate, or thick elastic plate. The velocity response and acoustic fields generated by point or line forces or moments have been studied. Like the cylindrical shell results, the plate results are usually confined to the farfield or to the drive-point behavior because they are quantities of physical interest and there are efficient analytical techniques to handle them. Although a complete historical description of these investigations would be too lengthy for our purpose, it would be appropriate to briefly mention some of the more pertinent contributions.

One of the earliest investigations of the power radiated from a point-excited elastic plate was given by Skudrzyk (1958). The farfield radiated pressure was investigated by Gutin (1965), Skudrzyk (1968), and [illegible]it (1970). An analysis of the radiated power due to a concentrated moment was given by Thompson and Rattaya (1964). Maidanik and Kerwin (1966) and Maidanik (1966) investigated the influence of fluid loading upon the radiation from an elastic plate. All of these investigations used classical thin plate theory. However, it is known that classical plate theory fails at high frequency where it predicts infinite flexural phase and group velocities. For this reason many investigators have used the more complicated Timoshenko-Mindlin plate theory because it includes the effects of shear deformation and rotary inertia that are important at high frequency. Timoshenko-Mindlin plate theory correctly predicts that the flexural phase and group velocities approach the

Rayleigh limit at high frequency. A similar dichotomy exists with shell theory between so-called thin and thick shell theory. However, since the cylindrical shell can be approximated by a plate above the plate coincidence frequency, the choice of thin or thick shell theory is not as important below the plate coincidence frequency unless the shell thickness-to-radius ratio is greater than one-tenth. Both Feit (1966) and Stuart (1972) investigated the radiated pressure field from a point-excited plate using Timoshenko-Mindlin plate theory.

Crighton (1977) has studied the driving point admittance of a point-excited elastic plate and concluded that at low frequency the admittance acts as a stiffness. This is in contrast to the line-excited plate where Crighton (1972) has shown that the admittance is mass-like at low frequency. Both Smith (1978) and Junger (1978) have offered physical explanations for this difference. Other recent work has been concerned with the modes and resonances of the fluid-loaded plate. An excellent example of the role scaling parameters and asymptotic analysis has played in these investigations is given in two papers by Crighton and Innes (1983, 1984) and one by Maidanik (1966). A discussion of the physical significance of the leaky waves has included investigations by Stuart (1976a, 1976b), Strawderman et al. (1979), and Crighton (1979). Pierucci and Graham (1979) and Pierucci (1981) have studied the free bending waves in thick plates.

1.3 Organization of the Investigation

A discussion of shell theory and the development of the Flugge equations is presented in Chapter 2. The differences and limitations between exact and approximate theories as well as between thin and thick shell theory are discussed. The relationship to plate theory is presented. Important concepts such as dispersion, phase velocity, and

group velocity are introduced. The geometry and coordinate system for the problem is defined and a normalization with respect to the shell's middle-surface radius of all length and wavenumber parameters is introduced. The Flugge equations are developed for a general applied radial force and acoustic loading. Details of the development using variational principles are presented in the Appendix. The governing set of three partial differential equations are reduced to a set of algebraic equations by expanding the shell deformations in a Fourier series over the circumferential coordinate and by applying an integral transform of the axial coordinate. The chapter ends by expressing the shell displacements in terms of a series of modal displacements, each represented by an inverse Fourier integral.

Chapter 3 discusses the shell vibrating in the absence of fluid loading. The canonical form of the shell equations are used to develop eigenfunction solutions known as branches that represent frequency spectra. An asymptotic analysis at large wavenumber is performed in order to specify a branch nomenclature. The concept of a cutoff frequency is introduced and the behavior of the branches in its vicinity is investigated on a modal basis. Frequency spectra, dispersion curves, and group velocity predictions are presented. The effect of varying the shell's thickness is discussed. A comparison is made between the Flugge shell theory and a theory developed by Gazis (1959) based on the exact three-dimensional equations of motion. The comparison indicates that Flugge theory is adequate at frequencies below the classical plate coincidence frequency. Forced motion of the shell is considered and developed in a form convenient for later work when fluid loading is included. A modal mechanical impedance in the transform domain is introduced that represents the total contribution of the shell to the fluid-loaded problem.

The vibration of a shell in the presence of an external fluid is discussed in Chapter 4. Boundary conditions at the shell-fluid interface and at infinity are used to specify a spectral modal specific acoustic impedance that modifies the in vacuo integral representations of the radial displacement and acoustic pressure. These boundary conditions introduce a radial wavenumber that is a multi-valued function of the axial wavenumber. Both physical and mathematical reasons are introduced to favor the use of the Sommerfeld branch lines to force a single-valued behavior of the radial wavenumber in the domain of interest. The behavior of the normalized spectral modal acoustic radiation impedance is presented over the entire radial wavenumber domain. Existence properties of the singularities are developed and the location and behavior of both the real and complex singularities are investigated. Comparison is made with the in vacuo modes of free vibration. For each circumferential mode order number, fluid loading is found to require both a lower and an upper cutoff frequency which define a frequency bandwidth of free mode propagation. As circumferential mode order increases, the associated bandwidth decreases such that above a critical mode order no free propagation is possible.

Chapter 5 discusses the solution by Cauchy's theorem and integral formula of both the shell's radial displacement and the acoustic radiation field for a point-excited cylindrical shell immersed in a fluid medium. Numerical examples are presented in the acoustic nearfield defined as $a \leq r \leq 2a$ and $0 \leq x \leq 10a$. The radial displacement of the shell and the acoustic pressure loading on the shell are presented. A summary of the problem and conclusions drawn from the study are presented in Chapter 6.

Chapter 2

SHELL THEORY

2.1 Introduction

Shell theory is a diverse field which has been the continuing subject of many textbooks and hundreds of papers. This thesis has an interest in shell theory primarily as a displacement boundary surface for an acoustic field. In order to place the shell theory chosen for this study in perspective, the initial discussion will deal with the general types and characteristics of shell theories. Specific reference is made to Timoshenko (1940), Flugge (1973), Leissa (1969 and 1973), and Graff (1975) for background material, and to Graff, Greenspon (1960), Frymoyer (1967), and Walter (1979) for historical discussion. The general discussion will be followed by a development of the Flugge shell equations and their solution using integral transform techniques.

2.2 Exact and Approximate Theories

The so-called "exact" shell theories are based upon a three-dimensional analysis for an elastic continuum in which mass, momentum, moment of momentum, and energy are conserved. The usual approximations are based upon assumptions that the strains are small, a linear relationship exists between stress and strain, and terms associated with higher-order ratios of shell thickness to mean radius can be ignored. Often a homogeneous, isotropic material is assumed. Both the linearized elastic theory and the boundary conditions which result from such an analysis are complex and difficult to use. Reference is made to the

work of Gazis (1959) as an example of an exact shell theory. In addition to the elastic assumptions discussed above, an exact theory can also account for material anisotropy, piezoelectric effects, thermal effects, viscoelastic effects, plasticity effects, nonlinear effects, and fluids. As might be expected, for all but the fluid case, the resulting equations would be much more complicated than those for the linear elastic, homogeneous, isotropic material situation.

Approximate shell theories are usually based upon a strength-of-materials approach where assumptions have been made about the material deformations that approximate the detailed behavior of a solid. Approximate shell theories are usually characterized as membrane, bending, and higher-order theories. Additionally, both membrane and bending theories are generally referred to as thin shell theories, while the higher-order theories are known as thick shell theories. Thin shell theories use the three displacement components of the shell's middle surface as degrees of freedom. Consequently, thin shell theories have a third-order stiffness matrix and a characteristic equation which yields three roots. Thick shell theories usually allow for two additional degrees of freedom by including two rotations of the normal to the shell's middle surface. Consequently, a more complex fifth-order stiffness matrix results, and the characteristic equation yields five roots. This is contrasted with the exact theory which has an infinite number of roots. The increased complexity of both exact theory and thick shell theory is such that, when applicable, the thin shell approximation is both analytically and computationally advantageous. The zero-order Flugge shell equations used in this work are an example of a bending theory and represent the thin shell form of the Mirsky-Herrmann (1956-59) higher-order theory which contains both rotary inertia and shear deformation effects.

Classical flat membrane theory is the two-dimensional analog of the string. Restoring forces arise from in-plane tensile forces, and there is no resistance to shear and bending forces. In membrane shell theory, only normal and shear forces acting in the mid-surface of the shell are considered. Transverse shear forces and bending moments are considered to be negligibly small. The shell is thus assumed to behave as a curved membrane. Membrane theory is often adequate for relatively uniformly distributed, applied radial loading. In regions in which larger loading gradients exist, such as in the vicinity of concentrated loads and near boundaries, or for applied loading which is not radial, such as a twisting moment or in-plane surface tractions, membrane theory will not be sufficient, and a bending or higher-order theory would be required.

Classical plate theory represents a two-dimensional analog of a beam in which bending moments and transverse shear forces are active. Bending shell theory accounts for moments and transverse shear forces in addition to the membrane forces. The shell is thus assumed to behave as a curved, thin plate. From experience with beam theories based upon the exact equations of elasticity, it is known that shear deformation is important at higher frequencies. Since shear deformation requires a rotation of the normal to the shell's middle surface (or a contradiction of the hypothesis that plane sections remain plane), bending theory assumes no shear deformation. Ignoring rotary inertia effects omits the rotational kinetic energy contribution to the system's energy. This is acceptable at low frequencies where the rotational velocity is small. However, at high frequencies where the rotational velocity is appreciable, rotary inertia must be included. Therefore, bending theory would not be expected to be adequate at high frequencies. Also, in regions of

high loading gradients, both rotary inertia and shear deformation become more important, and a higher-order shell theory would be required.

Higher-order shell theories are related to bending theory in a manner analagous to the relationship between thick plate and thin plate theory. Higher-order theories account for rotary inertia effects, shear deformation effects, or both. In addition to the shell's middle-surface displacements, higher-order theories also utilize two rotations of a normal to the shell's middle surface. Both membrane and bending theory are formulated by neglecting higher-order ratios of shell thickness to mean radius, while thick shell theory includes more of these effects. In general, the range of validity of thick shell theories is greater than that for thin shell theories. However, the added complexity of the equations presented by thick shell theory may not be justified, especially for problems with a ratio of shell thickness to radius less than 1/20. When frequencies get so high that the displacement distributions are no longer linear across the shell thickness, then all approximate shell theories lose their meaning and only exact theories that allow nonlinear behavior would be adequate.

2.3 Dispersion

The displacement distribution predicted by exact and approximate shell theory is generally dispersive. That is, each harmonic component propagates at a different wave speed such that a pulse would distort with time. In this context, a differentiation must be made between the phase velocity and the group velocity. The phase velocity refers to the propagating velocity of a constant phase wavefront associated with a harmonic component and is defined as

$$C_\phi = \frac{\omega}{k}$$

where k is the wavenumber of the wave and $C=C(\omega)$ is true for a dispersive system. The group velocity refers to a dispersive system having many harmonic components, such as a pulse. The disturbance that arrives at a particular point x at time t will be the result of several harmonic contributions and will have traveled with a group velocity $C_g=x/t$. This disturbance will have a dominant frequency ω_o determined from a stationary phase treatment of the problem. According to Brillouin (1960), the group velocity is represents the rate at which energy is transported. A more common definition is given by

$$C_g = \frac{d\omega}{dk} = C_\phi + k \frac{dC_\phi}{dk} \quad .$$

For a nondispersive medium $C_g = C_\phi$.

Two methods of displaying dispersion characteristics are commonly used. The first is the frequency spectrum of the system which relates frequency to wavenumber. A straight line passing through the origin represents a nondispersive system. The group velocity is, therefore, the local slope at a point of the frequency spectrum, while the phase velocity is the slope of the chord to a point. The second method is a dispersion curve which relates phase velocity to wavenumber. A constant phase velocity line indicates a nondispersive system. Often, normalized parameters are used, as well as logarithmic scales. By inspection of a dispersion curve, it is possible to determine frequency, wavelength, phase velocity, and group velocity. If the frequency is taken as the independent variable, as is physically more appropriate, then both the frequency spectrum and the dispersion curve will yield wavenumbers in a complex wavenumber space. Reference is made to Frymoyer for examples of frequency spectra in the complex wavenumber domain for a cylindrical shell in-vacuo developed using the Flugge equations. When studying

coincidence phenomena, the phase velocity along the boundary of two media must match to allow constructive interference as the waves propagate. It is not necessary that the group velocities be the same.

Dispersive systems are often associated with a phenomenon known as "mode cutoff." Systems which have a finite phase velocity at infinite frequency, such as dispersive acoustic and elastic systems, have a frequency spectrum that can yield complex or imaginary wavenumbers below a certain frequency, known as the "cutoff" frequency. Below the cutoff frequency, the imaginary component of the wavenumber acts as an attenuation such that the mode cannot be said to propagate as a wave. At driving frequencies above the cutoff frequency, the mode will propagate. The cutoff frequency can be found by evaluating the characteristic equation in the limit as the wavenumber tends to zero. This implies an infinite wavelength which represents a zero frequency in a nondispersive system, but which can yield a nonzero frequency for a dispersive system.

2.4 Shell Displacements and Wave Types

The eigenvalues of any shell theory that are related by continuity of frequency considerations are known as branches. Generally, there is one branch for each degree of freedom of the system. In contrast to plate theory, continuity requirements in the shell's circumferential coordinate give rise to an infinite number of circumferential mode order numbers. For each of these integer mode order numbers, a unique characteristic equation exists that defines the eigenvalues. For fixed circumferential mode order number, the branches represent frequency spectra of free wave propagation in the shell where the associated eigenfunction represents the relatioship between the degrees of freedom that comprise that propagation.

Approximate shell theories are usually based upon a displacement field which is linear in the thickness coordinate. For a bending shell theory, the longitudinal (axial), tangential (circumferential), and transverse (radial) displacements of the shell middle surface represent the system's degrees of freedom. For all circumferential mode orders except the axisymmetric mode, all of the modal displacements within each branch are coupled. Often, the branch is named after the displacement component which contributes the most energy to the vibratory mode over some range of interest. For example, many authors speak of a longitudinal branch. Since the contribution to the total energy is a function of a normalized wavenumber, the branch nomenclature may not be appropriate over an entire frequency range of interest.

Exact theory is based upon a displacement field that is nonlinear in the thickness coordinate. In addition to the infinite number of allowable modes, wave types exist within the structure that do not exist in thin shell theory, which yields only coupled displacement modes. Graff (1975) summarizes two of these for the case of an infinite elastic solid. One of these is a dilatational wave which is irrotational and associated with a change in volume. Graff calls this the P wave, or primary wave, and it can be thought of as longitudinal wave associated with elongation of material fibers and it propagates with a phase velocity given by

$$C_1^2 = \frac{E(1-\mu)}{\rho(1+\mu)(1-2\mu)}$$

for the axisymmetric mode. Here E is the material's elastic modulus, ρ its mass density, and μ its Poisson's ratio. The coupled longitudinal-flexural wave velocity for the axisymmetric mode of a cylindrical membrane shell is given by

$$C_b^2(\omega \to 0) = E/\rho \leq C_1^2$$

in the low frequency limit and is the same as the longitudinal bar velocity. In the high frequency limit, this becomes

$$C_b^2(\omega \to \infty) = \frac{E}{\rho(1-\mu^2)} \leq C_1^2$$

which is also the low frequency phase velocity, C_p, for compressional waves in a thin plate. For $\mu = 0.28$,

$$C_b(\omega \to 0) = 0.88\ C_1$$

and

$$C_b(\omega \to \infty) = 0.92\ C_1\ .$$

The second type of wave is a distortional wave that is equivoluminal and associated with distortion of the angle between two fibers but without elongation of the fibers. Graff calls this the S wave, or shear wave, which can be thought of as a torsional wave. The S wave has a phase velocity given by

$$C_s^2 = \frac{E}{2\rho(1+\mu)}$$

in the axisymmetric mode. The shear wave speed C_s for an infinite elastic solid is equal to the torsional wave speed of both a membrane cylindrical shell and a solid circular rod.

The addition of a boundary to the system, such as a semi-infinite elastic medium and a vacuum half-space, introduces a reflective surface. Under such a condition, a phenomenon known as mode conversion may exist upon reflection such that pure P or S waves reflect both P and S waves. For a doubly bounded structure such as a shell, the characterization can

become quite complicated. The addition of a boundary also gives rise to a third wave type known as a surface wave. It contains only transverse displacements and is confined close to the surface. For a vacuum half-space this wave is known as a Rayleigh surface wave, and it has a phase velocity given by Viktorov (1967) as

$$C_R \approx C_s \, (0.87 + 1.12\mu)/(1+\mu) < C_s$$

$$\approx 0.92 \, C_s \qquad \text{for } \mu \approx 0.28 \, .$$

The Rayleigh (1887) wave speed serves as the high frequency limit for flexural waves in the exact theory of wave propagation in an infinite, cylindrical shell in air, since for very high frequency the shell curvature approximates a flat plate and the shell thickness approximates a semi-infinite medium. Both Pochhammer (1876) and Chree (1886) investigated the propagation of waves in a solid cylinder. These solutions, the Pochhammer modes, form the thick shell limit of modes which exist in cylindrical shells.

For two semi-infinite elastic media with a common boundary, each incident P or S wave will produce P and S reflected and refracted waves. In addition, Stoneley (1924) showed that a surface wave can exist at the interface between the two media if the shear wave velocities C_s of the two media are nearly the same. Such a generalized Rayleigh wave is called the Stoneley wave. If the system is comprised instead of an elastic layer over a semi-infinite elastic media, a situation can exist such that S waves are trapped in the layer and propagate by multiple reflections. Such waves are known as Love waves. Love waves cannot exist in a fluid layer since the fluid cannot support shear.

While an analysis based upon an exact elastic theory yields wave types which are pure dilatation or shear, the addition of boundaries can

make the analysis very complicated. On the other hand, approximate shell theories must deal with coupled displacement behavior. However, their use is much less complicated than the exact theory. The errors introduced by an approximate theory can often be reduced over some frequency range of interest by introducing correction factors called adjustment coefficients or shear constants to the approximate theory which force agreement with the exact theory at specific points.

2.5 Development of the Flugge Thin Shell Equations

The Flugge shell equations represent a bending theory. They were chosen to describe the shell deformations for several reasons. Bending theories in general are attractive in that they represent a considerable reduction in analytical and numerical complexity over higher-order approximate theories and exact theories. Since the frequency regime below the classical plate coincidence frequency is of more practical interest than higher frequencies, many of the advantages offered by higher-order and exact theories are not as important. Of the available bending theories, the Flugge theory results in a symmetric stiffness matrix. This feature has the important consequence that it represents a system in which energy is conserved. Other bending theories which result in nonsymmetric stiffness matrices are known a priori to be non-conservative, which brings into question the adequacy of the fundamental assumptions upon which those theories are based. Another advantage of the Flugge theory is that it is a zero order theory that is a derivation from a higher-order theory. The development would allow future modification to include shear deformation and rotary inertia effects as a first-order theory, or a still higher-order theory, if desired. This is a feature which the Flugge theory has in common with Mirsky-Herrmann thick shell theory. In fact, the zero-order Flugge theory yields the

same equations as the zero-order Mirsky-Herrmann theory, although their higher-order theories differ.

The coordinate system and geometry of the infinite cylindrical shell are shown in Figure 2.1. The shell has a thickness h and a middle surface radius R. A circular-cylindrical coordinate system (r,θ,x) is established such that radial distances are measured from the cylinder axis. The circumferential and axial coordinates are measured from the point of application of an applied harmonic point force directed radially outward. All axial and radial distances, as well as all wavenumbers, are normalized by the shell's middle-surface radius R such that they are non-dimensional. The shell's thickness h is also normalized by the radius. An additional radial coordinate ρ is introduced and measured from the middle surface of the shell with the positive sense taken as outward such that $r=1+\rho$. The coordinate system can therefore be referenced to (ρ,θ,x) with derivatives with respect to r replaced by derivatives with respect to ρ. The normalized external radius of the shell is denoted by $a=1+h/2$. The cylindrical shell is surrounded by a fluid medium of characteristic acoustic impedance ρc on its exterior and a vacuum on its interior. Since the fluid medium will not be fully considered until Chapter 4, no ambiguity concerning the variable ρ should occur during the development of the Flugge shell equations.

The deformation at any point in the shell will be referenced to displacement components u, v, and w of the shell's middle surface which respectively represent axial, circumferential, and radial displacements. All displacement components are also normalized by the shell's middle-surface radius R. The shell is assumed to be a homogeneous, isotropic, elastic material with elastic modulus E, Poisson's ratio μ, and mass density ρ_s. Unless otherwise noted, Table 2.1 represents the geometric

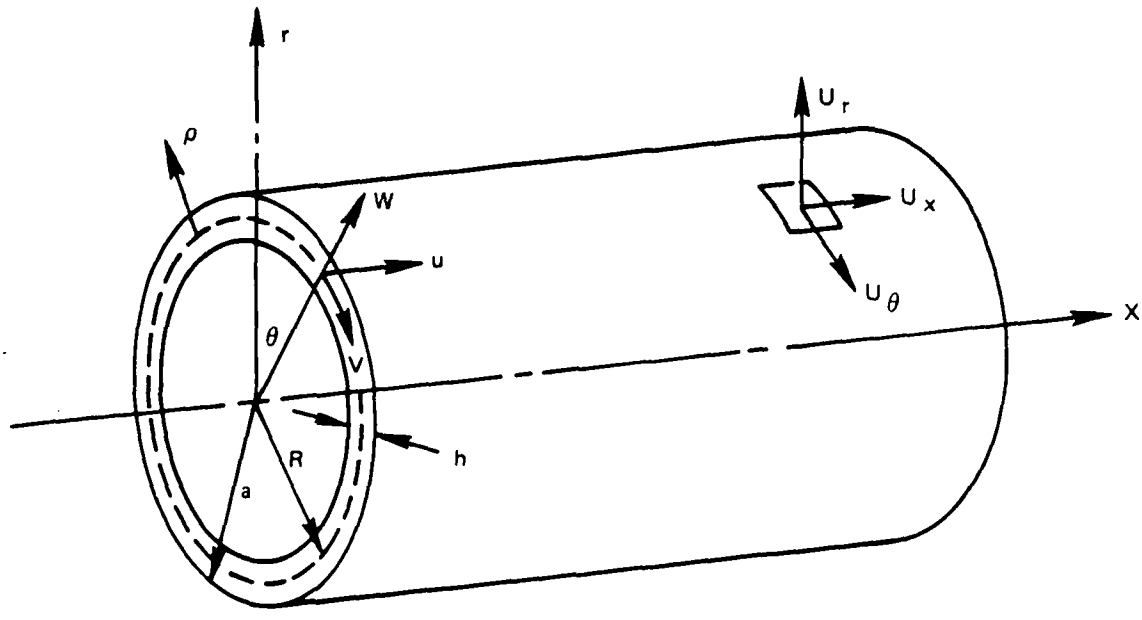

ELASTIC MODULUS, E
POISSON'S RATIO, μ
MASS DENSITY, ρ_s

Figure 2.1. Coordinate system and geometry.

Table 2.1 Geometric and material parameters.

Symbol	Description	Value
a	ratio of shell outer radius to mean radius	1.005
h	ratio of shell thickness to mean radius	0.01
E	shell material elastic modulus	$19.5 \times 10^{10} N/m^2$
ρ_s	shell material density	$7700\ Kg/m^3$
μ	shell material Poisson's ratio	0.28
ρ	fluid density	$1026\ Kg/m^3$
c	fluid acoustic velocity	1500 m/sec

and material parameter values used throughout this study. Initially, no damping is assumed. A small amount of damping will be added later by considering a complex modulus in order to evaluate contour integrals in the complex plane. The shell is assumed to be freely supported at its ends, which will be useful in the derivation of the governing equations of motion using Hamilton's principle.

Let us begin by assuming that at any point within the shell the displacement due to loading can be given by the components u_r, u_θ, and u_x which represent radial, circumferential, and axial deformations. In general, these components will be dependent upon ρ, θ, x, and time. If we expand these deformations in a Taylor series about the middle surface (ρ=0) of the shell, we would yield

$$u_r(\rho,\theta,x,t) = \sum_{m=0}^{\infty} \frac{\rho^m}{m!} u_r^{(m)}(\theta,x,t)$$

$$u_\theta(\rho,\theta,x,t) = \sum_{m=0}^{\infty} \frac{\rho^m}{m!} u_\theta^{(m)}(\theta,x,t) \qquad (2.1)$$

$$u_x(\rho,\theta,x,t) = \sum_{m=0}^{\infty} \frac{\rho^m}{m!} u_x^{(m)}(\theta,x,t)$$

where $u_r^{(m)}$, $u_\theta^{(m)}$ and $u_x^{(m)}$ represent the m^{th} derivative of u_r, u_θ, and u_x with respect to ρ evaluated at $\rho=0$.

The first term in each series represents the displacement of the shell's middle surface, the second term refers to rotation, and higher-order terms quickly lose their physical definition. Flugge theory can be characterized by the highest-order derivative term which is retained in the expansions. First-order theory would be approximated by

$$\begin{aligned} u_x(\rho,\theta,x,t) &= u(x,\theta,t) + \rho\, u_x^{(1)}(x,\theta,t) \\ u_\theta(\rho,\theta,x,t) &= v(x,\theta,t) + \rho\, u_\theta^{(1)}(x,\theta,t) \\ u_r(\rho,\theta,x,t) &= w(x,\theta,t) + \rho\, u_r^{(1)}(x,\theta,t) \end{aligned} \tag{2.2}$$

where u, v, and w have been introduced as the normalized displacements of the shell's middle surface. This assumption essentially requires that all points which lie on a normal to the shell's middle surface before deformation must also do so after deformation. Higher-order derivatives are considered to be negligible compared to unity. If the strain variation in the radial direction is assumed small and neglected, then u_r would not be dependent upon ρ and

$$u_r^{(1)} = 0 \quad \text{and} \quad u_r(\rho,\theta,x,t) = w(x,\theta,t).$$

The first-order theory includes membrane, bending, shear deformation, and rotary inertia effects.

The three-dimensional, strain-displacement relations in cylindrical coordinates are given by

$$
\begin{aligned}
\varepsilon_{xx} &= \frac{\partial u_x}{\partial x} \\
\varepsilon_{\theta\theta} &= \frac{1}{r}\frac{\partial u_\theta}{\partial \theta} + \frac{1}{r}u_r \\
\varepsilon_{rr} &= \frac{\partial u_r}{\partial \rho} \\
\varepsilon_{\theta x} &= \frac{1}{r}\frac{\partial u_x}{\partial \theta} + \frac{\partial u_\theta}{\partial x} \\
\varepsilon_{xr} &= \frac{\partial u_r}{\partial x} + \frac{\partial u_x}{\partial \rho} \\
\varepsilon_{r\theta} &= \frac{\partial u_\theta}{\partial \rho} + \frac{1}{r}\frac{\partial u_r}{\partial \theta} - \frac{1}{r}u_\theta \quad ,
\end{aligned}
\tag{2.3}
$$

and the strains are symmetric such that $\varepsilon_{ij} = \varepsilon_{ji}$. If the first-order approximation of the displacements is introduced into the relations for ε_{rr}, ε_{xr}, and $\varepsilon_{r\theta}$ we find that $\varepsilon_{rr}=0$, as assumed, and

$$
\begin{aligned}
\varepsilon_{xr} &= \frac{\partial w}{\partial x} + u_x^{(1)} \\
\varepsilon_{r\theta} &= \frac{1}{r}\left[u_\theta^{(1)} + \frac{\partial w}{\partial \theta} - v\right] \quad .
\end{aligned}
$$

Classical bending theory neglects thickness shear stresses, which for an isotropic material is equivalent to neglecting thickness shear strains. This is often referred to as neglecting shear deformation and is valid for a thin shell. This assumption reduces the problem to one of plane strain. Setting $\varepsilon_{xr}= \varepsilon_{\theta r}=0$ results in

$$
\begin{aligned}
u_x^{(1)} &= -\frac{\partial w}{\partial x} \\
u_\theta^{(1)} &= v - \frac{\partial w}{\partial \theta} \quad ,
\end{aligned}
\tag{2.4}
$$

which relates the slopes at a point in the shell to the displacement and slopes of the shell's middle surface. Since the shell motion is now

characterized entirely by the middle-surface displacements, the negligible shear deformation assumption reduces the first-order theory to a zero-order theory.

The displacement components at any point within the shell can now be written as

$$u_x(\rho,\theta,x,t) = u(\theta,x,t) - \rho \frac{\partial w(\theta,x,t)}{\partial x}$$

$$u_\theta(\rho,\theta,x,t) = r\, v(\theta,x,t) - \rho \frac{\partial w(\theta,x,t)}{\partial \theta} \qquad (2.5)$$

$$u_r(\rho,\theta,x,t) = w(\theta,x,t) \quad .$$

Introducing these expressions into the remaining strain relations for ε_{xx}, $\varepsilon_{\theta\theta}$, and $\varepsilon_{\theta x}$ yields

$$\varepsilon_{xx} = \frac{\partial u}{\partial x} - \rho \frac{\partial^2 w}{\partial x^2}$$

$$\varepsilon_{\theta\theta} = \frac{\partial v}{\partial \theta} - \frac{\rho}{r} \frac{\partial^2 w}{\partial \theta^2} + \frac{1}{r} w \qquad (2.6)$$

$$\varepsilon_{\theta x} = \frac{1}{r} \frac{\partial u}{\partial \theta} + r \frac{\partial v}{\partial x} - \frac{\rho}{r} (2+\rho) \frac{\partial^2 w}{\partial \theta \partial x} \quad .$$

The strains can be written in terms of the membrane strains e for a cylindrical shell and some curvature effects κ as

$$\varepsilon_{xx} = e_{xx} - \rho\, \kappa_{xx}$$

$$\varepsilon_{\theta\theta} = e_{\theta\theta} - \rho\, \kappa_{\theta\theta} \sum_{m=0}^{\infty} (-\rho)^m \qquad (2.7)$$

$$\varepsilon_{\theta x} = e_{\theta x} - \rho \left[\kappa_{x\theta} + \kappa_{\theta x} \sum_{m=0}^{\infty} (-\rho)^m\right]$$

where $1/r = 1/(1+\rho)$ has been expanded into a geometric progression. The membrane strains are given as

$$e_{xx} = \frac{\partial u}{\partial x}$$

$$e_{\theta\theta} = \frac{\partial v}{\partial \theta} + w \qquad (2.8)$$

$$e_{\theta x} = \frac{\partial u}{\partial \theta} + \frac{\partial v}{\partial x} \quad ,$$

which represent middle surface extensions. The curvature changes are given by

$$\kappa_{xx} = \frac{\partial^2 w}{\partial x^2}$$

$$\kappa_{\theta\theta} = \frac{\partial^2 w}{\partial \theta^2} + w \qquad (2.9)$$

$$\kappa_{\theta x} = \frac{\partial u}{\partial \theta} + \frac{\partial^2 w}{\partial \theta \partial x}$$

$$\kappa_{x\theta} = \frac{\partial^2 w}{\partial \theta \partial x} - \frac{\partial v}{\partial x}$$

where κ_{xx} and $\kappa_{\theta\theta}$ represent change of curvature in a single plane, and $\kappa_{\theta x}$ and $\kappa_{x\theta}$ are coupled curvature changes, or twists. Note that

$$e_{\theta x} = \kappa_{\theta x} - \kappa_{x\theta}$$

is true.

If we assume small deformations, then we can apply the linearly elastic Hooke's Law for a homogeneous, isotropic material in order to relate the stress state to the state of strain through the elastic constants E and μ. If we assume that the radial stress σ_{rr} is negligible compared to the axial and circumferential stress, which is a valid approximation for a thin shell, then the stress state is given by

$$\sigma_{xx} = \frac{E}{(1-\mu^2)} [\varepsilon_{xx} + \mu \varepsilon_{\theta\theta}]$$

$$\sigma_{\theta\theta} = \frac{E}{(1-\mu^2)} [\varepsilon_{\theta\theta} + \mu \varepsilon_{xx}] \qquad (2.10)$$

$$\sigma_{\theta x} = \frac{E}{2(1+\mu)} \varepsilon_{\theta x} \quad ,$$

which are identical in form to those derived for classical plate theory. The stresses and strains are defined in terms of the middle-surface deformations by Equations (2.6) - (2.8). Enough information now exists to apply a variational energy method known as Hamilton's Principle in order to find the differential equations of motion governing the shell.

Wave motion in an elastic system is characterized by the dynamic transfer between the scalar kinetic and potential energies. These energies are invariant with respect to the choice of coordinates and represent fundamental properties of the system. From a knowledge of these energies and the application of Hamilton's variational principle, it is possible to derive the differential equations governing the motion of the shell in terms of the middle-surface deformations. A description of the method and the details of the development are given in the Appendix. The results, Equations (A.33), are presented here for time harmonic excitation in differential operator form as

$$\begin{aligned} L_{11}u + L_{12}v + L_{13}w &= -\omega^2 \frac{R^2}{c_p^2} u \\ L_{21}u + L_{22}v + L_{23}w &= -\omega^2 \frac{R^2}{c_p^2} v \\ L_{31}u + L_{32}v + L_{33}w &= \omega^2 \frac{R^2}{c_p^2} w + \frac{1}{D} (f_d - p_a) \end{aligned} \qquad (2.11)$$

where c_p is the low frequency phase velocity for compressional waves in a plate, defined as

$$c_p^2 = \frac{E}{\rho_s(1-\mu^2)} \quad ,$$

and D is the normalized extensional rigidity of the shell, defined as

$$D = \frac{Eh}{(1-\mu^2)} = \rho_s c_p^2 h \quad .$$

The fluid loading on the shell is denoted as p_a, while f_d denotes the distributed radial forces applied to the shell. The differential operators are given as

$$L_{11} = \frac{\partial^2}{\partial x^2} + [\frac{1-\mu}{2}][1+\beta]\frac{\partial^2}{\partial \theta^2}$$

$$L_{12} = [\frac{1+\mu}{2}] \frac{\partial^2}{\partial \theta \partial x}$$

$$L_{13} = \mu \frac{\partial}{\partial x} + [\frac{1-\mu}{2}]\beta \frac{\partial^3}{\partial x \partial \theta^2} - \beta \frac{\partial^3}{\partial x^3}$$

$$L_{21} = L_{12}$$

$$L_{22} = [\frac{1-\mu}{2}][1+3\beta] \frac{\partial^2}{\partial x^2} + \frac{\partial^2}{\partial \theta^2} \qquad (2.12)$$

$$L_{23} = \frac{\partial}{\partial \theta} - [\frac{3-\mu}{2}]\beta \frac{\partial^3}{\partial \theta \partial x^2}$$

$$L_{31} = L_{13}$$

$$L_{32} = L_{23}$$

$$L_{33} = 1 + \beta[\frac{\partial^4}{\partial x^4} + 2 \frac{\partial^4}{\partial \theta^2 \partial x^2} + \frac{\partial^4}{\partial \theta^4} + 2 \frac{\partial^2}{\partial \theta^2} + 1]$$

where

$$\beta = h^2/12$$

is the normalized thickness-to-radius ratio. For a thin shell, with a normalized thickness $h \leq 0.10$, then $\beta < 8.3 \times 10^{-4}$. Terms proportional to β are due to bending, while the remaining terms are membrane terms.

These equations are the same as those developed by Flugge using a strength-of-materials approach based upon stress resultants and balance of forces. The symmetric, differential-operator matrix [L] represents a self-adjoint system. This system is positive definite such that any change in state from an equilibrium condition acts to increase the total energy of the system. The system is conservative and obeys the Maxwell-Betti Reciprocity Theorem [e.g. Love (1927)]. Put in cannonical form, the system will yield positive real eigenvalues and eigenfunctions which are orthogonal.

2.6 Wavenumber Space Representation of the Shell Equations

The Flugge equations represent a coupled set of differential equations in the dependent displacement variables u, v, and w and the independent coordinate variables x and θ. Since the fluid surrounding the shell will respond only to the radial deformations $w(\theta,x)$, it will be necessary to determine w in order to match boundary conditions at the shell-fluid interface. Unfortunately, the Flugge equations in differential form are too complicated for standard solution techniques to apply. However, by transforming the equations into wavenumber space, they will be reduced to a set of algebraic equations which can readily be solved for the transformed radial deformation. Inverse transform techniques can then be used to determine the deformation w, or ultimately the acoustic pressure, in coordinate space. The difficulty in solving the differential equations is replaced by the difficulties of an inverse Fourier integral in the complex domain and convergence considerations of an infinite Fourier series. A characterization of the shell in wave-

number space will display the dispersive nature of the shell vibrations.

Let us begin by assuming a separable solution in the axial and circumferential directions. Let us further assume that the shell deformations can be expanded in a Fourier series over the circumferential coordinate θ as

$$
\begin{aligned}
u(\theta,x,t) &= \sum_{n=0}^{\infty} U_n(x) \left\{ \begin{matrix} \cos n\theta \\ \sin n\theta \end{matrix} \right\} \exp(-j\omega t) \\
v(\theta,x,t) &= \sum_{n=0}^{\infty} V_n(x) \left\{ \begin{matrix} \cos n\theta \\ \sin n\theta \end{matrix} \right\} \exp(-j\omega t) \\
w(\theta,x,t) &= \sum_{n=0}^{\infty} W_n(x) \left\{ \begin{matrix} \cos n\theta \\ \sin n\theta \end{matrix} \right\} \exp(-j\omega t)
\end{aligned}
\tag{2.13}
$$

where either a Fourier cosine or sine series is chosen. The parameter n is called the mode order and represents a wavenumber in the circumferential direction. Considerations based upon continuity restrict the wavenumber n to integer values. The functions $U_n(x)$, $V_n(x)$, and $W_n(x)$ represent the modal dependence in the axial direction. Relations (2.13) state that the middle-surface deformations can be expressed as the sum of their modal contributions. Of the eight possible θ-dependent combinations represented by Equations (2.13), only two are compatible with the strain and stress relationships given by Equations (2.6) and (2.10). These are

$$
\begin{array}{lcl}
u \propto \cos n\theta & & u \propto \sin n\theta \\
v \propto \sin n\theta & \text{or} & v \propto \cos n\theta \\
w \propto \cos n\theta & & w \propto \sin n\theta \quad ,
\end{array}
$$

and either set would ultimately yield the same results. We will arbitrarily choose the first set.

Introducing Equatons (2.13) with the above choice of series representation into the differential Equations (2.11), multiplying each equation by either $\sin(m\theta)$ or $\cos(m\theta)$ as appropriate, and integrating each equation over θ from $(0,2\pi)$ yields

$$M_{11}U_n(x) + M_{12}V_n(x) + M_{13}W_n(x) = -\Omega^2 U_n(x)$$

$$M_{21}U_n(x) + M_{22}V_n(x) + M_{23}W_n(x) = -\Omega^2 V_n(x) \qquad (2.14)$$

$$M_{31}U_n(x) + M_{32}V_n(x) + M_{33}W_n(x) = \Omega^2 W_n(x) + \frac{\varepsilon_n}{2\pi D}\int_0^{2\pi}(f_d - p_a)\cos(n\theta)\,d\theta$$

where the driving frequency ω has been normalized by the ring frequency of a membrane shell, given by

$$\Omega = \frac{\omega}{\omega_{ring}} = \omega\frac{R}{c_p} = \beta^{-1/2}\left(\frac{c}{c_p}\right)^2\frac{\omega}{\omega_c}$$

such that an Ω of unity represents a driving frequency with a wavelength equal to the circumference of the shell. The relationship between the normalized frequency Ω and the ratio of the driving frequency to the classical plate coincidence frequency, ω_c, is also shown. For nominal values of a steel shell in water with an h of .01, the plate coincidence condition would occur at about Ω equal to 28.4. Time dependence is implicit in Equation (2.14).

In deriving the above results the orthogonality relations

$$\int_0^{2\pi}\cos(n\theta)\cos(m\theta)\,d\theta = \frac{2\pi}{\varepsilon_n}\delta_{nm}$$

$$\int_0^{2\pi}\sin(n\theta)\sin(m\theta)\,d\theta = \pi(\varepsilon_n - 1)\delta_{nm} \qquad (2.15)$$

were used where

$$\varepsilon_n = \text{Neumann factor} = \begin{cases} 1 \text{ when } n = 0 \\ 2 \text{ when } n > 0 \end{cases}$$

$$\delta_{nm} = \text{Kronecker delta function} = \begin{cases} 0 \text{ when } n \neq m \\ 1 \text{ when } n = m \end{cases}.$$

The operator matrix is now defined as

$$\begin{aligned}
M_{11} &= \frac{\partial^2}{\partial x^2} - [\tfrac{1-\mu}{2}][1+\beta]\, n^2 \\
M_{12} &= [\tfrac{1+\mu}{2}] n \frac{\partial}{\partial x} \\
M_{13} &= \mu \frac{\partial}{\partial x} - [\tfrac{1-\mu}{2}]\beta n^2 \frac{\partial}{\partial x} - \beta \frac{\partial^3}{\partial x^3} \\
M_{21} &= - M_{12} \\
M_{22} &= [\tfrac{1-\mu}{2}][1+3\beta] \frac{\partial^2}{\partial x^2} - n^2 \\
M_{23} &= [\tfrac{3-\mu}{2}]\beta n \frac{\partial^2}{\partial x^2} - n \\
M_{31} &= M_{13} \\
M_{32} &= - M_{23} \\
M_{33} &= 1 + \beta[\frac{\partial^4}{\partial x^4} - 2n^2 \frac{\partial^2}{\partial x^2} + n^4 - 2n^2 + 1]
\end{aligned} \tag{2.16}$$

and is independent of the circumferential coordinate θ. The Fourier series expansion has transformed the governing equations from θ coordinate space into n wavenumber (or modal) space.

A Fourier integral transform will be used to relate the axial coordinate x to the continuous normalized axial wavenumber ξ. The

dimensional or unnormalized axial wavenumber has been multiplied by the shell's middle-surface radius R to yield the nondimensional ξ. In a similar manner the normalized acoustic wavenumber is denoted as k. The transform pair are defined as

$$\tilde{f}(\xi) = \int_{-\infty}^{+\infty} f(x) \exp(-j\xi x)\, dx \tag{2.17}$$

$$f(x) = \frac{1}{2\pi} \int_{-\infty}^{+\infty} \tilde{f}(\xi) \exp(+j\xi x)\, d\xi \tag{2.18}$$

where the form has been chosen such that a wave propagating in the positive axial direction $f(x) = A \exp[j(kx - \omega t)]$ yields a positive wavenumber spectrum $\tilde{f}(\xi) = A\, \delta(\xi - k)$ where $\delta(y)$ is the Dirac delta function. A superior tilda is used to denote the Fourier transform. The Fourier inversion formula, given by Equation (2.18), is a generalization of the Fourier series over an infinite interval of x. The Fourier transform of a derivative can be shown to be

$$\tilde{f}\left[\frac{\partial^m f}{\partial x^m}\right] = \int_{-\infty}^{+\infty} \frac{\partial^m f}{\partial x^m} \exp(-j\xi x)\, dx = (j\xi)^m\, \tilde{f}(\xi) \tag{2.19}$$

subject to the condition that f(x) and all of its derivatives up to the m^{th} derivative approach zero as $|x|$ approaches infinity.

By applying a Fourier transform to the governing Equations (2.14) and with use of Equation (2.19) for derivatives, we yield

$$\begin{aligned}
\tilde{M}_{11}\tilde{U}_n(\xi) + \tilde{M}_{12}\tilde{V}_n(\xi) + \tilde{M}_{13}\tilde{W}_n(\xi) &= \Omega^2\, \tilde{U}_n(\xi) \\
\tilde{M}_{21}\tilde{U}_n(\xi) + \tilde{M}_{22}\tilde{V}_n(\xi) + \tilde{M}_{23}\tilde{W}_n(\xi) &= \Omega^2\, \tilde{V}_n(\xi) \\
\tilde{M}_{31}\tilde{U}_n(\xi) + \tilde{M}_{32}\tilde{V}_n(\xi) + \tilde{M}_{33}\tilde{W}_n(\xi) &= \Omega^2\, \tilde{W}_n(\xi) + \frac{\varepsilon_n}{2\pi D} \int_0^{2\pi} (\tilde{f}_d - \tilde{p}_a) \cos(n\theta)\, d\theta
\end{aligned} \tag{2.20}$$

where $\tilde{p}_a$ and $\tilde{f}_d$ are the Fourier transforms of the acoustic pressure loading and the applied forces. The transforms of U_n, V_n, and $W_n(x)$ are denoted by $\tilde{U}_n$, $\tilde{V}_n$, and $\tilde{W}_n(\xi)$. Relations (2.20) are independent of the x-coordinate. The operator matrix is now purely algebraic in n and ξ and is given by

$$\tilde{M}_{11} = \xi^2 + [\tfrac{1-\mu}{2}][1+\beta]n^2 = \tilde{m}_{11}$$

$$\tilde{M}_{12} = -j[\tfrac{1+\mu}{2}]n\xi = j\,\tilde{m}_{12}$$

$$\tilde{M}_{13} = -j\xi[\mu + \beta\xi^2 - (\tfrac{1-\mu}{2})\beta n^2] = j\,\tilde{m}_{13}$$

$$\tilde{M}_{21} = -\,\tilde{M}_{12} = -j\,\tilde{m}_{12}$$

$$\tilde{M}_{22} = [\tfrac{1-\mu}{2}][1+3\beta]\xi^2 + n^2 = \tilde{m}_{22} \qquad (2.21)$$

$$\tilde{M}_{23} = n[(\tfrac{3-\mu}{2})\beta\xi^2 + 1] = \tilde{m}_{23}$$

$$\tilde{M}_{31} = -\,\tilde{M}_{13} = -j\,\tilde{m}_{13}$$

$$\tilde{M}_{32} = \tilde{M}_{23} = \tilde{m}_{23}$$

$$\tilde{M}_{33} = 1 + \beta[\xi^4 + 2n^2\xi^2 + n^4 - 2n^2 + 1] = \tilde{m}_{33} \quad .$$

Note that the system is Hermitian for real ξ.

In general, if the transforms of the acoustic pressure loading and the applied forces were known, Equations (2.20) could easily be solved for $\tilde{U}_n$, $\tilde{V}_n$, and $\tilde{W}_n(\xi)$. In that case, the displacements would be given by

$$u(\theta,x,t) = \frac{1}{2\pi} \sum_{n=0}^{\infty} \cos(n\theta) \int_{-\infty}^{+\infty} \tilde{U}_n(\xi)\, e^{j(\xi x-\omega t)}\, d\xi$$

$$v(\theta,x,t) = \frac{1}{2\pi} \sum_{n=0}^{\infty} \sin(n\theta) \int_{-\infty}^{+\infty} \tilde{V}_n(\xi)\, e^{j(\xi x-\omega t)}\, d\xi \qquad (2.22)$$

$$w(\theta,x,t) = \frac{1}{2\pi} \sum_{n=0}^{\infty} \cos(n\theta) \int_{-\infty}^{+\infty} \tilde{W}_n(\xi)\, e^{j(\xi x-\omega t)}\, d\xi \quad .$$

The applied force f_d is a harmonic point source located at x=0 and θ=0. The acoustic pressure loading will be developed in Chapter 4 and will be dependent upon the radial displacement w such that it would appear on the left hand side of Equation (2.20). The next chapter will deal with the shell in a vacuum such that the acoustic pressure loading is zero.

Chapter 3

THE BEHAVIOR OF A SHELL IN VACUO

3.1 Introduction

This chapter will discuss the vibration of a shell in the absence of a fluid loading. Concepts and nomenclature will be introduced which will be useful in later work. The in vacuo behavior will also serve as a basis for comparison when fluid loading is considered. The first section deals with the canonical form of the shell equations where the applied forces are taken as zero. The eigenvalue solutions at large axial wavenumber are then used as a basis for developing a branch nomenclature. The eigenvalue behavior near the lower cutoff frequency is investigated. Frequency spectra, dispersion curves, and group velocity data are presented, and the effect of varying the shell's thickness is discussed. Physical insight into the vibration modes is introduced. A comparison is made between the approximate Flugge theory based upon a thin shell theory and a theory developed by Gazis from the exact three-dimensional equations of elasticity. Finally, the problem of the forced motion of the shell is considered and developed in a form convenient for later work when fluid loading is added.

3.2 The Eigenvalue Problem

In the absence of applied and fluid loading, the equations of motion governing the middle-surface displacements of the shell assume a canonical form given as

$$[\tilde{M}]\ [\tilde{X}] = \lambda\ [\tilde{X}] \qquad (3.1)$$

where $[\tilde{M}]$ and $[\tilde{X}]$ are understood to be matrix quantities. The scalar λ represents the eigenvalues of the system. The column matrix $[\tilde{X}]$ is the transformed modal deformations $\tilde{U}_n$, $\tilde{V}_n$ and $\tilde{W}_n$. The square matrix $[\tilde{M}]$ is effectively a stiffness matrix with elements which act as stiffness influence coefficients.

$$[\tilde{M}] = \begin{bmatrix} \tilde{m}_{11} & j\tilde{m}_{12} & j\tilde{m}_{13} \\ -j\tilde{m}_{12} & \tilde{m}_{22} & \tilde{m}_{23} \\ -j\tilde{m}_{13} & \tilde{m}_{23} & \tilde{m}_{33} \end{bmatrix} \tag{3.2}$$

The coefficients $\tilde{m}_{ij}$ are defined by Equation (2.21).

Equation (3.1) could also be written as

$$([\tilde{M}] - \lambda [I])\,[\tilde{X}] = [\tilde{\Lambda}]\,[\tilde{X}] = 0 \tag{3.3}$$

where $[I]$ is the identity matrix and $[\tilde{\Lambda}]$ is the characteristic matrix. For a nontrivial solution, the determinant of the characteristic matrix must be zero, thus yielding the characteristic equation

$$\det([\tilde{\Lambda}]) = s_1\lambda^3 + s_2\lambda^2 + s_3\lambda + s_4 = 0 \quad , \tag{3.4}$$

which is third order in λ. The coefficients are given as

$$\begin{aligned} s_1 &= -1 \\ s_2 &= \tilde{m}_{11} + \tilde{m}_{22} + \tilde{m}_{33} \\ s_3 &= \tilde{m}_{12}^2 + \tilde{m}_{13}^2 + \tilde{m}_{23}^2 - \tilde{m}_{11}\tilde{m}_{22} - \tilde{m}_{11}\tilde{m}_{33} - \tilde{m}_{22}\tilde{m}_{33} \\ s_4 &= \tilde{m}_{11}\tilde{m}_{22}\tilde{m}_{33} + 2\tilde{m}_{12}\tilde{m}_{13}\tilde{m}_{23} - \tilde{m}_{12}^2\tilde{m}_{33} - \tilde{m}_{13}^2\tilde{m}_{22} - \tilde{m}_{23}^2\tilde{m}_{11} \end{aligned} \tag{3.5}$$

For real ξ, $[\tilde{\Lambda}]$ is Hermitian. An investigation of the coefficients s_j of the characteristic equation shows that for real ξ the signs of the coefficients alternate. From a theorem presented by Wilf (1962), such a

system is positive definite, and all of the resulting eigenvalues are real and positive. Therefore, for each real ξ, three positive real eigenvalues, or natural frequencies, must exist. If frequency is taken as a parameter, which is physically appropriate, each eigenvalue will represent a point on a frequency spectrum. These spectra are often referred to as the shell branches.

Each eigenvalue represents an orthogonal mode of vibration, or eigenfunction, in which the middle-surface displacements are coupled by the governing equations of motion. Because of the coupling between displacements, pure wave types generally cannot exist in a shell. However, the concept of a primarily longitudinal, torsional, or flexural shell motion does provide some physical meaning to the interpretation of the branches and to the discussion of various results. In general, the displacement coupling is not constant at all axial wavenumbers, and any nomenclature associated with a branch is usually applicable over only some wavenumber region of interest. The nomenclature used in this study is be based upon the behavior of the branches at large axial wavenumber where the shell behaves much like a flat plate.

3.3 Establishment of the Branch Nomenclature at Large Axial Wavenumber

The characteristic equation will yield three eigenvalues at each mode order n of the form

$$\lambda = \lambda(\xi, n, \mu, \beta) = \lambda_{nq}(\xi) \qquad q=1,2,3$$

for fixed μ and β. The natural frequencies would therefore be

$$\Omega_{nq}(\xi) = \sqrt{\lambda_{nq}(\xi)} \qquad q=1,2,3 \qquad (3.6)$$

which is recognized as a dispersive frequency spectrum. In the axisym-

metric mode, the circumferential displacement is independent of both the axial and radial displacements at all wavenumbers. This is one of only two pure wave types which can exist in a shell. The characteristic equation decomposes into the following set of two equations

$$\begin{aligned}(\tilde{m}_{11} - \lambda_{0q})(\tilde{m}_{33} - \lambda_{0q}) - \tilde{m}_{13}^2 = 0 \qquad &\text{for } q=1 \text{ or } 3 \\ \tilde{m}_{22} - \lambda_{02} = 0 \qquad &\text{for } q=2\end{aligned} \tag{3.7}$$

where $\tilde{m}_{ij}$ are defined by Equation (2.21) with n=0. The initial association of values of q with particular eigenvalues for the purpose of nomenclature is arbitrary. If the eigenvalue of the decoupled equation is denoted by q=2, then this second branch can also be designated as the torsional branch since it is only dependent upon the circumferential displacement and is described by

$$\lambda_{02} = \tilde{m}_{22} \simeq (\tfrac{1-\mu}{2})(1+3\beta)\ \xi^2$$

which is valid at all axial wavenumbers.

The other two eigenvalues can be found from the first of Equations (3.7) to be

$$\lambda_{01,3} = \tfrac{1}{2}\left[\beta\xi^4 + \xi^2 + 1 \pm \sqrt{\beta^2\xi^8 - 2\beta\xi^6 + \xi^4 - 2\xi^2 + 1}\ \right]$$

where only the lowest order β term of each power of ξ has been retained. At large ξ, the eigenvalues are approximated by

$$\lambda_{01,3} \simeq \tfrac{1}{2}\left[\beta\xi^4 + \xi^2 + 1 \pm \xi^2(\beta\xi^2 - 1)\right] \quad . \tag{3.8}$$

Let us associate the negative sign with the first branch (q=1), then

$$\lambda_{01} \simeq \xi^2$$

which yields a frequency spectrum given by $\Omega_{01}=\xi$. Introducing this eigenvalue into the decomposed equations of motion as given by Equation (3.3) yields the displacement ratio

$$\lim_{\xi\to\infty} \{|\tilde{U}_0/\tilde{W}_0| \text{ evaluated at } \lambda_{01}\} >> 1 \quad .$$

This indicates that the eigenfunction associated with λ_{01} represents primarily axial displacement at large ξ. Therefore, let us also call the first branch the longitudinal branch.

In Equation (3.8) the eigenvalue associated with the positive sign is denoted by q=3 and given by

$$\lambda_{03} \simeq \beta\xi^4 + 0.5 \simeq \beta\xi^4$$

for $\beta>0$. At this eigenvalue, it can be shown that

$$\lim_{\xi\to\infty} \{|\tilde{W}_0/\tilde{U}_0| \text{ evaluated at } \lambda_{03}\} >> 1$$

which indicates that λ_{03} has an associated eigenfunction that represents primarily radial displacement at short axial wavelength. Therefore, let us also refer to the third branch as the flexural branch. Note that for a membrance shell, $\lambda_{03}=1$ is the solution of Equation (3.7).

At higher mode orders the characteristic equation becomes quite complicated. If we simplify the system for the moment by considering a membrane shell, we see that the eigenvalues at large wavenumber are

$$\lim_{\xi\to\infty} \lambda_{nq} = (\xi^2 + n^2),\ (\tfrac{1-\mu}{2})(\xi^2 + n^2),\ 1 \quad \text{for } q=1,2,3. \qquad (3.9)$$

By solving the equations of motion for displacement ratios, it can be shown that

$$\lim_{\xi\to\infty} \{|\tilde{U}_n/\tilde{W}_n| \text{ evaluated at } \lambda_{n1} = (\xi^2 + n^2)\} >> 1$$

$$\lim_{\xi\to\infty} \{|\tilde{V}_n/\tilde{W}_n| \text{ evaluated at } \lambda_{n1} = (\xi^2 + n^2)\} << 1$$

which indicates that $\lambda_{n1}=\xi^2+n^2$ is associated with a primarily axial displacement and is a generalization of the axisymmetric solultion to account for circumferential mode order number. Likewise,

$$\lim_{\xi\to\infty} \{|\tilde{U}_n/\tilde{W}_n| \text{ evaluated at } \lambda_{n2} = (\tfrac{1-\mu}{2})(\xi^2 + n^2)\} << 1$$

$$\lim_{\xi\to\infty} \{|\tilde{V}_n/\tilde{W}_n| \text{ evaluated at } \lambda_{n2} = (\tfrac{1-\mu}{2})(\xi^2 + n^2)\} >> 1$$

indicates that $\lambda_{n2}=(1-\mu)(\xi^2+n^2)/2$ is associated with a primarily circumferential displacement. This is also a generalization of the axisymmetric solution. Finally,

$$\lim_{\xi\to\infty} \{|\tilde{U}_n/\tilde{W}_n| \text{ evaluated at } \lambda_{n3} = 1\} = 0$$

$$\lim_{\xi\to\infty} \{|\tilde{V}_n/\tilde{W}_n| \text{ evaluated at } \lambda_{n3} = 1\} = 0$$

which indicates that $\lambda_{n3}=1$ is associated with primarily radial motion. This is not surprising since the large wavenumber approximation of λ_{03} of a membrane shell is unity.

For the general theory containing bending terms, these results can be extended to yield

$$\begin{aligned} \lambda_{n1} &\simeq \xi^2 + n^2 \\ \lambda_{n2} &\simeq (\tfrac{1-\mu}{2})(\xi^2 + n^2) \\ \lambda_{n3} &\simeq \beta\xi^4 + 1 \end{aligned} \qquad (3.10)$$

which are valid at large axial wavenumber for all n. Note that these results indicate that neither the longitudinal nor torsional branch is sensitive to changes in shell thickness at large wavenumber. This will be found to be true not only at high wavenumber, but over the entire wavenumber range.

It is interesting to note that the axisymmetric, large wavenumber behavior of the longitudinal branch matches the behavior of the longitudinal vibration of both an infinite plate and an infinite bar, and that this behavior is nondispersive. Similarly, the axisymmetric mode of the torsional branch at high wavenumber approximates the nondispersive behavior of the torsional vibration of a solid circular rod, which is the analog of horizontally polarized S waves in a plate. Likewise, the axisymmetric mode of the flexural branch approximates the dispersive behavior of flexural waves in a plate at large wavenumber. Examination of Equation (3.10) indicates that for each branch the higher mode order numbers behave like the axisymmetric mode in the region $n<<\xi$.

3.4 Branch Behavior Near the Cutoff Frequencies

The lower cutoff frequency represents the transition between real and complex wavenumber space. The lower cutoff frequency nomenclature is introduced to distinguish between an upper cutoff frequency which exists when fluid loading is present. For the shell in vacuo, the upper cutoff frequency is infinite and the lower cutoff frequency can be referred to as simply the cutoff frequency without ambiguity. Above the cutoff frequency, a real wavenumber exists, the characteristic matrix $[\tilde{\Lambda}]$ is Hermitian, and wave motion can propagate freely at a finite wave velocity. At the cutoff frequency the phase velocity in the axial direction becomes infinite while the group velocity goes to zero, indicating that energy is no longer propagating. Below the branch cutoff

frequency, only a complex wavenumber can exist and free wave propagation in the axial direction is no longer possible. In this region, the characteristic matrix is no longer Hermitian but remains symmetric.

The branch cutoff frequencies can be found by evaluating the characteristic equation at infinite wavelength (zero axial wavenumber) where the motion is independent of the axial coordinate. For nonzero mode order, the characteristic equation becomes

$$(\tilde{m}_{11} - \lambda^c_{nq})[(\tilde{m}_{22} - \lambda^c_{nq})(\tilde{m}_{33} - \lambda^c_{nq}) - \tilde{m}^2_{23}] = 0 \qquad (3.11)$$

at infinite wavelength. The modal cutoff eigenvalue of the q^{th} branch is denoted by λ^c_{nq}. The coefficients $\tilde{m}_{ij}$ are given by Equations (2.21) calculated at $\xi=0$. The association of a branch nomenclature with a cutoff frequency is done by extending the nomenclature introduced at large axial wavenumber down to zero axial wavenumber by continuity of the frequency spectra. In the vicinity of the cutoff frequency, the branch nomenclature no longer indicates the primary vibrational mode associated with the eigenfunction.

At zero axial wavenumber, the longitudinal displacement is independent of both the circumferential and radial displacements. This longitudinal shear vibration is the second pure wave type possible in a shell and can exist only at the cutoff frequency of the torsional branch given by

$$\lambda^c_{n2} = \tilde{m}_{11} = (\tfrac{1-\mu}{2})(1+\beta)\, n^2 \quad . \qquad (3.12)$$

This is essentially a generalization of the purely torsional, axisymmetric mode at higher mode orders. Above the cutoff eigenvalue, the longitudinal displacement is again coupled. In the vicinity of the cutoff eigenvalue, the second branch exhibits a primarily axial displacement.

The right hand term in Equation (3.11) corresponds to plane-strain shell vibrations and yields cutoff eigenvalues given by

$$\lambda_{n1}^{c} \simeq \frac{(n^2 + 1)^2 + \beta(n^2 - 1)^2}{n^2 + 1} \tag{3.13}$$

$$\lambda_{n3}^{c} = \beta \frac{(n^2 - 1)^2}{n^2 + 1} n^2 \tag{3.14}$$

where a truncated, binomial expansion has been used to approximate the square root. It can be shown that

$$\lim_{\xi \to 0} \{ |\tilde{V}_n / \tilde{W}_n| \text{ evaluated at } \lambda_{n1}^{c} \} = n \geq 1$$

which represents a predominately circumferential displacement. Hence, in the vicinity of the cutoff eigenvalue, the first branch exhibits primarily circumferential vibration for n>0. Likewise,

$$\lim_{\xi \to 0} \{ |\tilde{V}_n / \tilde{W}_n| \text{ evaluated at } \lambda_{n3}^{c} \} = n^{-1} \leq 1$$

indicates that the third branch exhibits primarily radial motion at low wavenumbers for n>0.

For the axisymmetric mode, Equations (3.12)-(3.14) still correctly predict the cutoff eigenvalues. However, the branch behavior changes near cutoff due to the uncoupling of the circumferential displacement at all wavenumbers. It can be shown that

$$\lim_{\xi \to 0} \{ |\tilde{U}_0 / \tilde{W}_0| \text{ evaluated at } \lambda_{01}^{c} \} = 0$$

which indicates a totally radial displacement. Therefore, near the cutoff eigenvalue, the first branch exhibits primarily radial motion. Note that $\Omega_{01}^{c} = \sqrt{1+\beta}$ is the normalized ring frequency for flexural waves on a

thin, cylindrical shell. As expected, the normalized ring frequency would be unity for a membrane shell. Likewise,

$$\lim_{\xi \to 0} \{ |\tilde{U}_0 / \tilde{W}_0| \text{ evaluated at } \lambda_{03}^c \} = \infty$$

indicates that the third branch consists primarily of axial motion at low wavenumber.

Figure 3.1 shows the behavior of the cutoff frequencies versus circumferential mode order for each branch at several normalized shell thicknesses. The curves are shown as a continuous function for convenience only. As is expected from Equations (3.12) and (3.13), for thin shells, variations in shell thickness have little effect upon the low wavenumber behavior of the longitudinal and torsional branches. At large mode order, the cutoff frequencies can be approximated by

$$\begin{aligned} \Omega_{n1}^c &\simeq n \\ \Omega_{n2}^c &\simeq \sqrt{\frac{1-\mu}{2}}\, n \quad \text{for } n \gg 1 \\ \Omega_{n3}^c &\simeq \sqrt{\beta}\, n^2 \ . \end{aligned} \tag{3.15}$$

Figure 3.1 demonstrates that the low-frequency spectrum consists of a finite number of propagating modes for each branch. That is, the shell displacement distribution can be described by a finite number of terms in the series representation given by Equations (2.13). For example, below the ring frequency (Ω=1.0) the longitudinal branch does not contribute at any mode order. Below Ω=0.5, only a single torsional mode (the axisymmetric) and a finite number of flexural modes contribute. In general, thinner shells contribute more flexural modes to the displacement field than do thicker shells.

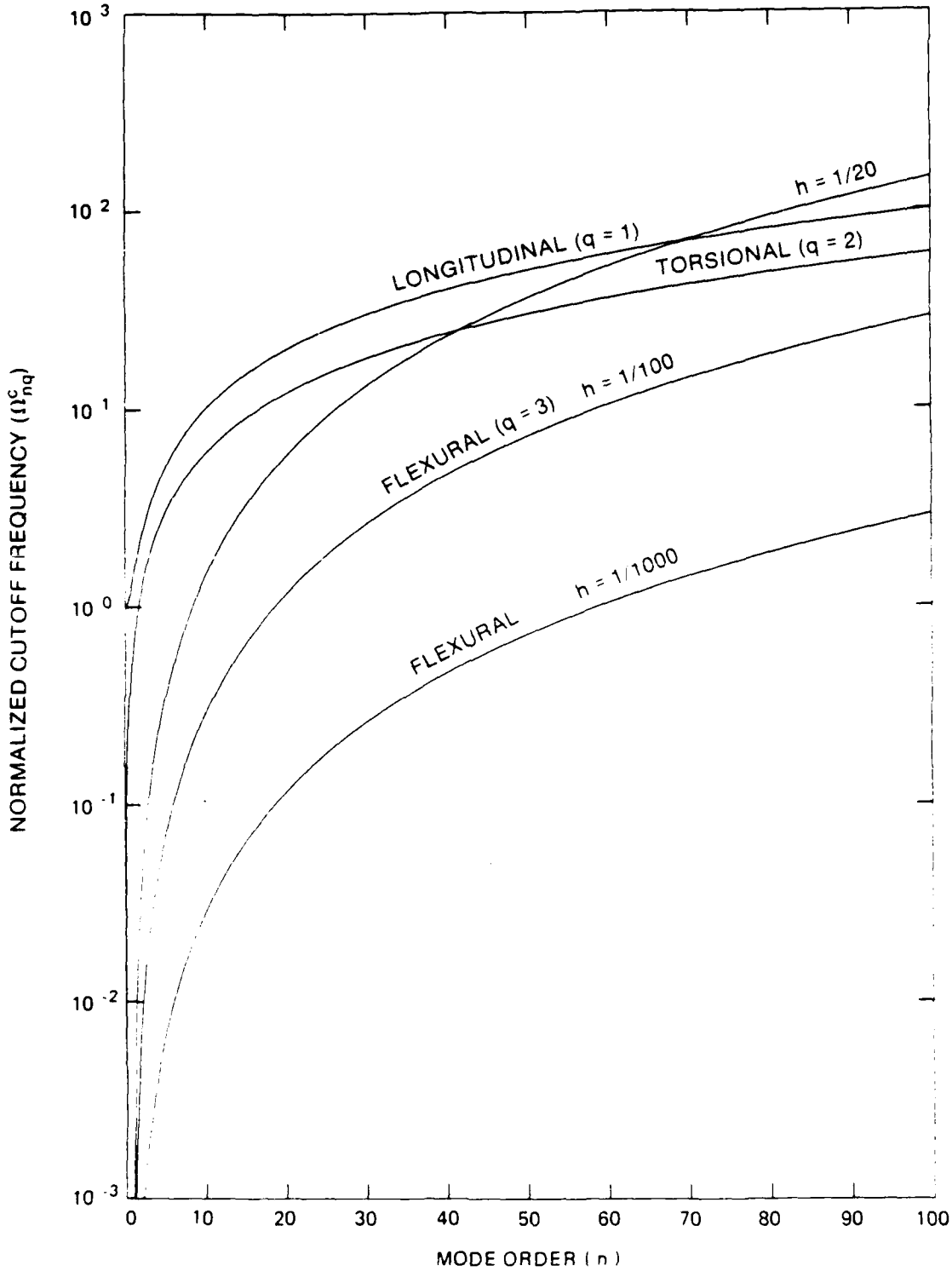

Figure 3.1. Branch behavior of the lower cutoff frequency versus circumferential mode order number for a cylindrical shell in vacuo at several values of normalized shell thickness. Continuous curves are shown for convenience only.

3.5 Physical Description of the Branches

The total displacement field of a shell consists of the sum of the contributions from each circumferential mode order. Similarly, the modal displacement field consists of the contributions from each branch which, in turn, depend upon contributions from each degree of freedom. For the Flugge theory, the degrees of freedom are the axial, circumferential, and radial displacements of the shell's middle surface.

Figure 3.2 shows the fundamental, dynamic motions associated with the axisymmetric mode. Each branch is characterized by a frequency dependent, weighted sum of these fundamental motions. From this perspective, a zero cutoff frequency must be physically associated with a rigid body motion. In the axisymmetric mode, both the second (torsional) and third (flexural) branches have a zero cutoff frequency. At this frequency, the branches respectively exhibit circumferential or axial motions. This is physically realizable as a rigid-body rotation or translation of the shell. Since a rigid-body radial motion is not possible in the axisymmetric mode, the primarily radial motion exhibited by the first branch (longitudinal) at low wavenumber must have a nonzero cutoff frequency. Also, since the cutoff frequency implies motion independent of the axial coordinate, the shell acts like a ring of rectangular cross section. The fundamental resonance must be the ring resonance $\sqrt{1+\beta}$ which is, indeed, the cutoff frequency of the first branch.

The fundamental, dynamic motions of the first mode order (beam mode) are shown in Figure 3.3. Each dynamic motion is proportional to either $\cos(\theta)$ or $\sin(\theta)$. A rigid-body translation in the radial direction is now possible. This is reflected by the zero cutoff frequency of the third branch (flexural) which consists of primarily radial motion at long wavelength. Figure 3.4 shows the dynamic motions of the second

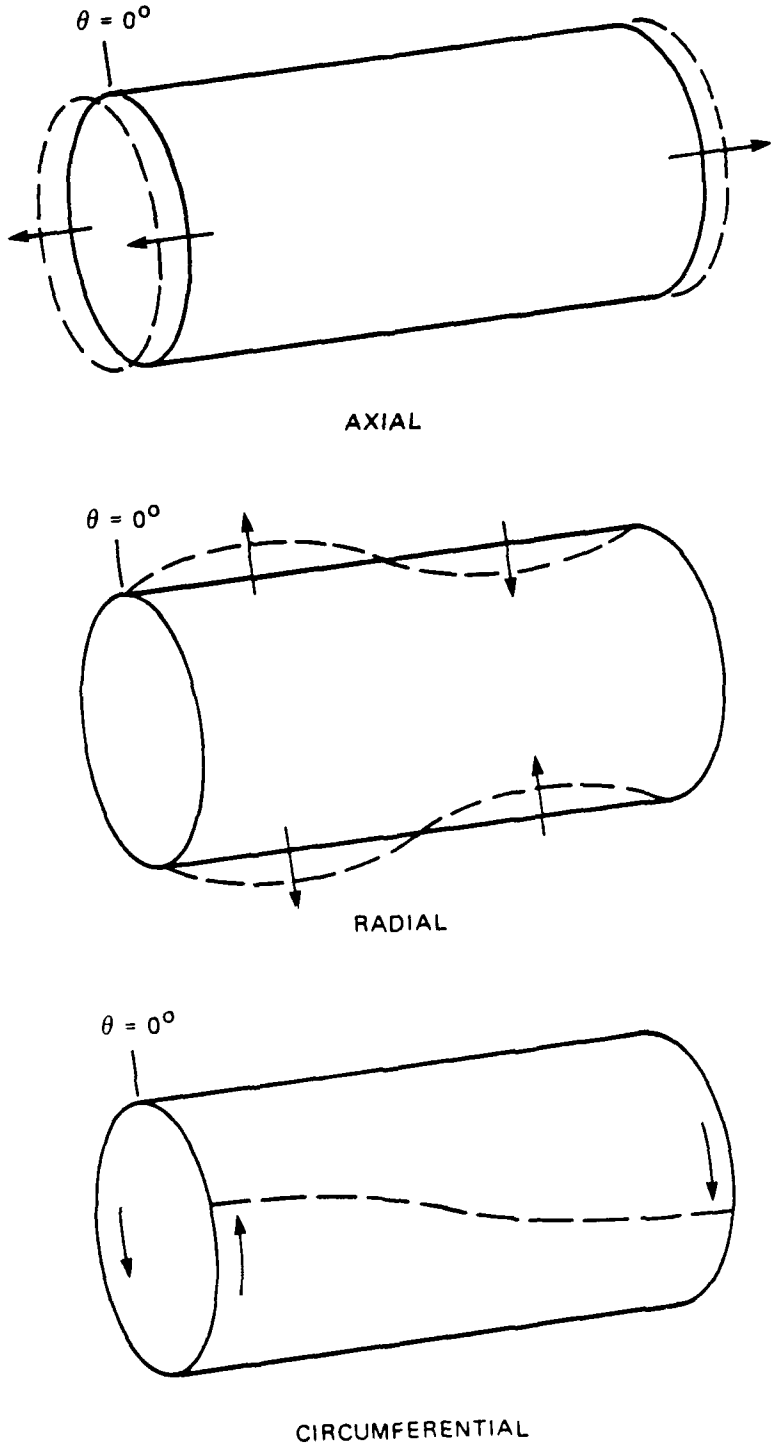

Figure 3.2. Axisymmetric dynamic motions of a vibrating thin cylindrical shell.

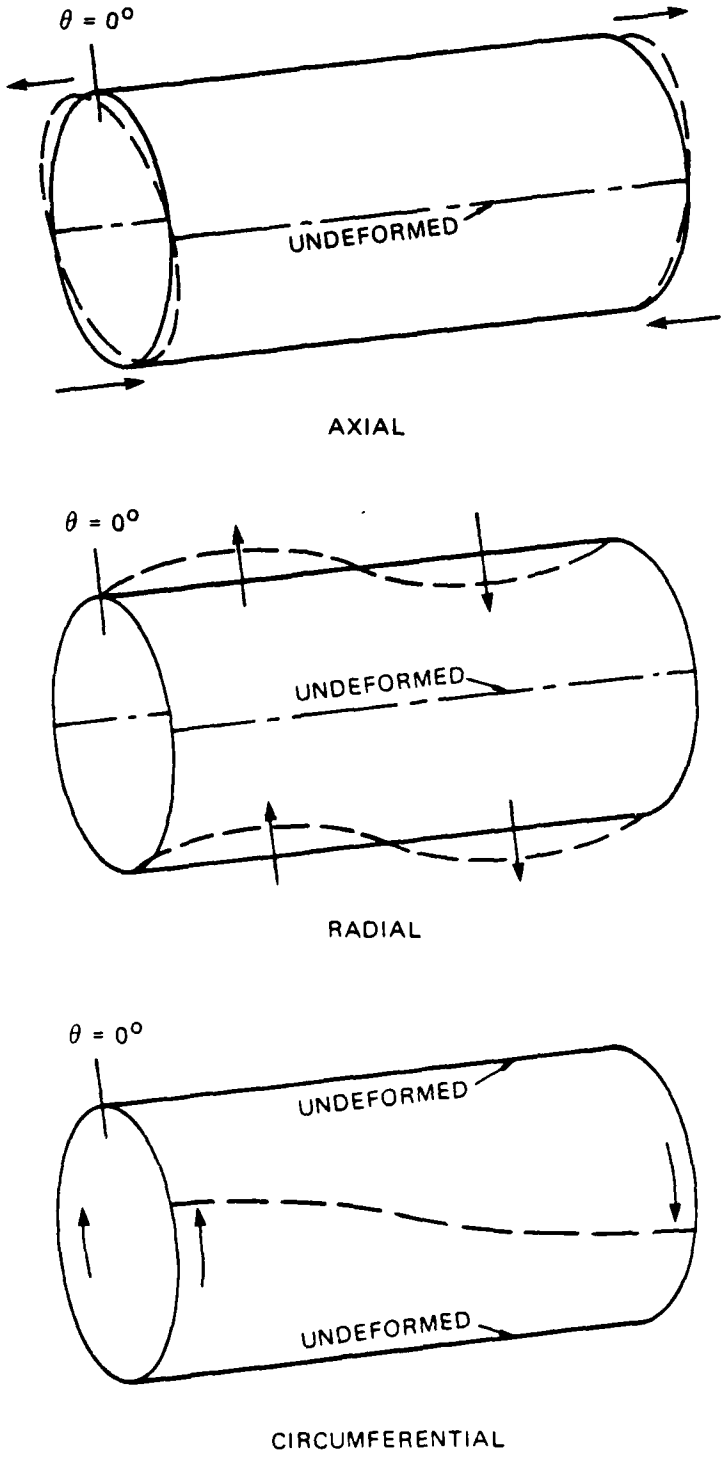

Figure 3.3. First mode order dynamic motions of a vibrating thin cylindrical shell.

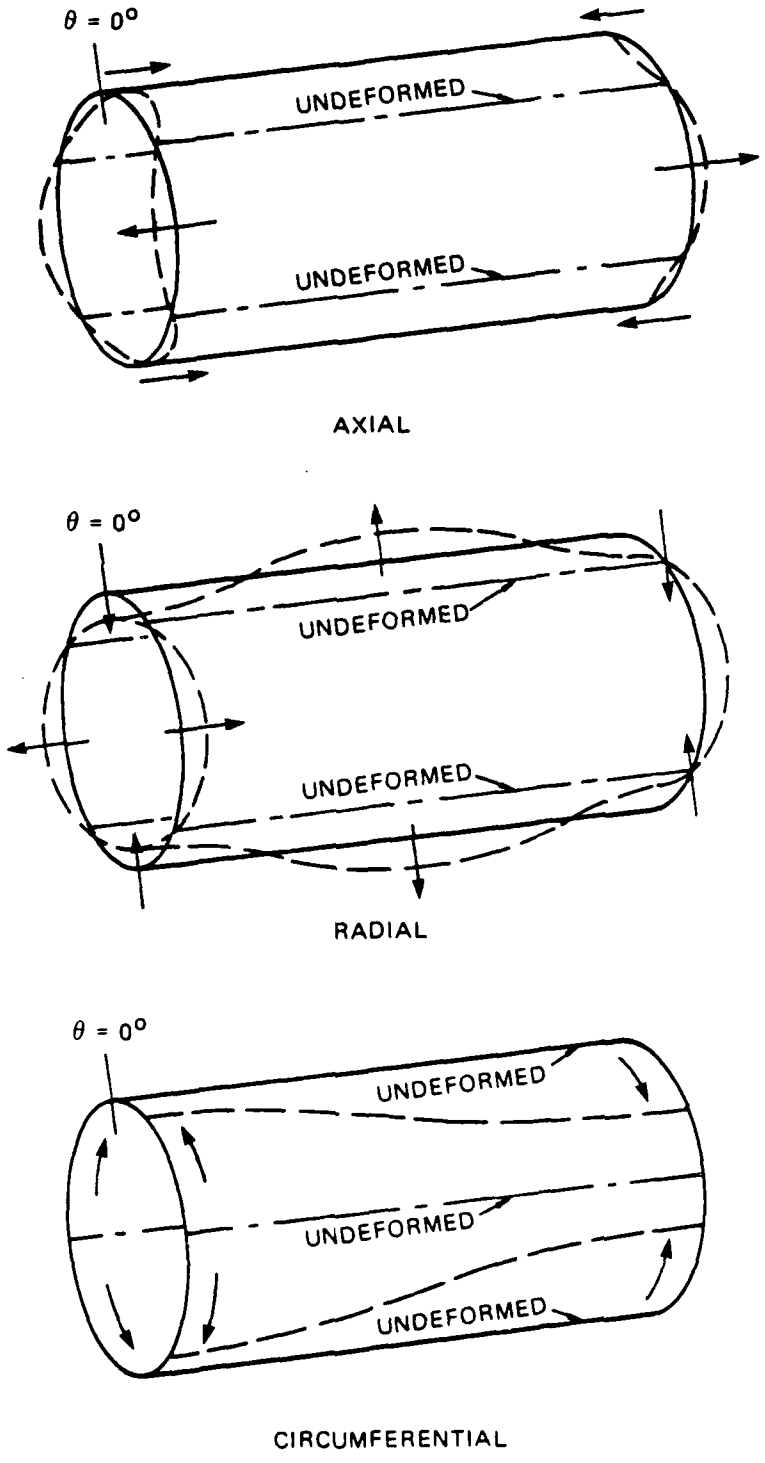

Figure 3.4. Second mode order dynamic motions of a vibrating thin cylindrical shell.

mode order. For this and all higher mode orders, each dynamic motion will exhibit 2n nodal lines in the circumferential coordinate. However, the general displacement field of the branch would be quite complicated.

3.6 Frequency Spectra, Dispersion Curves, and Group Velocity

Frequency spectra for the real positive branches of the shell in vacuo are shown by Figures 3.5 to 3.7 for n=0 to 10. The symmetric extension into negative, wavenumber space is not shown. The frequency spectra were computed from Equation (3.4) by use of Laguerre's method. The nomenclature A, C, and R on the figures indicates the primary displacement is either axial, circumferential, or radial within the indicated wavenumber region. The frequency spectra of the shell's longitudinal branch is also compared to that of the longitudinal vibration of a bar, namely

$$\Omega = \sqrt{1 - \mu^2}\ \xi \ .$$

Similarly, the torsional branch is compared to the torsional vibration of a bar or membrane shell with a frequency spectra given by

$$\Omega = \sqrt{\frac{1-\mu}{2}}\ \xi \ .$$

The flexural branch is compared to the behavior of both the classical and Timoshenko–Mindlin plates. The frequency spectra of a classical plate in vacuo is

$$\Omega = \sqrt{\beta}\ \xi^2 \ ,$$

while

$$\xi^2 = \left[(S+I)\ \Omega^2 + \sqrt{(S-I)^2\Omega^4 + 4I\ \Omega^2}\ \right] / \ 2I$$

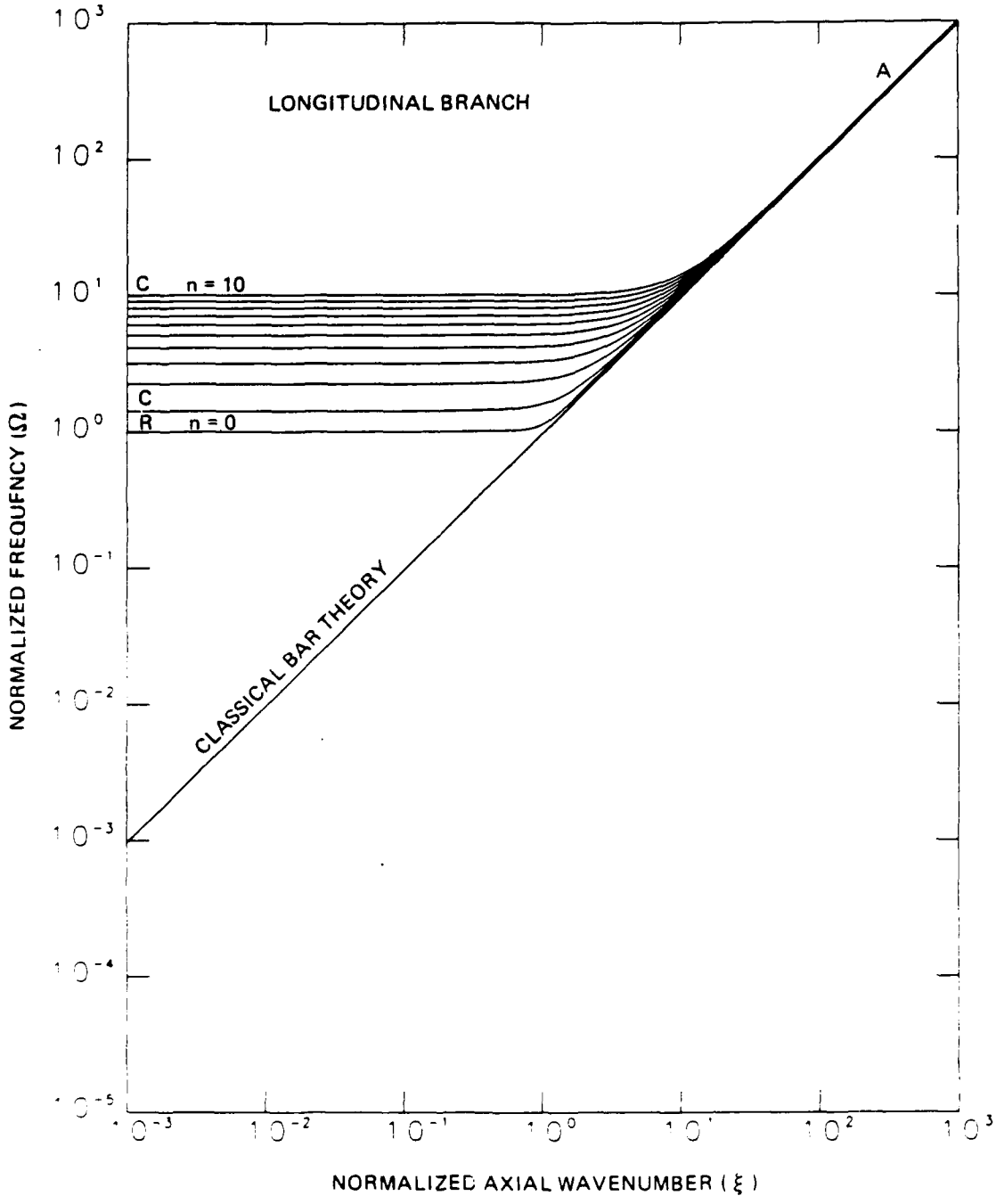

Figure 3.5. Real, positive frequency spectra predicted by Flugge theory for the longitudinal branch of a cylindrical shell in vacuo at various mode order numbers. A, C, R designate that the displacement field is primarily axial, circumferential, or radial in the indicated wavenumber region. Comparison is also shown with classical bar theory.

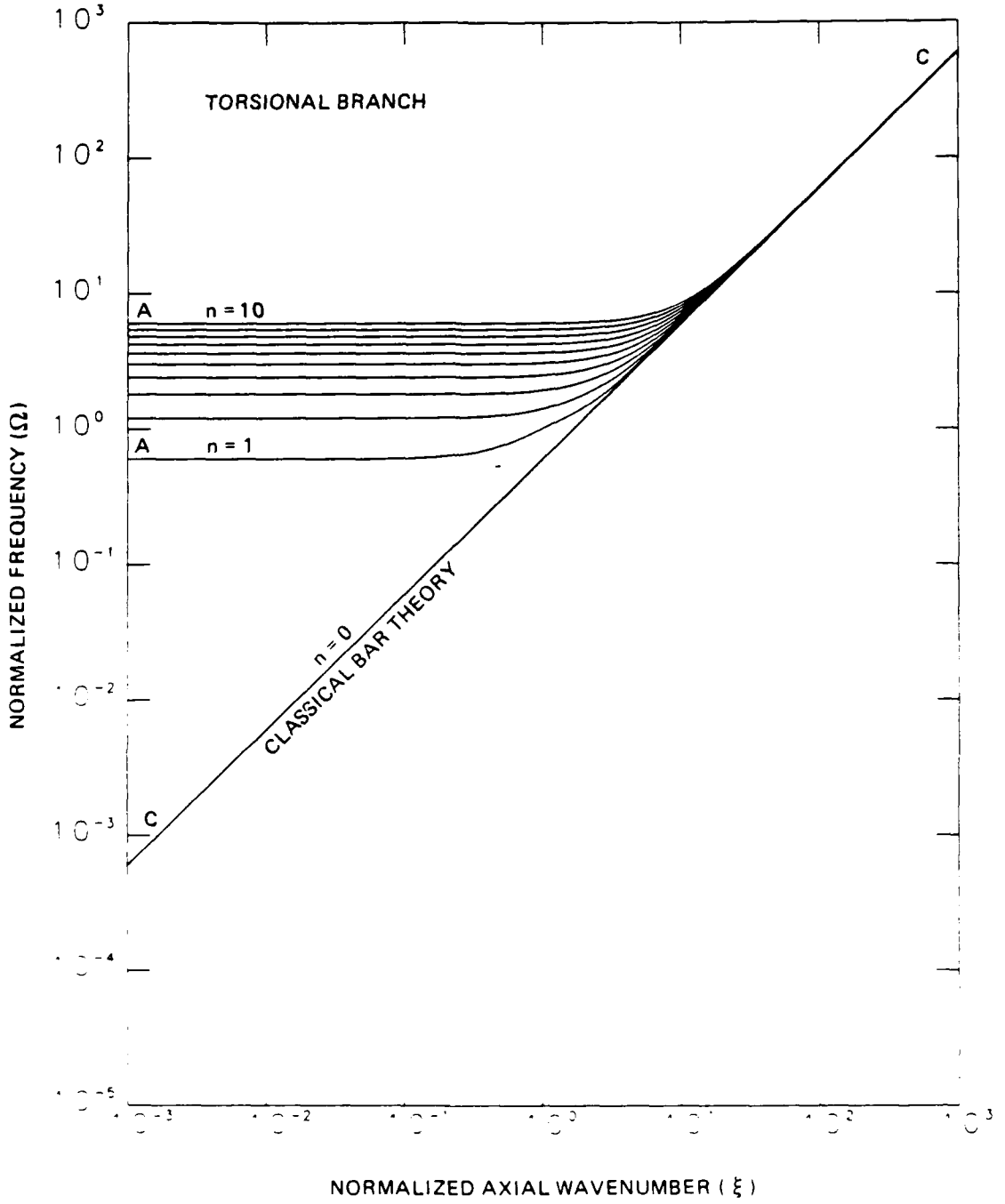

Figure 3.6. Real, positive frequency spectra predicted by Flugge theory for the torsional branch of a cylindrical shell in vacuo at various mode order numbers. A, C, R designate that the displacement field is primarily axial, circumferential, or radial in the indicated wavenumber region. Comparison is also shown with classical bar theory.

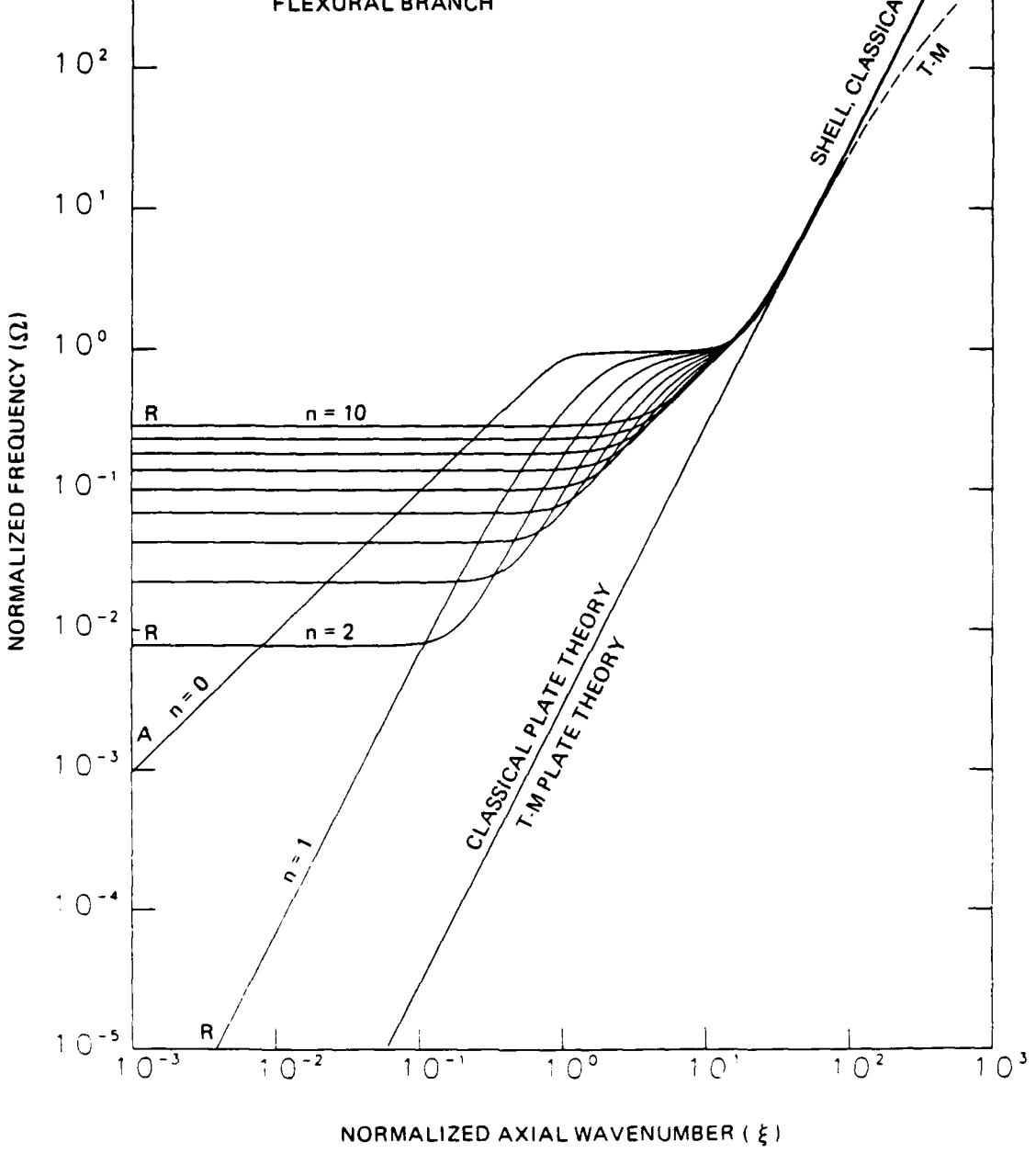

Figure 3.7. Real, positive frequency spectra predicted by Flugge theory for the flexural branch of a cylindrical shell in vacuo at various mode order numbers. A, C, R designate that the displacement field is primarily axial, circumferential, or radial in the indicated wavenumber region. Comparison is also shown with classical and Timoshenko-Mindlin plate theory.

defines the frequency spectra of a Timoshenko-Mindlin plate in vacuo [Mindlin (1951)]. The normalized plate moment of inertia is $I = \beta$ and the normalized shear deformation factor is

$$S = \frac{24I}{\pi^2(1-\mu)} \quad .$$

The classical bar and plate represent the high frequency limit of Flugge shell theory, as can be seen by comparison with Equation (3.10).

The central region of the wavenumber spectrum is characterized by strong coupling of the middle-surface displacements. As can be seen, the frequency spectra agree with the previous large and small wavenumber discussion. Note that the large linear regions of the curves indicate that the large and small wavenumber approximations are valid over a wide range. Also, the range of validity of the zero wavenumber approximation tends to increase with increasing mode order for all modes with a non-zero cutoff frequency. A similar behavior is observed with the thickness parameter β. A region of nondispersive behavior would be indicated on these logarithmic frequency spectra as a linear region with a slope of unity as is the case in Figures 3.5 and 3.6 for classical bar theory.

Dispersion curves are given by Figures 3.8 to 3.10 for n=0 to 10. Note that in terms of normalized parameters, the normalized phase velocity is given by

$$C_\Phi = \frac{C_\phi}{C_p} = \frac{\Omega}{\xi}$$

where c_p is the low frequency phase velocity of compressional waves in a plate. Nondispersive regions of the wavenumber spectrum would be indicated by a zero slope.

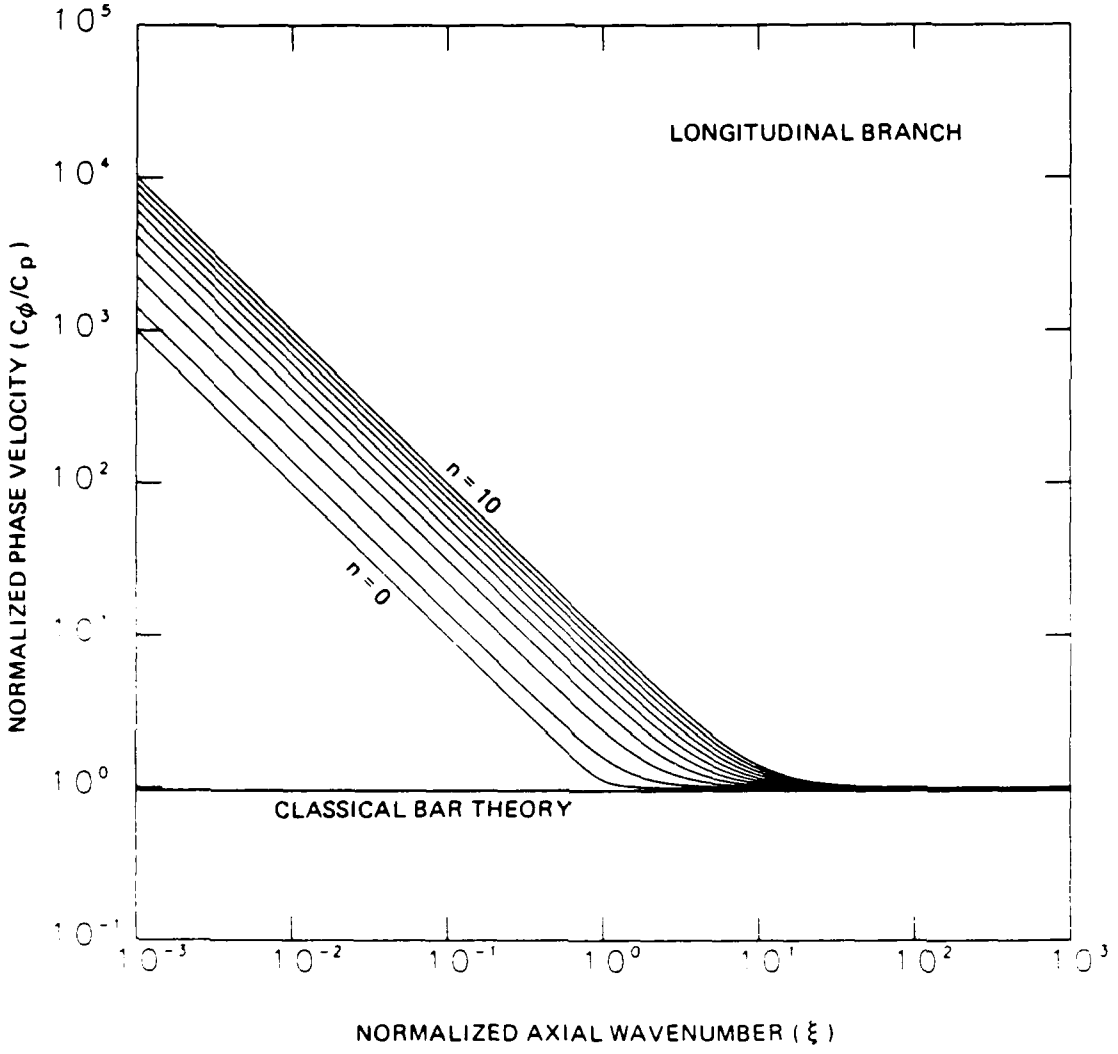

Figure 3.8. Normalized dispersion curves predicted by Flugge theory for the longitudinal branch of a cylindrical shell in vacuo at various mode order numbers. Comparison is also shown with classical bar theory.

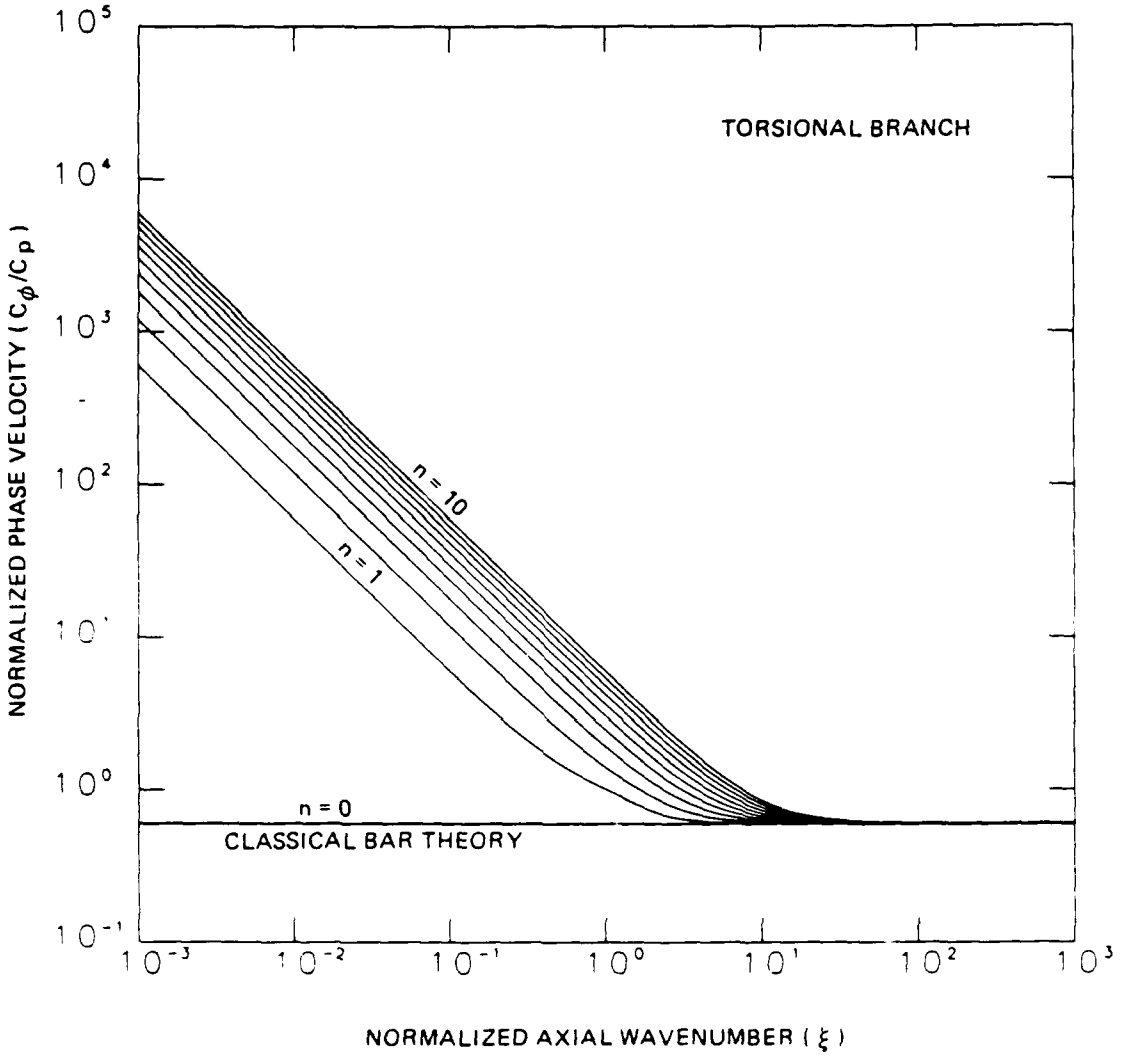

Figure 3.9. Normalized dispersion curves predicted by Flugge theory for the torsional branch of a cylindrical shell in vacuo at various mode order numbers. Comparison is also shown with classical bar theory.

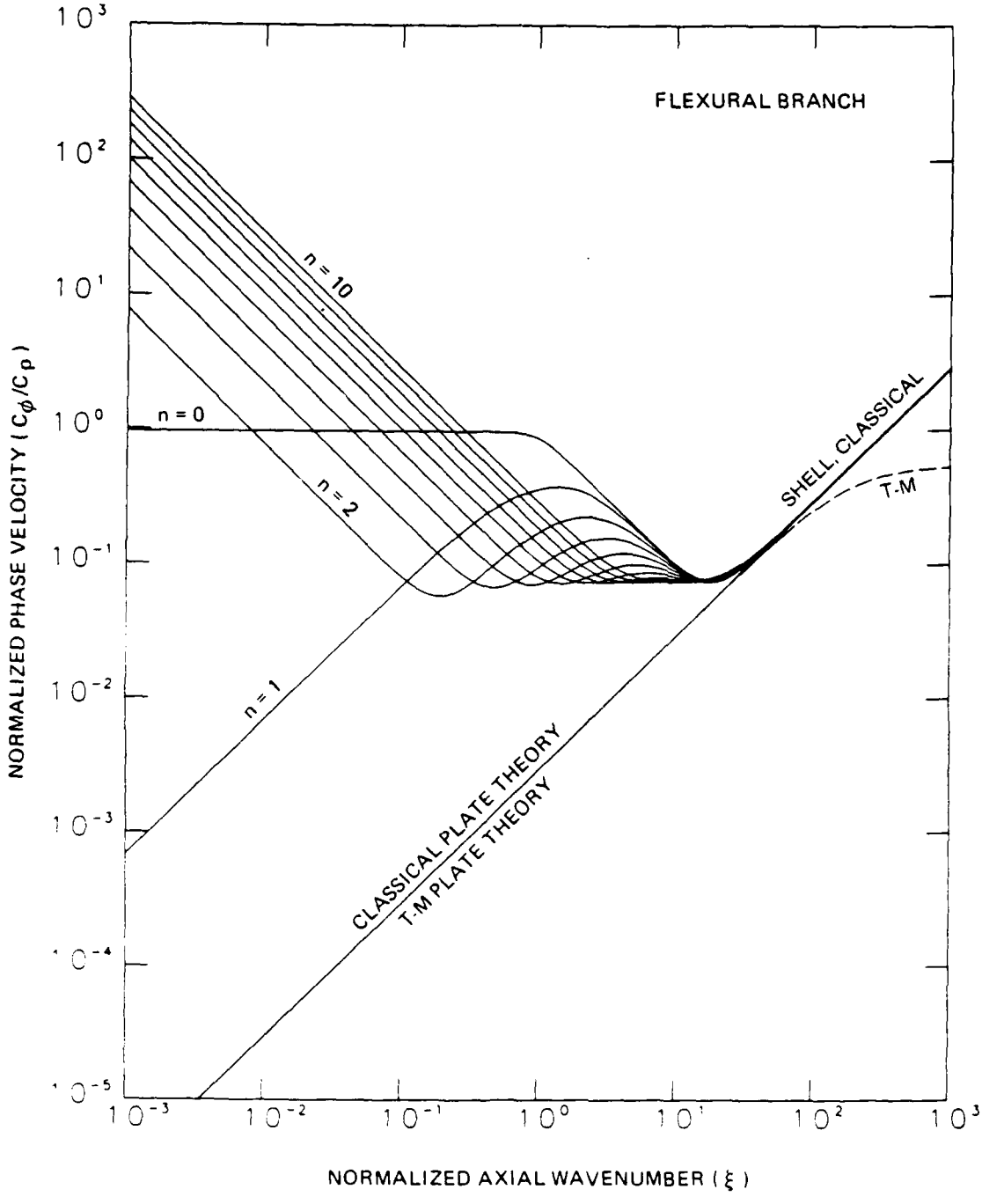

Figure 3.10. Normalized dispersion curves predicted by Flugge theory for the flexural branch of a cylindrical shell in vacuo at various mode order numbers. Comparison is also shown with classical and Timoshenko-Mindlin plate theory.

In terms of normalized parameters, the group velocity is given by

$$C_G = \frac{C_g}{C_p} = \frac{d\Omega}{d\xi} \quad .$$

Normalized group velocity versus wavenumber curves are given by Figures 3.11 to 3.13 for n=0 to 10. The group velocity was calculated from the frequency spectra by use of a five-point, cubic spline function and then by differentiating the resulting approximation. Reference is made to Forsythe, Malcom, and Moler (1977). The technique locally approximates the frequency spectra over five points centered on the point of interest by fitting cubic polynomials between each pair of points. Adjacent polynomials join continuously with continuous, first and second derivatives. The resulting spline function minimizes its potential energy and, in this sense, uniquely possesses the minimum curvature property of all functions interpolating the data. The resulting approximate polynomial function can then be easily differentiated and evaluated at the center point to yield the normalized group velocity.

Comparison of the phase velocity and group velocity curves shows that, for those modes with a nonzero cutoff frequency, the normalized phase velocity approaches infinity and the normalized group velocity approaches zero as the wavenumber approaches zero, indicating energy is ceasing to propagate. For both the longitudinal and torsional branches, the high wavenumber behavior is nondispersive. If both C_Φ amd C_G were plotted together versus wavenumber, the result would be the classical behavior associated with normal mode propagation in a duct. For the longitudinal branch this relationship would be given by $C_\Phi C_G=1$ while for the torsional branch it would be $C_\Phi C_G=(1+\mu)/2$. At large axial wave-

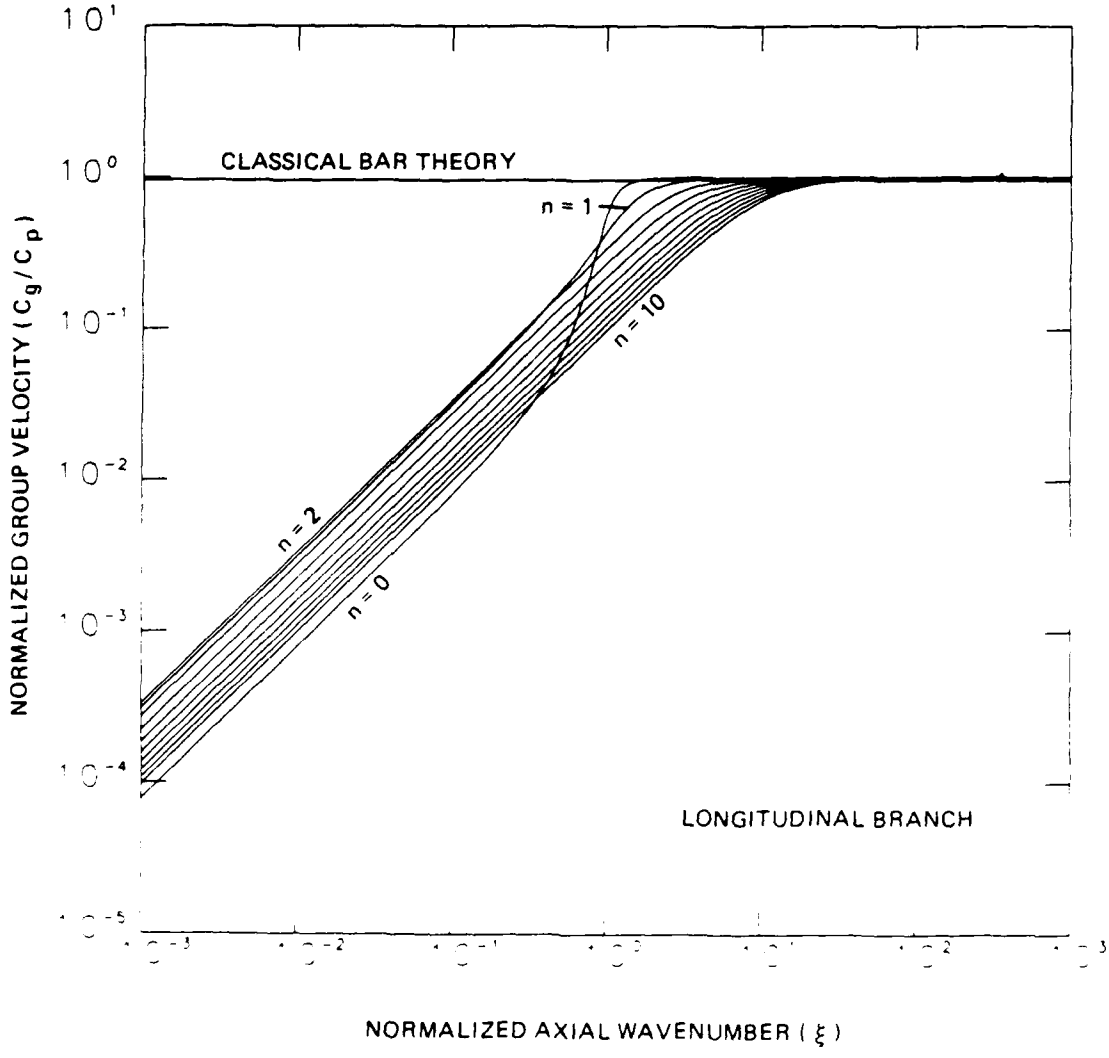

Figure 3.11. Normalized group velocity versus axial wavenumber curves predicted by Flugge theory for the longitudinal branch of a cylindrical shell in vacuo at various mode order numbers. Comparison is also shown with classical bar theory.

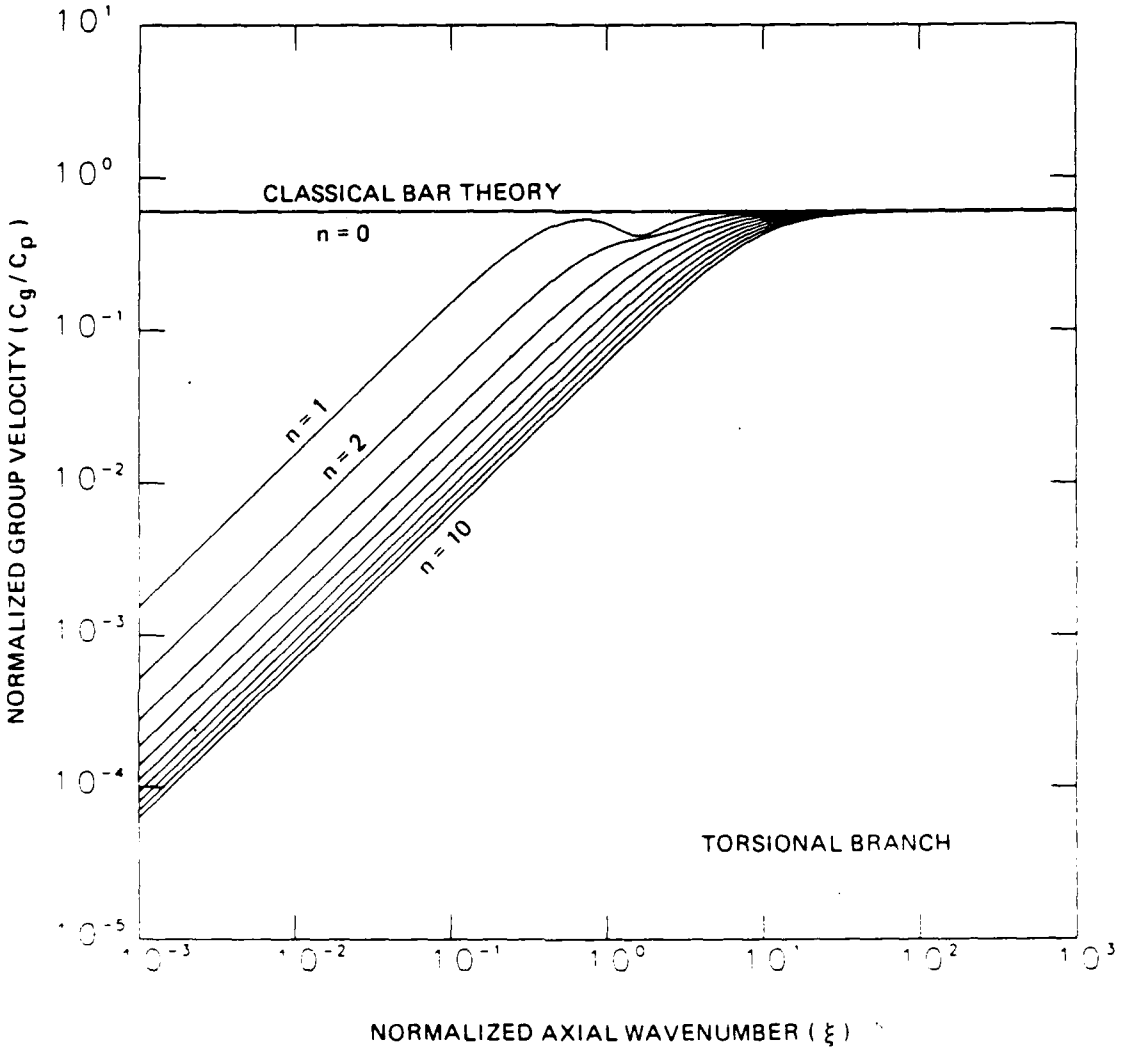

Figure 3.12. Normalized group velocity versus axial wavenumber curves predicted by Flugge theory for the torsional branch of a cylindrical shell in vacuo at various mode order numbers. Comparison is also shown with classical bar theory.

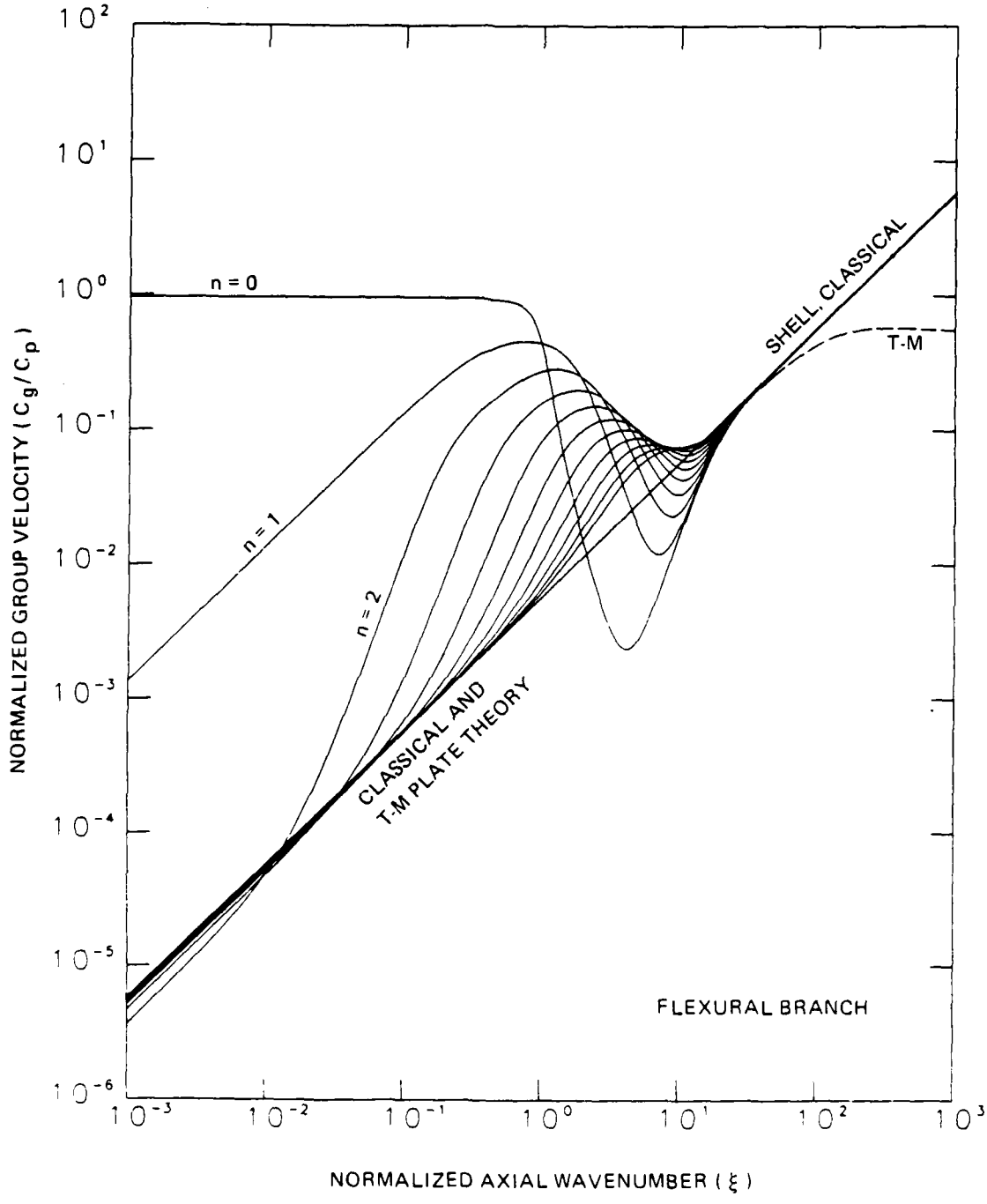

Figure 3.13. Normalized group velocity versus axial wavenumber curves predicted by Flugge theory for the flexural branch of a cylindrical shell in vacuo at various mode order numbers. Comparison is also shown with classical and Timoshenko-Mindlin plate theory.

number, the flexural branch exhibits the behavior $C_\phi=2C_G$, which is the dispersive behavior governing flexural waves in a plate.

The effect of the normalized shell thickness upon the behavior of the flexural branch is shown in Figures 3.14 to 3.18. For those modes which have a zero cutoff frequency, namely the axisymmetric and first beam modes, the branch behavior clearly has three regions of distinction. At low frequency (below $\Omega=1$), the branch acts in a manner similar to a membrane shell. At normalized frequencies above approximately two, the flexural branch behaves like flexural waves on a classical plate. A transition region exists between the membrane and plate regions in which bending terms become important. As the mode order increases above one and the shell becomes thicker, bending effects begin to dominate the entire wavenumber spectrum. Both the longitudinal and torsional branches are insensitive to variation in normalized shell thickness.

3.7 Comparison of Flugge and Gazis Theory

Approximate thin shell theories and shell theories based upon the exact three-dimensional equations of elasticity were discussed in the previous chapter. This section compares the results obtained by the approximate theory of Flugge with a theory developed by Gazis (1959) based upon elasticity. Graff (1975) provides an excellent discussion of Gazis' theory.

Upon examination, the equations developed by Gazis are quite complicated. Evaluation of the characteristic equation requires the solution of a 6X6 determinant whose terms contain Bessel and modified Bessel functions of the first and second kind. Spurious solutions may be generated in the transition region between the Bessel and modified Bessel functions. These and other numerical problems are discussed in the original references. Since the main purpose in using an approximate

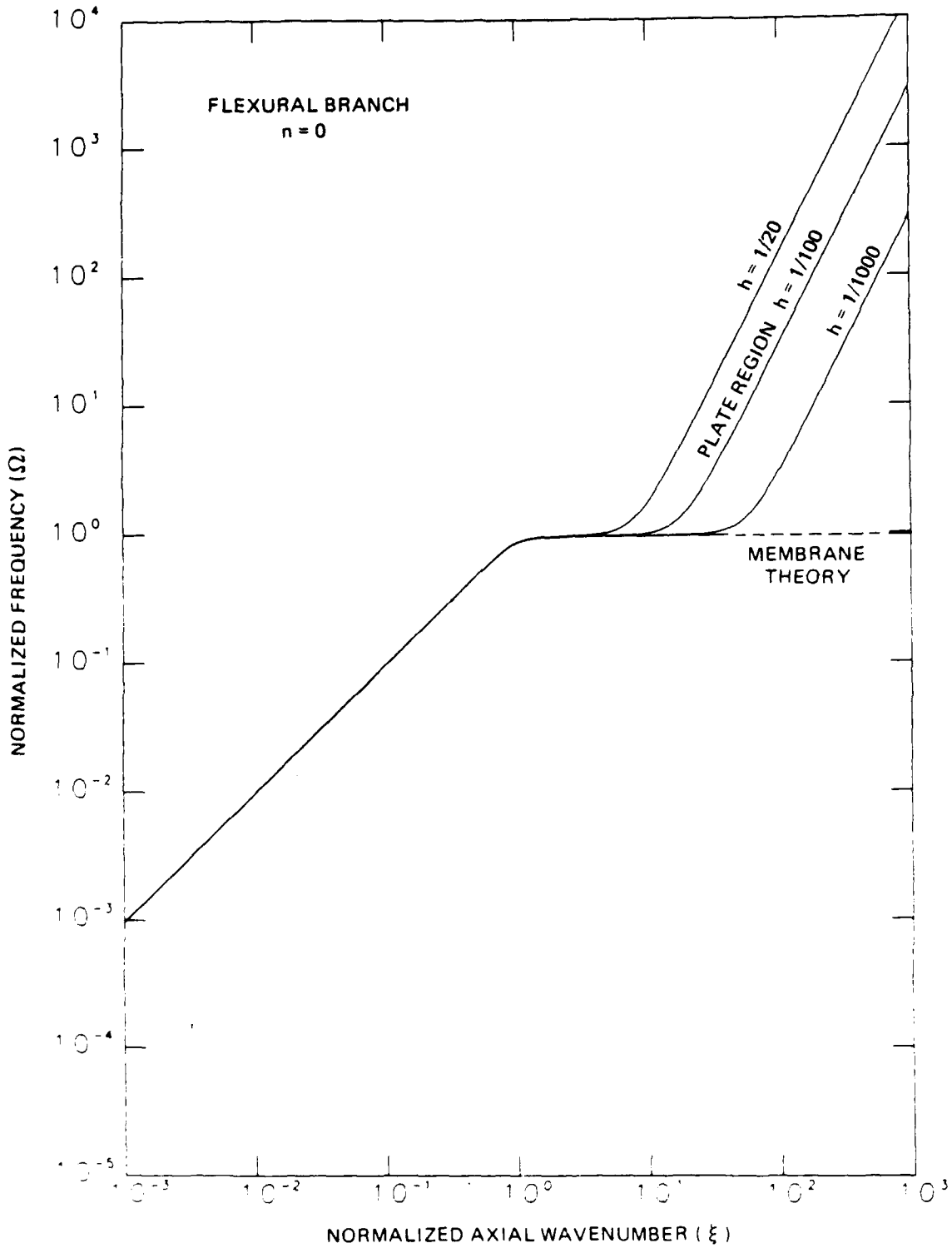

Figure 3.14. Effect of shell thickness variation upon the frequency spectrum of the n=0 mode of the flexural branch of a cylindrical shell in vacuo.

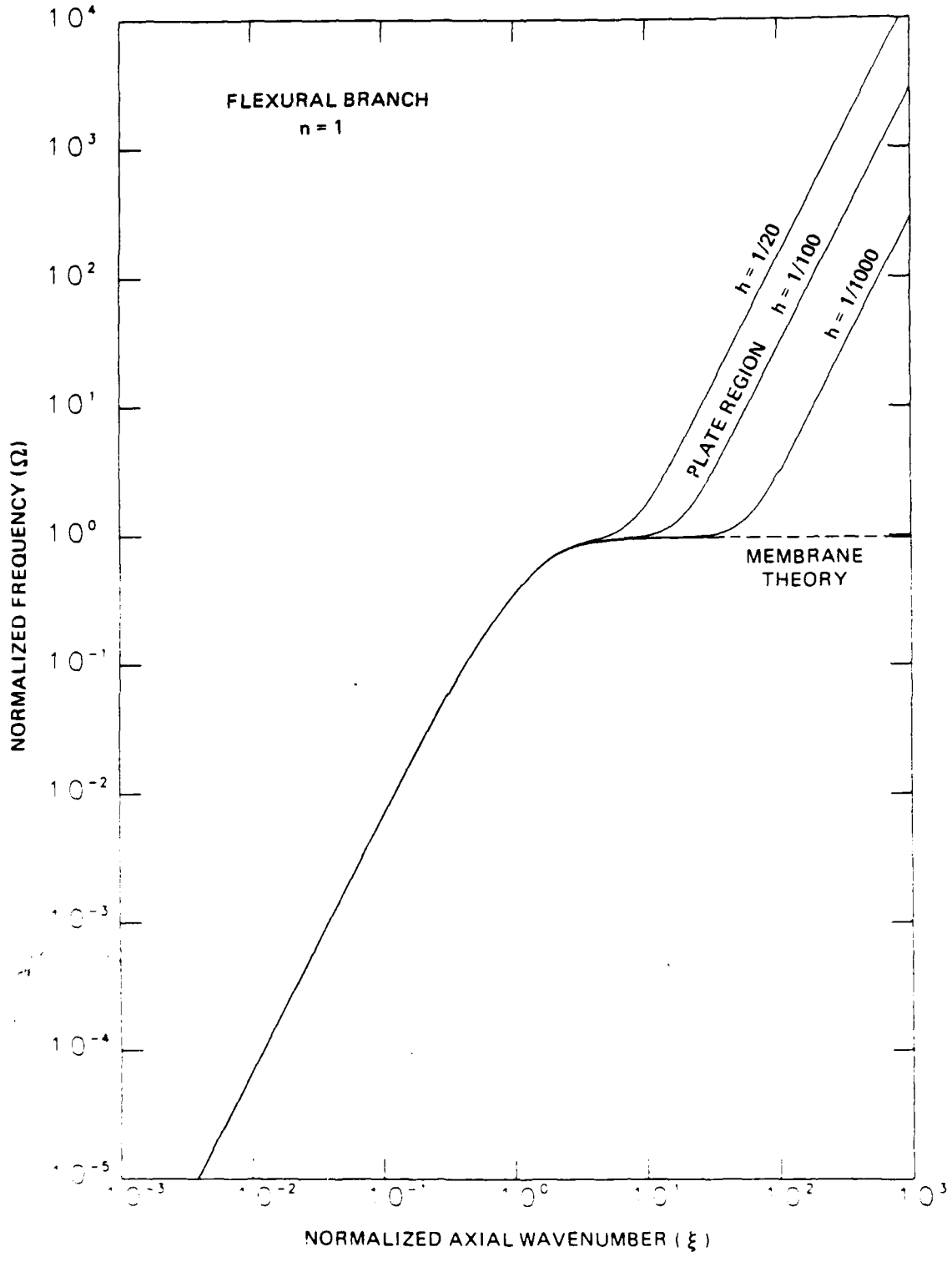

Figure 3.15. Effect of shell thickness variation upon the frequency spectrum of the n=1 mode of the flexural branch of a cylindrical shell in vacuo.

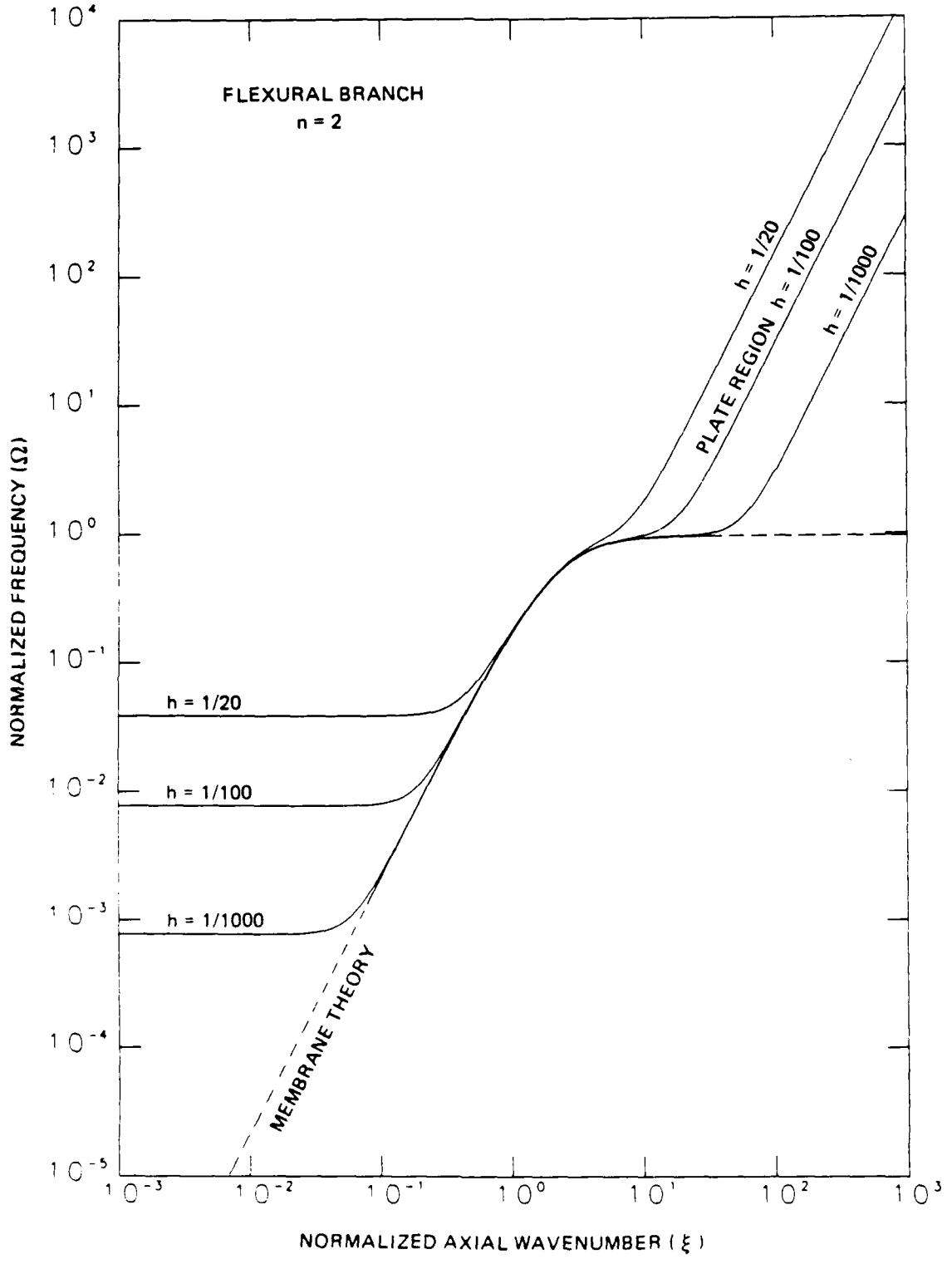

Figure 3.16. Effect of shell thickness variation upon the frequency spectrum of the n=2 mode of the flexural branch of a cylindrical shell in vacuo.

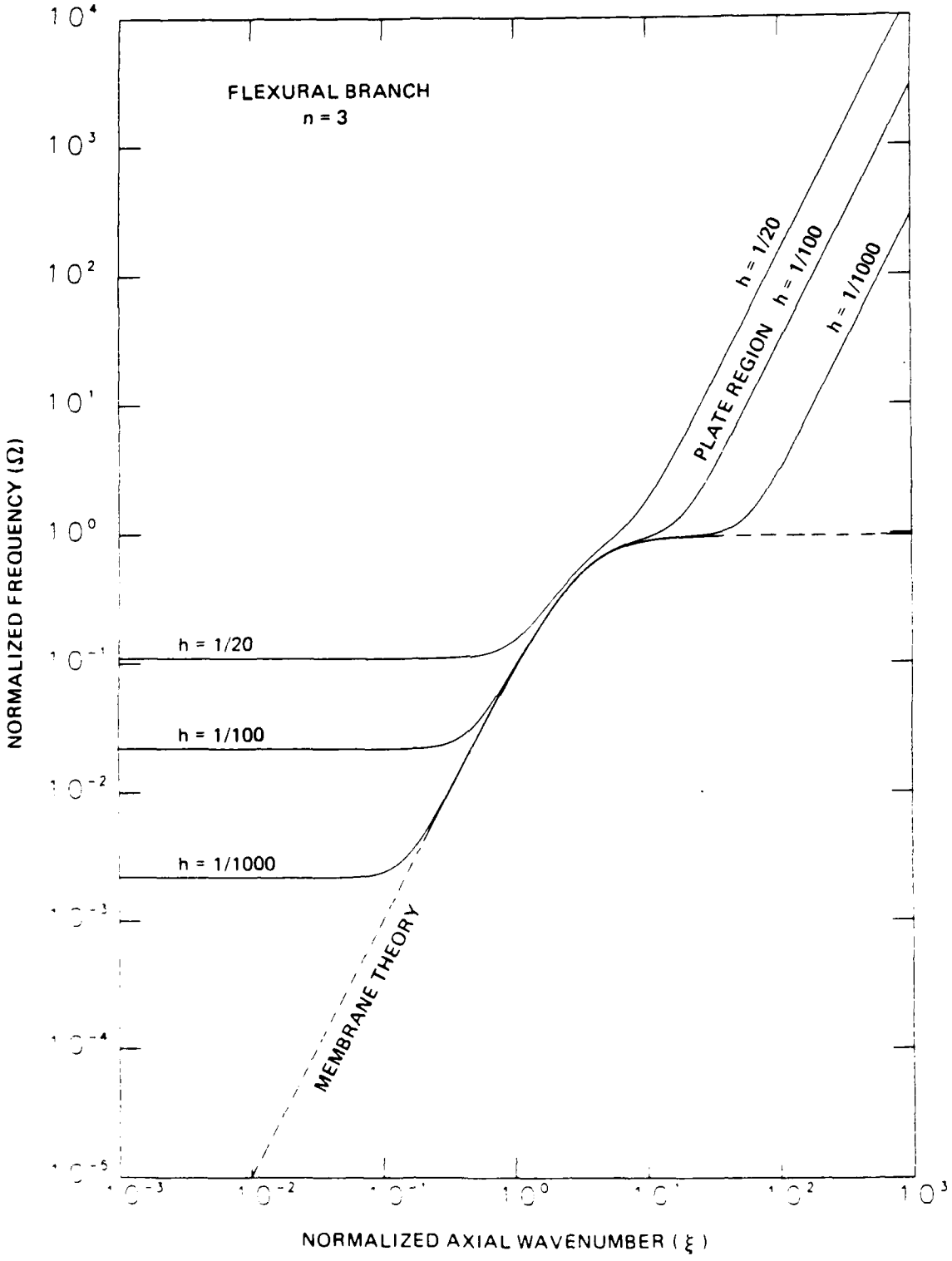

Figure 3.17. Effect of shell thickness variation upon the frequency spectrum of the n=3 mode of the flexural branch of a cylindrical shell in vacuo.

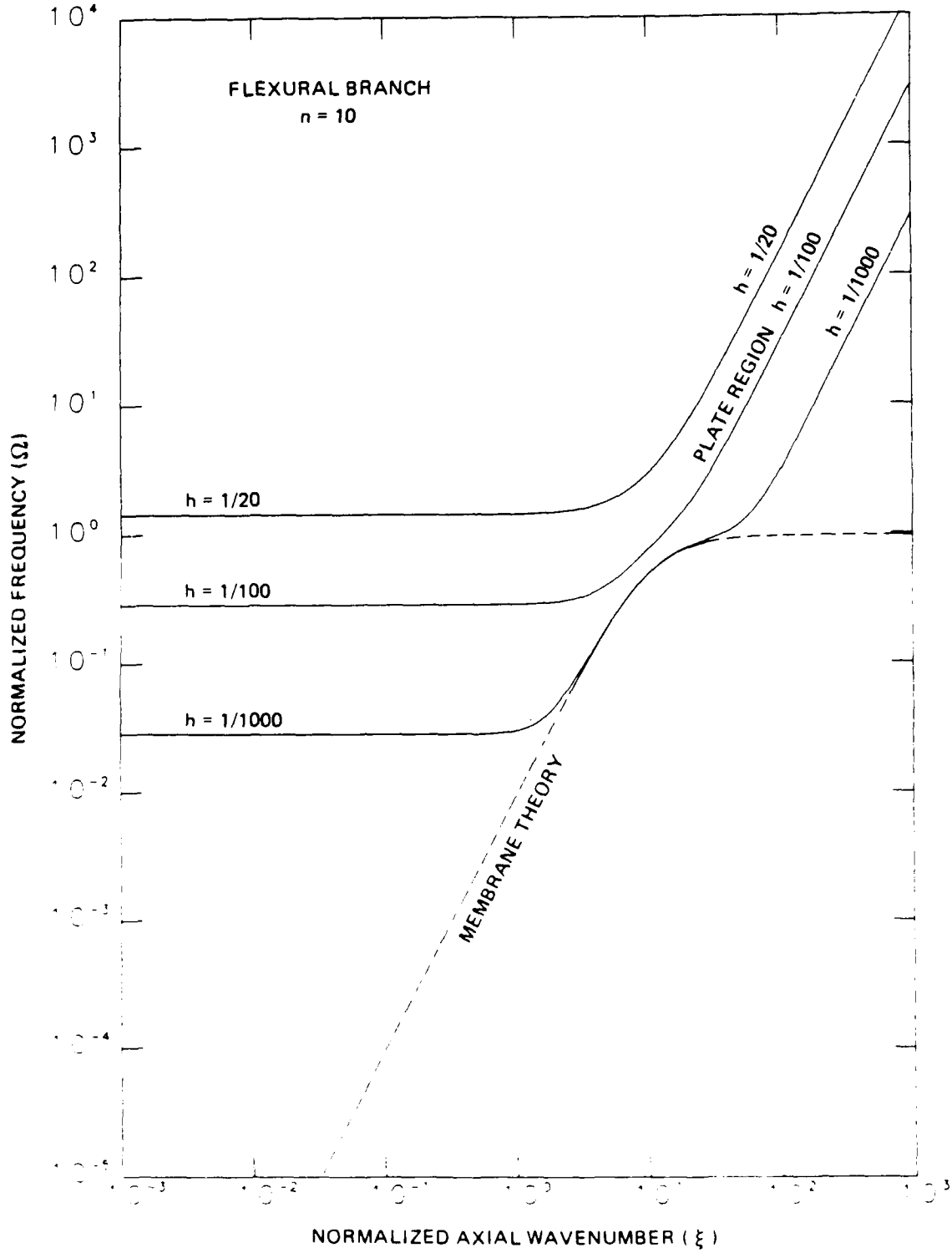

Figure 3.18. Effect of shell thickness variation upon the frequency spectrum of the n=10 mode of the flexural branch of a cylindrical shell in vacuo.

theory was to avoid the complexities of an exact, elastic theory, Gazis' equations were not evaluated directly. Instead, selected results presented in the original papers were reproduced and enlarged by a duplication process and then compared with results generated by Flugge theory using similar parameters.

In all cases, only the lowest three branches predicted by Gazis' theory were used. Poisson's ratio was taken as 0.30 and the normalized thickness was taken as 1/30. All variables from Gazis' work have been converted to the parameters used in this thesis. Figure 3.19 shows a frequency spectra comparison of Flugge theory and Gazis theory at axial wavenumbers less than 3π for the n=1 and 2 modes. As can be seen, all three branches exhibit excellent agreement between the two theories over the wavenumber range. Figure 3.20 extends the frequency-spectra comparison to large wavenumber. The torsional branch has excellent agreement over the entire wavenumber range shown and the longitudinal branch exhibits reasonable agreement up to ξ=70. The flexural branch shows a reasonable agreement between the two theories below ξ=30. Figure 3.21 compares the normalized phase velocity predicted by the two theories for the first and second mode orders for wavenumbers less than 12π. The theories show reasonable agreement over the entire range.

While the limits of validity of the Flugge theory in wavenumber space are interesting from a mathematical view, the limits in frequency space are of more practical interest. The forced motion of the shell is dependent upon all three branches, as will be discussed in the next section. If we assume that Gazis' elastic theory is correct at large wavenumber, then the Flugge theory will be limited by frequencies at which the flexural branch is reasonably valid. For h=1/30, this would be below a normalized frequency of 25 which corresponds to a frequency

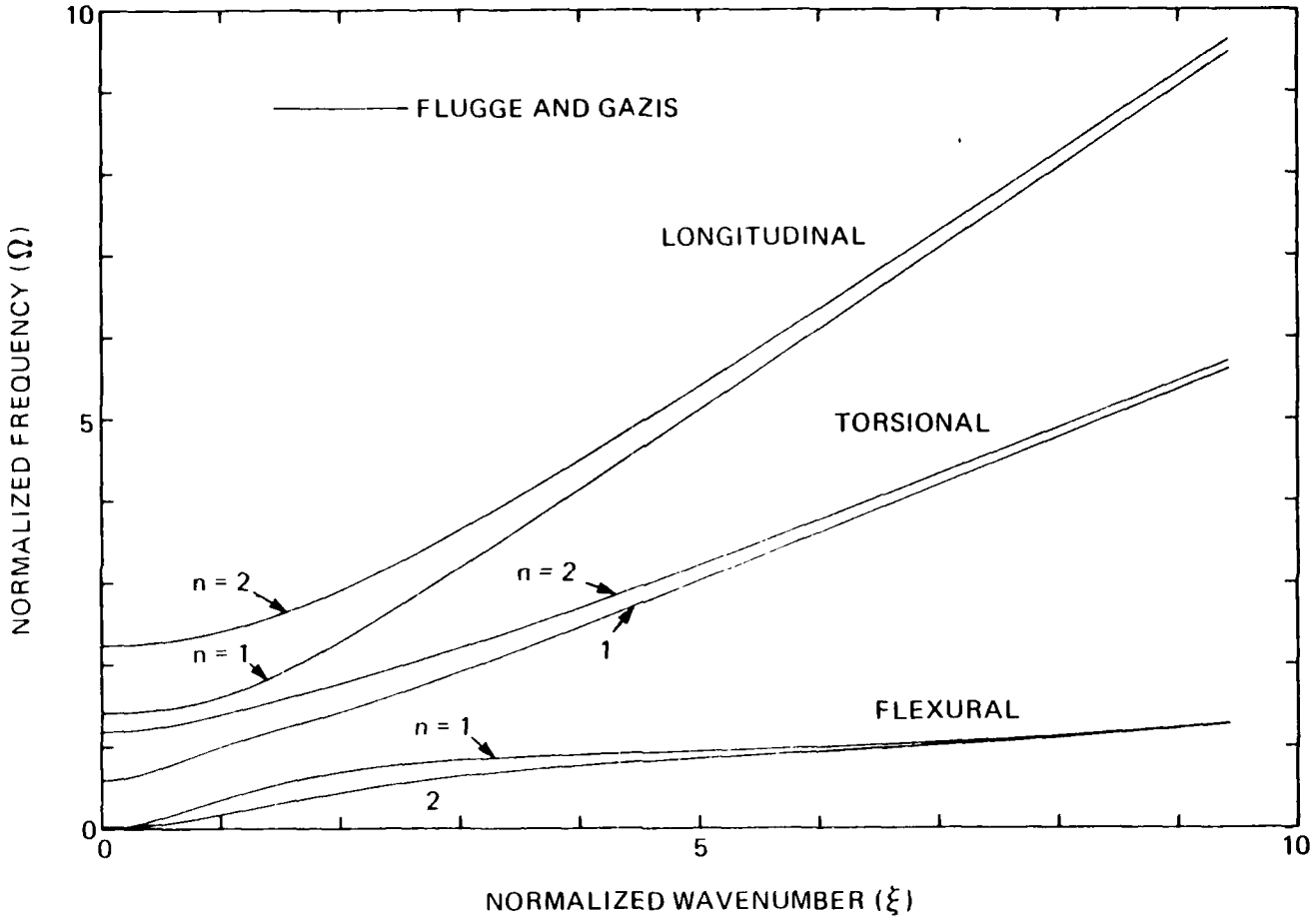

Figure 3.19. Comparison of frequency spectra predicted at low axial wavenumber by Flugge's theory and the lowest three branches of Gazis' theory for n=1,2 (h=1/30 and μ=0.30). [Gazis (1959, Figure 7) data printed with permission.]

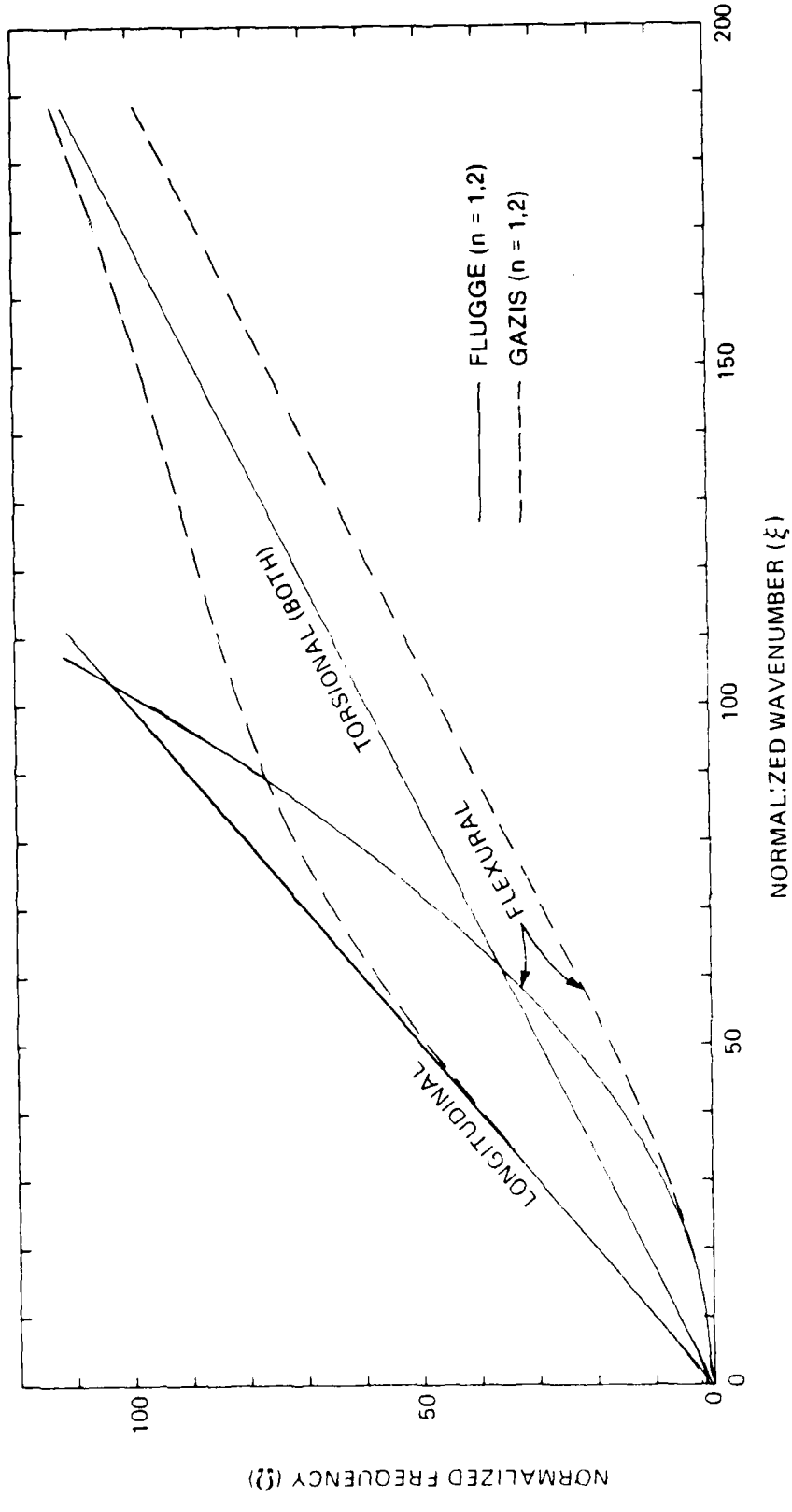

Figure 3.20. Comparison of frequency spectra predicted at high axial wavenumber by Flugge's theory and the lowest three branches of Gazis' theory for n=1,2 (h=1/30 and μ=0.30). [Gazis (1959, Figure 6) data printed with permission.]

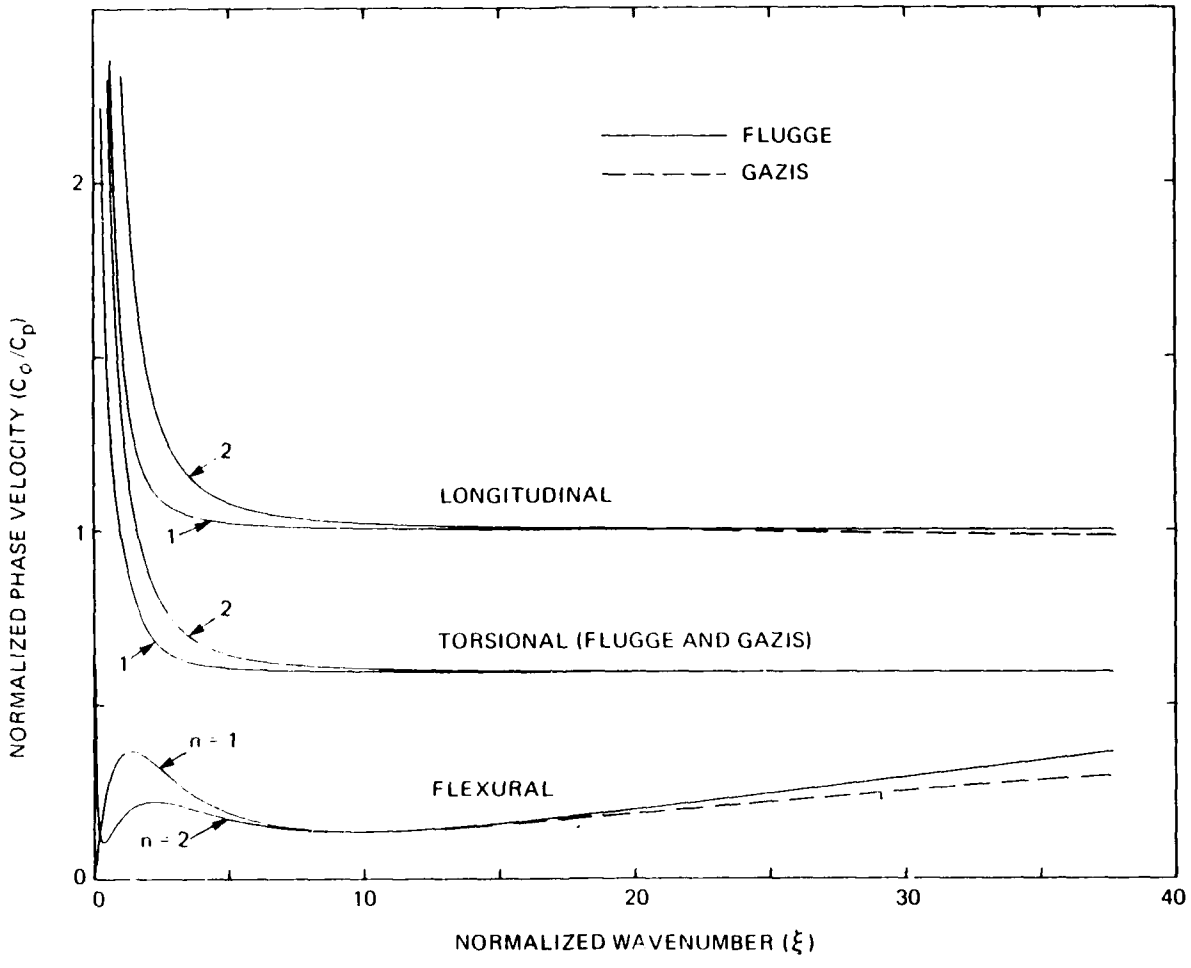

Figure 3.21. Comparison of dispersion curves predicted by Flugge's theory and the lowest three branches of Gazis' theory for n=1,2 (h=1/30 and μ=0.30). [Gazis (1959, Figure 11) data printed with permission.]

AD-A197 282 NEARFIELD ACOUSTIC RADIATION FROM A POINT-EXCITED CYLINDRICAL SHELL(U) NAVAL UNDERWATER SYSTEMS CENTER NEW LONDON CT NEW LONDON LAB R D VOGELSONG 26 MAY 88 NUSC-TD-8043 F/G 20/1 NL

2/3

UNCLASSIFIED

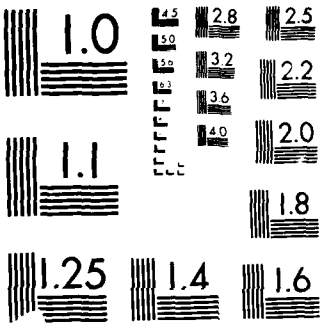

UTION TEST CHART

approximately three times the coincidence frequency of a plate with the same thickness. In terms of plate coincidence frequency, this limit will also be taken as an approximation of the upper frequency limit of validity for h=1/100 for a shell in vacuo. It is expected that the addition of fluid loading to the problem would increase this frequency limit since the contribution of the shell would only be part of the total solution.

Although the comparison with Gazis' work has been limited to the n=1 and 2 modes, it is expected that the higher-order modes behave similarly. Gazis shows a convergence of mode behavior above $\xi=3\pi$ in Figure 3.21 which also occurs for modes above n=2. Similarly, the Flugge theory shows mode behavior convergence in Figures 3.5 to 3.7 above $\xi=30$, such that the relationship between the two theories above $\xi=30$ for all mode orders should be represented by Figures 3.19 to 3.21.

3.8 Forced Motion of a Shell In Vacuo

Assume the shell in vacuo is harmonically excited by a point force applied radially outward at the origin of the form

$$f_d(x,\theta,t) = \frac{F_r}{R}\,\delta(xR)\,\delta(\theta)\,\exp(-j\omega t) \tag{3.16}$$

such that

$$\tilde{f}_d(\xi,\theta,t) = \frac{F_r}{R^2}\,\delta(\theta)\,\exp(-j\omega t)$$

where F_r is the force magnitude, and ω is the driving frequency. In matrix notation, the equations of motion, Equations (2.20), become

$$([\tilde{M}] - \Omega^2\,[I])\,[\tilde{X}] = [\tilde{F}] \tag{3.17}$$

where the force matrix is given by

$$[\tilde{F}] = F_n \begin{bmatrix} 0 \\ 0 \\ 1 \end{bmatrix} \quad , \text{ and } \qquad F_n = \frac{\varepsilon_n F_r}{2\pi DR^2} \tag{3.18}$$

is a nondimensional modal force. $[\tilde{M}]$ and $[\tilde{X}]$ have been previously defined, and $[I]$ is again the identity matrix. An applied axial or circumferential force would generate nonzero elements in row 1 or 2 of the force matrix. A distributed load would yield elements which were a function of mode order or axial wavenumber. The specified system has a modal solution given for n>0 by

$$\begin{aligned} \tilde{U}_n(\xi) &= jF_n \frac{\tilde{m}_{12}\tilde{m}_{23} - \tilde{m}_{13}(\tilde{m}_{22} - \Omega^2)}{\det([\tilde{M}] - \Omega^2 [I])} \\ \tilde{V}_n(\xi) &= F_n \frac{\tilde{m}_{12}\tilde{m}_{13} - \tilde{m}_{23}(\tilde{m}_{11} - \Omega^2)}{\det([\tilde{M}] - \Omega^2 [I])} \\ \tilde{W}_n(\xi) &= F_n \frac{(\tilde{m}_{11} - \Omega^2)(\tilde{m}_{22} - \Omega^2) - \tilde{m}_{12}^2}{\det([\tilde{M}] - \Omega^2 [I])} \end{aligned} \tag{3.19a}$$

For the axisymmetric mode, $\tilde{V}_o(\xi)=0$ and

$$\begin{aligned} \tilde{U}_0(\xi) &= -j\, F_0 \frac{\tilde{m}_{13}^2}{(\tilde{m}_{11} - \Omega^2)(\tilde{m}_{22} - \Omega^2) - \tilde{m}_{13}^2} \\ \tilde{W}_0(\xi) &= F_0 \frac{\tilde{m}_{11} - \Omega^2}{(\tilde{m}_{11} - \Omega^2)(\tilde{m}_{22} - \Omega^2) - \tilde{m}_{13}^2} \end{aligned} \tag{3.19b}$$

In general, the determinant of the coefficients can be written as

$$\det([\tilde{M}] - \Omega^2 [I]) = s_1\Omega^6 + s_2\Omega^4 + s_3\Omega^2 + s_4 \tag{3.20}$$

where the s_j were previously defined in Equation (3.5). An equivalent form is given by

$$\det([\tilde{M}] - \Omega^2\,[I]) = s_1(\Omega^6 - \Omega_{nq}^6) + s_2(\Omega^4 - \Omega_{nq}^4) + s_3(\Omega^2 - \Omega_{nq}^2) \qquad (3.21)$$

with Ω_{nq} taken as any of the natural frequencies of the shell in vacuo.

Let us now define a spectral modal mechanical impedance for the shell as

$$Z_{sn}(\xi) = \frac{DF_n}{-j\omega R\tilde{W}_n(\xi)} = j\,\frac{\rho_s c_p h}{\Omega}\,X_{sn} \quad \text{where} \quad X_{sn} = \frac{D_{sn}(\xi)}{N_{sn}(\xi)}\ , \qquad (3.22)$$

which is purely reactive for an undamped shell. Note that the dimensional form of the transformed displacement has been used. This will be a useful definition for the fluid-loaded problem. Further note that $Z_{sn}(\xi)$ is not related to the transform of the driving-point impedance of the shell, since multiplication (and division) in one domain is represented by a convolution in the transformed domain. In this sense, the nomenclature is artificial. However, $Z_{sn}(\xi)$ does represent the total contribution of the shell to the fluid-loaded problem and, in that sense, is analogous to an impedance. The normalized reactance $X_{sn}(\xi)$ acts as a normalized spectral stiffness that is defined by polynomials in ξ^2 given by

$$\begin{aligned} D_{sn}(\xi) &= \det([\tilde{M}] - \Omega^2\,[I]) && \text{for } n>0 \\ &= (\tilde{m}_{11} - \Omega^2)(\tilde{m}_{33} - \Omega^2) - \tilde{m}_{13}^2 && \text{for } n=0 \end{aligned} \qquad (3.23a)$$

and

$$\begin{aligned} N_{sn}(\xi) &= (\tilde{m}_{11} - \Omega^2)(\tilde{m}_{22} - \Omega^2) - \tilde{m}_{12}^2 && \text{for } n>0 \\ &= \tilde{m}_{11} - \Omega^2 && \text{for } n=0 \end{aligned} \qquad (3.23b)$$

at fixed, normalized, driving frequency Ω. In general, these components

can be written as

$$D_{sn}(\xi) = a_1\xi^8 + a_2\xi^6 + a_3\xi^4 + a_4\xi^2 + a_5$$
$$N_{sn}(\xi) = b_1\xi^4 + b_2\xi^2 + b_3 \tag{3.24}$$

where a_j and b_j are constants dependent upon n, Ω, β, and μ and where $a_1=b_1=0$ for the axisymmetric mode.

At high frequency the normalized shell spectral stiffness function can be approximated by

$$\lim_{\Omega\to\infty} X_{sn}(\xi) = \beta(\xi^2+ n^2)^2 - \Omega^2 \ . \tag{3.25}$$

If we define an effective structural wavenumber as

$$k_s = \sqrt{\xi^2+ n^2}$$

then the high frequency approximation can be put into a form analogous to the plate impedance function but where the higher mode order nature of the shell has been preserved. The functional relationship expressed by Equation 3.25 is also valid for either large axial wavenumber or mode order at any frequency.

The transformed displacement solutions to the forced vibration problem given by Equations (3.19) could be introduced into the displacement relations given by Equations (2.22). For each displacement, the denominator of the inverse Fourier integral would be $D_{sn}(\xi)$. If the integration were carried out over the complex ξ-domain, the roots of $D_{sn}(\xi)$, which are the shell branches, are seen to represent the poles of the problem. For fixed Ω, each mode would contain eight poles representing both the positive and negative wavenumber spectrum. At driving

frequency less than the cutoff frequency of one or more branches, some of the poles would be complex. Second-order poles and complex-conjugate poles may also exist. The total solution would be given by the double sum of the residues over all of the mode orders.

Only radial vibrations can radiate energy into an inviscid fluid medium. Therefore, the acoustic field generated by a vibrating shell will be dependent only upon the shell's radial motion. If fluid loading upon the shell was not considered, such as for a low-density medium like air, then this radial displacement would be given by Equation (2.22) for a shell in vacuo as

$$w(x,\theta,t) = w_{ref} \sum_{n=0}^{\infty} \varepsilon_n \cos(n\theta) \int_{-\infty}^{\infty} \frac{\exp(j\xi x)}{X_{sn}(\xi)} d\xi \exp(-j\omega t) , \qquad (3.26)$$

written in terms of the normalized shell stiffness. The term

$$w_{ref} = \frac{F_r}{(2\pi R)^2 D}$$

is a convenient normalized reference displacement. Since an acoustic field cannot create surface tractions, the effect of including fluid loading upon the shell will be only a radial effect. As will be seen, fluid loading will reduce the number of real branches from three to one, and this remaining branch will be a deformed version of the flexural branch in vacuo. In addition, the concept of a cutoff frequency will become more generalized to include the dual concept of a cutoff wavenumber. These topics will be covered in the next chapter.

Chapter 4

VIBRATION OF A FLUID-LOADED CYLINDRICAL SHELL

4.1 Introduction

This chapter will discuss the vibration of a shell in the presence of an external fluid. Important mathematical preliminaries will be introduced that are required in the next chapter where Cauchy's theorem and integral formula are used as a solution of the acoustic pressure field. Boundary conditions at the shell-fluid interface and at infinity are used to specify a spectral modal specific acoustic impedance that modifies the in vacuo integral representations of the radial displacement and the transformed acoustic pressure. Unlike the in vacuo case, the addition of fluid loading requires that both the radial displacement field and the acoustic pressure field be dependent upon a radial wavenumber that is a multi-valued function of the axial wavenumber. Concepts of branch points and branch lines are introduced to force single-valued behavior. The behavior of the normalized spectral modal acoustic radiation impedance is presented over the entire complex radial wavenumber domain. Physical and mathematical reasons are presented to favor the choice of the Sommerfeld branch lines for this problem. Existence properties of the singularities are developed. The location and behavior of both real and complex singularities of the fluid-loaded problem are presented. Their behavior is compared to the in vacuo branches of free vibration. For circumferential mode orders greater than one, the real branch of the fluid-loaded problem has a finite bandwidth defined by both a lower and an upper cutoff frequency. As mode order increases,

this bandwidth decreases such that above a critical mode order no real branch exists.

4.2 The Acoustic Loading Term

Assume the shell is externally surrounded by a fluid medium of characteristic acoustic impedance ρc. A harmonic point force directed radially outward is applied to the shell in the manner discussed in Section 3.8 for a shell in vacuo. The internal region of the shell is again taken as a vacuum such that acoustic energy is only radiated externally into the fluid. The acoustic pressure field is governed by the wave equation

$$\nabla_R^2 \, p(r,\theta,x,t) = \frac{1}{c^2} \, \frac{\partial^2}{\partial t^2} \, p(r,\theta,x,t) \tag{4.1}$$

in normalized coordinates. The normalized Laplacian operator is related to the un-normalized operator by $\nabla^2 = R^2(\nabla_R)^2$ where R is the normalizing constant taken as the middle-surface radius of the shell. Therefore, in normalized cylindrical coordinates

$$(\nabla_R)^2 = R^{-2} \left(\frac{\partial^2}{\partial r^2} + r^{-1} \frac{\partial}{\partial r} + r^{-2} \frac{\partial^2}{\partial \theta^2} + \frac{\partial^2}{\partial x^2} \right) . \tag{4.2}$$

For time harmonic excitation, the governing equation can be written as

$$(\nabla_R^2 + R^{-2}k^2) \, p(r,\theta,x) = 0 \tag{4.3}$$

where

$$k = R\omega/c = c_p \Omega/c \tag{4.4}$$

is the normalized acoustic wavenumber.

Equation (4.3) can be solved by first taking the Fourier transform in the axial coordinate and then assuming a separation-of-variables

solution [e.g. Morse and Ingard (1968)]. The transformed acoustic pressure would generally be given by

$$\tilde{p}(r,\theta,\xi) = \sum_{m=0}^{\infty} \left[a_m(\xi)H_m^{(1)}(\gamma r) + b_m(\xi)H_m^{(2)}(\gamma r)\right] \begin{Bmatrix}\sin(m\theta)\\ \cos(m\theta)\end{Bmatrix} \qquad (4.5)$$

with ξ the normalized axial wavenumber. Parameter γ is a separation-of-variables constant which represents the normalized radial wavenumber and is subject to the constraint

$$\gamma^2 = k^2 - \xi^2 \quad . \qquad (4.6)$$

The infinite Fourier series representation is due to another separation-of-variables constant which has been restricted to integer values by continuity considerations on the circumferential coordinate. The integers m represent mode orders and, as in the case of shell displacements, the transformed acoustic pressure is expressed as the sum of modal contributions. The functions $H_m^{(1)}(\gamma r)$ and $H_m^{(2)}(\gamma r)$ are Hankel functions of the first and second kind defined by Abramowitz and Stegun (1972) as

$$H_m^{(1)}(z) = J_m(z) + j\, Y_m(z)$$

$$H_m^{(2)}(z) = J_m(z) - j\, Y_m(z)$$

where $J_m(z)$ and $Y_m(z)$ are Bessel functions of the first and second kind of argument z and order m. In order to account for a logarithmic singularity in $Y_m(z)$ at zero argument, the γ-plane will be cut along the negative real axis so that $-\pi \leq \arg(\gamma) \leq +\pi$ defines the principal valued branch of the Hankel functions. Parameters $a_m(\xi)$ and $b_m(\xi)$ are coefficients to be determined from the boundary conditions.

In addition to the constraints on the separation-of-variables constants γ and m, implicit boundary conditions exist which can also be

applied to the solution as given by Equation (4.5). The first of these concerns the circumferential dependence of the pressure field. Since the acoustic field is due solely to the radial vibrations of the shell, the pressure field must have the same circumferential dependence as the radial vibration distribution, namely $\cos(m\theta)$. The radiation condition also serves as an implicit boundary condition. For harmonic excitation of the form $\exp(-j\omega t)$, the large argument approximation of the Hankel function of the first kind represents energy propagating outward for an implied positive sign associated with the square root of Equation (4.6). Conversely, the Hankel function of the second kind represents energy propagating inward. In the absence of acoustic sources other than the vibrating shell, the field in the surrounding homogeneous medium of infinite extent can contain only waves propagating outward, or $b_m(\xi)=0$ and

$$\tilde{p}(r,\theta,\xi) = \sum_{m=0}^{\infty} a_m(\xi)\, H_m^{(1)}(\gamma r)\, \cos(m\theta) \quad . \tag{4.7}$$

For brevity the Hankel function of the first kind will be denoted simply as $H_m(z)$, except in situations where ambiguity might occur with the function of the second kind.

The unknown modal coefficients $a_m(\xi)$ can be found by application of the continuity-of-particle-velocity boundary condition

$$\rho R \frac{\partial}{\partial t} \dot{w}(\theta,x,t) = - \frac{1}{R} \frac{\partial}{\partial r} p(r,\theta,x,t)$$

at the normalized outer radius of the shell a. In normalized transformed variables, this condition becomes

$$\rho c_p^2 \Omega^2 \tilde{w}(\theta,\xi) = \frac{\partial}{\partial r} \tilde{p}(r,\theta,\xi) \tag{4.8}$$

evaluated at $r = a$. By introducing Equation (4.7) for $\tilde{p}$ and the transform of Equation (2.13) for $\tilde{w}$, multiplying through by $\cos(n\theta)$, integrating θ over $0 \leq \theta \leq 2\pi$, and applying the orthogonality condition given by Equation (2.15), we yield the modal relation

$$a_m(\xi) = \rho c_p^2 \varrho^2 \frac{\tilde{W}_m(\xi)}{\gamma H_m'(\gamma a)} \quad . \tag{4.9}$$

The prime notation designates the derivative of the Hankel function with respect to its total argument such that

$$H_m'(z) = \frac{\partial}{\partial z} H_m(z) \quad .$$

The transformed acoustic pressure at any point in the fluid medium is a known function of the transformed radial displacement of the shell.

It will be convenient to define a spectral modal specific acoustic impedance as

$$Z_{fm}(\gamma r) = \frac{\tilde{p}_m(\xi)}{-j\omega R \tilde{W}_m(\xi)} = j\rho ck \frac{H_m(\gamma r)}{\gamma H_m'(\gamma a)} \tag{4.10}$$

which represents the contribution of the fluid to the problem. Let us also define a normalized spectral modal acoustic radiation impedance as

$$Z_{am}(\gamma) = \frac{H_m(\gamma a)}{\gamma H_m'(\gamma a)} \tag{4.11}$$

such that at the shell $Z_{fm}(\gamma a) = j\rho ck Z_{am}(\gamma)$. The transformed acoustic pressure could now be written in the form

$$\tilde{p}(r,\theta,\xi) = -jck \sum_{m=0}^{\infty} Z_{fm}(\gamma r)\, \tilde{W}_m(\xi)\, \cos(m\theta) \quad . \tag{4.12}$$

The inverse Fourier transform of this expression would be valid at all points in the fluid medium and will be extensively discussed in the next chapter. The transformed acoustic loading on the cylindrical shell would therefore be given by $\tilde{p}_a(\theta,\xi) = \tilde{p}(a,\theta,\xi)$.

4.3 The Fluid-loaded Characteristic Equation

In the absence of an applied force, introduction of the acoustic loading term $\tilde{p}_a(\theta,\xi)$ into the transformed equations of motion of the shell, given by Equation (2.20) yields

$$\{[\tilde{M}] + [\tilde{M}_f]\}\ [\tilde{X}] = \Omega^2[\tilde{X}] \tag{4.13}$$

where $[\tilde{M}]$ remains the shell stiffness matrix defined by Equation (3.2), $[\tilde{M}_f]$ is the fluid reaction matrix, and $[\tilde{X}]$ is the transformed modal deformation matrix. The fluid reaction upon the shell is given by

$$[\tilde{M}_f] = \begin{bmatrix} 0 & 0 & 0 \\ 0 & 0 & 0 \\ 0 & 0 & \Delta Z_{an} \end{bmatrix} \tag{4.14}$$

where

$$\Delta = \rho c_p^2 \Omega^2 / D = \frac{\rho \Omega^2}{\rho_s h} \quad . \tag{4.15}$$

and D is the normalized extensional rigidity of the shell. In the deviation of Equation (4.13) the orthogonality condition was used to equate shell mode order n and the fluid medium mode order m.

Equation (4.13) can also be written in terms of a characteristic matrix $[\tilde{\Lambda}]$ such that

$$([\tilde{M}] + [\tilde{M}_f] - \Omega^2[I])[\tilde{X}] = [\tilde{\Lambda}]\ [\tilde{X}] = 0 \tag{4.16}$$

where $[I]$ is again the identity matrix. Since Z_{fn} is also a function of

frequency, neither Equations (4.13) nor (4.16) are in the canonical form of the eigenvalue problem. In any event, it is more physically reasonable to consider the values of ξ that are solutions of Equation (4.16) for real values of frequency. Non-trivial solutions are given by the characteristic equation

$$\det [\tilde{\Lambda}] = 0 \quad . \tag{4.17}$$

Recalling that the in vacuo characteristic matrix was Hermitian for all real ξ, it is seen that fluid loading restricts this Hermitian behavior to real values of the axial wavenumber such that $\xi^2 > k^2$. Therefore, it is expected that the free vibration of the fluid-loaded shell will likewise be restricted to this regime.

Solutions of the characteristics equation are also important because they represent the singularities associated with the inverse Fourier integral representation of the forced response of both the shell displacements and the acoustic pressure field. It is perhaps more informative to write the characteristic equation in terms of the transformed modal impedance functions Z_{sn} defined by Equation (3.22) and Z_{fn} to yield

$$\det[\tilde{\Lambda}] = Z_{sn}(\xi) + Z_{fn}(\gamma a) = 0 \quad . \tag{4.18}$$

In terms of these impedance functions, the forced transformed flexural deformation of the fluid-loaded shell is found to be

$$\tilde{W}_n(\xi) = j \frac{\rho_s c_p h}{\Omega} w_{ref} [Z_{sn}(\xi) + Z_{fn}(\gamma a)]^{-1} \tag{4.19}$$

were w_{ref} was previously defined. Introducing this expression into Equation (2.22) yields

$$w(\theta,x,t) = w_{ref} \sum_{n=0}^{\infty} \varepsilon_n \cos(n\theta) \int_{-\infty}^{+\infty} j \frac{\rho_s c_p h}{\varrho} \frac{e^{j(\xi x-\omega t)}}{Z_{sn}(\xi) + Z_{fn}(\gamma a)} \, d\xi$$

$$= w_{ref} \sum_{n=0}^{\infty} \varepsilon_n \cos(n\theta) \int_{-\infty}^{+\infty} \frac{e^{j(\xi x-\omega t)}}{X_{sn}(\xi) + \Delta Z_{an}(\gamma)} \, d\xi \quad . \qquad (4.20)$$

Likewise, the acoustic pressure field can be written using Equations (4.19) and (4.12) as

$$p(r,\theta,x,t) = p_{ref} \sum_{n=0}^{\infty} \varepsilon_n \cos(n\theta) \int_{-\infty}^{+\infty} \frac{Z_{fn}(\gamma r) \, e^{j(\xi x-\omega t)}}{Z_{sn}(\xi) + Z_{fn}(\gamma a)} \, d\xi \qquad (4.21)$$

where

$$p_{ref} = Dw_{ref} = \frac{F_r}{(2\pi R)^2} .$$

is a convenient reference pressure.

Before solutions of the characteristic equation can be determined, it will first be necessary to specify the mapping between the complex γ and ξ domains. Due to the dependence on $H_n(\gamma r)$ in the integrand of Equation (4.21), the pressure relation will place greater restrictions upon the allowable mappings than would the integral of the displacement field. The next section will introduce branch points, branch lines, and Riemann surfaces in order to specify γ as a single-valued function of ξ.

4.4 Specification of the Radial Wavenumber

The addition of fluid loading has introduced a transformed radial wavenumber that is a multi-valued function of ξ. If the function γ is

observed along any closed path in the complex ξ-domain that contains either of the points $\xi=\pm k$, it will be found that γ is discontinuous with phase shift π upon returning to the starting point. Any point which causes such behavior is defined as a branch point. If a second circuit about the branch point were made, the function γ would return to its original starting value. Clearly, all points on the complex ξ-plane with phase between 0 and 2π are mapped onto one-half of the complex γ-plane, while those points with phase between 2π and 4π are mapped onto the other half. In order to re-establish a single-valued behavior and continuity, it is necessary to distinguish between these two regions of the complex ξ-domain, each called a Riemann sheet. Their combination is called a Riemann surface, and a one-to-one correspondence exists between points on the Riemann surface and points on the complex γ-plane.

The branch points represent points at which the two Riemann sheets are connected. It can also be shown [e.g. Carrier, Krook, and Pearson (1966)] that branch points always occur in pairs and that for every finite branch point, a branch point also exists at infinity. In order to force γ to be a single-valued on each Riemann sheet, a cut can be made between each pair of branch points and the two sheets joined along this cut. Any path which attempts to cross this discontinuity would be transferred to the other Riemann sheet. Such a barrier path is called a branch line. If a branch line is formed between each finite branch point and a branch point at infinity, the branch lines would be continuous since in the theory of complex variables infinity is considered to be a single point.

If the radial wavenumber is specified in some region of the complex ξ-domain, analytic continuation can be used to specify γ everywhere on the Riemann surface. In considering the integrand of the inverse

Fourier integral representing the acoustic pressure field, two physical constraints are helpful in specifying γ and choosing branch lines. The radiation condition requires energy to decay to zero at infinity. The causality condition requires that energy propagate outward from the source at the origin.

Let us begin by specifying γ at the end points of the integration path such that both conditions are satisfied. Assume fluid damping is present such that

$$k = k_r + jk_i, \qquad \xi = \xi_r + j\xi_i, \qquad \text{and } \gamma = \gamma_r + j\gamma_i \ .$$

For negative time harmonic excitation it can be shown [e.g. Skudryzk (1971) p. 32] that both k_r and k_i are positive. At the integration path end points

$$\gamma \simeq \sqrt{-\xi_r^2 + 2jk_rk_i} \qquad \text{for } \xi = \xi_r = \pm\infty$$

such that $|\gamma| = |\xi_r|$ and $\arg(\gamma)$ equals $+\pi/2$ for the positive square root and $-\pi/2$ for the negative square root. Recalling the inital formulation of the acoustic field solution, Equation (4.5), both the Hankel function of the first and second kind were present. From the large argument approximation of these functions, it is obvious that if the radiation and causality conditions are to apply at the end points, then the function of the first kind must be associated with positive square root while the function of the second kind is associated with the negative square root. The choice of which pair to use is arbitrary. In keeping with convention, the positive square root has been assumed.

From this definition of γ at the end points of the real integration path, the radial wavenumber can be analytically continued throughout the complex ξ-domain. The choice of branch lines will uniquely

define how we wish the analytic continuation to be applied. In theory, any path connecting pairs of branch points is an acceptable branch line. Often physical arguments are used to restrict the choice. For example, a branch line connecting the two finite branch points at $\xi=\pm k$ along the real axis (or any other direct path) does result in a single-valued behavior on each Riemann sheet, even for paths which enclose both branch points (and the entire branch line). However, it can be shown that the integrand does not obey the radiation condition along this branch line and that in the presence of fluid damping the branch line breaks the integration path along the real axis. For either of these reasons, this particular branch line would be unacceptable for our problem.

The proper, or Sommerfeld, branch lines are chosen on physical grounds because along them the integrand obeys both the radiation and causality conditions. For large r, the Hankel function of the first kind must be restricted such that $0 \leq \arg(\gamma) \leq \pi/2$ if both the radiation and causality conditions hold. This is equivalent to stating that the phase of γ^2 must have a value between zero and π, or

$$0 \leq \tan^{-1}\left[\frac{2(k_r k_i - \xi_r \xi_i)}{k_r^2 - k_i^2 - \xi_r^2 + \xi_i^2}\right] \leq \pi \quad .$$

This relationship will be true for all $k_r k_i \geq \xi_r \xi_i$ for both k_r and k_i positive. The boundary of this region is equivalent to the condition of zero $\mathrm{Im}\{\gamma\}$ and is defined by

$$\xi_r \xi_i = k_r k_i \tag{4.22}$$

which is recognized as a rectangular hyperbola in the first and third quadrants, see Figure 4.1(a). We see that on this boundary

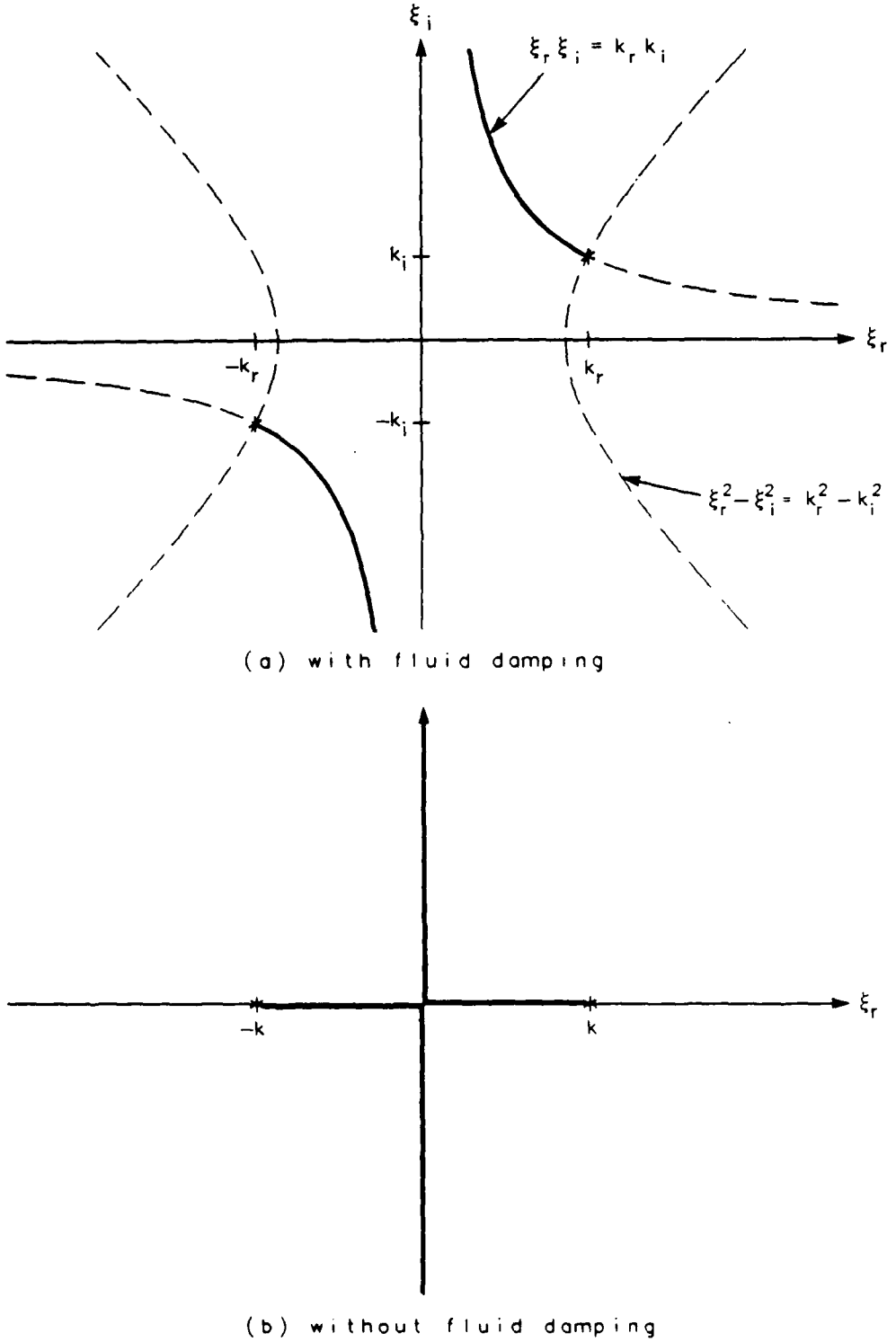

Figure 4.1. Proper, or Sommerfeld, branch lines; (a) with fluid damping, (b) without fluid damping.

$$\gamma = \gamma_r = \sqrt{k_r^2 - k_i^2 - \xi_r^2 + \xi_i^2} \quad .$$

Therefore a second requirement exists that

$$\xi_r^2 - \xi_i^2 \leq k_r^2 - k_i^2 \tag{4.23}$$

which is the region between a pair of equilateral hyperbolas with foci on the ξ_r axis for $k_r > k_i$ (assumed). At a branch point, the inequality becomes an equality, and the branch point is given by the intersection of these two pairs of hyperbolas, or $\xi = k$, as expected.

The addition of fluid damping results in the branch points rotating away from the real axis in a counter-clockwise manner. The singularities of the integrand can also be shown to rotate similarly when fluid damping is included. In the limit as $k_i \to 0$, the branch points return to the real axis, and the branch lines take the form of the classic L-shaped cuts, as shown in Figure 4.1(b). If structural damping is included in the shell through a complex elastic modulus, the singularities of the integrand again will rotate in a counter-clockwise direction from the undamped case. However, the acoustic wavenumber k will remain unchanged such that structural damping will have no effect upon the branch points or branch lines.

If we also consider the inverse Fourier kernel $e^{j\xi x}$ also present in the integrand, it is required that for both the radiation and causality condition to hold both ξ_r and ξ_i must have the same sign as x. Now it is clear that the branch point in the first quadrant is associated with positive axial distance and the branch point in the third quadrant is associated with negative axial distance. This implies that for $x>0$ the contour integral should be closed in the upper half-plane of either Riemann sheet of the complex ξ-domain, while for $x<0$ closure should be

in the lower half-plane. The proper, or Sommerfeld, branch lines would be given by Equation (4.22) in the region defined by Equation (4.23), as shown in Figure 4.1(a). Since the Riemann sheet that consists of points in the complex ξ-domain with phase between zero and 2π maps onto the upper half of the complex γ-plane, this sheet will be called the top Riemann sheet. Likewise, the other Riemann sheet will be called the bottom Riemann sheet. The mapping between the γ and ξ domains is shown in Figure 4.2 for the top Riemann sheet. The phase of γ would be negative on the bottom Riemann sheet. Note that the phase of γ is undefined at the branch points.

4.5 The Normalized Spectral Modal Acoustic Radiation Impedance

The normalized spectral modal acoustic radiation impedance $Z_{an}(\gamma)$ arises in problems governed by the wave equation in cylindrical coordinates. Many authors have studied this function for real or imaginary argument. An excellent example is Junger (1953). These studies are valuable when performing numerical integration along the real axial wavenumber axis or in some far field approximations. For problems that involve deformation of the integration path into the complex ξ-domain where γ is also complex, such as steepest descent approximations or the formal Cauchy integral solution, the general behavior of $Z_{an}(\gamma)$ is of interest. The behavior of the acoustic radiation impedance also provides rigorous mathematical grounds for choosing the Sommerfeld branch lines.

Branch lines are used to specify γ as a single-valued function of ξ. From a purely mathematical perspective, any branch line between two branch points is acceptable. One may choose whatever path is convenient for the particular problem at hand. Although physical reasoning was employed in the last section to select the Sommerfeld branch lines, this

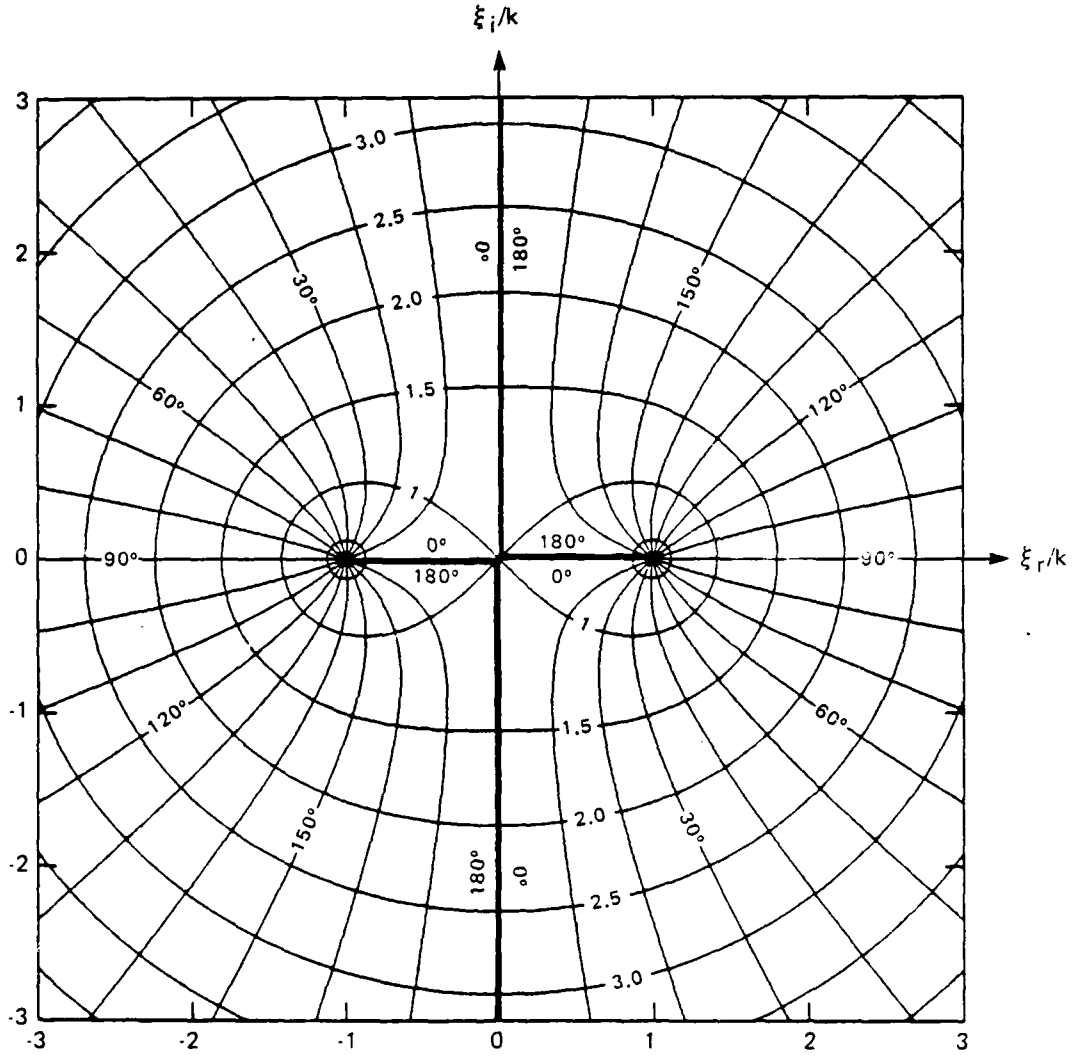

Figure 4.2. Mapping between the complex γ/k domain and the top Riemann sheet of the complex ξ/k domain. Contours of constant phase and magnitude of γ/k are shown for real acoustic wavenumber. Bold lines indicate the Sommerfeld branch lines.

was not a mathematical requirement. However, the choice of branch line will obviously effect the ease of mathematical solution or numerical simulation. Because the Sommerfeld branch lines coincide with the boundary between regions in which $Z_{an}(\gamma)$ exhibits "good" and "bad" behavior, they are superior to other possible branch lines. This dividing line is the real γ-axis. In the upper half-plane, $Z_{an}(\gamma)$ behaves nicely. It possesses symmetry and a monotonic behavior. The bad region, the lower half-plane, contains all of the poles and zeroes of the function. By using the Sommerfeld branch lines, we can confine our analysis to the region in which $Z_{an}(\gamma)$ is easiest to evaluate.

With the branch line associated with the logarithmic singularity of the Hankel function taken along the negative real γ-axis, $Z_{an}(\gamma)$ is conjugate symmetric in the upper half-plane about the imaginary γ-axis. For a general point γ_o in the first quadrant

$$Z_{an}(\gamma_o^* e^{j\pi}) = Z_{an}^*(\gamma_o) \tag{4.24a}$$

where the asterik denotes the complex conjugate. The proof is

$$Z_{an}(\gamma_o) = \frac{H_n^{(1)}(\gamma_o a)}{\gamma_o H_n^{(1)'}(\gamma_o a)} = \frac{H_n^{(1)}(\gamma_o e^{j\pi} e^{-j\pi})}{\gamma_o H_n^{(1)'}(\gamma_o e^{j\pi} e^{-j\pi})}$$

$$= -\frac{H_n^{(2)}(\gamma_o e^{-j\pi})}{\gamma_o H_n^{(2)'}(\gamma_o e^{-j\pi})} = -\frac{H_n^{(1)*}(\gamma_o^* e^{j\pi})}{\gamma_o H_n^{(1)'*}(\gamma_o^* e^{j\pi})} \quad .$$

By taking the complex conjugate of this relation, Equation (4.24a) results. Care must be taken to assure that the argument remains on the principal value branch $-\pi \leq \arg(\gamma) \leq \pi$. Analytic continuation relations from Abramowitz and Stegun (1972) were employed in this regard. This symmetry property will greatly ease the search for eigenvalues of the

characteristic equation. A lack of symmetry in the lower half-plane can be similarly demonstrated. Similar reasoning can be used to show that for $0 \leq \arg(\gamma) \leq \pi$ the spectral modal specific acoustic impedance obeys the symmetry property

$$Z_{fn}(\gamma_o^* e^{j\pi} r) = - Z_{fn}^*(\gamma_o r) \quad . \tag{4.24b}$$

Abramowitz and Stegun also discuss the locations of the complex zeroes of both the Hankel function of the first kind and its derivative. Excluding the point at the origin, both $H_n(\gamma a)$ and $H_n'(\gamma a)$ are analytic everywhere in the complex ξ-domain. Therefore, zeroes of the acoustic radiation impedance coincide with the zeroes of the Hankel function. Excluding points at infinity, these are confined to the lower half-plane. Likewise, poles of $Z_{an}(\gamma)$ will coincide with the zeroes of the derivative of the Hankel function, which again are confined to the lower half-plane. In the limit as γ approaches the origin, $Z_{an}(\gamma)$ remains nonzero and finite for all $n>0$. Only for the axisymmetric mode does a logarithmic singularity exist at the origin. Since $Z_{an}(\gamma)$ is analytic everywhere in the upper half-plane, by the maximum modulus theorem, $Z_{an}(\gamma)$ must also be monotonic in this region with its maximum modulus occurring on the boundary. It can easily be shown that for the axisymmetric mode the maximum modulus of $Z_{an}(\gamma)$ in the upper half-plane occurs at the origin. For $n>0$, the maximum modulus in the upper half-plane occurs between n-1 and n on both the positive and negative real γ-axis.

Constant phase and modulus contour plots in the complex γ-plane of the acoustic radiation impedance $Z_{an}(\gamma)$ are shown in Figures 4.3-4.5 for the n=0, 1, and 2 modes. The symmetry, monotonic, zero, and pole behavior discussed is clearly demonstrated. An infinity of alternating poles and zeroes exists in the lower half-plane extending along the neg-

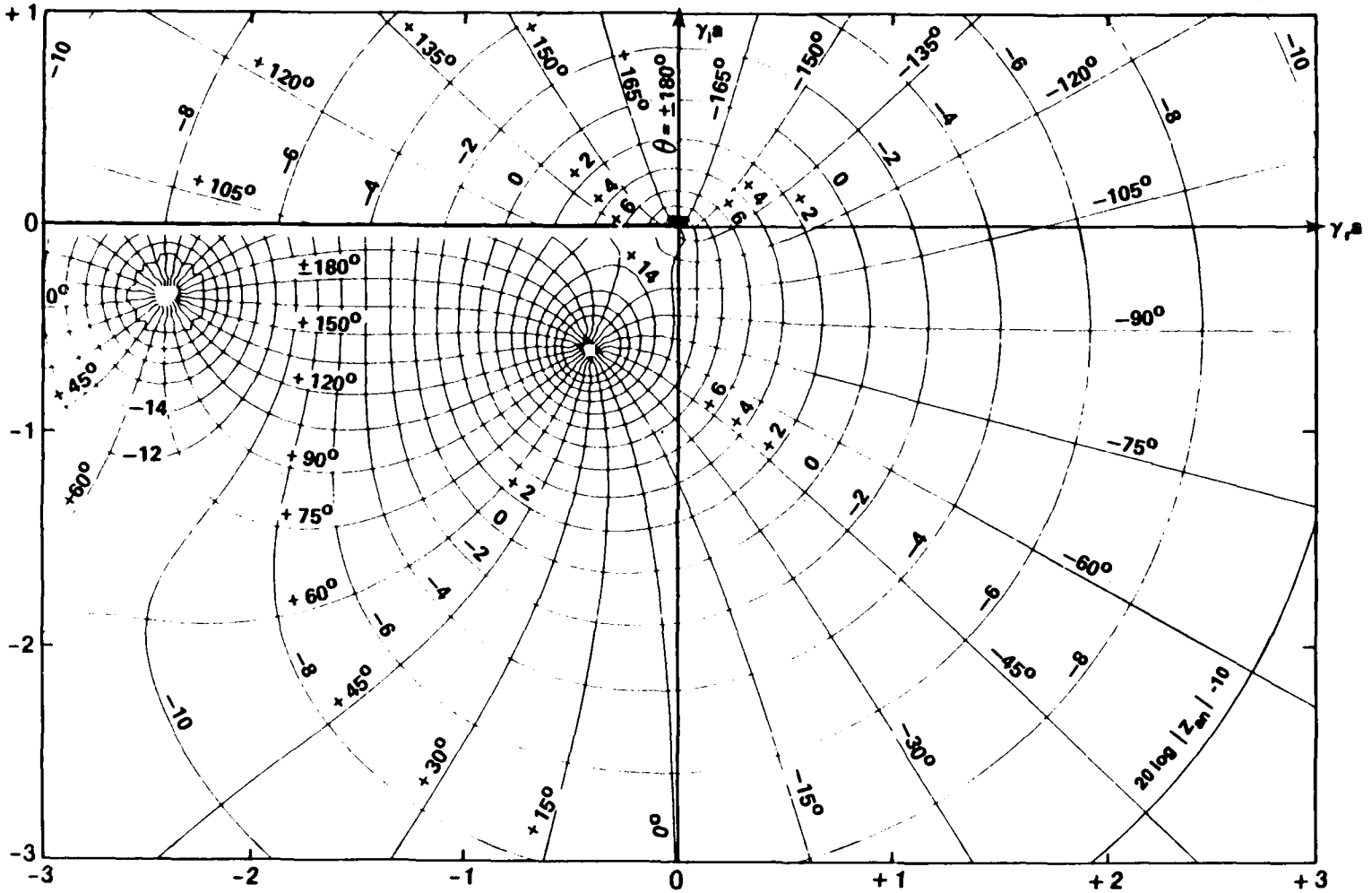

Figure 4.3. Behavior of the normalized spectral modal acoustic radiation impedance $Z_{an}(\gamma)$ in the complex γ-plane for the n=0 mode. Curves represent contour lines of constant phase and $20 \log|Z_{an}|$.

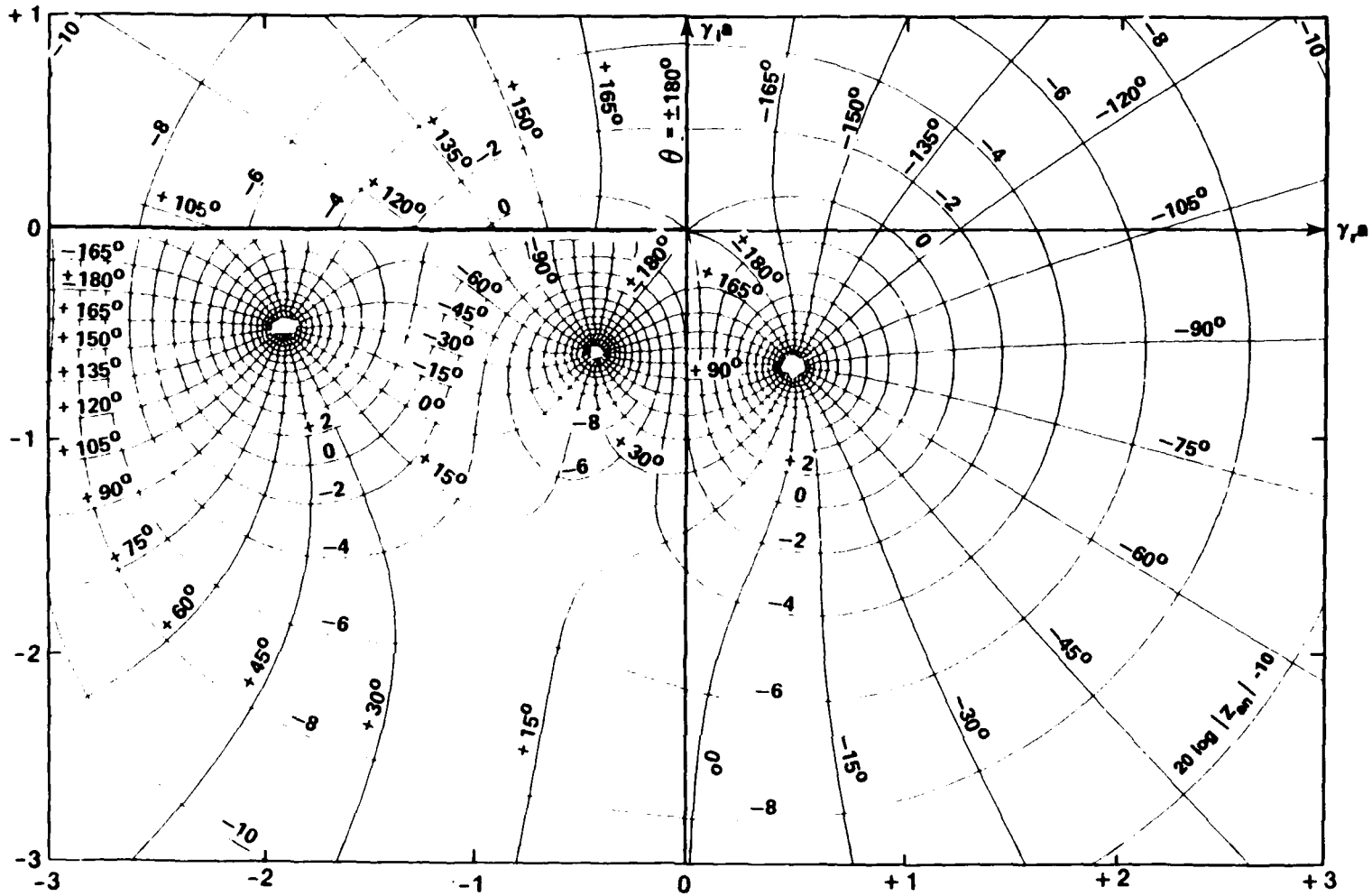

Figure 4.4. Behavior of the normalized spectral modal acoustic radiation impedance $Z_{an}(\gamma)$ in the complex γ-plane for the n=1 mode. Curves represent contour lines of constant phase and 20 $\log|Z_{an}|$.

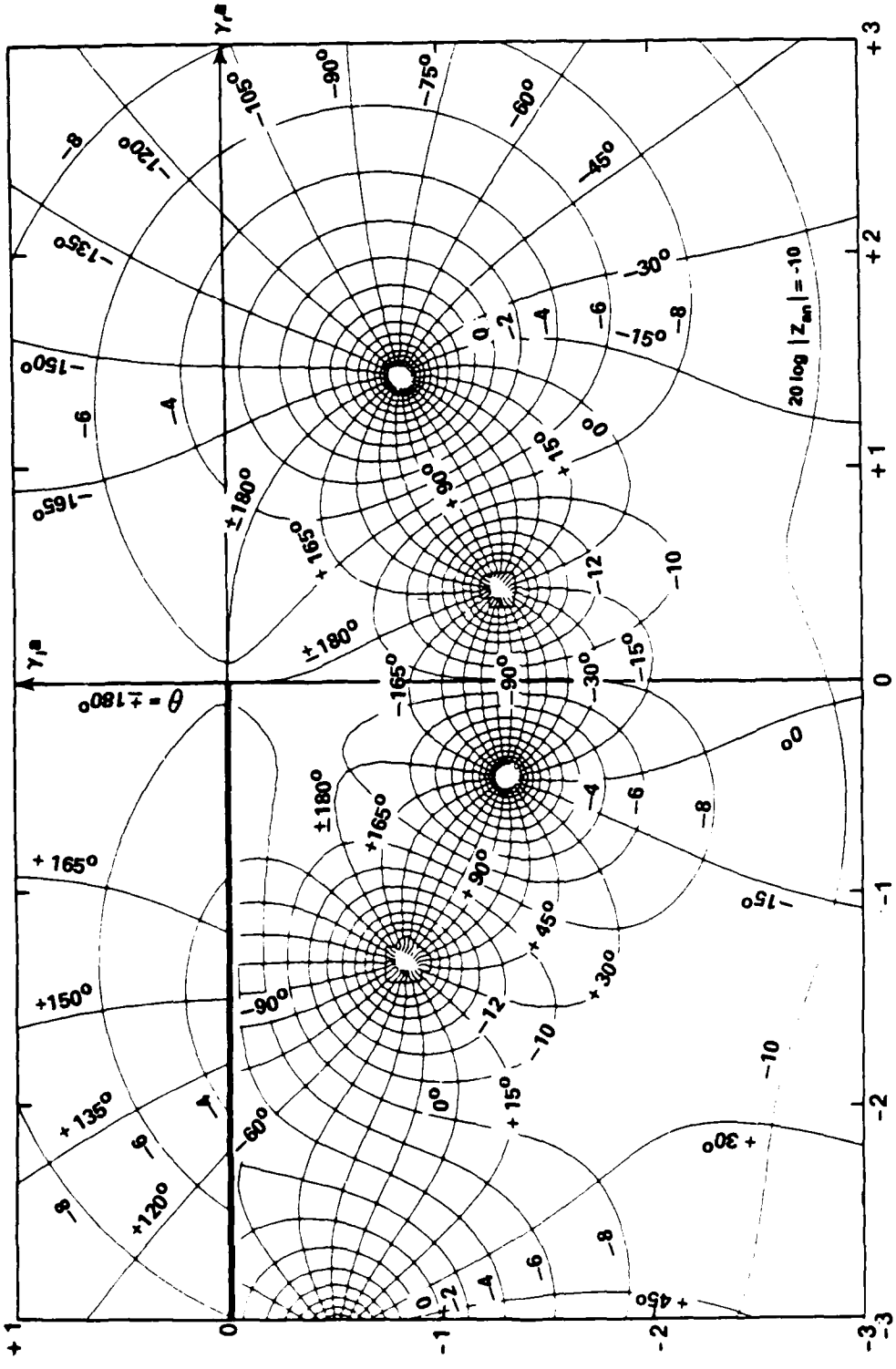

Figure 4.5. Behavior of the normalized spectral modal acoustic radiation impedance $Z_{an}(\gamma)$ in the complex γ-plane for the n=2 mode. Curves represent contour lines of constant phase and 20 $\log|Z_{an}|$.

ative real axis. The contrast is striking between the smooth, bounded behavior of $Z_{an}(\gamma)$ in the upper half-plane and its rapidly changing, singular behavior in the lower half-plane. These figures strongly indicate why contours of integration should be avoided that include any portion of the lower half-plane. The computational routines used to calculate Hankel functions of complex argument were developed at the Naval Research Laboratory and are described by Mason (1983).

By using the various asymptotic expressions for the Hankel functions found in Ambramowitz and Stegun, asymptotic approximations of the specific acoustic impedance $Z_{fn}(\gamma r)$ and the acoustic radiation impedance $Z_{an}(\gamma a)$ can be developed. These will prove useful throughout this chapter and the next. At large argument

$$\lim_{\gamma\to\infty} Z_{fn}(\gamma r) = j\,\frac{\rho c k}{\gamma}\sqrt{\frac{a}{r}}\left\{\left[\frac{4n^2-1}{8\gamma r}-\frac{4n^2+3}{8\gamma a}\right]-j\right\}e^{j(r-a)\gamma} \qquad (4.25a)$$

$$\lim_{\gamma\to\infty} Z_{an}(\gamma) = -\frac{1}{\gamma}\left\{\frac{1}{2\gamma a}+j\right\} . \qquad (4.25b)$$

The axisymmetric mode has the small argument approximations

$$\lim_{\gamma\to 0} Z_{f0}(\gamma r) = j\rho c k a\,\{\ln \gamma r - j\,\pi/2\} \qquad (4.25c)$$

$$\lim_{\gamma\to 0} Z_{a0}(\gamma) = a\,\{\ln \gamma a - j\,\pi/2\} \qquad (4.25d)$$

and

$$\lim_{\gamma\to 0} Z_{fn}(\gamma r) = -j\rho c k a\left\{\frac{1}{n}\left(\frac{a}{r}\right)^n + j\,\frac{\pi}{(n!)^2}\left[\left(\frac{a}{r}\right)^n+\left(\frac{r}{a}\right)^n\right]\left(\frac{\gamma a}{2}\right)^{2n}\right\} \qquad (4.25e)$$

$$\lim_{\gamma\to 0} Z_{an}(\gamma) = -a\left\{\frac{1}{n}+j\,\frac{2\pi}{(n!)^2}\left(\frac{\gamma a}{2}\right)^{2n}\right\} \qquad (4.25f)$$

for higher mode orders.

4.6 Existence Properties of the Singularities

The singularities of the integrand of Equation (4.21) can be found by solving for the zeroes of the characteristic equation in the complex ξ-domain. Since the choice of negative time harmonic excitation and the sense of a positive axial direction are arbitrary, physical reasoning indicates that the singularities must exhibit both symmetry and duality properties. Let us begin by investigating the existence properties of real and imaginary singularities.

In the complex ξ-domain, characteristic Equation (4.18) represents the two constraint equations

$$\mathrm{Im}\{Z_{sn}(\xi)\} + \mathrm{Im}\{Z_{fn}(\gamma a)\} = 0 \tag{4.26a}$$

and

$$\mathrm{Re}\{Z_{sn}(\xi)\} + \mathrm{Re}\{Z_{fn}(\gamma a)\} = 0 \tag{4.26b}$$

Since the shell impedance is a function of ξ^2, for both real and imaginary ξ

$$\mathrm{Re}\{Z_{sn}(\xi)\} = 0.$$

For imaginary ξ, $\arg(\gamma)$ will have a value of 0, $-\pi$, or $-\pi$ depending upon which side of the branch line and which Riemann sheet is of interest. If we consider the analytic continuation relating the Hankel functions of the first and second kinds, constraint Equation (4.26b) at imaginary ξ requires that

$$\mathrm{Im}\left\{\frac{H_n(\gamma a)}{H_n'(\gamma a)}\right\} = 0$$

or

$$\text{Wronskian}\{J_n(\gamma a),\ Y_n(\gamma a)\} = 2/(\pi\gamma a) = 0 \tag{4.27}$$

be true. Equation (4.27) is valid only at infinite frequency or axial wavenumber. The former case is not of practical concern and the later case is not a solution of constraint Equation (4.26a). Therefore, purely imaginary singularities cannot exist on either Riemann sheet.

Along the region $\xi^2<k^2$ of the real axis, $\arg(\gamma)$ again has a value of either 0, $+\pi$, or $-\pi$. The problem is essentially that just discussed except that Equation (4.27) is now valid only at infinite frequency, which again is not of practical concern. Therefore, real singularities with magnitude less than the acoustic wavenumber cannot exist on either Riemann sheet.

The existence of any other real singularities is also important since they will comprise the residue contribution at most field points. On the top Riemann sheet, $\arg(\gamma) = \pi/2$ for the region $\xi^2>k^2$ of the real axis. Along this region, the specific acoustic impedance becomes

$$z_{fn}(\bar{\gamma}e^{j\pi/2}r) = j\,\frac{\rho c k}{\bar{\gamma}}\,\frac{K_n(\bar{\gamma}r)}{K_n'(\bar{\gamma}a)} \tag{4.28}$$

where $\bar{\gamma}$ is taken as a magnitude and the phase term has been explicitly shown. The function $K_n(\bar{\gamma}a)$ is the modified Bessel function of the second kind of integer order n and with real argument $\bar{\gamma}a$. For positive real argument, the function K_n and its derivative are real. Therefore, constraint Equation (4.26b) is identically satisfied, and real singularities may exist subject to constraint Equation (4.26a). In the next section these real singularities will be located, and their behavior will be discussed. Note that the real singularities must always appear in positive- and negative-valued pairs.

On the bottom Riemann sheet, along the region $\xi^2>k^2$ of the real axis, $\arg(\gamma)$ has a value of $-\pi/2$ and the specific acoustic impedance is

$$z_{fn}(\bar{\gamma}e^{-j\pi/2}r) = -j\,\frac{\rho ck}{\bar{\gamma}}\,\frac{K_n(-\bar{\gamma}r)}{K_n'(-\bar{\gamma}a)} \tag{4.29}$$

where the function K_n and its derivative are no longer real. For negative real argument, K_n has an imaginary component proportional to the modified Bessel function of the first kind I_n. Introducing Equation (4.29) into constraint Equation (4.26b) can be shown to require that

$$(\bar{\gamma}a)^{-2}\left\{\left[I_n'(\bar{\gamma}a)\right]^2 + \left[K_n'(\bar{\gamma}a)\right]^2\right\}^{-1} = 0 \tag{4.30}$$

be true. Equation (4.30) is valid at infinite ξ, which is not a solution of constraint Equation (4.26a), or when $\bar{\gamma}$ is zero. Therefore, real singularities cannot exist anywhere on the bottom Riemann sheet except at the branch point.

It can also be demonstrated on physical grounds that this result is correct. With negative time-harmonic excitation, a real singularity on the bottom Riemann sheet would represent energy propagating inward from infinity. This is physically not possible. This behavior also points out the duality between Riemann sheets based upon the time harmonic excitation chosen. At large radial distance the Hankel function of the second kind is porportional to $\exp(-j\gamma r)$. Therefore, for positive time-harmonic excitation, a real singularity on the bottom Riemann sheet would correctly represent outward propagating energy. The real singularities which previously existed on the top Riemann sheet would now be found on the bottom Riemann sheet.

The location of the complex zeros of Equation (4.21) is a formidable task which can be facilitated by determining the symmetry properties of both the complex zeros and their residues. Instead of locating

the complex zeros of the characteristic equation as given, let us solve the related problem of finding the complex points at which the magnitude of the impedance terms in Equation (4.21) are equal. Since the specific acoustic impedance is non-symmetric on the lower Riemann sheet, let us restrict the discussion to the top Riemann sheet where $0 \leq \arg(\gamma) \leq \pi$.

For a general point ξ_1 located in the first quadrant, points symmetric about the real and imaginary axes can be defined such that

$$\xi_2 = \xi_1^* e^{j\pi}, \qquad \xi_3 = \xi_1 e^{j\pi}, \qquad \text{and } \xi_4 = \xi_1^* \ .$$

Noting that the shell impedance function $Z_{sn}(\xi)$ contains terms of the form ξ^{2m}, it is easy to show that

$$Z_{sn}(\xi_2) = Z_{sn}(\xi_4) = - Z_{sn}^*(\xi_1), \qquad \text{and} \quad Z_{sn}(\xi_3) = Z_{sn}(\xi_1) \ .$$

Observation of Figure 4.2 indicates that the radial wavenumber exhibits the symmetry property

$$\gamma(\xi_2) = \gamma(\xi_4) = \gamma^*(\xi_1) e^{j\pi}, \qquad \text{and} \quad \gamma(\xi_3) = \gamma(\xi_1) \ .$$

The symmetry property $Z_{fn}(\gamma^* e^{j\pi} r) = -Z_{fn}^*(\gamma r)$ of the specific acoustic impedance has been discussed previously. Since the magnitude of a complex quantity is equal to the magnitude of its conjugate, the complex zeroes of the characteristic equation must be symmetric about both the real and imaginary axes. Therefore, it is sufficient to restrict the search for complex singularities to any one quadrant.

4.7 Location and Behavior of the Real Singularities

Restricting the discussion to the region $\xi^2 > k^2$ of the real axis of the top Riemann sheet where $\arg(\gamma) = \pi/2$, the location of the real singularities can be found by analyzing the characteristic equation.

This equation can be written in terms of the normalized shell stiffness components and the normalized acoustic radiation impedance as

$$D_{sn}(\xi) + \Delta N_{sn}(\xi) Z_{an}(\bar{\gamma} e^{j\pi/2}) = 0 \qquad (4.31)$$

where the acoustic radiation impedance has the form of Equation (4.28) and is real, negative, and monotonically decreases to zero value at large argument. The variable $\bar{\gamma}$ is taken as a magnitude with the phase term explicitly shown. As was done for the in vacuo case, the location and behavior of the real frequency spectra can be analyzed by using asymptotic approximations. The large and small argument approximations of the acoustic radiation impedance are given by Equations (4.25). The shell stiffness component $D_{sn}(\xi)$ is a fourth order polynomial in ξ^2. The component $N_{sn}(\xi)$ is a second order polynomial in ξ^2 and is positive in the region of interest. Most of the algebraic details will be omitted from the discussion.

The axisymmetric (n=0) mode has a zero cutoff frequency and non-dispersive behavior at small axial wavenumber where the small argument approximation of the fluid impedance is valid at all frequencies. The frequency spectra is given by

$$\Omega^2 \simeq (c\ \xi/c_p)^2 \qquad (4.32)$$

which is actually valid into the transition region between small and large axial wavenumbers. Thicker shells exhibit nondispersive behavior up to higher wavenumbers. Figure 4.6 shows the calculated frequency spectra for the axisymmetric mode of a steel cylindrical shell in water for several values of normalized shell thickness. None of the asymptotic approximations were used in calculating Figure 4.6 or any other frequency spectra. Numerical root-finding algorithms searched the entire

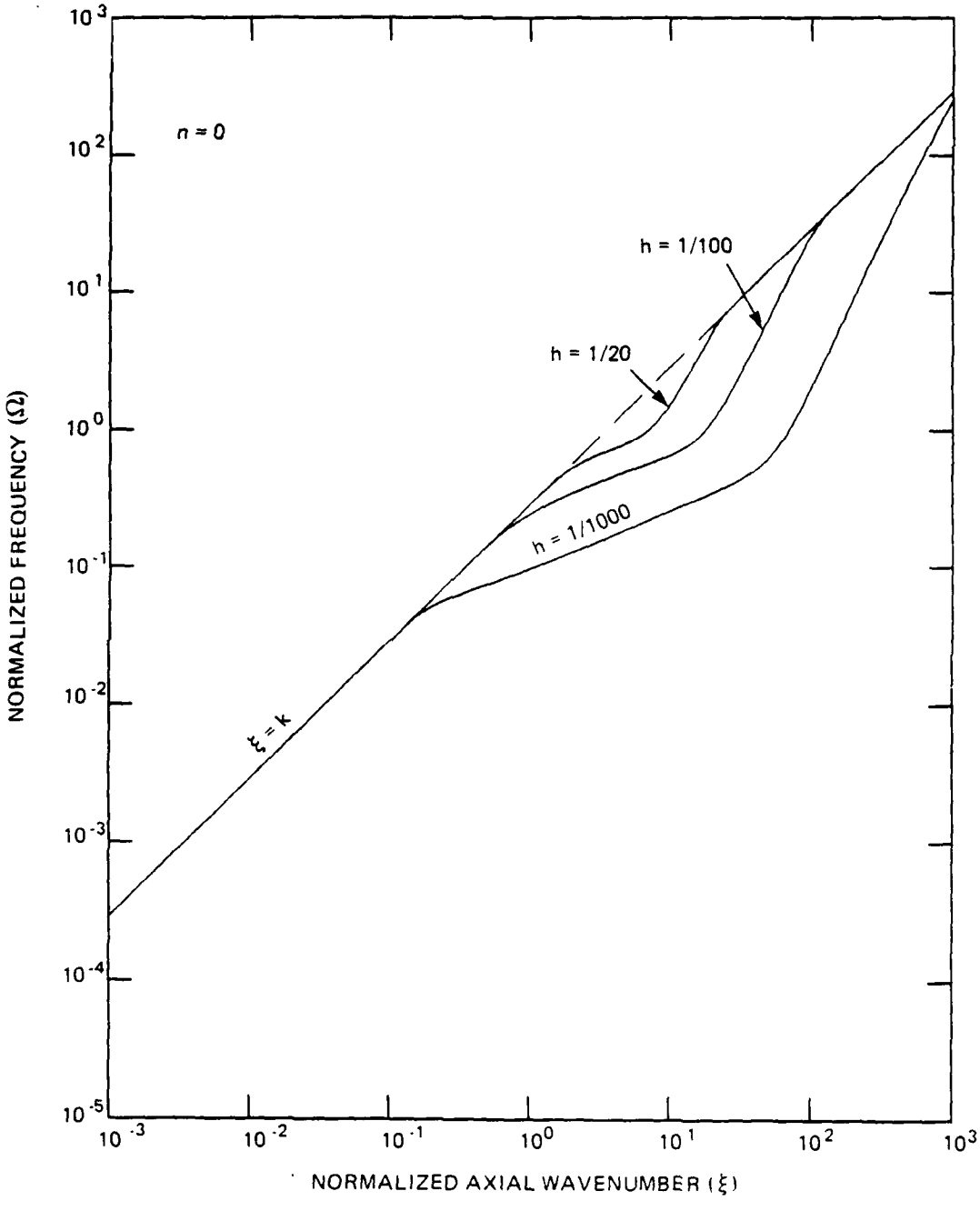

Figure 4.6. Effect of thickness variation upon the real, positive frequency spectra for the n=0 mode of a steel shell in water.

frequency spectra of interest. The approximations were used only to verify and interpret results.

At large axial wavenumber, either of the large or small argument asymptotic approximations or the general expression given by Equation (4.28) may describe the specific acoustic impedance depending upon the relationship between ξ and k. However, it is possible to show that at all mode orders only when ξ=k are real singularities possible. For lower frequencies, the shell impedance is much greater than the specific acoustic impedance, and roots are not possible. It can be shown that for the axisymmetric mode at large axial wavenumbers where

$$\xi^2 > (c/c_p)^2 \beta^{-1} \quad , \tag{4.33}$$

the frequency spectrum is again nondispersive and described by Equation (4.32). The frequency spectrum is continuous up to infinite frequency and wavenumber. The acoustic radiation impedance is approximated by Equation (4.25d) at both small and large axial wavenumber.

In the transition region, the acoustic radiation impedance becomes smaller until it is proportional to γ^{-1}. For wavenumbers in the upper portion of the transition region, $D_{so}(\xi)$ dominates $N_{so}(\xi)$, and the real roots are approximately those of the flexural branch of the shell in vacuo. In the lower portion of the transition region, the behavior is more complicated with the shell stifnnes component $N_{so}(\xi)$ becoming more of a factor. The effect is to cause the real branch of the fluid-loaded shell to occur below that of the shell in vacuo. This is true at all real wavenumbers, not only for the axisymmetric mode, but for all mode orders. By comparing Figure 4.6 with the in vacuo data presented in Figure 3.14, it is seen that the effect of fluid loading on the n=0 mode is to translate the flexural branch downward and to confine it to

the region $\xi^2 > k^2$. As in the in vacuo case, the real branch remains continuous from a zero cutoff frequency up to infinite wavenumber. As expected, neither the longitudinal nor torsional branches have a real counterpart in the fluid-loaded case.

As with the shell in vacuo, the first beam mode (n=1) of the fluid-loaded case has a zero cutoff frequency. However, unlike the axisymmetric mode, the behavior at small axial wavenumber is dispersive with a frequency spectra given by

$$\Omega = \frac{(1-\mu^2)\rho_s h}{2\rho_s h + \rho a}\ \xi^2 \ . \tag{4.34}$$

This is a good approximation of the frequency spectra up to axial wavenumbers at which the small argument approximation of the specific acoustic impedance is no longer valid. This occurs at approximately $\gamma a = 0.3$. Using this relation to solve for ξ, it is found that the upper limit of the dispersive behavior defined by Equation (4.34) is relatively insensitive to variation in shell thickness or material and fluid parameters. This upper limit occurs at approximately $\xi = \pm 0.3$.

At large axial wavenumber, the first mode order is nondispersive with a frequency spectra described by Equation (4.32). In this respect, it is similar to the axisymmetric mode at large wavenumber. However, it can be shown that a frequency exists above which real wavenumbers cannot exist. Extending the terminology adopted previously, let us call this the upper cutoff frequency, and let us call its associated axial wavenumber the upper cutoff wavenumber. If we denote the upper cutoff frequency of the n^{th} mode order as Ω_n^u, then it can be shown that

$$\Omega_n^u = \beta^{-1/2} \sqrt{1 + \frac{\rho a}{n\rho_s h}}\ (c/c_p)^2 \ . \tag{4.35}$$

Above the upper cutoff frequency, the frequency spectra enters the complex ξ-plane. All of the higher order modes will have an upper cutoff frequency. The transition region behaves in a manner similar to that of the axisymmetric mode.

Figure 4.7 shows the frequency spectrum of the n=1 mode of the fluid-loaded real branch for various values of normalized shell thickness. By comparison with Figure 3.15 for the shell in vacuo, fluid-loading has confined the first beam mode to the region $\xi^2>k^2$ and moved it downward with respect to the flexural branch in vacuo. This will be a characteristic of the frequency spectra at all mode orders.

Figures 4.8-4.10 show the frequency spectra for the real branch of the n=2, 3, and 10 modes of a water-loaded shell at various values of normalized shell thickness. As in the in vacuo case, the lower cutoff frequencies are nonzero for all mode orders greater than one. Denoting the fluid-loaded, lower cutoff frequencies of mode order n as Ω_n^c, they can be approximated by

$$\Omega_n^c = \sqrt{\beta}\, n(n^2-1) \sqrt{\left[n^2 + \frac{\rho a}{\rho_s h}\, n + 1 - 2(2+\mu)\beta\left(\frac{c_p}{c}\right)^2 (n^2-1)^2\right]^{-1}} \quad . \quad (4.36)$$

The lower cutoff frequencies increase with increasing mode order number, and as would be expected, the fluid-loaded lower cutoff frequencies are smaller than their flexural branch counterparts for a shell in vacuo. However, unlike the in vacuo case, the axial wavenumber associated with the lower cutoff frequency is no longer zero, but would be given by

$$\xi = (c_p/c)\Omega_n^c \quad . \quad (4.37)$$

The behavior of the frequency spectra above the lower cutoff frequency and wavenumber is relatively independent of axial wavenumber. By com-

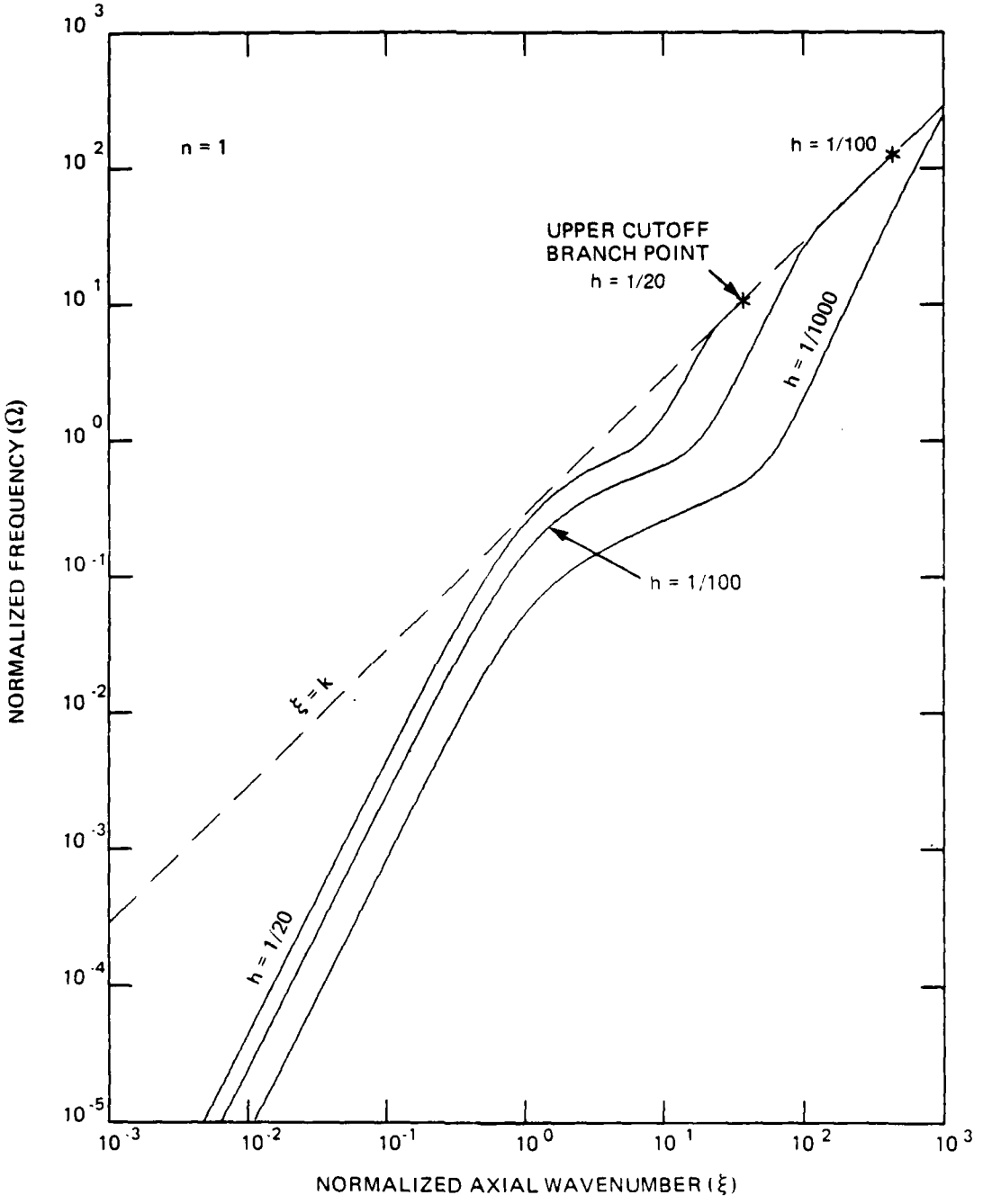

Figure 4.7. Effect of thickness variation upon the real, positive frequency spectra for the n=1 mode of a steel shell in water.

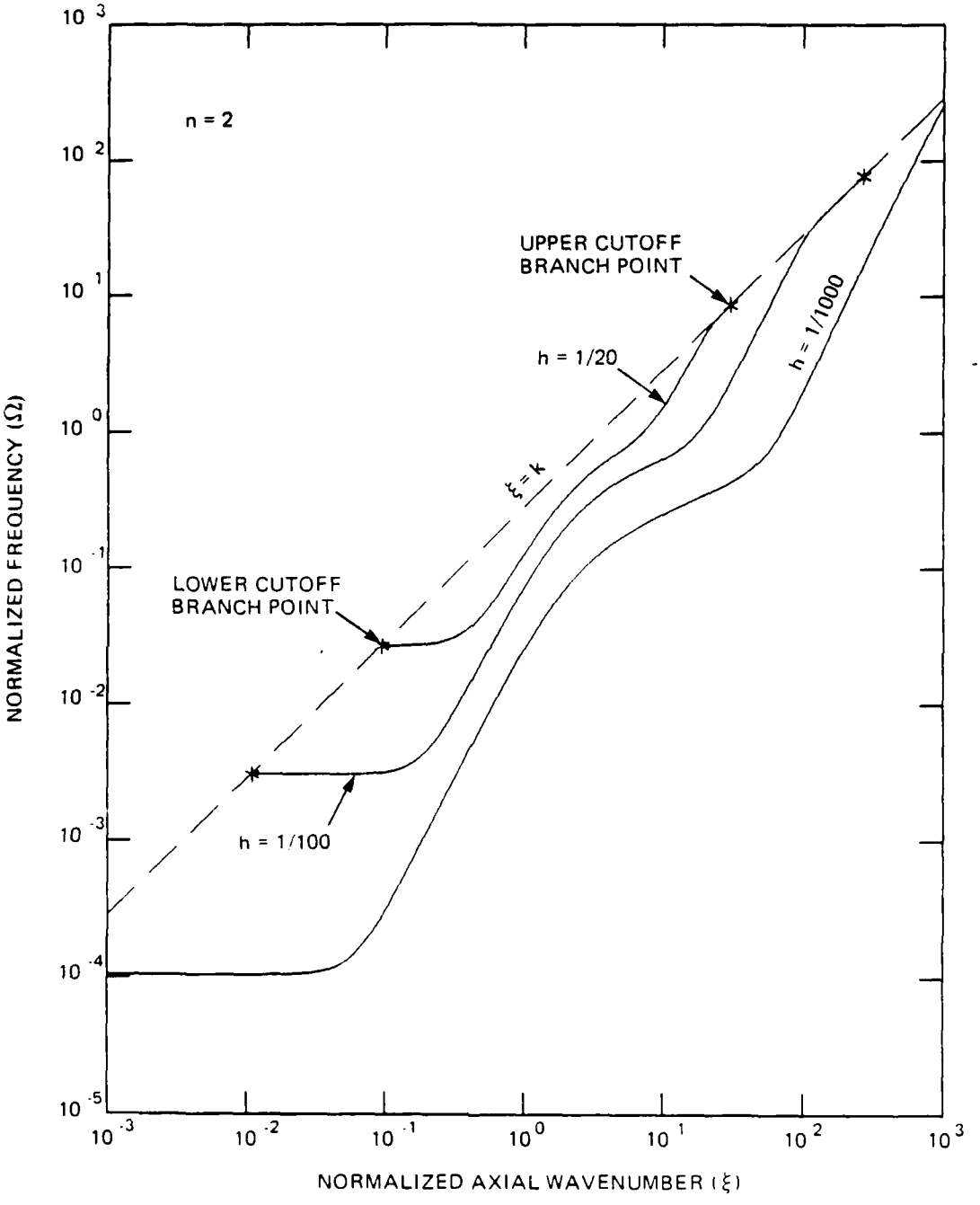

Figure 4.8. Effect of thickness variation upon the real, positive frequency spectra for the n=2 mode of a steel shell in water.

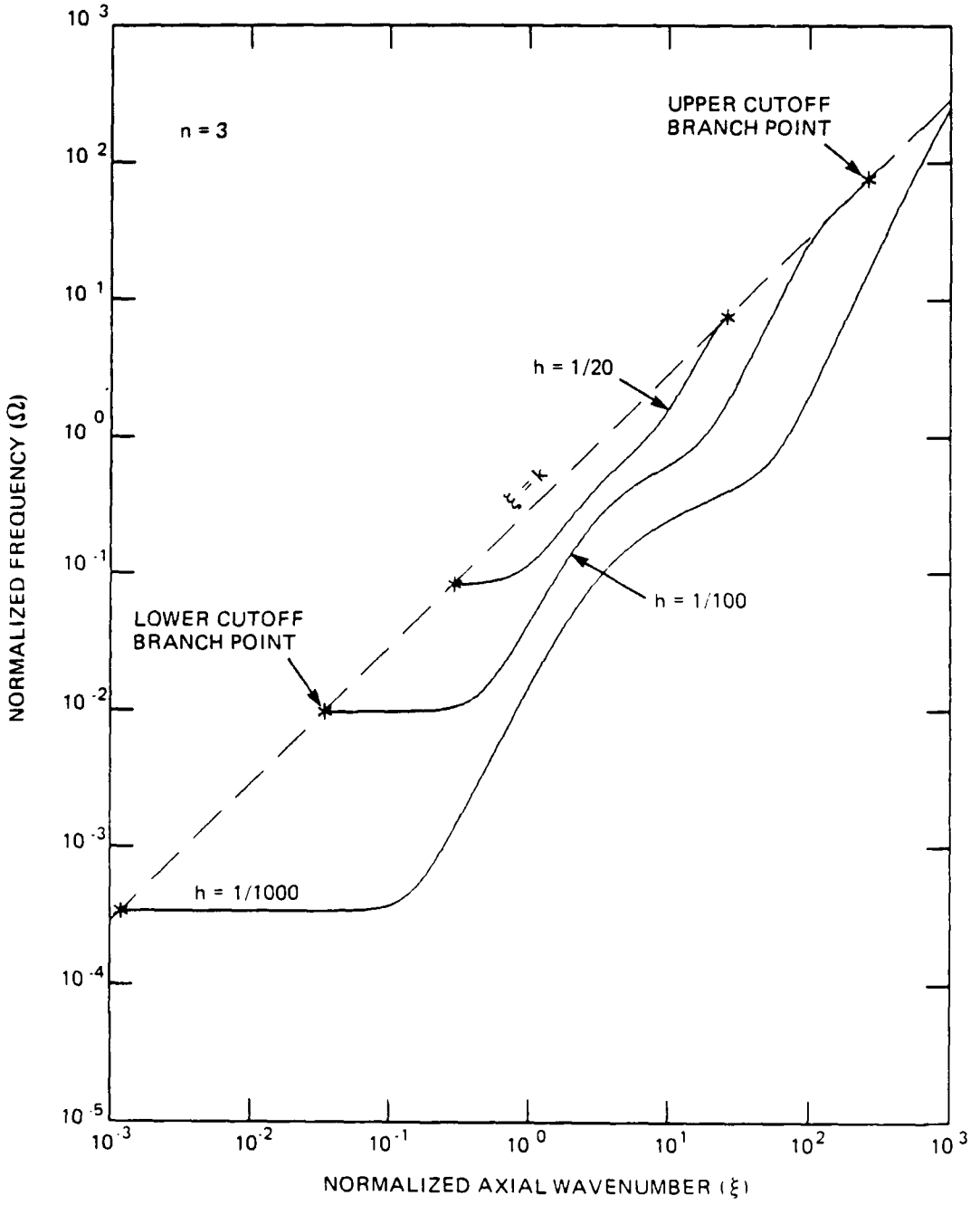

Figure 4.9. Effect of thickness variation upon the real, positive frequency spectra for the n=3 mode of a steel shell in water.

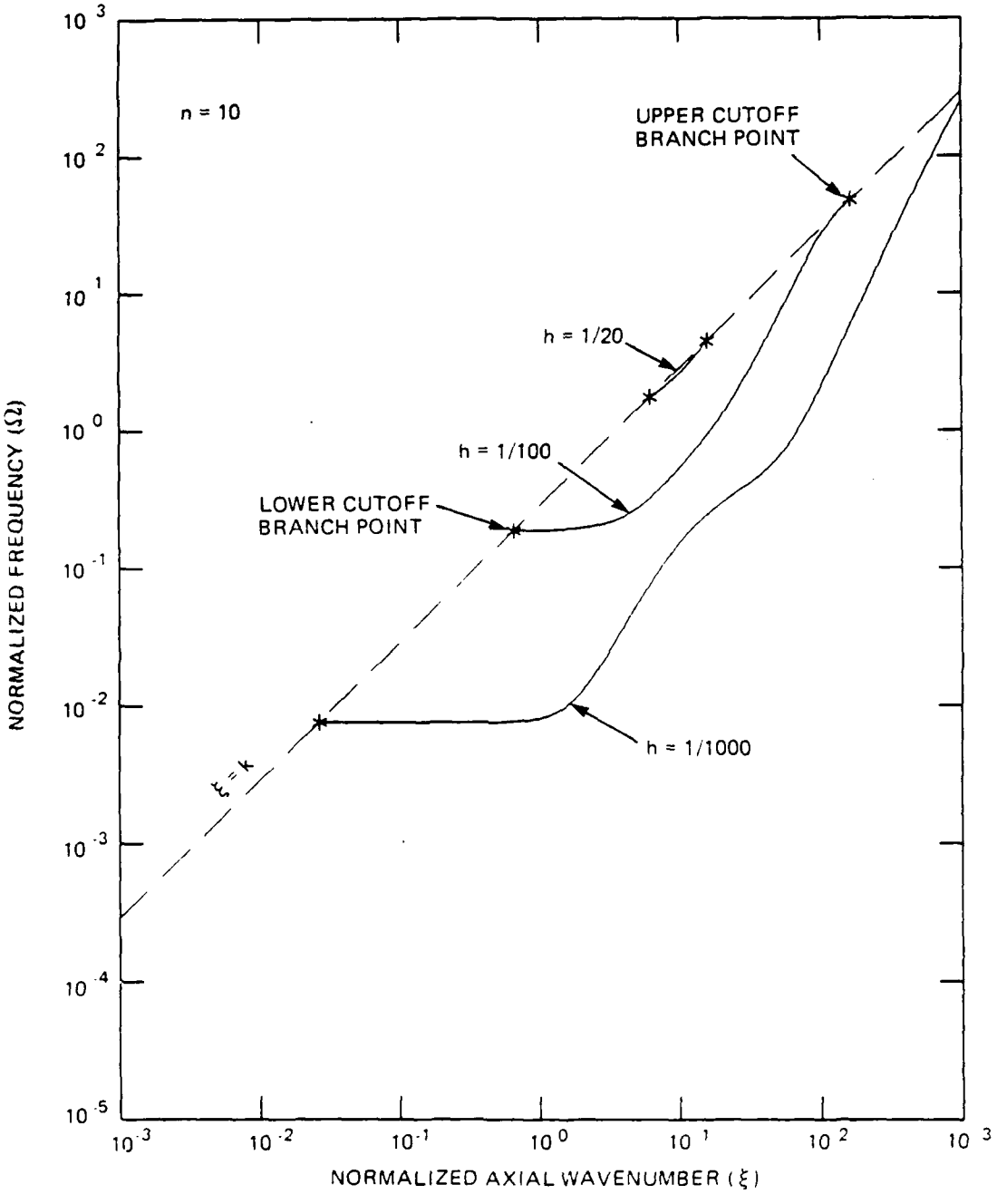

Figure 4.10. Effect of thickness variation upon the real, positive frequency spectra for the n=10 mode of a steel shell in water.

parison with Figures 3.16-3.18, it can be seen that this behavior is consistent with that of the flexural branch of a shell in vacuo. The large wavenumber behavior of the higher order modes is similar to the n=1 mode, except that the upper cutoff frequency is smaller for increasing mode order.

Figure 4.11 shows the frequency spectra for the first eleven mode orders of a steel shell in water. The normalized shell thickness is 0.01. A comparison with the frequency spectra of the flexural branch of a shell in vacuo, Figure 3.7, highlights the behavior discussed. Also shown is the real frequency spectra of a fluid-loaded classical plate calculated as

$$\sqrt{\xi^2-k^2}\ (\beta\xi^4-1) = \Delta\ .$$

As an example, see Junger and Feit (1972, pp. 160-62). Figure 4.12 shows the dispersion curves for this same situation. If a comparison is made with the in vacuo dispersion curves, Figure 3.10, the effect of fluid loading is to decrease the normalized phase velocity and to limit the real phase velocity to finite values at low wavenumber. The maximum real phase velocity would be the acoustic velocity c. The normalized group velocity is plotted against axial wavenumber for the water-loaded shell in Figure 4.13. Similar data is presented in Figure 3.13 for the flexural branch of a shell in vacuo. Similarly fluid loading generally decreases the normalized group velocity from its in vacuo values. Since the group velocity represents the velocity at which energy is transported along the shell, fluid loading is seen to reduce the energy flow and in that sense acts as an added impedance.

If only the real singularities are considered, the cutoff frequency behavior can be used to limit the infinite Fourier series in the

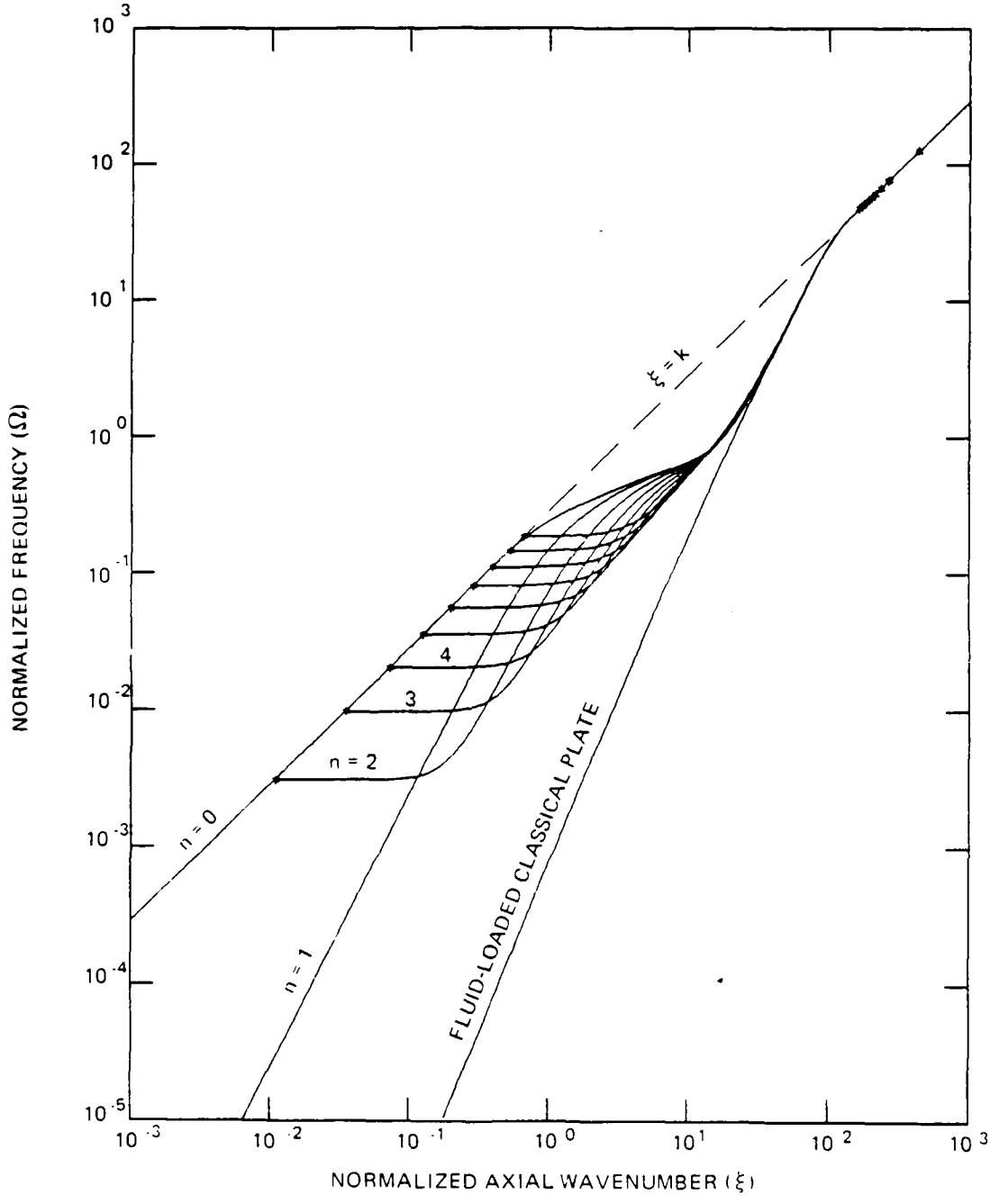

Figure 4.11. Real, positive frequency spectra at various mode order numbers for a steel shell in water with a normalized thickness of 0.01.

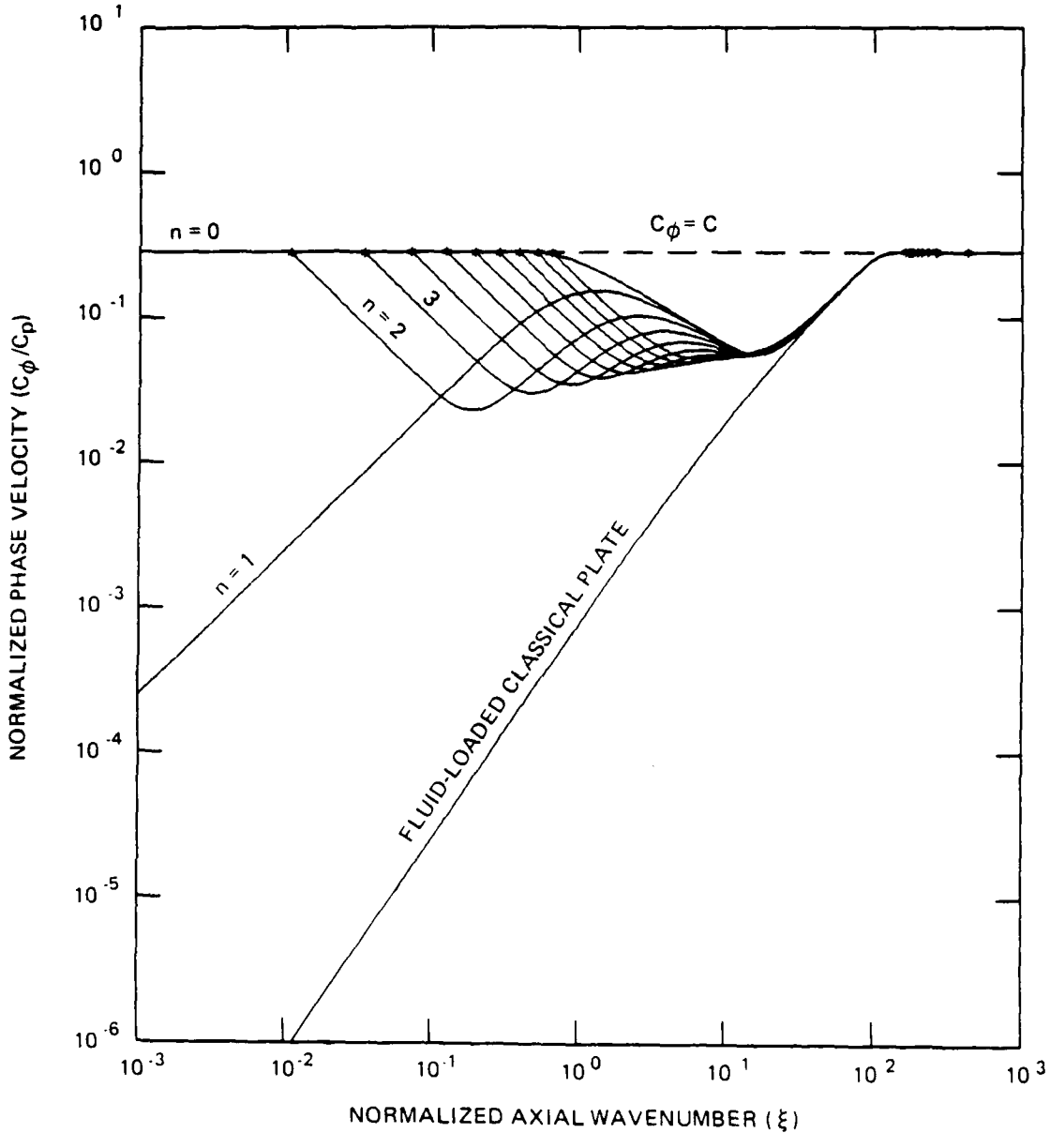

Figure 4.12. Normalized dispersion curves at various mode order numbers for the real branch of a steel shell in water with a normalized thickness of 0.01.

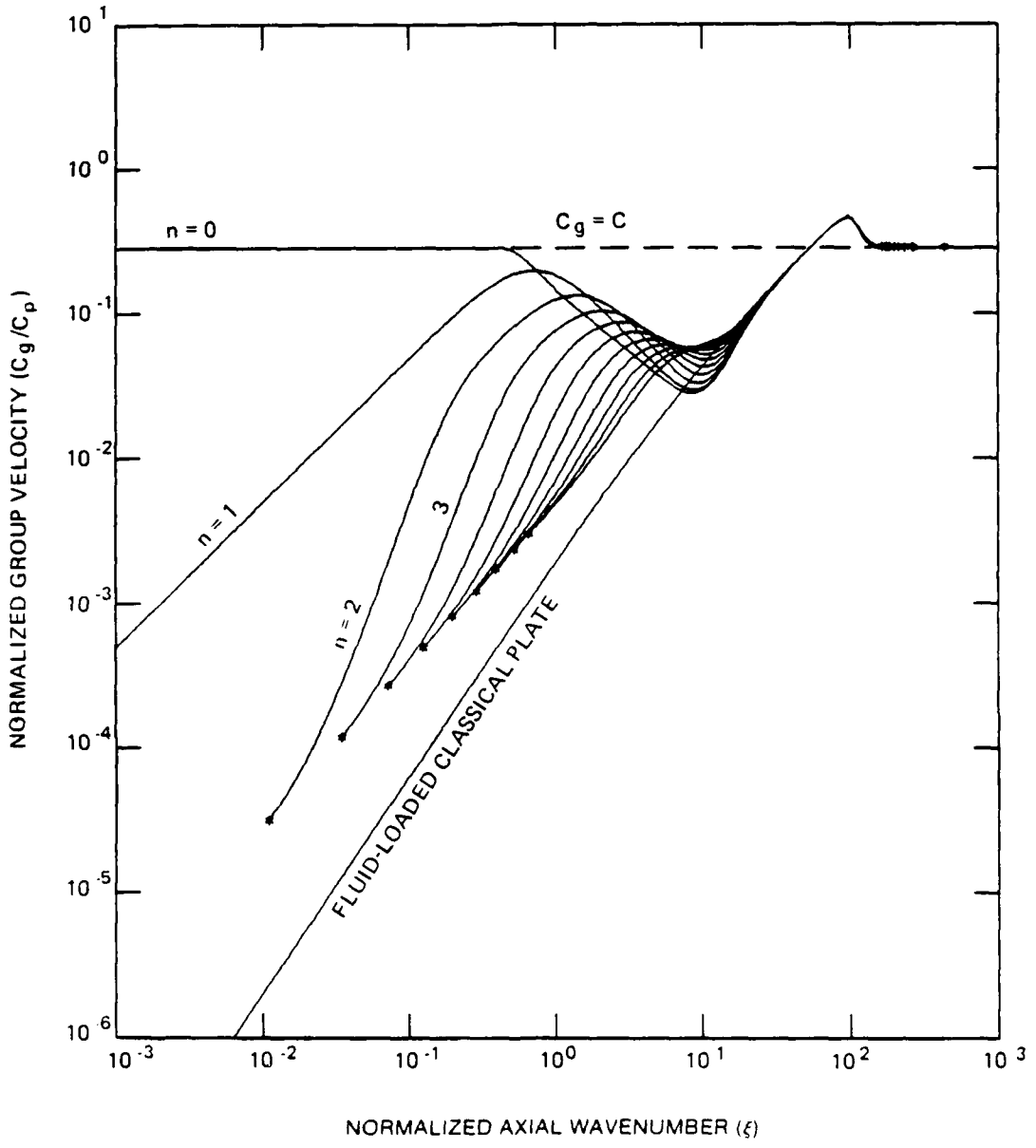

Figure 4.13. Normalized group velocity versus axial wavenumber curves at various mode order numbers for the real branch of a steel shell in water with a normalized thickness of 0.01.

solution of the acoustic pressure, Equation (4.21). The axisymmetric mode with a zero lower cutoff frequency and an infinite upper cutoff frequency acts as an all-pass filter. At all driving frequencies, the axisymmetric mode contributes a residue term to the solution. The first mode order with a finite upper cutoff frequency acts as a low-pass filter. Since the upper cutoff frequency decreases with increasing mode order, at frequencies above the upper cutoff frequency of the first mode order, the residue term would be consist only of the contribution due to the axisymmetric mode. The second and higher mode orders have both a nonzero lower cutoff frequency and a finite upper cutoff frequency. These higher mode orders act as bandpass filters and contribute only for driving frequencies within the band. Since the lower cutoff frequency increases with increasing mode order, at frequencies below the lower cutoff frequency of the second mode order, only the axisymmetric and first mode order will contribute to the residue term.

The increasing behavior of the lower cutoff frequencies and the decreasing behavior of the upper cutoff frequencies require that a mode order exists beyond which no real singularities are possible. This implies that the Fourier summation of the residues of the real singularities has a finite number of terms. Figure 4.14 is a plot of the lower and upper cutoff frequencies of a water-loaded shell as a function of mode order. Several values of normalized shell thickness are shown. The curves were computed by requiring $\xi=k$ in the impedance relations of te characteristic equation for mode orders greater than zero. The acoustic radiation impedance was taken as its small argument asymptotic expansion which is exact at zero argument. The resulting polynomial was solved for its real roots using Laguerre's method. At any driving frequency, all mode orders to the left of the curve will contribute a

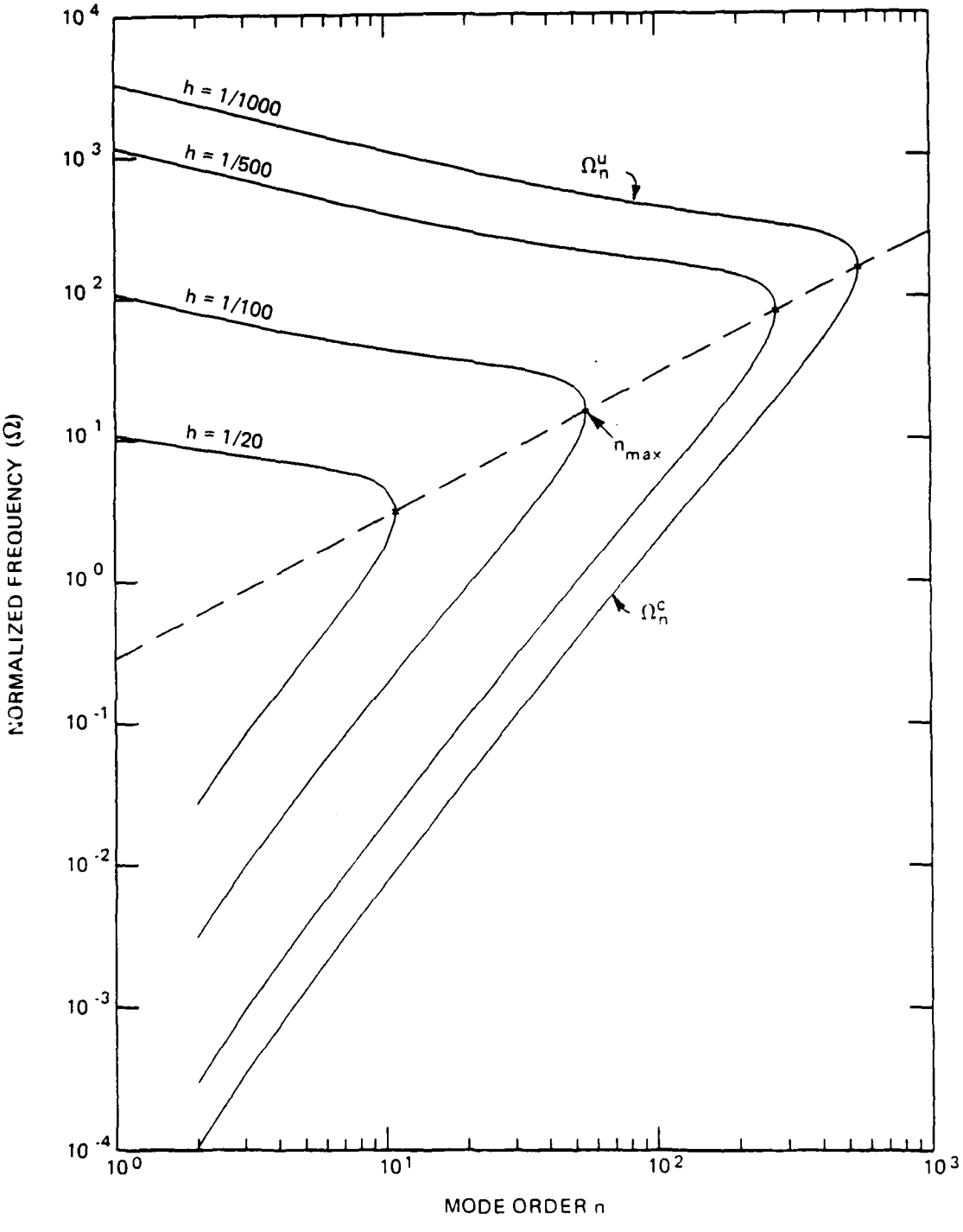

Figure 4.14. Effect of shell thickness variation upon the behavior of the lower and upper cutoff frequencies versus circumferential mode order number for a steel shell in water. Continuous curves are shown for convenience only.

residue term. It can be shown that the maximum allowable mode order at which real singularities can exist, denoted as n_{max}, occurs when $n=\xi=k$. In terms of the parameters of the shell and the fluid, n_{max} is given as the truncated integer value of

$$n_{max} = (c/c_p)\ (3\beta)^{-1/2}\ \cos\Psi \tag{4.38}$$

where Ψ is the principal angle calculated from

$$\Psi = \frac{1}{3}\ \cos^{-1}\left[\frac{3\rho c_p}{2\rho_s c}\right] \quad . \tag{4.39}$$

Since n_{max} is an integer, a small band of frequency exists at which the maximum number of modes contribute a residue term. The center frequency of this band is

$$\Omega_{max} = (c/c_p)\ n_{max} \tag{4.40}$$

which represents the maximum allowable lower cutoff frequency and the minimum allowable upper cutoff frequency for the fluid-loaded shell.

4.8 Location of the Complex Singularities

The complex singularities have been very difficult to locate. Although analytic techniques are helpful in a global manner, due to the complexity of the characteristic equation they are inadequate to determine specific singularities. Analysis can be used to define regions in which singularities cannot exist, such as on the imaginary axis, or to define the properties a singularity must possess if it is to exist in a region. Analytic methods are also useful in determining symmetry properties that allow the search to be confined to a portion of the two-dimensional space. However, generally the actual location of the singularities can only be determined by numerical methods.

Numerical methods can generate ambiguous results whenever the problem has employed branch lines to assure that all functions are single-valued in the space of interest. Since all machine algorithms represent angular measure as modulo 2π, association of a point with a particular Riemann sheet is not numerically possible without the use of complicated tracking algorithms. When possible, an easier approach is to work in a variable space in which the characteristic equation is represented by a single Riemann sheet. For our problem this would be the radial wavenumber γ. Therefore, the complex roots of the characteristic equation written in terms of γ were located and then transformed into axial wavenumber. The phase of γ makes the association with a particular Riemann sheet obvious.

A problem common to all numerical search methods is choosing the proper point or points at which to begin the search. Most search methods are local methods and require the starting point to be reasonably close to the zero of the function in order to yield correct results. A general partitioning of the space of interest often leads to confusing and erroneous results. A method which eventually had some success was based upon the postulation that since an infinite system has a continuous wavenumber spectrum, each branch must also be continuous. This is another way of stating that as frequency is varied, a particular vibratory mode decays or grows without discontinuity. A consequence of this postulation is the expectation that all vibratory modes must have a response at all frequencies, even though the response may rapidly decay or be very small. In particular, each branch must touch the zero frequency plane at exactly one point in the complex γ and ξ domains. Otherwise, the particular vibratory mode would not remain a single-valued function of frequency. Frymoyer's calculations for a shell in

vacuo as well as Stuart's (1972) results for a fluid-loaded plate both confirm this postulation. Nothing in this discussion precludes singularities of order greater than one or the concept of branch splitting.

At zero frequency, the specific acoustic impedance is identically zero, and the characteristic equation degenerates into the shell impedance $Z_{sn}(\xi)$. Ignoring the roots at infinity, the characteristic equation further degenerates at zero frequency into the shell stifness component $D_{sn}(\xi)$. These roots were used as starting values in a numerical search for complex singularities.

The roots were mapped through the complex plane by iterating upon frequency. In the appropriate regions, results were verified using the asymptotic approximations of the specific acoustic impedance given by Equation (4.25). The resultant polynomials were solved by standard procedures. Even when a reasonable starting point is known, numerical problems associated with the search method may prevent a valid numerical solution in certain parametric regions. A classical example is the failure of Newton's method in the region where the derivative of the function under evaluation approaches zero. For this reason, several search methods must often be employed. The most successful approach was a generalization of the secant method due to Muller (1956). Instead of linearly approximating the root based upon two initial approximations, Muller used three initial approximations and fit a parabola to estimate the root. Unlike the linear secant method, Muller's generalization will converge on a complex root even when real initial approximations are used. In this respect, Muller's method is ideal to study the behavior of the complex branches in the vicinity of the lower and upper cutoff frequencies where the real roots enter the complex plane. The specific implementation of Muller's method used was algorithm ZANLYT of the IMSL

(1982) library. Like Newton's method, both the linear and parabolic secant methods can fail in regions where the derivative of the characteristic equation approaches zero. Another method employed was a bisection method adapted to the complex plane by Dubbelday (1983). Although this method will always converge to a root, the convergence can be quite slow compared with Muller's method.

At zero frequency, one nonzero γ-root exists in each quadrant for both the axisymmetric and n=1 mode. This root has a large magnitude and as frequency increases the root initially moves toward the origin and then asymptotically approaches either the real or negative imaginary axis as frequency continues to increase depending upon whether the root is respectively in the upper or lower half-plane. The roots in the upper half-plane are symmetric about the imaginary axis. Although the roots in the lower half-plane are not theoretically symmetric, at large magnitude their behavior is quite similar such that they are also essentially symmetric about the negative imaginary axis.

Each root in the γ-plane is represented by two roots on a single Riemann sheet of the ξ-domain. The frequency spectra in the top Riemann sheet of the ξ-domain associated with the upper half-plane γ-roots is shown in Figure 4.15. These frequency spectra are symmetric about both the real and imaginary axis of the top Riemann sheet. The branch nomenclature convention used for the shell in vacuo is not appropriate in the fluid-loaded case since all known branches exhibit predominantly radial motion at large ξ. Instead let us associate the zero frequency intercept of the fluid-loaded branch to the complex extension of the real in vacuo branches at zero frequency. That is, the zero frequency roots of the shell stiffness term $D_{sn}(\xi)$ are recognized as the complex singularities of the shell in vacuo as presented by Frymoyer. On this basis the

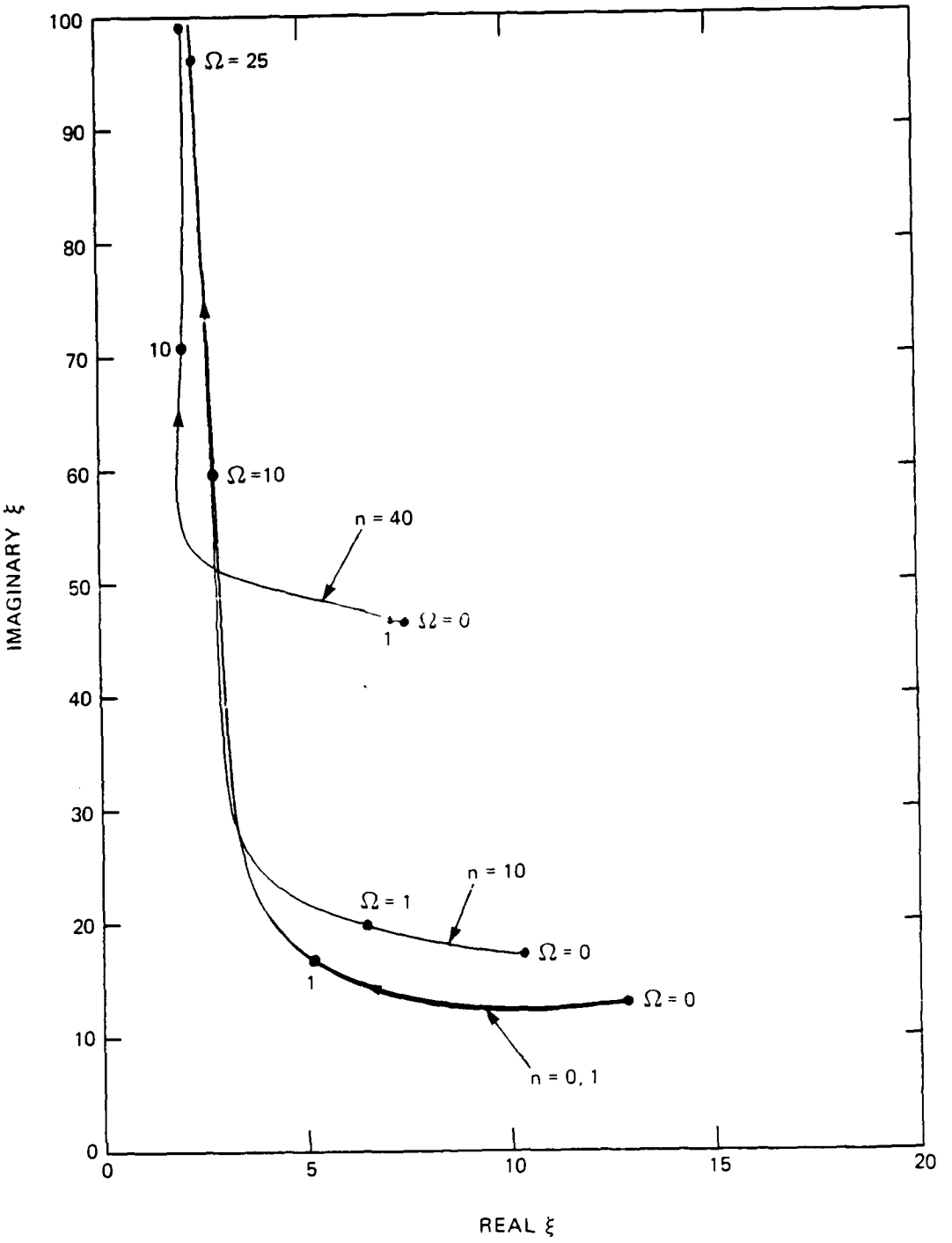

Figure 4.15. Frequency spectra of complex branch L_1 at various mode order numbers for a steel shell in water with a normalized thickness of 0.01. Frequency is indicated at various points along the complex branch.

frequency spectra of Figure 4.15 can be associated with the in vacuo longitudinal branch and are therefore designated as branch L_1. As also shown in Figure 4.15, branch L_1 exists for mode orders greater than the first. By performing a large mode order asymptotic expansion of the impedance functions, it can be shown that branch L_1 exists for all mode orders. Although complex roots on the bottom Riemann sheet are not of direct interest and therefore not graphically presented, their behavior is to asymptotically approach the real ξ-axis as frequency increases.

For mode orders greater than one, a second root exists in each quadrant of the γ-plane at zero frequency. The upper half-plane roots represent the zero frequency intercept of the complex extension of the real branch below the lower cutoff frequency. Since this zero frequency intercept can also be associated with that of the flexural branch in vacuo, this branch is designated as L_3. The behavior of branch L_3 on the top Riemann sheet below the lower cutoff frequency is shown in Figure 4.16 for n=2 and 3. Frequency is indicated at various points along the spectra. As can be seen, the complex singularity remains in the vicinity of its zero frequency intercept over most of the frequency range. Like branch L_1, complex branch L_3 is symmetric about both the real and imaginary ξ-axes. Consequently, at the lower cutoff frequency the complex extensions in the first and fourth quadrants merge and continue out along the real axis. Similar behavior occurs for the complex extensions in the second and third quadrants. The behavior over the real axis was previously described in Figures 4.6 through 4.14. At the upper cutoff frequency the branch L_3 splits to form the complex extensions shown in Figure 4.17. As frequency increases to infinity the complex extension of L_3 above the upper cutoff frequency asymptotically approaches the real axis again.

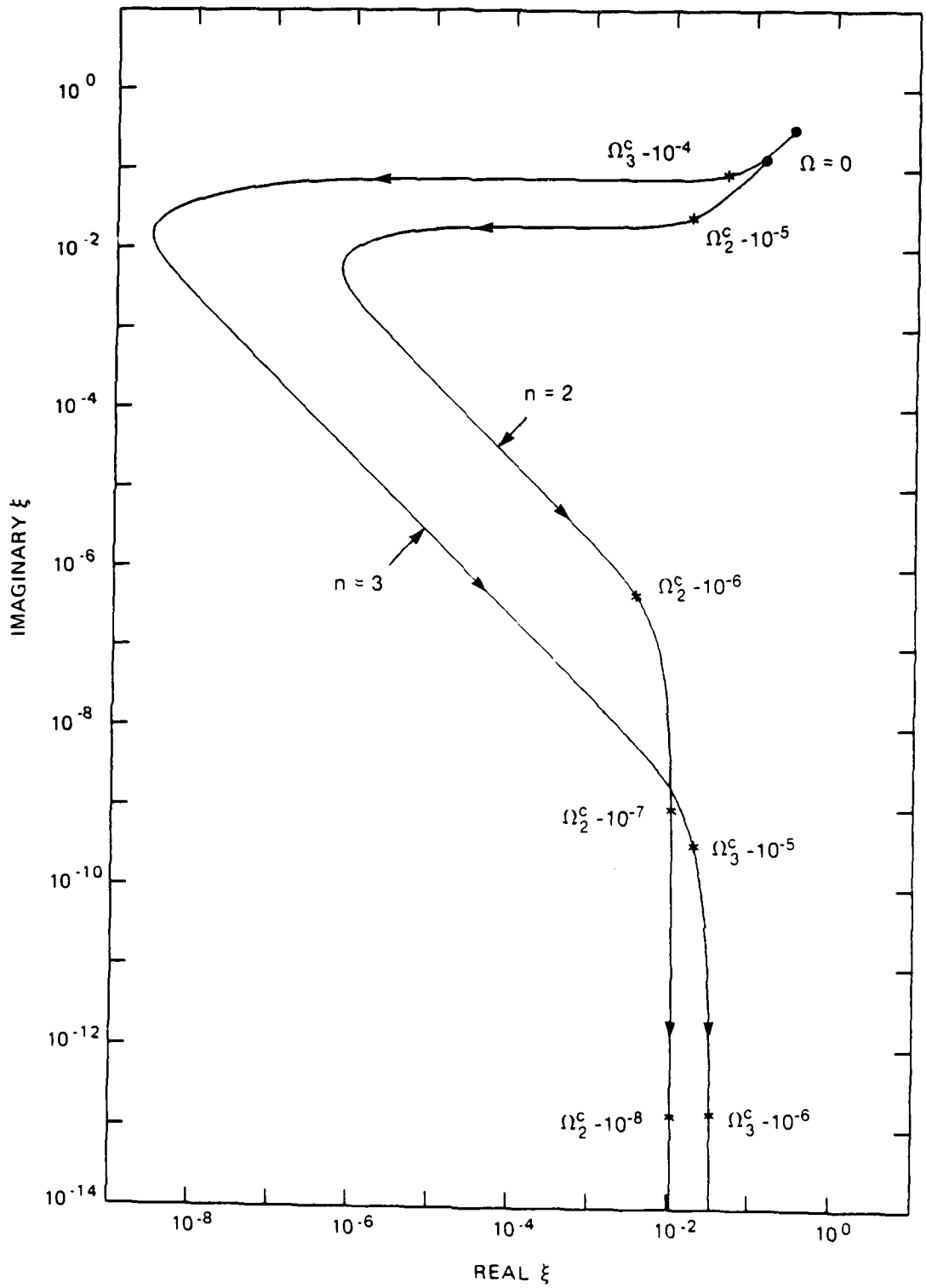

Figure 4.16. Frequency spectra of complex branch L_3 below the lower cutoff frequency for the n=2 and 3 modes of a steel shell in water with a normalized thickness of 0.01. Frequency is indicated at various points along the complex branch.

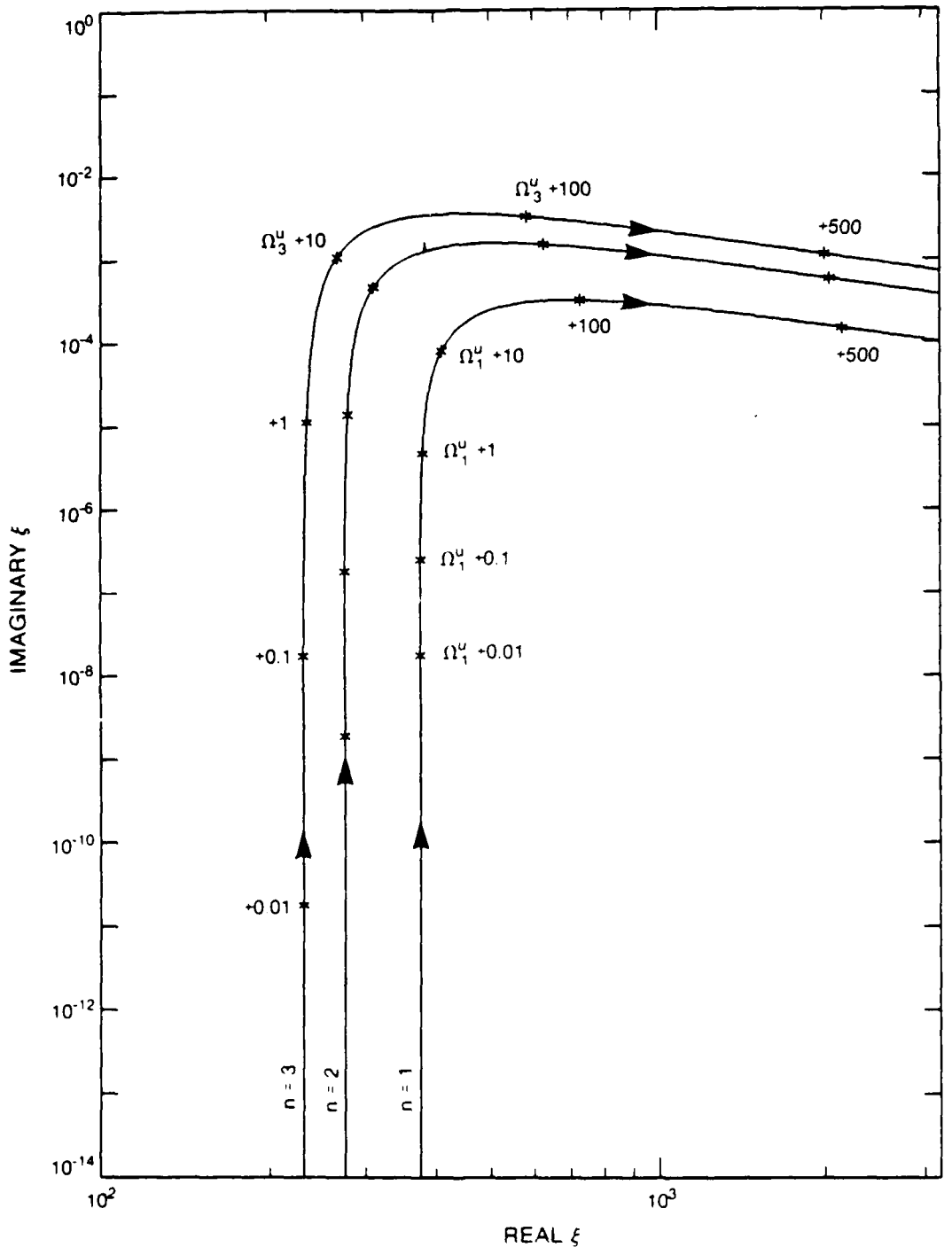

Figure 4.17. Frequency spectra of complex branch L_3 above the upper cutoff frequency for the n=2 and 3 modes of a steel shell in water with a normalized thickness of 0.01. Frequency is indicated at various points along the complex branch.

Chapter 5

CAUCHY'S THEOREM SOLUTION OF THE NEARFIELD ACOUSTIC RADIATION FROM A HOMOGENEOUS FLUID-LOADED CYLINDRICAL SHELL

5.1 Introduction

This chapter will discuss the Cauchy's theorem and integral formula solution of the acoustic radiation from a point-excited cylindrical shell immersed in a homogeneous fluid medium. In the last chapter, the radiated acoustic pressure at any point in the fluid was found to be

$$p(r,\theta,x) = p_{ref} \sum_{n=0}^{\infty} \varepsilon_n \cos(n\theta) \int_{-\infty}^{+\infty} G_n(\xi)\, e^{j\xi x}\, d\xi \qquad (5.1)$$

where

$$G_n(\xi) = \frac{Z_{fn}(\gamma r)}{Z_{sn}(\xi) + Z_{fn}(\gamma a)} = \frac{H_n(\gamma r)}{H_n(\gamma a)} \frac{\Delta Z_{an}(\gamma)}{X_{sn}(\xi) + \Delta Z_{an}(\gamma)} \quad . \qquad (5.2)$$

Both the radial wavenumber γ and the behavior of the specific acoustic impedance $Z_{fn}(\gamma r)$ were specified by using the Sommerfeld branch lines.

The major difficulty in obtaining a solution of Equation (5.1) is the evaluation of the inverse Fourier integral. If a numerical integration is performed along the real axis, real singularities of the integrand will obviously cause severe numerical difficulties. A technique which is sometimes used to deal with this problem is to add a small amount of damping to the system in order to move the singularities off the real axis. However, the value of the numerical integration remains heavily dependent upon the contribution of the integrand along that por-

tion of the real axis nearest to the now complex singularity. In this sense, real singularities usually dominate any numerical integration process. The value of the integral is also a function of how close the integration path comes to a singularity, that is, the amount of damping added to the system. A technique sometimes employed is to calculate the value of the integral numerically for several damping values and then numerically or graphically extrapolate a value for the zero damping limit. Unfortunately, the results from this method can sometimes be very dependent upon the damping values chosen.

Numerical integration can also have problems with accumulated round-off error, with convergence in the truncation of the infinite integration range, and with mesh size selection. A successful numerical integration, especially for integrands with the complexity of ours, usually requires quite a bit of investigation into the behavior of the integrand as well as attention to computational detail. In the end, numerical integration yields a number, and only by repeated parameter changes can any of the relationships which govern the radiated acoustic pressure field begin to be known. A more informative approach is to investigate the problem analytically and to utilize numerical integration only for those portions of the solution which cannot be further solved by analytic methods. However, along the way, numerical investigation is often a useful adjunct to the analytic methods.

The integral can be evaluated analytically by extension into the complex ξ-plane and use of Cauchy's theorem. This method is exact if all of the singularities can be found and their residue contributions calculated. Additionally, the contribution of the path of integration through the complex plane must be found. This chapter will develop the various parts of the Cauchy theorem solution and discuss their behavior

as a function of the parameters of the problem. Asymptotic techniques will be employed where appropriate. Both the shell displacement field and the nearfield acoustic pressure will be calculated.

5.2 Cauchy's Theorem Formulation of the Pressure Field

Cauchy's theorem states that the integral of a function between any two points is independent of the path linking those points if the function remains analytic along the path. If the path is closed then the integral would be zero. Therefore, the integration along the real axis in Equation (5.1) could be replaced by another path in the complex plane along which, hopefully, the function $G_n(\xi)$ has some simple form and the integration is more easily performed. Since the integrand function $G_n(\xi)$ is known to contain singularities, Cauchy's theorem can only be used if some multiply connected region is defined that excludes these singularities.

Unfortunately, along the interior paths necessary to exclude the singularities, $G_n(\xi)$ will not be a simple function. However, by introducing Cauchy's integral formula, which relates the integral of a function over a closed contour to its value at a point inside that contour, the integrals over the interior paths can be solved. Formally, it is given by

$$G(z_o) = (2\pi j)^{-1} \oint \frac{G(z)}{z-z_o} \, dz \tag{5.3}$$

which is written in its more popular form as

$$\oint g(z) \, dz = 2\pi j \sum_m \text{residue}(z_m) \tag{5.4}$$

where z_m represents the first order singularities of $g(z)$ enclosed by the contour, and residue(z_m) stands for the residue of $g(z)$ evaluated at

$z=z_m$. The residue of a first order singularity is defined as the coefficient associated with the term $(z-z_m)^{-1}$ of the Laurent series expansion of $g(z)$ about the singularity z_m. The left-hand side of Equation (5.3) therefore represents the residue of the function $G(z)/(z-z_o)$ at the singularity $z=z_o$. Green's theorem is a higher order manifestation of Cauchy's integral formula.

If a very small amount of propagation loss is introduced into the acoustic medium, then a possible contour of integration in the complex ξ-domain is shown in Figure 5.1 where circular contours C_1 and C_2 exist at infinite radius. The contour of integration around the branch line is designated by paths Γ_1, Γ_2, Γ_3, Γ_4, and Γ_5. The original path of interest along the real axis from minus to plus infinity is designated as path R. The contour shown is valid for $x>0$ and the integrand is single-valued everywhere. Closure in the lower half-plane for $x<0$ would yield identical results. By use of both Cauchy's theorem and integral formula we can write

$$\oint G_n(\xi)\, e^{j\xi x}\, d\xi = \int_R + \int_{C_1} + \int_{\Gamma_1} + \int_{\Gamma_2} + \int_{\Gamma_3} + \int_{\Gamma_4} + \int_{\Gamma_5} + \int_{C_2} G_n(\xi)\, e^{j\xi x}\, d\xi$$

$$= 2\pi j \sum \text{residue}(\xi_m) \qquad (5.5)$$

where $G_n(\xi)$ was previously defined.

Over paths C_1 and C_2 the magnitude of ξ is infinite. For $|\xi|$ large, it can be shown that

$$\lim_{|\xi|\to\infty} G_n(\xi) = 0(\xi^{-5} e^{-\xi r})$$

which implies $G_n(\xi)$ approaches zero uniformly in the limit. If a simple translation of axis $\xi = k+\varepsilon$ is introduced it can also be shown that

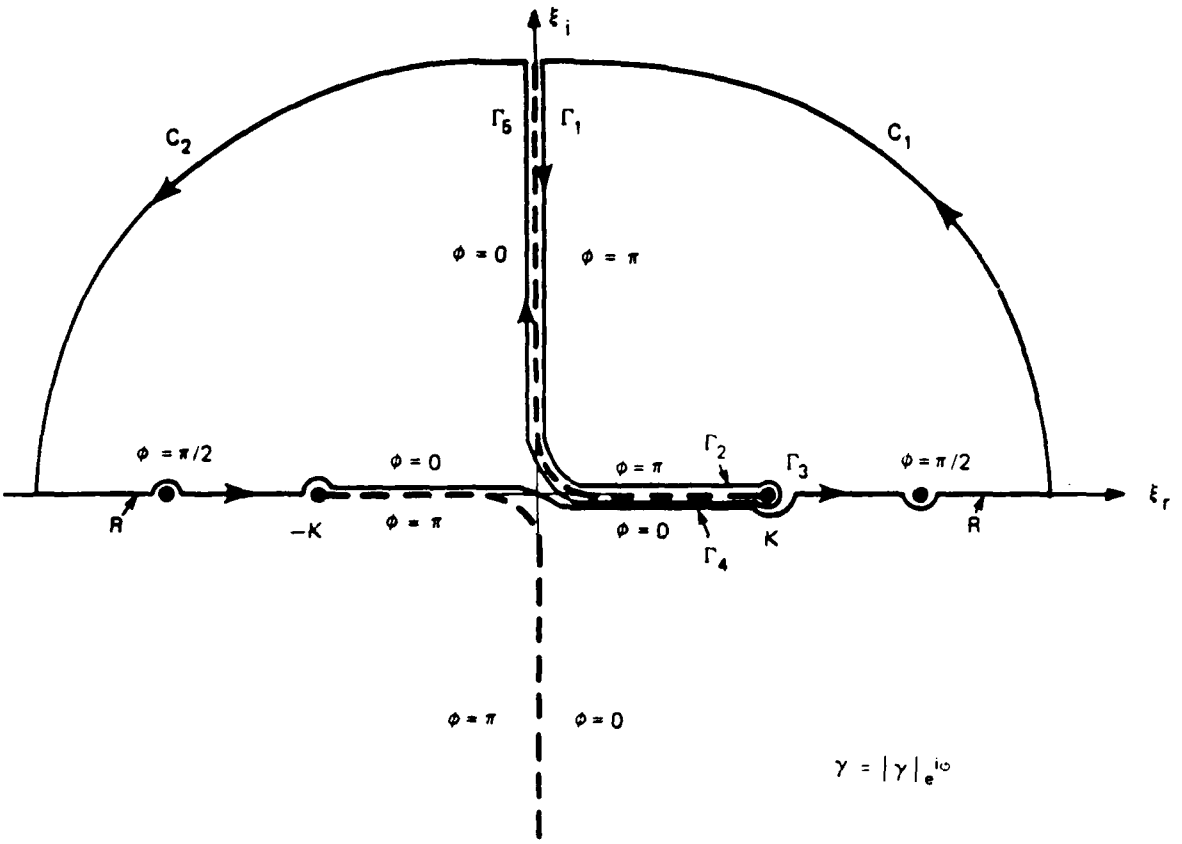

Figure 5.1. Closed contour of integration for x>0 on the top Riemann sheet of the complex ξ-plane. Branch points and branch lines are shown for a very small component of acoustic propogation loss. The phase of γ is indicated in various regions of interest.

$$\lim_{|\varepsilon|\to 0} G_n(\varepsilon) = 0(1)$$

which is applicable to the integration along path Γ_3. Application of Jordan's Lemma in these two asymptotic regions indicates that

$$\int_{C_1} G_n(\xi)\, e^{j\xi x}\, d\xi = \int_{C_2} G_n(\xi)\, e^{j\xi x} d\xi = \int_{\Gamma_3} G_n(\xi)\, e^{j\xi x}\, d\xi = 0 \qquad (5.6)$$

such that

$$\int_R G_n(\xi)\, e^{j\xi x}\, d\xi = 2\pi j \sum_m \text{residue}(\xi_m) - \int_B G_n(\xi)\, e^{j\xi x}\, d\xi \qquad (5.7)$$

is the desired integral. The integration over the real axis is thus replaced by an integral evaluation around the branch line, given by

$$\int_B G_n(\xi)\, e^{j\xi x}\, d\xi = \int_{\Gamma_1} + \int_{\Gamma_2} + \int_{\Gamma_4} + \int_{\Gamma_5} G_n(\xi)\, e^{j\xi x}\, d\xi \quad , \qquad (5.8)$$

and by the contribution of the residues of the integrand at the singularities ξ_m located in the upper half-plane of the top Riemann sheet.

5.3 Evaluation of the Branch Line Integrals

While the use of Cauchy's integral formula obviates the numerical integration along the real axis where the integrand has singularities, the method does introduce new integrals along the branch lines. On a modal basis, the total branch line integral consists of the four segments Γ_1, Γ_2, Γ_4, and Γ_5. Let us treat them as pairs such that integral $B_{1n}(r,x)$ consists of segments Γ_1 and Γ_5 along the imaginary axis, and integral $B_{2n}(r,x)$ consists of segments Γ_2 and Γ_4 along the real axis where $0 \le \xi \le k$. The branch integral contributions to the radiated pressure field would be given by

$$B_1(r,\theta,x) = p_{ref} \sum_{n=0}^{\infty} \varepsilon_n B_{1n}(r,x) \cos(n\theta) \tag{5.9a}$$

$$B_2(r,\theta,x) = p_{ref} \sum_{n=0}^{\infty} \varepsilon_n B_{2n}(r,x) \cos(n\theta) \ . \tag{5.9b}$$

Recalling that neither imaginary singularities nor real singularities with a magnitude less than the acoustic wavenumber can exist, then the integrands of both B_{1n} and B_{2n} must be analytic. Although the branch line integrals can generally only be solved numerically, their analytic behavior would justify using Cauchy's theorem over numerical integration along the real axis if the singularities of the problem were known. Furthermore, in certain asymptotic limits of interest, an analytic solution of the branch line integrals exists.

Let us begin be evaluating integral B_{2n} along paths Γ_2 and Γ_4 where the axial wavenumber is real. By noting that along segment Γ_2 the radial wavenumber has a phase of π and a zero phase along segment Γ_4, as shown in Figure 5.1, and by introducing the symmetry property of the specific acoustic impedance function, Equation (4.24), integral B_{2n} can be placed in the form

$$B_{2n}(r,x) = \int_{\Gamma_2+\Gamma_4} G_n(\xi)\, e^{j\xi x}\, d\xi = \int_0^k Q_n(\xi)\, e^{j\xi x}\, d\xi \tag{5.10}$$

where

$$Q_n(\xi) = \left[\frac{Z_{fn}(\gamma r)}{Z_{sn}(\xi) + Z_{fn}(\gamma a) - 2Re\{Z_{sn}(\xi)\}}\right]^* - \left[\frac{Z_{fn}(\gamma r)}{Z_{sn}(\xi) + Z_{fn}(\gamma a)}\right]$$

and where γ has zero phase. For zero structural damping the shell's spectral mechanical impedance is imaginary and $Q_n(\xi)$ reduces to the form

$$Q_n(\xi) = -2j \text{ Im } \{G_n(\xi)\} \quad . \tag{5.11}$$

The integral B_{2n} is complex at all field points except where the axial distance is zero and it is imaginary.

Although the solution of branch line integral B_{2n} must generally be found numerically, an analytic solution is available in the nearfield at low frequency. In this limiting case, the specific acoustic impedance can be approximated by its small argument limit over the entire integration path. Furthermore, at low frequency the shell's normalized stiffness function is only weakly dependent upon the axial wavenumber and can be approximated by

$$\lim_{\Omega \to 0} X_{sn}(\xi) \simeq \begin{cases} 1 & \text{for } n=0 \\ \beta(n^2-1)^2 - (n^2+1)\left(\frac{\Omega}{n}\right)^2 & \text{for } n>0 \end{cases} \quad . \tag{5.12}$$

Introducing these approximations into Equation (5.10) yields

$$\lim_{\substack{\Omega \to 0 \\ r \to a}} B_{2n}(r,x) = A_n \int_0^k (k^2 - \xi^2)^n \, e^{j\xi x} \, d\xi \tag{5.13a}$$

where

$$A_n = -2j \, \frac{\Delta a m^2}{(n!)^2} \left\{ \frac{\left[\left(\frac{r}{a}\right)^n - \left(\frac{a}{r}\right)^n\right] \Delta an - \left[\left(\frac{r}{a}\right)^n + \left(\frac{a}{r}\right)^n\right] n^2 X_{sn}}{\left[n^2 X_{sn} - \Delta an\right]^2} \right\} \left(\frac{a}{2}\right)^{2n}$$

for $n>0$. The integral has solution

$$\int_0^k (k^2 - \xi^2)^n \, e^{j\xi x} \, d\xi = \sqrt{\frac{\pi k}{2x}} \left(\frac{2k}{x}\right)^n (n!) \left\{ J_{n+1/2}(kx) + j\bar{H}_{n+1/2}(kx) \right\}$$

where $J_{n+1/2}(kx)$ is the half-order Bessel function (spherical Bessel function) and $\bar{H}_{n+1/2}(kx)$ is the half-order Struve function of real

argument kx. For the axisymmetric mode

$$\lim_{\substack{\varrho\to 0 \\ r\to a}} B_{20}(r,x) = A_o \frac{e^{jkx} - 1}{jx} \tag{5.13b}$$

where

$$A_0 = -j\Delta a\pi \frac{\Delta a \ln(r/a) - 1}{[1 + \Delta a \ln(ka)]^2}.$$

For zero axial distance

$$\lim_{\substack{\varrho\to 0 \\ r\to a}} B_{2n}(r,x=0) = A_n \int_0^k (k^2 - \xi^2)^n \, d\xi \quad \text{for } n>0 \tag{5.13c}$$

where

$$\int_0^k (k^2 - \xi^2)^n d\xi = \frac{k^{2n+1}(n!)\, 2^n}{1\cdot 3\cdot 5\cdot\cdots\cdot(2n+1)}$$

while

$$\lim_{\substack{\varrho\to 0 \\ r\to a}} B_{20}(r,x=o) = A_0 k \tag{5.13d}$$

for the axisymmetric mode. The low frequency solutions represented by Equations (5.13) would be valid for field points such that kr is small.

In the numerical evaluation of integral sequences as represented by Equation (5.9), two important considerations generally are integrand convergence along the path and modal convergence of the series. Since the integration interval of B_{2n} is finite, integrand convergence will not be of concern. The modal convergence behavior of the series can be assessed by introducing the large order approximations

$$\lim_{n\to\infty} X_{sn}(\xi) = \beta(n^2+\xi^2)^2 - \Omega^2 \tag{5.14a}$$

$$\lim_{n\to\infty} Z_{an}(\gamma) = -\frac{a}{n}\left\{1 + j\left(\frac{e\gamma a}{2n}\right)^{2n}\right\} \tag{5.14b}$$

$$\lim_{n\to\infty} Z_{fn}(\gamma r) = -j\rho ck\,\frac{a}{n}\left\{\left(\frac{a}{r}\right)^n + \frac{1}{2}\,j\left(\frac{e\gamma a}{2n}\right)^{2n}\left[\left(\frac{a}{r}\right)^n + \left(\frac{r}{a}\right)^n\right]\right\} \tag{5.14c}$$

where e is the base of the Napierian logarithm taken as 2.718··· and $n>e\gamma r/2$ has been assumed. At large order, the shell stiffness function has the same asymptotic behavior as exhibited at high frequency. Introducing these relations into Equation (5.11) yields

$$\lim_{n\to\infty} |Q_n(\xi)| = \left| \frac{\Delta a}{n}\left(\frac{e\gamma a}{2n}\right)^{2n} \frac{X_{sn}\left[\left(\frac{r}{a}\right)^n + \left(\frac{a}{r}\right)^n\right] - \frac{\Delta a}{n}\left[\left(\frac{r}{a}\right)^n - \left(\frac{a}{r}\right)^n\right]}{\left(X_{sn} - \frac{\Delta a}{n}\right)^2 + \left(\frac{\Delta a}{n}\right)^2\left(\frac{e\gamma a}{2n}\right)^{4n}} \right|. \tag{5.15}$$

For fixed axial wavenumber, d'Alembert's ratio test would yield

$$\lim_{n\to\infty} \left|\frac{Q_{n+1}(\xi)}{Q_n(\xi)}\right| = \lim_{n\to\infty} O(n^{-2}) = 0.$$

Therefore, for large n, the integrand function $Q_{n+1}(\xi)<Q_n(\xi)$ for all $\xi<k$ and the Fourier series is uniformly convergent.

The numerical algorithms used to generate Bessel functions are based upon recurrence and asymptotic relationships that are numerically correct only within parametric regions of argument and order. Although limitations are sometimes due to the algorithm itself, often problems arise from machine limitations on precision or exponent range. In order to avoid the numerical difficulties associated with these limitations, it is generally preferable to perform the Fourier series summation within the integral. Since Q_n is both continuous (since it is analytic)

and uniformly convergent, Bromwitch (1959) has shown that

$$B_2(r,\theta,x) = p_{ref} \sum_{n=0}^{\infty} \varepsilon_n \cos(n\theta) \int_0^k Q_n(\xi)\, e^{j\xi x}\, d\xi$$

$$= p_{ref} \int_0^k Q(r,\theta,\xi)\, e^{j\xi x}\, d\xi \qquad (5.16)$$

where

$$Q(r,\theta,\xi) = \sum_{n=0}^{\infty} \varepsilon_n\, Q_n(\xi) \cos(n\theta) = \sum_{n=0}^{N} \varepsilon_n\, Q_n(\xi) \cos(n\theta) \ .$$

Figure 5.2 shows a numerical evaluation of the modal truncation value N as a function of axial wavenumber for r=a and θ=0 at Ω=1, 10, and 100. The numerical data is compared with an estimate N=γa+10 based upon uniform convergence criteria. The numerical data represents the mode order at which the last five mode orders each contributed less than 0.2% to the modal sum.

Generally both the acoustical farfield and the region close to the cylindrical shell are of interest while the intermediate region has little practical application. The farfield is logically defined in terms of acoustical wavelength as is done in specifying the Fraunhofer ($a/r \ll 1$ and $ka^2/r \ll 1$) or Fresnel ($kr \gg 1$) zones. However, the practical scale of importance for the region close to the cylindrical shell is the cylinder outer radius a. Although the theory developed has been for an infinitely long cylinder, real structures are generally on the order of 10 cylindrical radii or less in length. Also sensing equipment and decoupling treatments are usually located within one cylindrical radius from the surface. Therefore, the region $a \leq r \leq 2a$ and $x \leq 10a$ will serve as a practical definition of the nearfield.

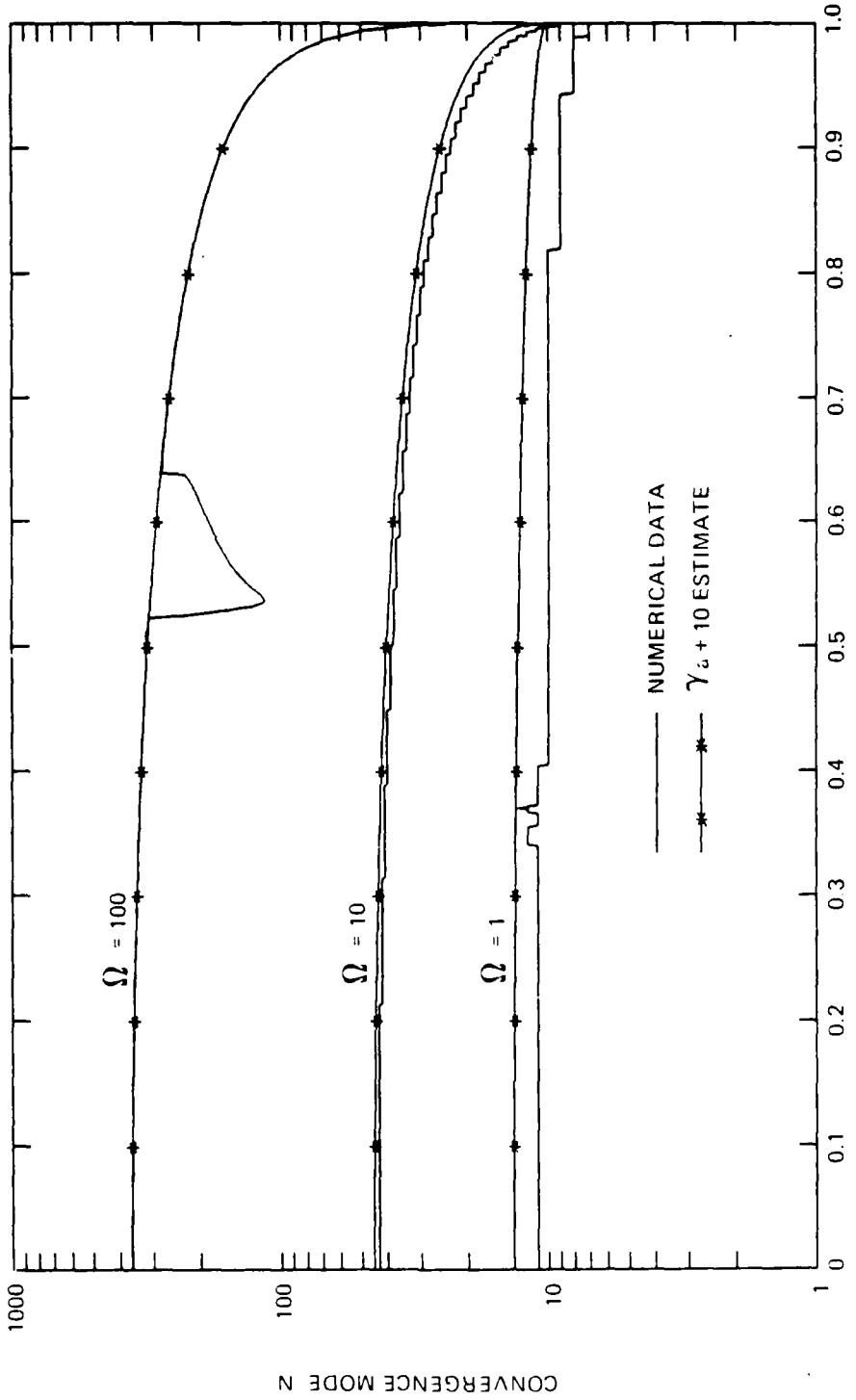

Figure 5.2. Modal truncation value N versus axial wavenumber for the integrand function Q(r=a,θ=0°,ξ) at Ω=1, 10, and 100.

Figure 5.3 shows the contribution of branch integral $B_2(r,\Theta=0,x)$ to the nearfield acoustic pressure for $\Omega=0.1$ in the plane $\Theta=0$ using the analytic relations (5.13). The prediction is presented as contours of the pressure amplitude in dB referenced to p_{ref} plotted in one dB increments. This figure is compared to Figure 5.4 which was computed numerically using Equation (5.9). The agreement is rather good. Figures 5.5 through 5.7 show results for $\Omega=1$, 10, and 100 but where a 10 dB contour increment has been used. Note that a coincidence effect is apparent in the high frequency results. For the nominal parameters used in this study, the normalized plate coincidence frequency is 28.36. Therefore for $\Omega=100$ a coincidence angle would be expected at

$$\phi_c = \sin^{-1}\sqrt{\frac{\Omega_c}{\Omega}} = 32^\circ$$

from the normal to the plate (or cylinder) surface. Figure 5.8 expands the $\Omega=100$ results out to a radial distance of 10a using equal scaling factors along the r and x axes. A beaming effect is clearly shown at the coincidence angle.

The integral B_{1n} can be evaluated in a manner similar to integral B_{2n}. Again referring to Figure 5.1, we see that along segment Γ_1 $\arg(\gamma)$ is π while along segment Γ_5 the radial wavenumber has zero phase. Also noting that along paths Γ_1 and Γ_5 the axial wavenumber is imaginary, we can write

$$B_{1n}(r,x) = \int_{\Gamma_1+\Gamma_5} G_n(\xi)\, e^{j\xi x}\, d\xi = \int_0^\infty Q_n(j\xi)\, e^{-\xi x}\, d\xi \qquad (5.17)$$

where the radial wavenumber has zero phase and the symmetry properties of Equation (4.24) have again been used. The integrand function $Q_n(j\xi)$

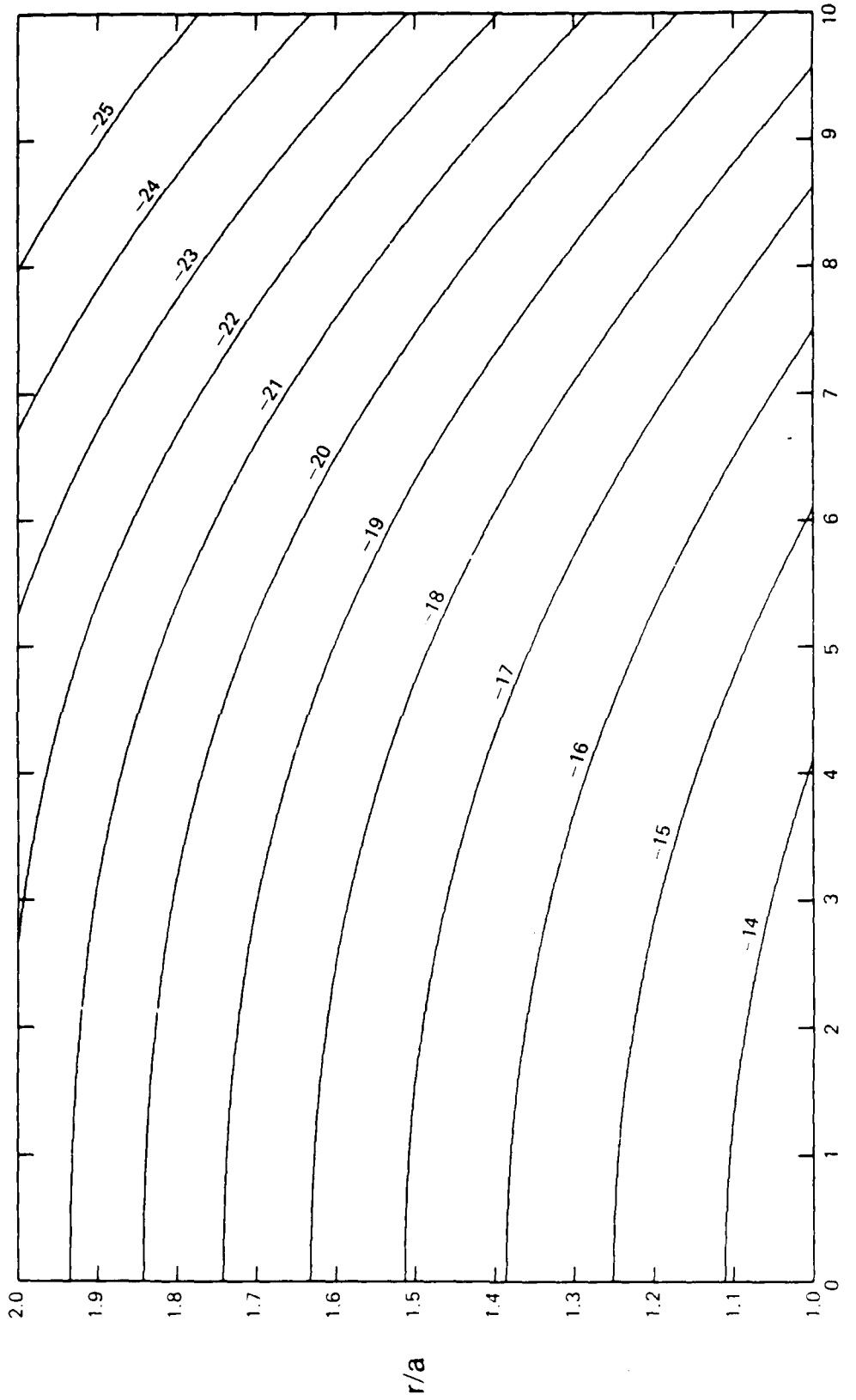

Figure 5.3. Constant magnitude contours of $B_2(r,\theta=0°,x)$ in the acoustic nearfield calculated using Equation (5.13) and expressed in dB re $\hat{p}_{ref}$ for Ω=0.1.

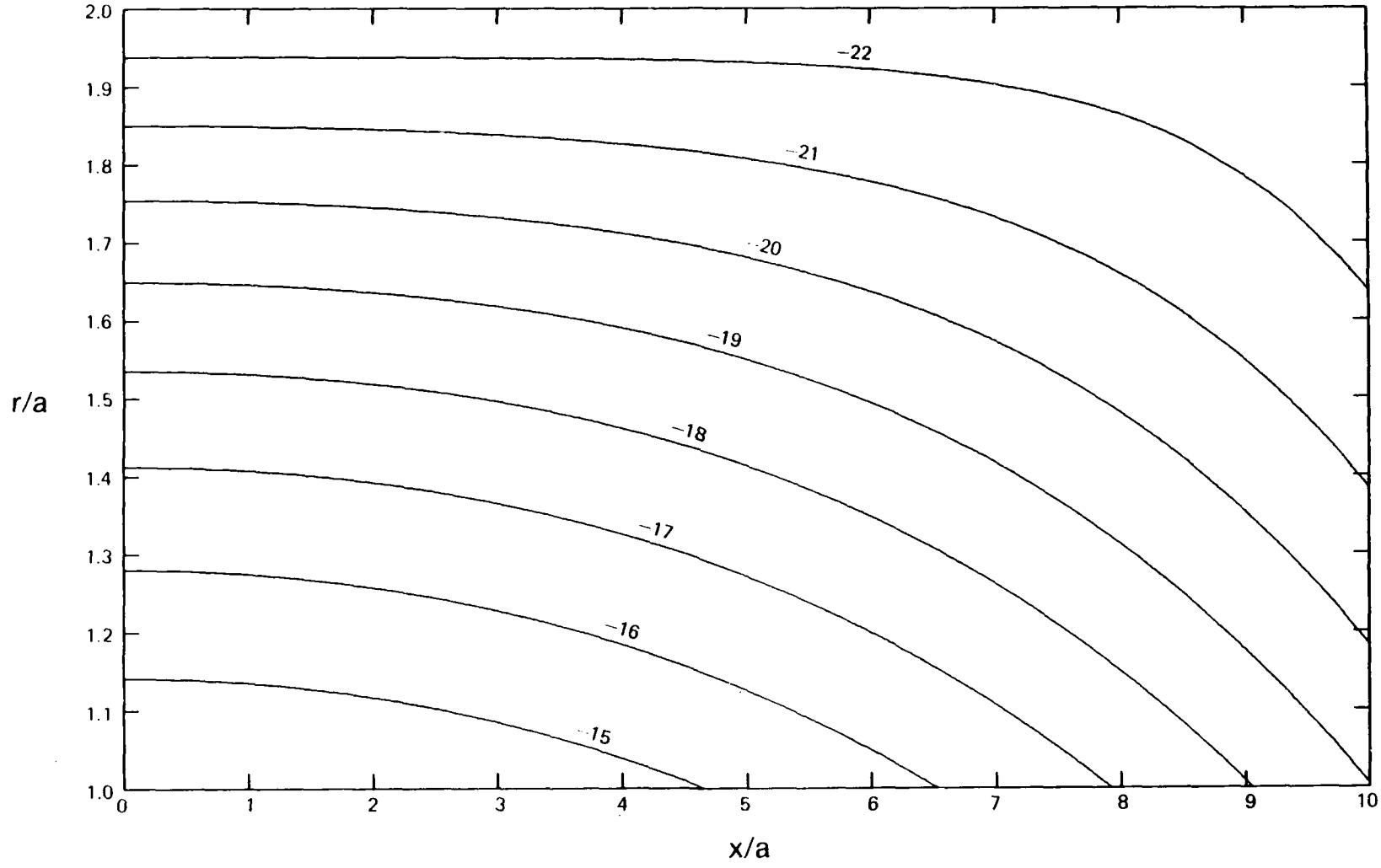

Figure 5.4. Constant magnitude contours of $B_2(r,\theta=0°,x)$ in the acoustic nearfield calculated using Equation (5.10) and expressed in dB re $\hat{p}_{ref}$ for $\Omega=0.1$.

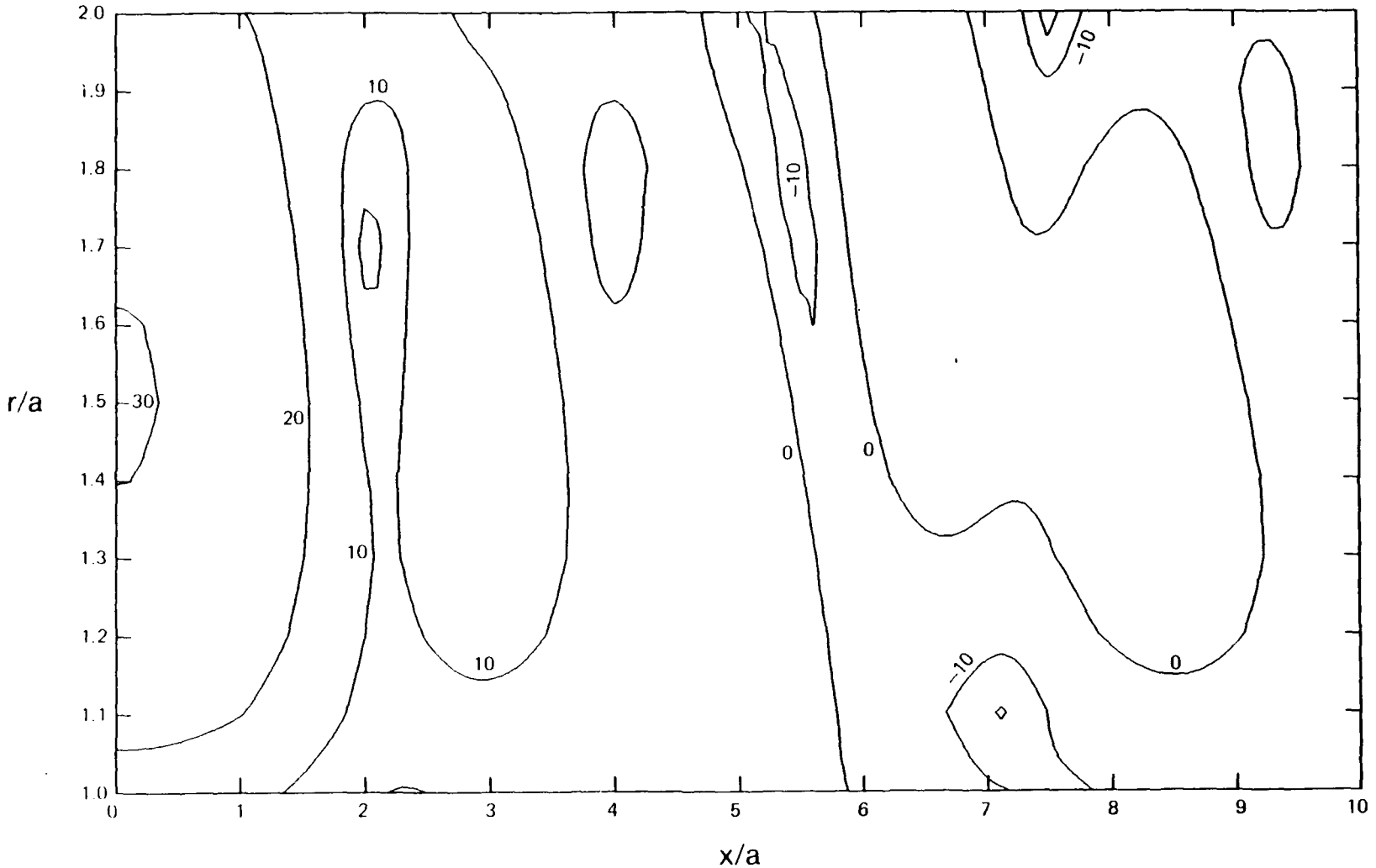

Figure 5.5. Constant magnitude contours of $B_2(r,\theta=0°,x)$ in the acoustic nearfield calculated using Equation (5.10) and expressed in dB re $\hat{p}_{ref}$ for $\Omega=1$.

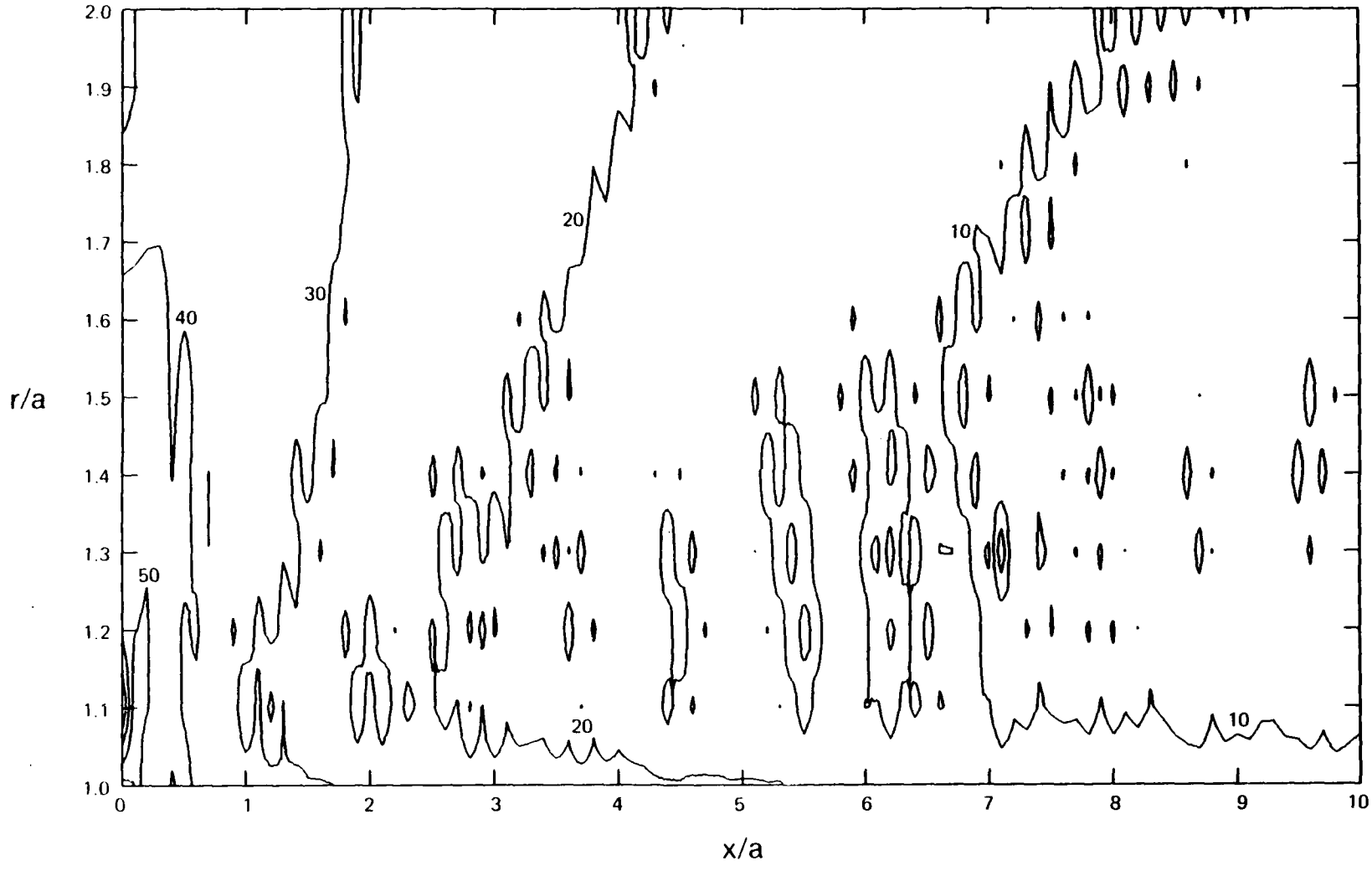

Figure 5.6. Constant magnitude contours of $B_2(r,\theta=0°,x)$ in the acoustic nearfield calculated using Equation (5.10) and expressed in dB re $\hat{p}_{ref}$ for $\Omega=10$.

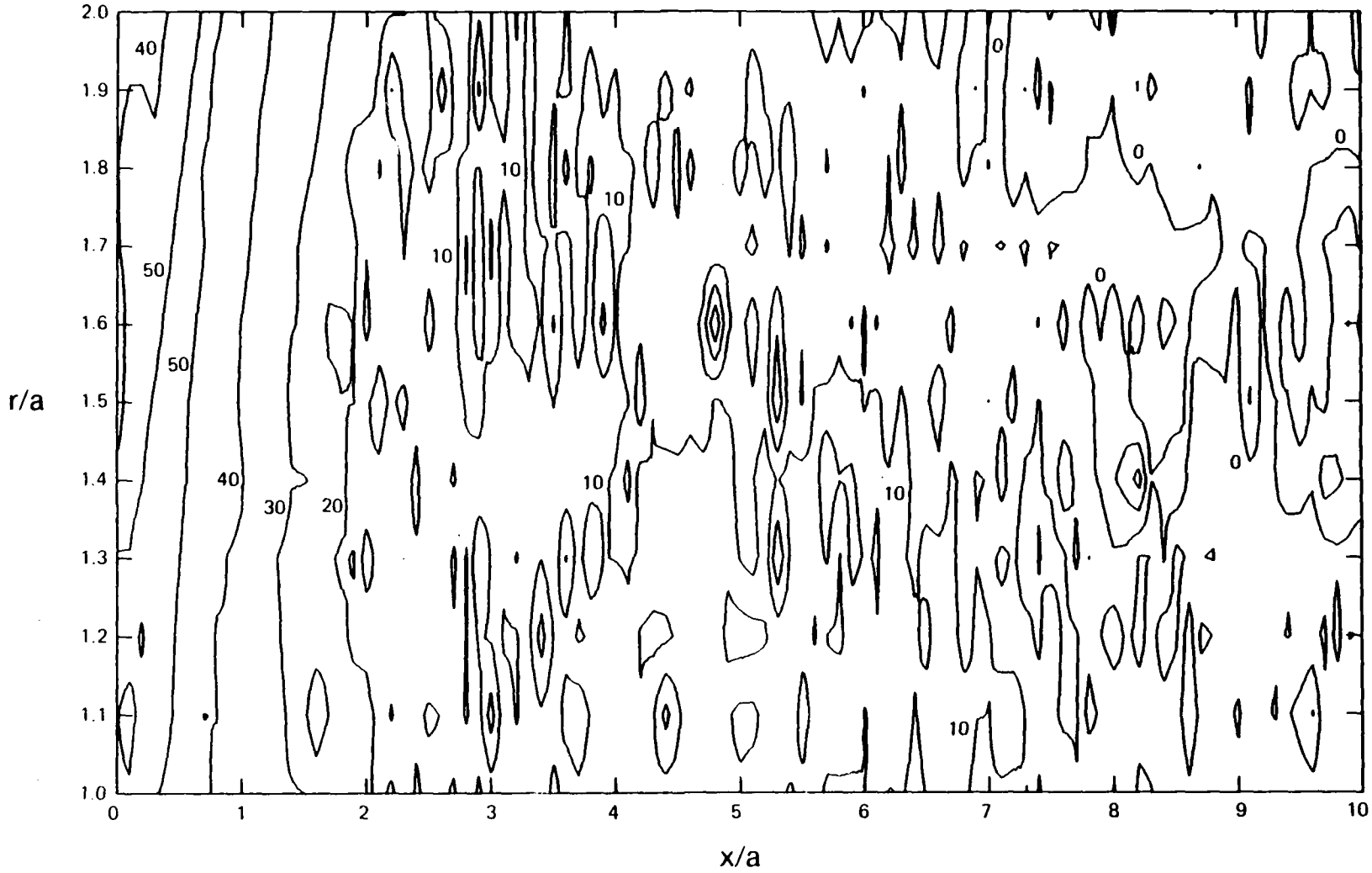

Figure 5.7. Constant magnitude contours of $B_2(r,\theta=0°,x)$ in the acoustic nearfield calculated using Equation (5.10) and expressed in dB re p_{ref} for $\Omega=100$.

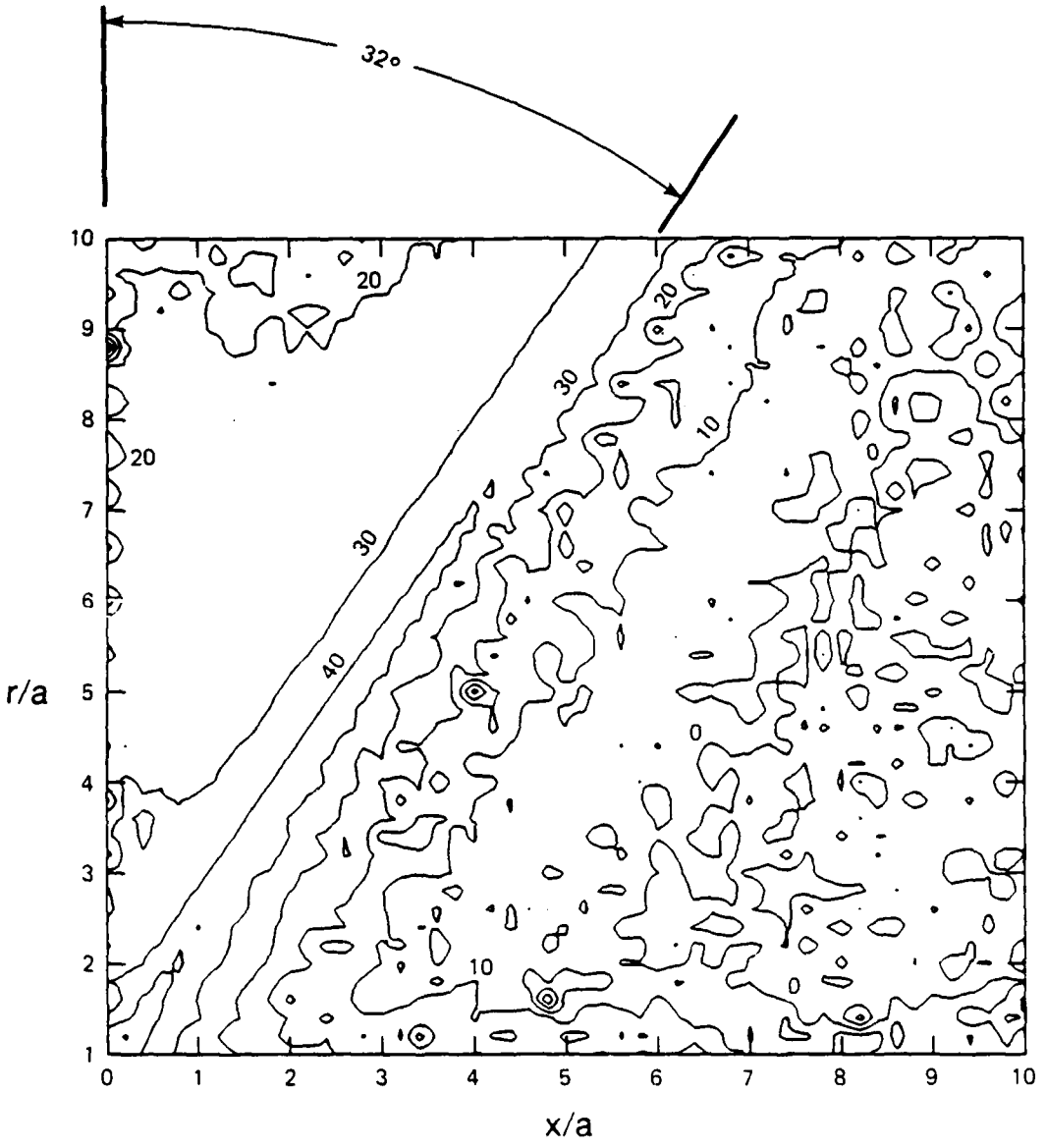

Figure 5.8. Constant magnitude contours of $B_2(r,\theta=0°,x)$ in the acoustic nearfield calculated using Equation (5.10) and expressed in dB re p_{ref} for $\Omega=100$ with radial distance expanded to 10a. The plate coincidence angle occurs at 32° from the normal.

is defined as

$$Q_n(j\xi) = -2 \text{ Im } \{G_n(j\xi)\} \tag{5.18}$$

where Equation (5.11) can be used to define $\text{Im}\{G_n(j\xi)\}$ using the interpretation

$$\gamma = \sqrt{k^2 + \xi^2} \quad . \tag{5.19}$$

Unlike integral B_{2n}, integral B_{1n} will be real at all field points.

Modal convergence of the integrand function $Q_n(j\xi)$ can be demonstrated in a manner similar to $Q_n(\xi)$ except where the radial wavenumber now has the form of Equation (5.19). D'Alembert's ratio test would again yield

$$\lim_{n\to\infty} \left| \frac{Q_{n+1}(j\xi)}{Q_n(j\xi)} \right| = \lim_{n\to\infty} O(n^{-2}) = 0$$

and the Fourier series is again uniformly convergent at large mode order. As before, we can write

$$B_1(r,\theta,x) = p_{ref} \sum_{n=0}^{\infty} \varepsilon_n \cos(n\theta) \int_0^{\infty} Q_n(j\xi)\, e^{-\xi x}\, d\xi$$

$$= p_{ref} \int_0^{\infty} Q(r,\theta,j\xi)\, e^{-\xi x}\, d\xi \quad . \tag{5.20}$$

Figure 5.9 shows a numerical evaluation of the convergence mode N as a function of axial wavenumber for r=a and θ=0 at Ω=1, 10, and 100. Again the numerical data is compared with the estimate N=γa+10. Due to the form of the radial wavenumber, it is expected that N would increase with increasing axial wavenumber, as is shown.

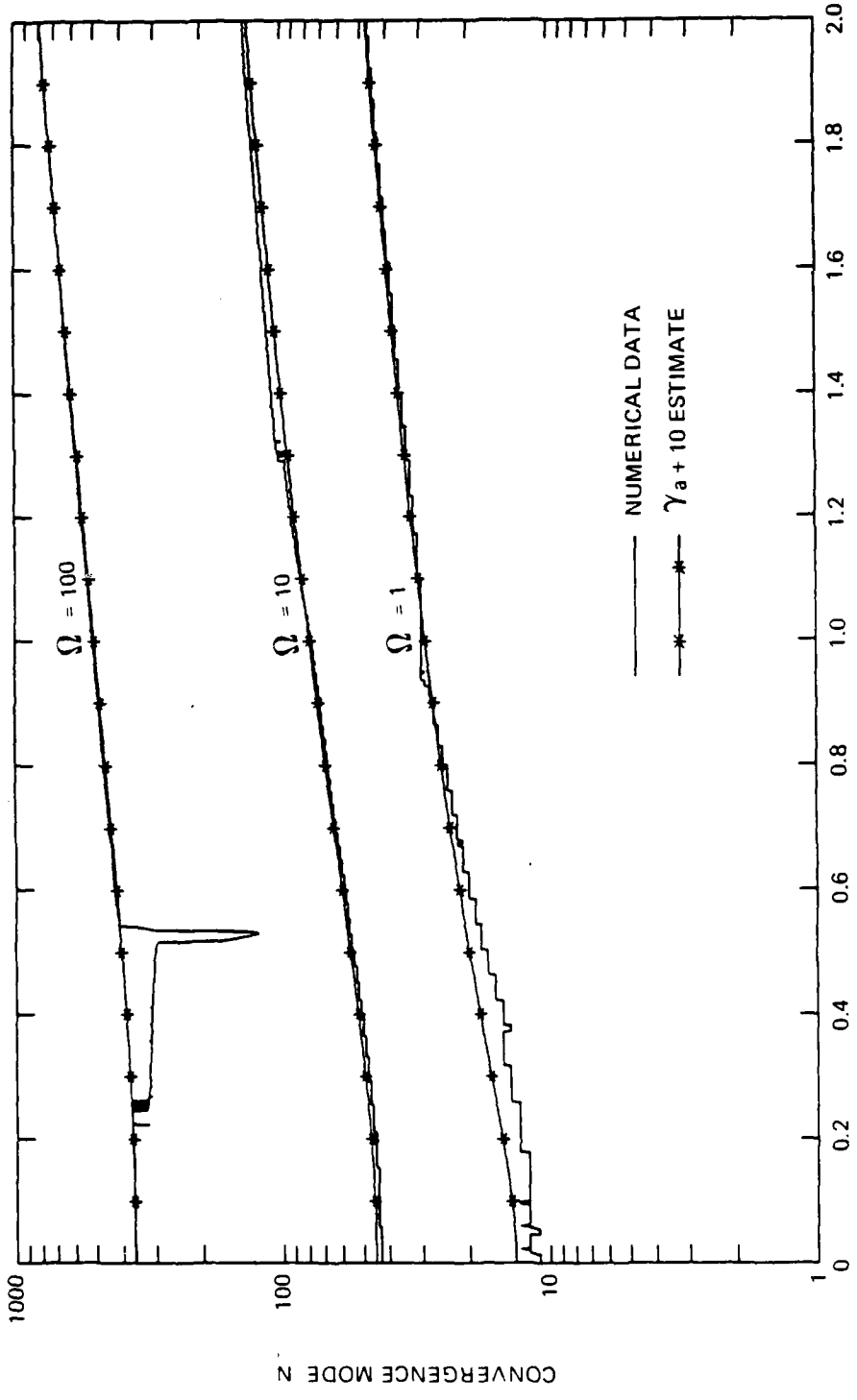

Figure 5.9. Modal truncation value N versus axial wavenumber for the integrand function Q(r=a,θ=0°,jξ) at Ω=1, 10, and 100.

Since the integration interval is semi-infinite, the requirement to consider more and more modal contributions as the integration variable increases would normally lead to an untenable numerical situation. Fortunately, the integrand converges well before modal convergence is a serious issue. Since modal convergence occurs when the argument γa is approximately equal to the order n, for large axial wavenumber where $\xi > k$ and $\xi > k_p$

$$Z_{sn}(j\xi) = O(\xi^4)$$

$$Z_{an}(\gamma) = O(\gamma^{-1}\xi^{1/3}) < \xi^{-2/3}$$

$$Z_{fn}(\gamma r) = O\left(\sqrt{\frac{a}{r}}\ \gamma^{-1}\right) < \sqrt{\frac{a}{r}}\ \xi^{-1}$$

such that

$$Q(j\xi) = O\left(\sqrt{\frac{a}{r}}\ \xi^{-5} e^{-\xi x}\right)$$

at all field points. Convergence will be faster for lower frequency, larger axial distance, or greater radial distance.

As before, integral B_{1n} can generally only be solved numerically. However, if the axial distance is large, an analytic solution is possible based upon Laplace's method. This method states that if the integrand function $Q_n(j\xi)$ is reasonably well behaved and analytic at the origin, as x increases the largest contribution to the integral will come from the vicinity of the origin due to the strength of the decaying exponential term. The integral can therefore be approximated by its behavior near the origin. Examination of $Q_n(j\xi)$ indicates that, except at low frequency, it is a smoothly varying function near the origin with a small (or zero) slope. By expanding $Q_n(j\xi)$ into a Taylor series about

$\xi=0$, it is found that

$$\int_0^\infty Q_n(j\xi)\, e^{-\xi x}\, d\xi = \int_0^\infty \left[Q_n(0) + \xi\, Q_n'(0) + \frac{\xi^2}{2} Q_n''(0) + \ldots \right] e^{-\xi x}\, d\xi$$

$$= x^{-1} Q_n(0) + x^{-2} Q_n'(0) + x^{-3} Q_n''(0) + \ldots \quad . \qquad (5.21)$$

Since both γ and Z_{sn} are even functions of the axial wavenumber, all of the odd ordered derivatives of Q_n are identically zero when evaluated at zero, yielding

$$\int_0^\infty Q_n(j\xi)\, e^{-\xi x}\, d\xi = \frac{1}{x} \left[Q_n(0) + \frac{1}{x^2} Q_n''(0) + \frac{1}{x^4} Q_n^{iv}(0) + \ldots. \right] \quad .$$

For large x and smoothly varying $Q_n(j\xi)$, this series can be truncated after the first term, yielding

$$\lim_{x \to \infty} B_{1n}(r,x) = \frac{1}{x} Q_n(0) \qquad (5.22)$$

where γ can be replaced by the acoustic wavenumber k in the evalution of the integrand function. For additional discussion of the method, reference is made to Carrier, Krook, and Pearson.

Figures 5.10 through 5.13 show a nearfield evaluation of branch integral $B_1(r,\theta=0,x)$ in the plane $\theta=0$ for $\Omega = 0.1$, 1, 10, and 100 using a numerical evaluation of relation (5.20). As was done with integral B_2, the predictions are presented as contours of pressure amplitude in dB referenced to p_{ref} in 10 dB increments. Also shown by dashed lines in Figures 5.11 through 5.13 is a prediction based upon the analytic solution at large axial distance given by Equation (5.22). The analytic solution is a good approximation for $x>a$ except at low frequency.

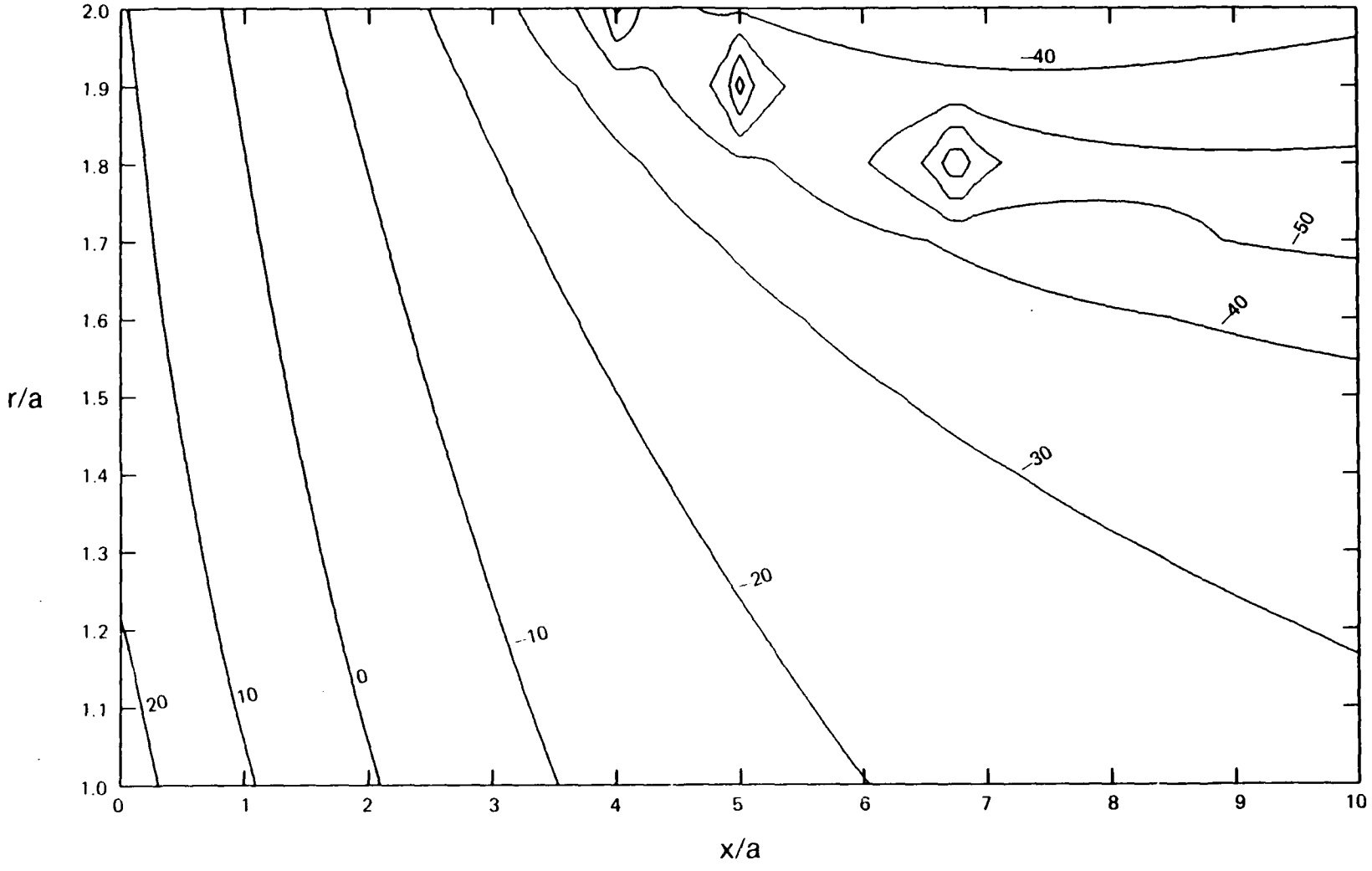

Figure 5.10. Constant magnitude contours of $B_1(r,\theta=0°,x)$ in the acoustic nearfield calculated using Equation (5.17) and expressed in dB re p_{ref} for $\Omega=0.1$.

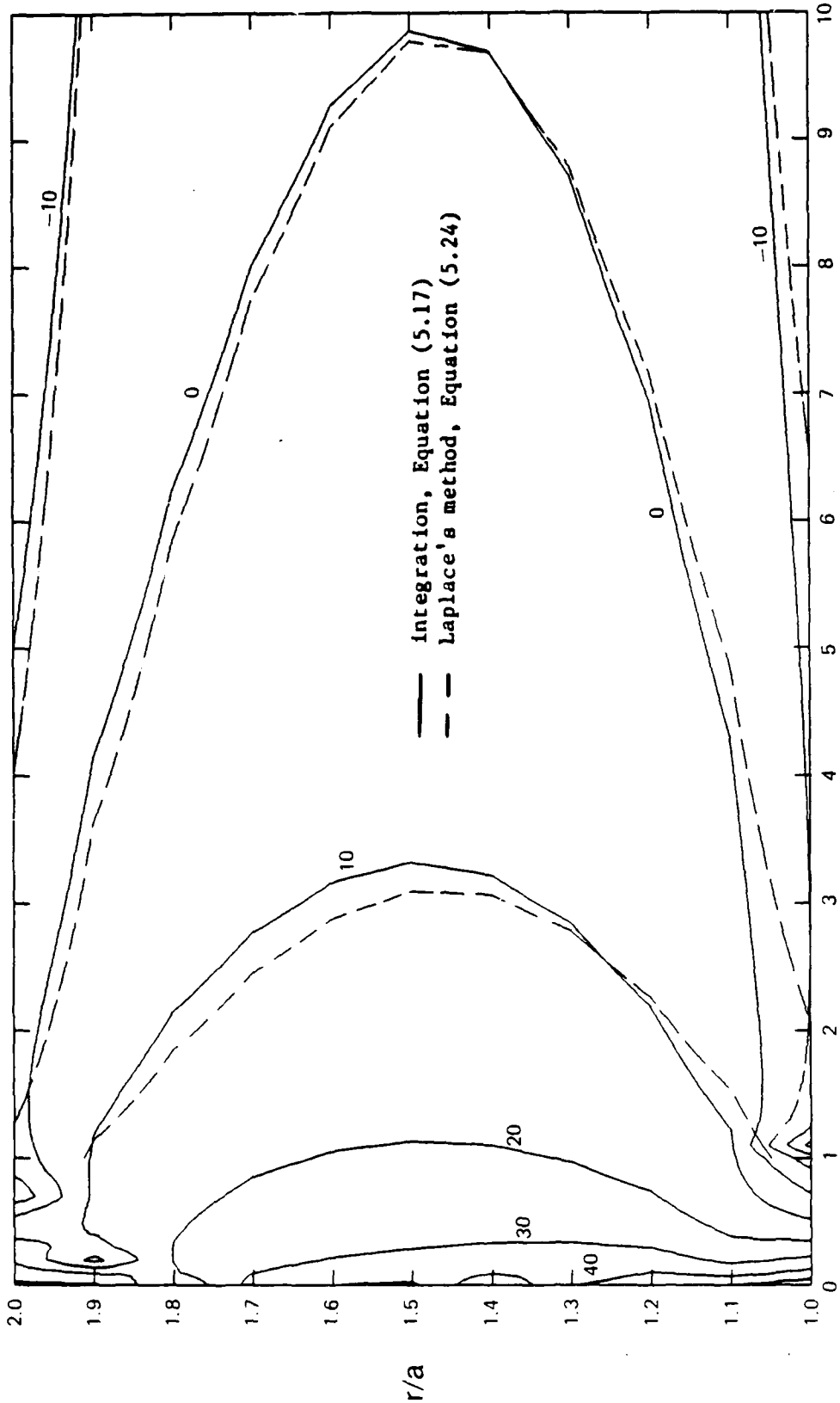

Figure 5.11. Constant magnitude contours of $B_1(r,\theta=0°,x)$ in the acoustic nearfield expressed in dB re p_{ref} for Ω=1.

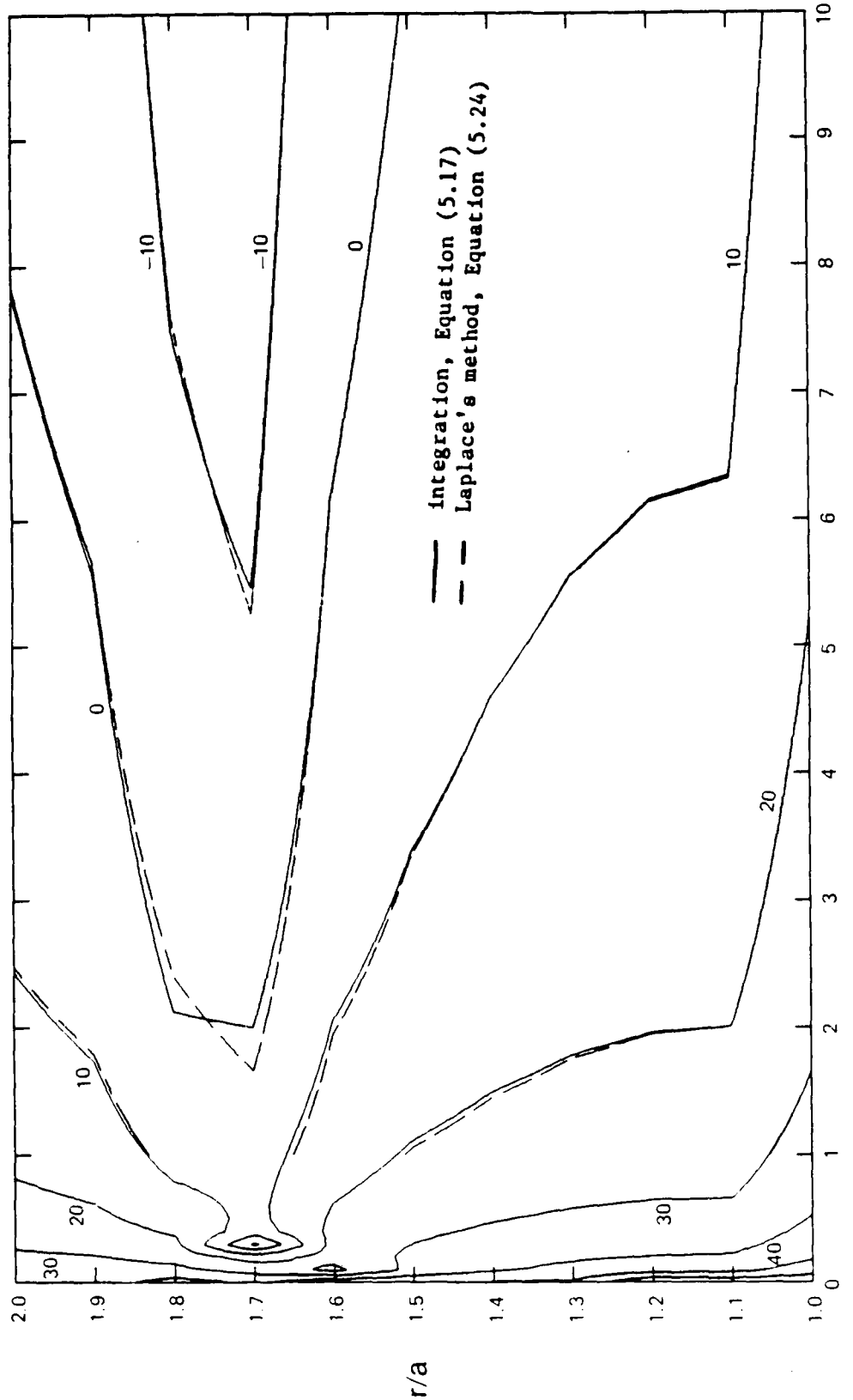

Figure 5.12. Constant magnitude contours of $B_1(r,\theta=0°,x)$ in the acoustic nearfield expressed in dB re p_{ref} for Ω=10.

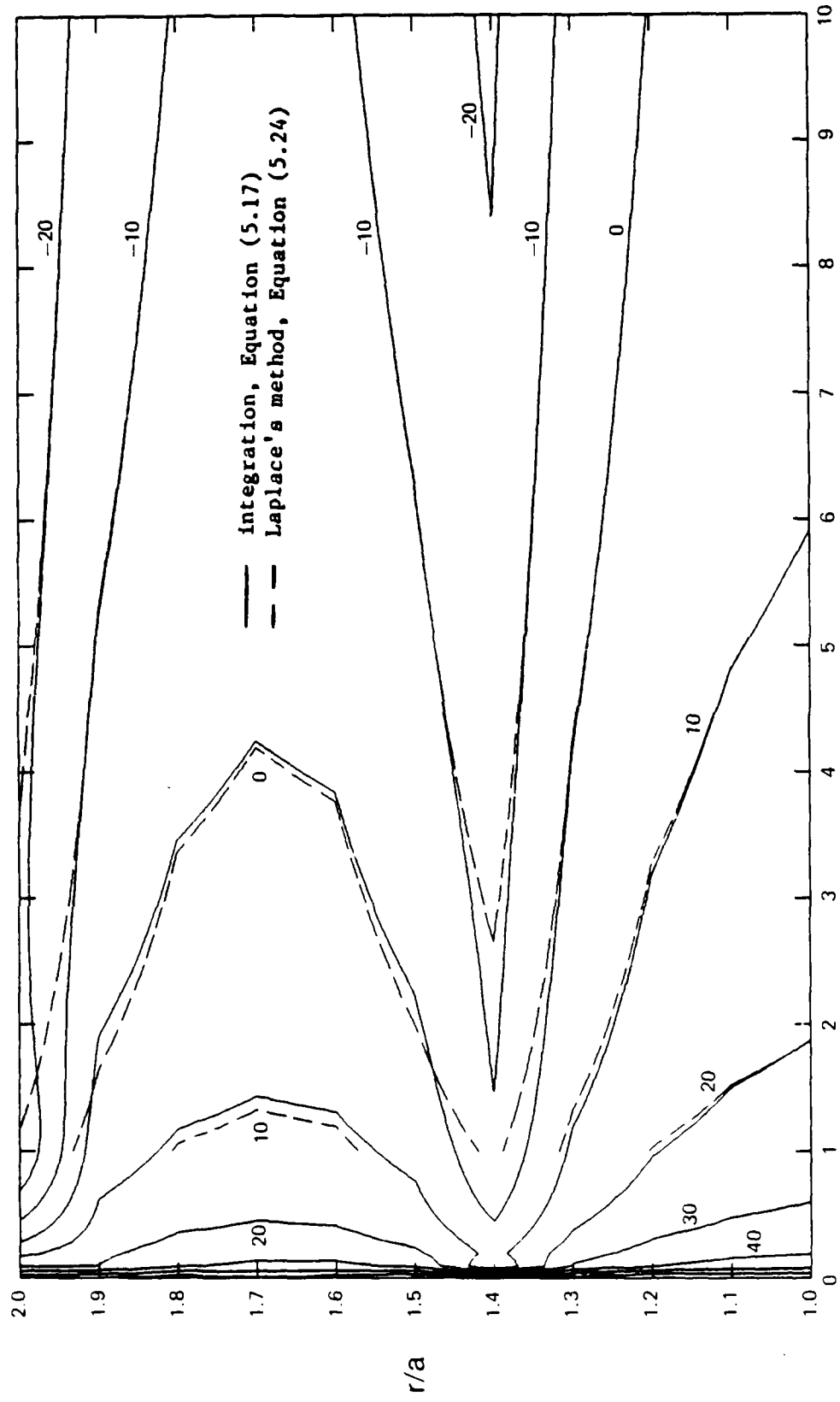

Figure 5.13. Constant magnitude contours of $B_1(r,\theta=0°,x)$ in the acoustic nearfield expressed in dB re p_{ref} for Ω=100.

5.4 Residue Contribution of the Real Singularities

As was mentioned earlier, the residue of a first order singularity is the coefficient of the negative first power term in the Laurent expansion of the integrand about the singularity. For an integrand that is the quotient of two functions, such as Equation (5.2), Hayek (1980) gives the residue about the singularity ξ_o as

$$\text{residue}(\xi_o) = \frac{Z_{fn}(\gamma r)\, e^{j\xi x}}{\frac{\partial}{\partial \xi}\left[Z_{sn}(\xi) + Z_{fn}(\gamma a)\right]} \quad \text{evaluated at } \xi = \xi_o \,. \qquad (5.23)$$

This relation assumes that the singularity is of order one such that the denominator is nonzero.

Evaluation of the residues of both the positive and negative valued pair of real singularities can be performed by considering the Cauchy Principal Value of the integral along the real path R. In order to assure that the formulation represents a progressive wave solution the indentation about the negative valued singularity must lie above the real axis while the indentation about the positive real singularity must lie below the real axis. For further details see Skudrzyk (1971, pp 46-48, 651-56). Only the positive valued singularity would be included within the closed contour of integration and would therefore contribute to the solution. Alternatively, a small amount of structural damping could be included that would cause the singularities to rotate slightly in a counter-clockwise manner. Since the positive valued singularity would move into the first quadrant of the complex ξ-plane, and the negative valued singularity would move into the third quadrant, again only the positive valued singularity would be enclosed by the closed contour of integration and would consequently have a residue contribution. In the limit as the damping goes to zero both methods would yield the same

result. Therefore, at most a single residue contribution due to real singularities exists at a given mode order, where the total contribution to the pressure field is given by

$$\mathrm{Res}(r,\theta,x) = p_{ref} \sum_{n=0}^{N} \varepsilon_n R_n(r,x) \cos(n\theta) \quad . \tag{5.24}$$

The infinite Fourier series has been truncated due to the cutoff frequency behavior discussed in Section 4.7 and shown in Figure 4.14. The modal contribution can be written as

$$R_n(r,x) = \frac{K_n(\gamma r)}{K_n(\gamma a)} \frac{2\pi j \, X_{sn}(\xi) \, e^{j\xi x}}{\frac{a\xi}{\Delta}\left(\frac{n^2}{\gamma^2 a^2} + 1\right) X_{sn}^2(\xi) - X_{sn}'(\xi) - \frac{a\xi\Delta}{\gamma^2}} \tag{5.25}$$

evaluated at $\xi=\xi_o$. In the derivation of this equation, the relation $Z_{sn}(\xi) = -Z_{fn}(\gamma a)$ at $\xi=\xi_o$ which defines the singularities has been used. Since $\xi_o > k$, the radial wavenumber is now taken as a magnitude, or

$$\gamma = \sqrt{\xi^2 - k^2}$$

and the alternative forms of the specific acoustic impedance given by Equation (4.28) have been introduced.

Since the modified Bessel function of the second kind is a monotonically decreasing function, the residue of a real singularity will represent a wave propagating in the axial direction and decaying in the radial direction. This decay will be very rapid for all modes except the axisymmetric and can be approximated by

$$R_n = O\left(\sqrt{\frac{a}{r}} \, e^{-\gamma(r-a)}\right) \quad \text{large } \gamma \text{ for all } n$$

$$R_n = O\left(\left(\frac{a}{r}\right)^n\right) \quad \text{small } \gamma \text{ for } n>0.$$

This second relation would be true for $r<\gamma^{-1}$, beyond which the decay would become even more rapid. For the axisymmetric mode the radial decay is on the order of

$$R_0 = O\left(1 + \frac{\ln r}{\ln \gamma} \right) \qquad \text{small } \gamma$$

which is very slow except in the farfield. In general, the axisymmetric mode would be expected to dominate the residue contribution of the real singularities in the farfield.

The behavior of $\text{Res}(r,\theta=0,x)$ in the nearfield is shown by Figures 5.14 through 5.17 as contours of constant magnitude in dB referenced to p_{ref} for normalized frequency of 0.1, 1, 10, and 100. The radial decay discussed is shown. At frequencies above the plate coincidence frequency, the real residue contribution takes the form of axial standing waves that add little to the acoustic field.

5.5 Residue Contribution of the Complex Singularities

Of all of the complex singularities which exist, only those above the real axis on the top Riemann sheet are of interest. As was shown in the last chapter, complex singularities must exist as a pair symmetric about the imaginary axis. For a complex singularity in the first quadrant of the complex ξ-plane denoted by

$$\xi_1 = \xi_r + j\xi_i$$

such that

$$\gamma_1 = \gamma(\xi_1) = \gamma_r + j\gamma_i$$

the residue would be given by Equation (5.23). If the symmetric singularity in the second quadrant

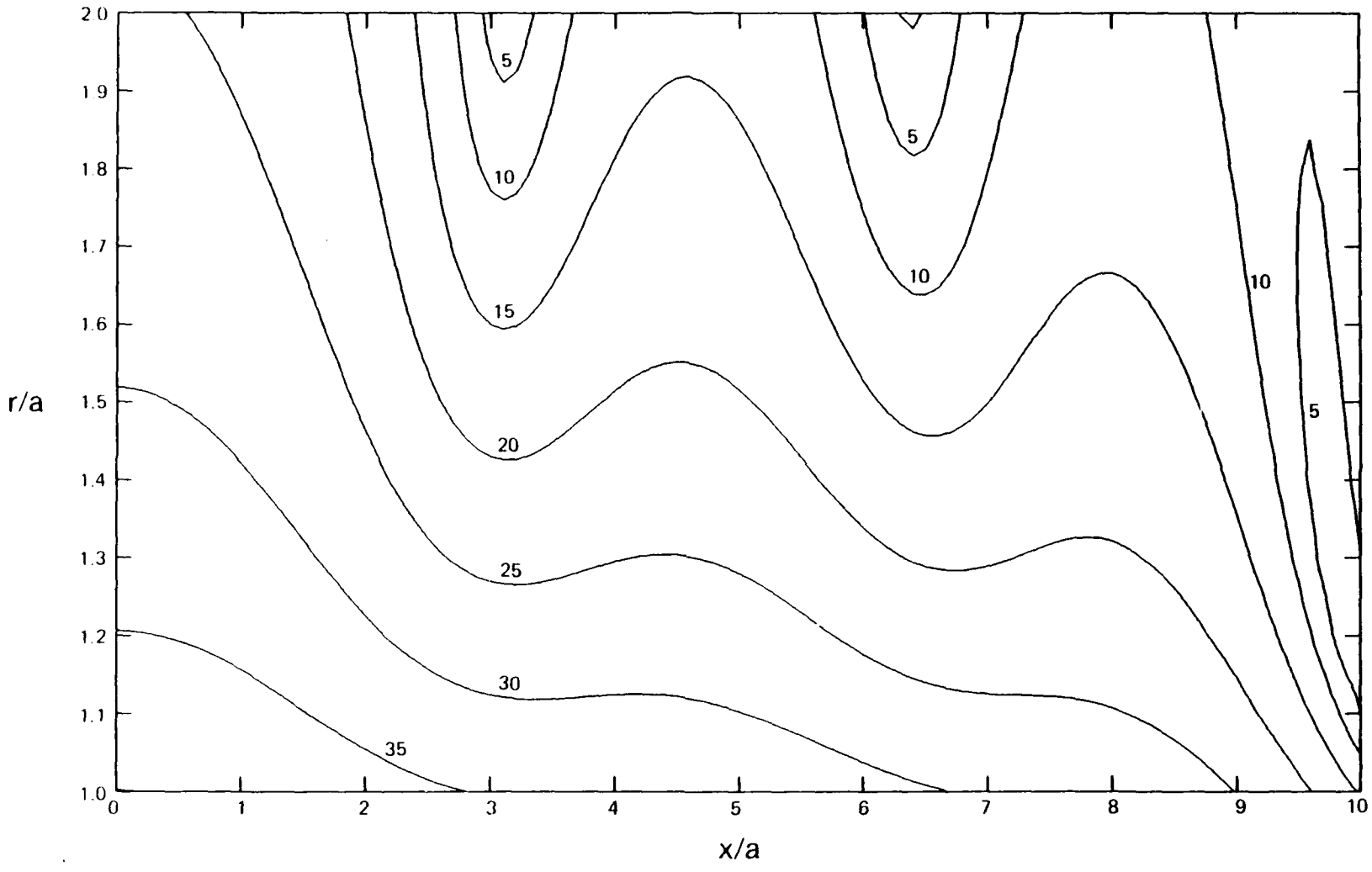

Figure 5.14. Constant magnitude contours of Res(r,θ=0°,x) in the acoustic nearfield expressed in dB re p_{ref} for Ω=0.1. Curves also represent the nearfield acoustic pressure p(r,θ=0°,x).

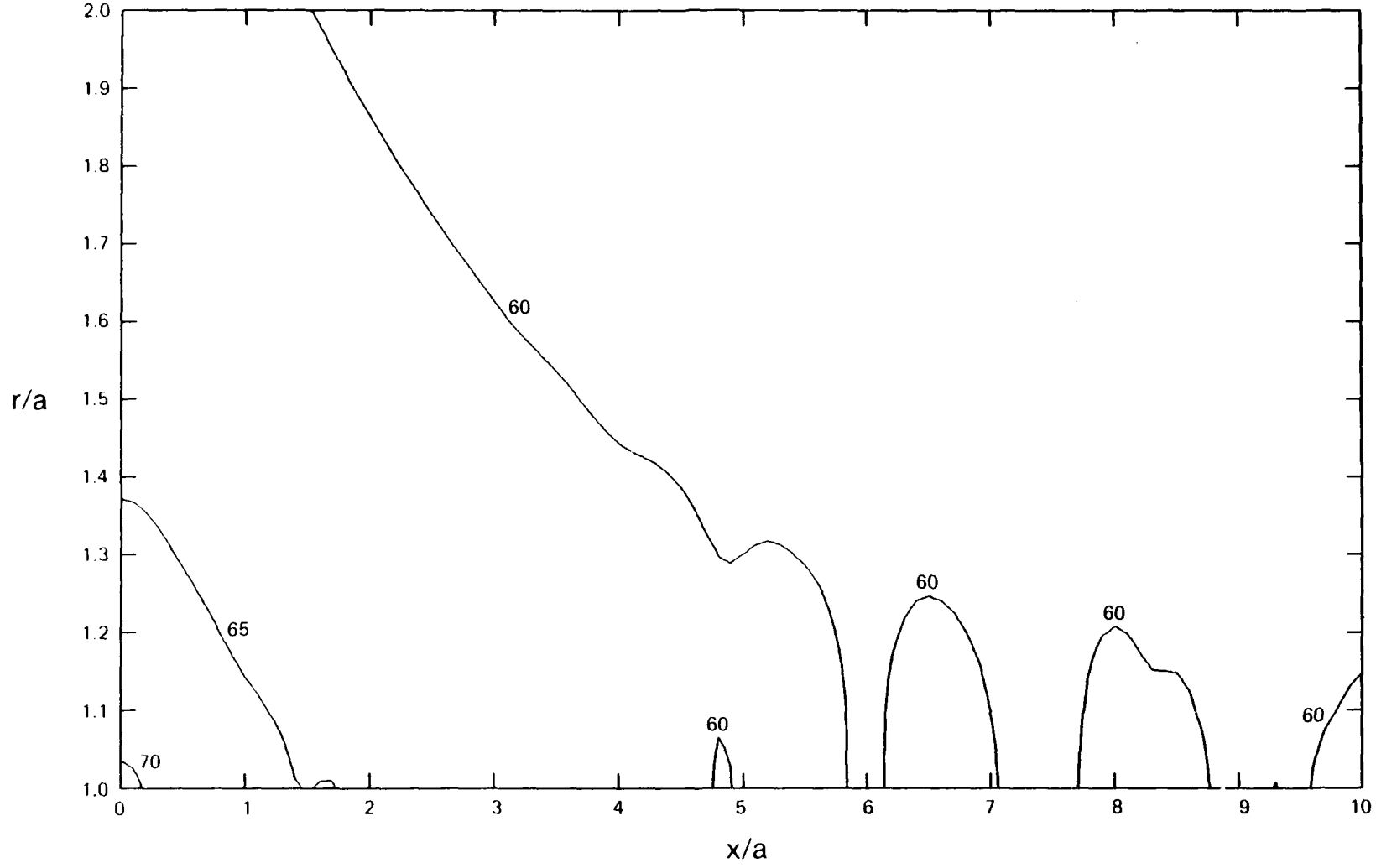

Figure 5.15. Constant magnitude contours of Res(r,θ=0°,x) in the acoustic nearfield expressed in dB re p_{ref} for Ω=1. Curves also represent the nearfield acoustic pressure p(r,θ=0°,x).

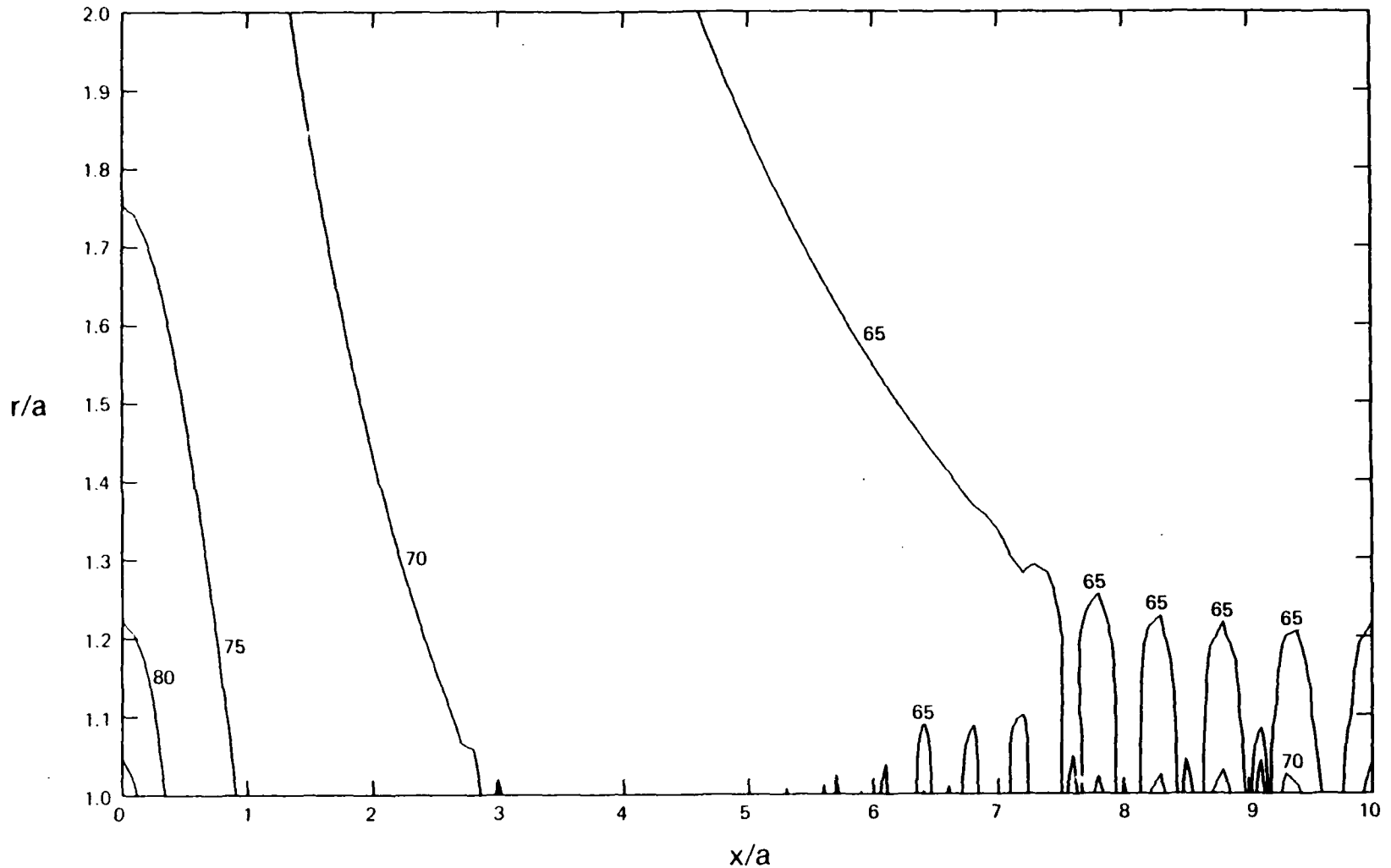

Figure 5.16. Constant magnitude contours of Res(r,θ=0°,x) in the acoustic nearfield expressed in dB re p_{ref} for Ω=10. Curves also represent the nearfield acoustic pressure p(r,θ=0°,x).

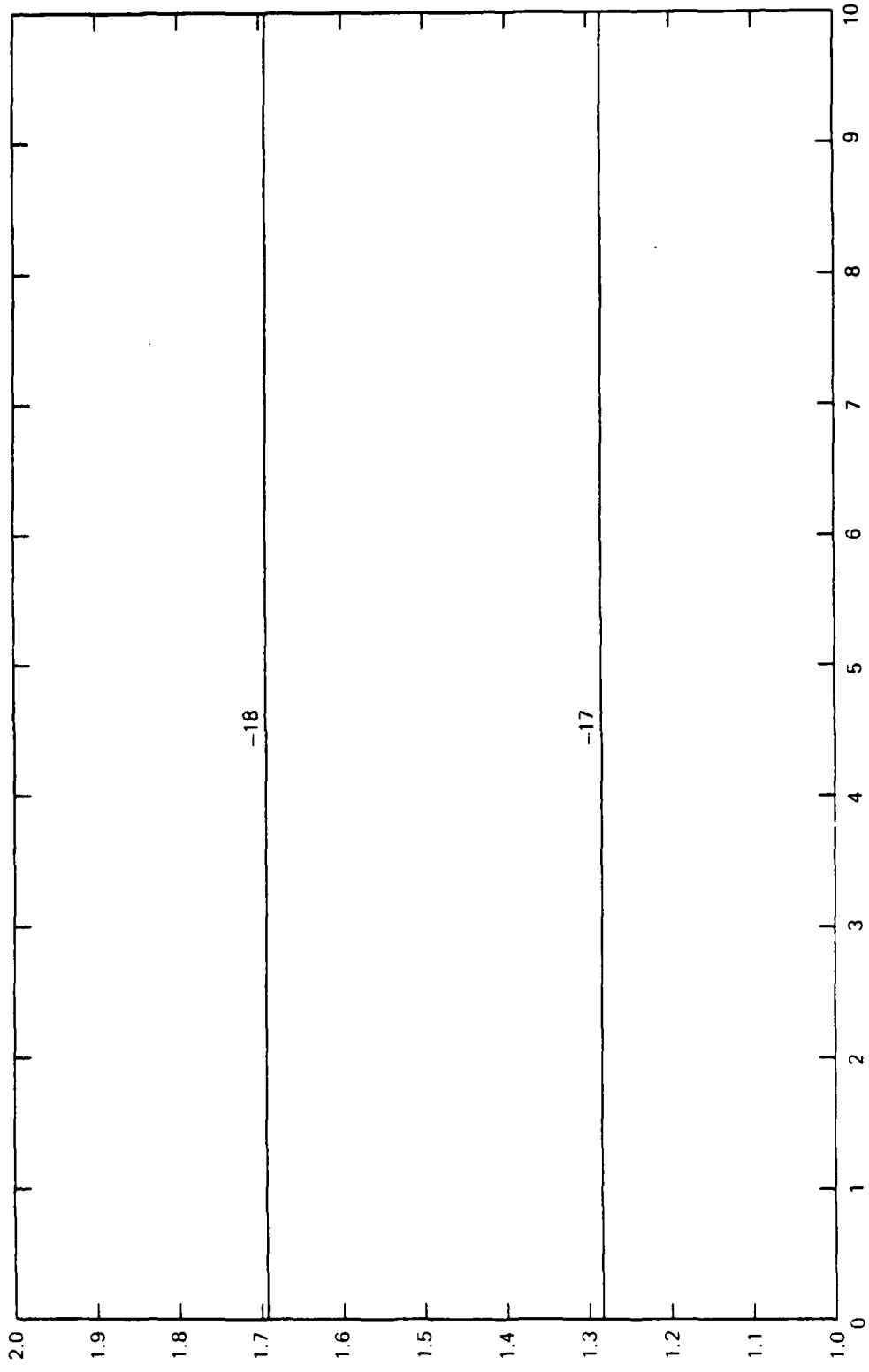

Figure 5.17. Constant magnitude contours of Res(r,θ=0°,x) in the acoustic nearfield expressed in dB re p_{ref} for Ω=100.

$$\xi_2 = -\xi_1^*$$

is also considered, it can be shown that

$$\text{residue}(\xi_2) = -\text{residue}^*(\xi_1)$$

such that the sum of the pair is

$$\text{residue}(\xi_1) + \text{residue}(\xi_2) = 2j\ \text{Im}\{\text{residue}(\xi_1)\}\ .$$

The sum of the symmetric pair of complex singularities would yield an imaginary result.

On a modal basis, the pair would have a contribution

$$C_n(r,x) = 4\pi\ \text{Im}\left\{ \frac{H_n(\gamma r)}{H_n(\gamma a)} \frac{X_{sn}(\xi)\ e^{j\xi x}}{\frac{a\xi}{\Delta}\left(\frac{n^2}{\gamma^2 a^2} - 1\right) X_{sn}^2(\xi) - X_{sn}'(\xi) - \frac{a\xi\Delta}{\gamma^2}} \right\} \qquad (5.26)$$

evaluated at $\xi = -\xi_1$ where $\pi/2 \leq \arg(\gamma) \leq \pi$.

Since the residue contribution is proportional to $\exp(-\xi_i x)$, complex singularities will represent waves that decay axially . At either large radial distance or radial wavenumber, C_n will also be proportional to $\exp(-\gamma_i r)$ and exhibit strong radial decay. As an example, the complex branch denoted as L_1 discussed in section 4.8 would exhibit this behavior. Complex singularities will contribute little to the solution if the axial distance, radial distance, ξ_i, or γ_i are not all small. In general, one or more of these conditions can be expected to exist except at frequencies just below the lower cutoff frequency and field points very close to the point of excitation. Therefore, the contribution of the complex singularities will be ignored.

5.6 Nearfield Acoustic Pressure

Examination of the previous results reveals that for frequencies below the plate coincidence frequency the magnitude of the real residue contribution dominates the branch line integral contributions by at least 15 dB at all field points shown. This result is also valid for nonzero θ. Therefore, in this region the acoustic pressure can be approximated by

$$p(r,\theta,x) = \mathrm{Res}(r,\theta,x) = p_{ref} \sum_{n=0}^{N} \varepsilon_n R_n(r,x) \cos(n\theta) \qquad (5.27)$$

where the much more complicated expression given by Equation (5.1) has been replaced by a finite series. Therefore, Figures 5.14 through 5.16 also represent the nearfield pressure. As can be seen, the pressure magnitude maintains a value within 20 dB of the driving-point pressure over most of the acoustic nearfield.

At frequencies above the plate coincidence frequency the nearfield pressure is dominated by the branch line integrals, primarily B_2. Figure 5.18 shows the acoustic nearfield pressure calculated at a normalized frequency of 100. The coincidence angle effect and the overall character are similar to the results shown in Figure 5.7 for B_2. Note that except for the coincidence beam region, the magnitude of the nearfield pressure is at least 30 dB down from the driving-point value.

The surface pressure field is also of interest. Figures 5.19 through 5.22 show the pressure at r=a for Ω=0.1, 1, 10, and 100. The circumferential coordinate ranges from zero to π and the pressure field is symmetric about the θ=0 plane. Although not shown, the real residue contribution dominates the surface pressure field at frequencies below the plate coincidence frequency while the branch line integrals, again

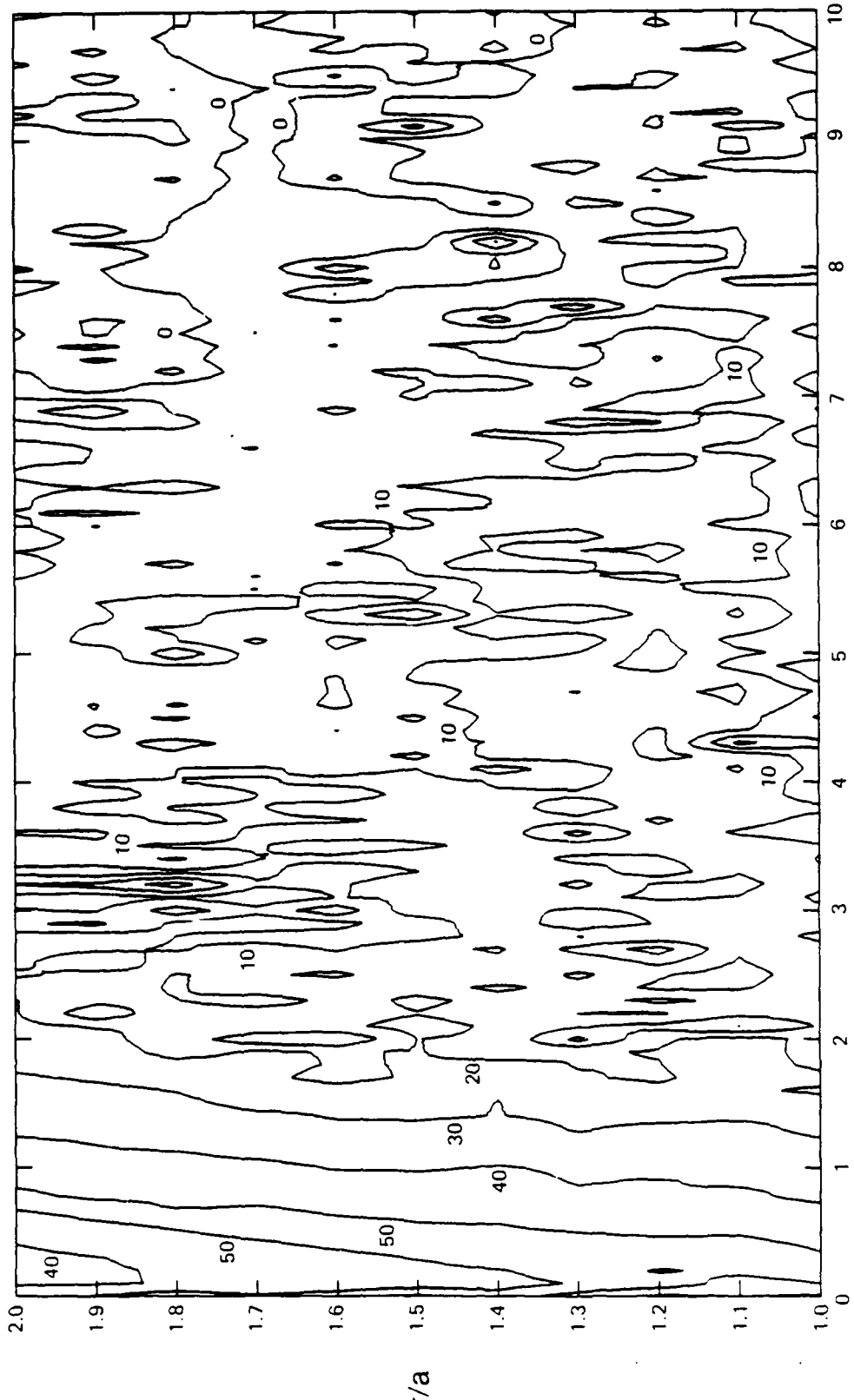

Figure 5.18. Constant magnitued contours of the nearfield acoustic pressure $p(r,\theta=0°,x)$ expressed in dB re p_{ref} for $\Omega=100$.

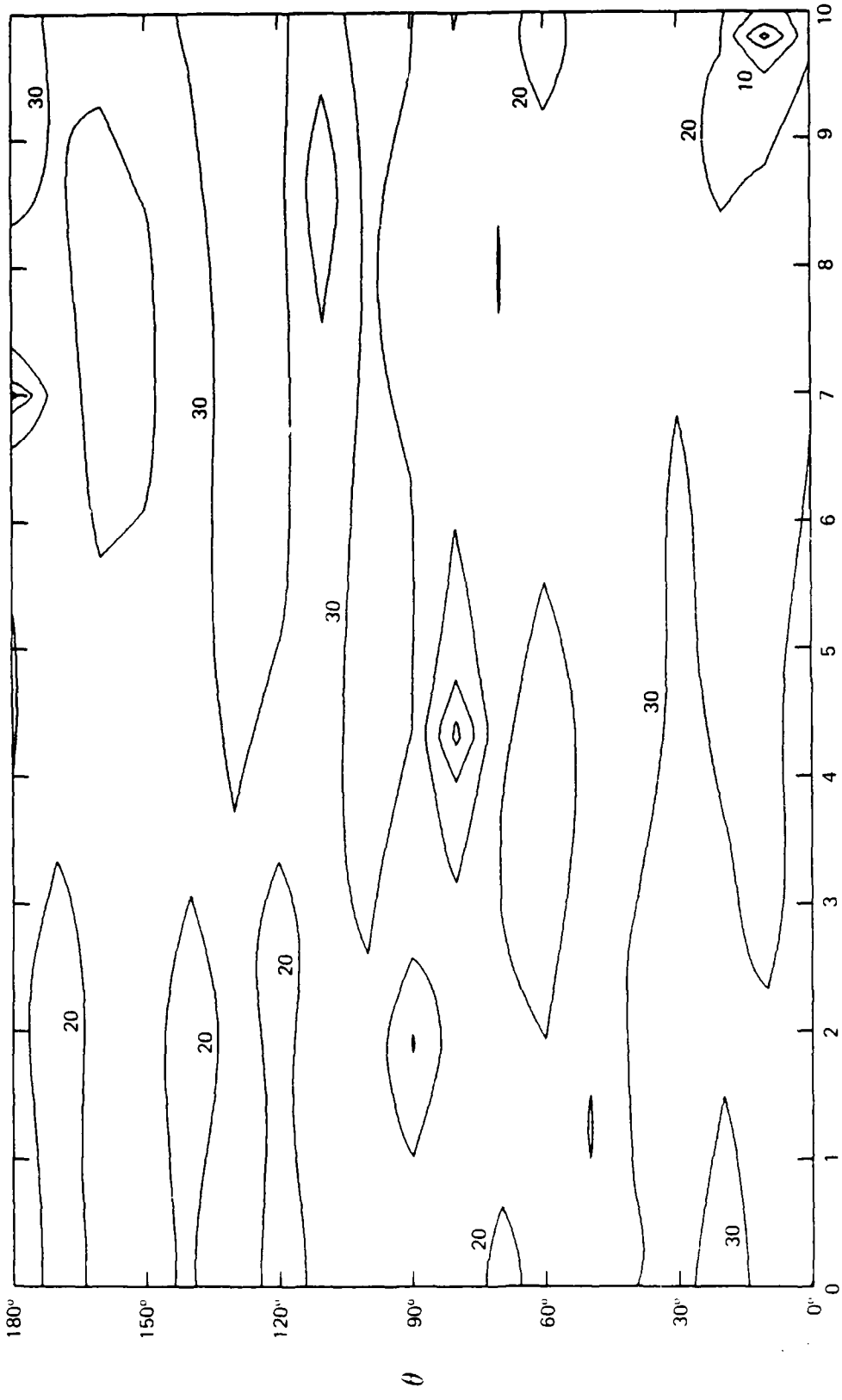

Figure 5.19. Constant magnitude contours of p(r=a,θ,x) on the surface of the cylindrical shell expressed in dB re p_{ref} for Ω=0.1.

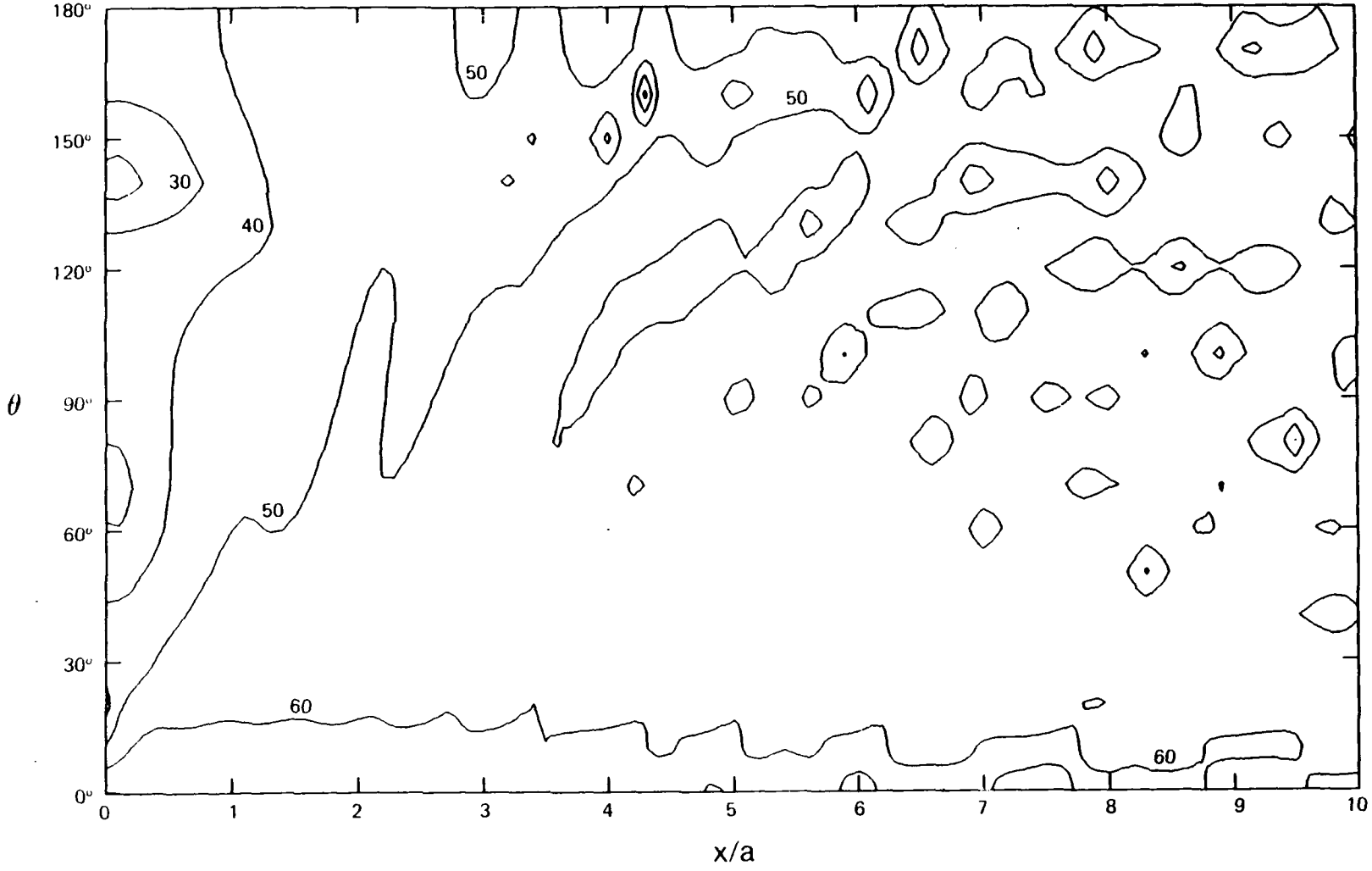

Figure 5.20. Constant magnitude contours of p(r=a,θ,x) on the surface of the cylindrical shell expressed in dB re p_{ref} for Ω=1.

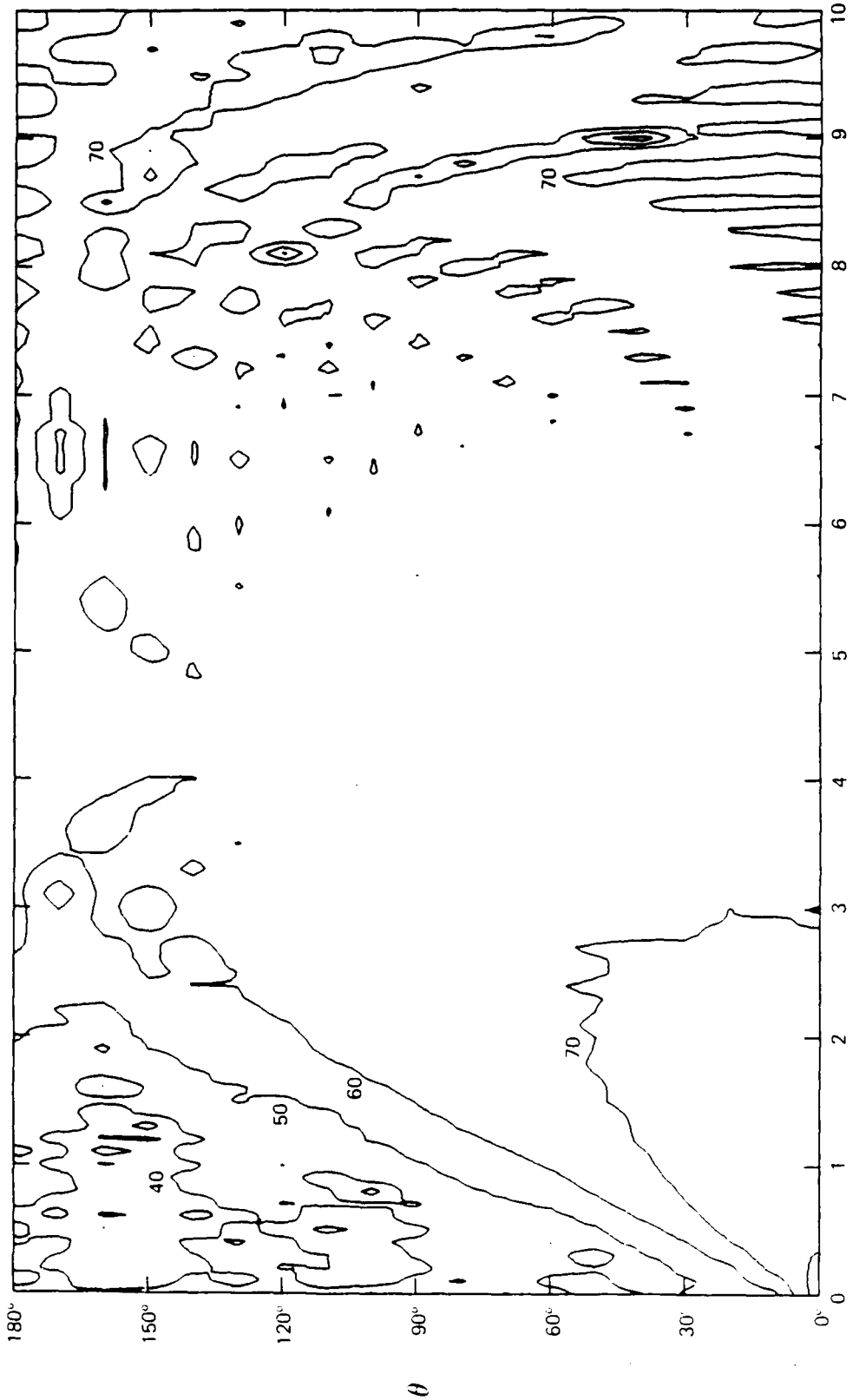

Figure 5.21. Constant magnitude contours of $p(r=a,\theta,x)$ on the surface of the cylindrical shell expressed in dB re p_{ref} for Ω=10.

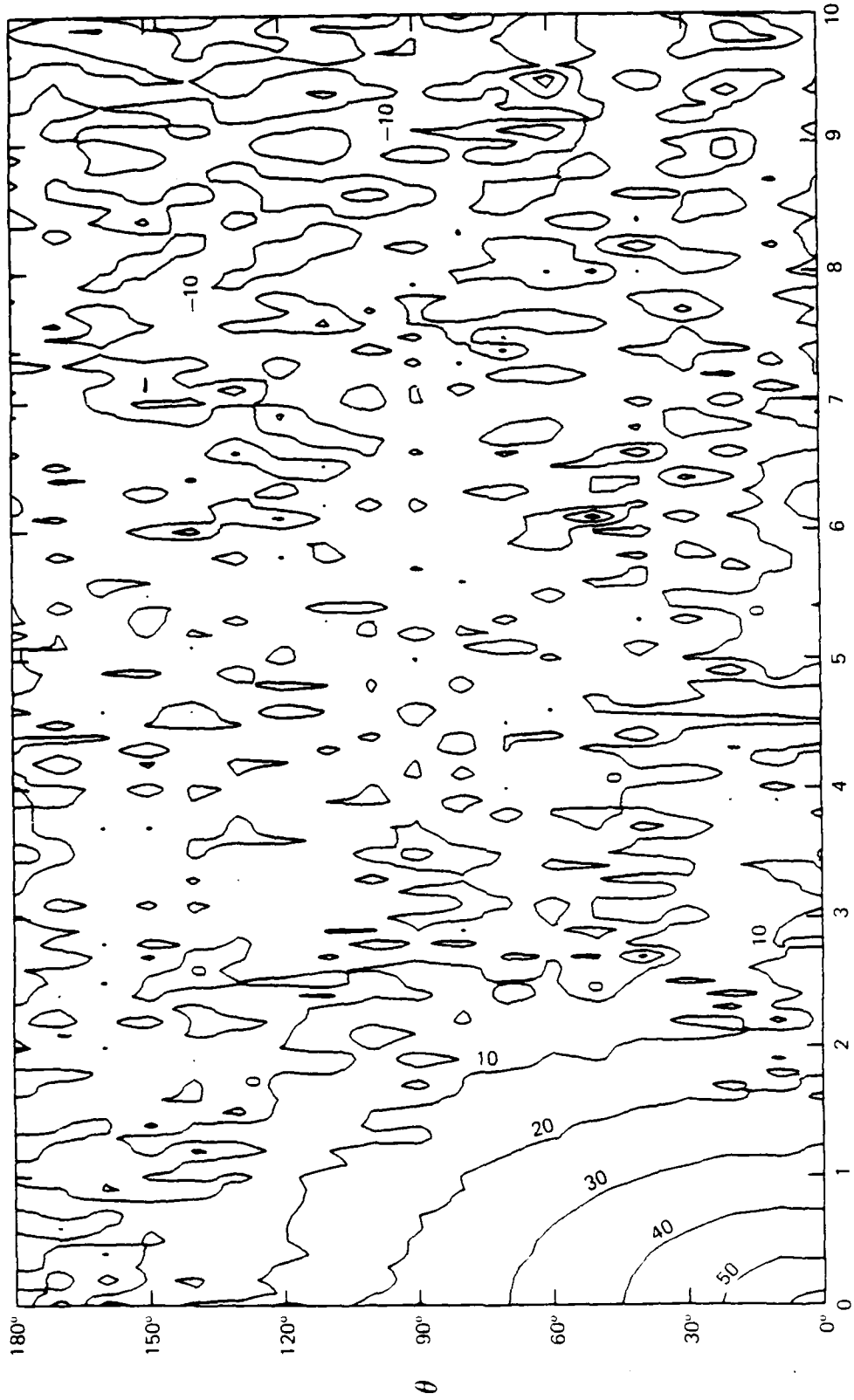

Figure 5.22. Constant magnitude contours of p(r=a,θ,x) on the surface of the cylindrical shell expressed in dB re P_{ref} for Ω=100.

primarily B_2, dominate the field at higher frequencies. For frequencies below the plate coincidence frequency the surface pressure field maintains a magnitude within 20 dB of the driving-point value over most of the cylinder surface. At higher frequencies the surface pressure field is similar to that for a point-excited plate.

5.7 The Fluid-Loaded Displacement Field

The cylindrical shell's radial displacement is given in terms of integral relation (4.20). The form is very similar to that of the acoustic pressure and it can be solved by similar techniques. For

$$w(\theta,x) = w_{ref} \sum_{n=0}^{\infty} \varepsilon_n \cos(n\theta) \int_{-\infty}^{+\infty} g_n(\xi)\, e^{j\xi x}\, d\xi \qquad (5.28)$$

where

$$g_n(\xi) = \frac{j\rho_s c_p h/\Omega}{Z_{sn}(\xi) + Z_{fn}(\gamma a)} = \frac{1}{X_{sn}(\xi) + \Delta Z_{an}(\gamma)} \quad ,$$

Cauchy's theorem can again be employed to solve the integral, yielding

$$w(\theta,x) = res(\theta,x) - b_1(\theta,x) - b_2(\theta,x) \quad . \qquad (5.29)$$

The contribution over paths Γ_3, C_1, and C_2 is again zero by application of Jordon's Lemma.

The contribution over branch paths Γ_2 and Γ_4 is now written as

$$b_2(\theta,x) = w_{ref} \sum_{n=0}^{\infty} \varepsilon_n \cos(n\theta) \int_{0}^{k} q_n(\xi)\, e^{j\xi x}\, d\xi \qquad (5.30)$$

where

$$q_n(\xi) = j \frac{\rho_s c_p h}{\Omega} \frac{Z_{fn}(\gamma a) + Z_{fn}^*(\gamma a)}{Z_{sn}^2(\xi) + Z_{sn}(\xi)\left[Z_{fn}(\gamma a) - Z_{fn}^*(\gamma a)\right] - \left|Z_{fn}(\gamma a)\right|^2}$$

and where the radial wavenumber has zero phase. For zero structural damping $q_n(\xi)$ reduces to

$$q_n(\xi) = -2j \ \mathrm{Im}\{g_n(\xi)\} \ .$$

An analytic solution exists at low frequency that follows the development of Equations (5.12) and (5.13), but where now the constants are specified to be

$$A_0 = - \frac{\Delta a \pi}{[1 + \Delta a \ \ln(ka)]^2}$$

$$A_n = -j \frac{4 \Delta a \pi}{(n!)^2 (n X_{sn} - \Delta a)^2} \left(\frac{a}{2}\right)^{2n}$$

for $n>0$. Similarly, the contribution over branch paths Γ_1 and Γ_5 can be designated as

$$b_1(\theta,x) = w_{ref} \sum_{n=0}^{\infty} \varepsilon_n \cos(n\theta) \int_0^{\infty} q_n(j\xi) \ e^{-\xi x} \ d\xi \qquad (5.31)$$

where for an undamped cylindrical shell

$$q_n(j\xi) = -2 \ \mathrm{Im}\{g_n(j\xi)\}$$

with the interpretation

$$\gamma = \sqrt{k^2 + \xi^2} \ .$$

As before, an analytic solution of the integral exists at large axial distance based upon Laplace's method which yields

$$\int_0^{\infty} q_n(j\xi) \ e^{-\xi x} \ d\xi \simeq \frac{1}{x} \ q_n(0)$$

at large axial distance.

The real residue contribution to the fluid-loaded radial displacement field is given by

$$res(\theta,x) = w_{ref} \sum_{n=0}^{N} \varepsilon_n \, r_n(x) \cos(n\theta) \tag{5.32}$$

where the modal residue term

$$r_n(x) = \frac{-2\pi j \, e^{j\xi x}}{\frac{a\xi}{\Delta}\left(\frac{n^2}{\gamma^2 a^2} + 1\right) X_{sn}^2(\xi) - X_{sn}'(\xi) - \frac{a\xi\Delta}{\gamma^2}} \tag{5.33}$$

is evaluated at the real residue. Again the radial wavenumber has been implicitly specified as the magnitude

$$\gamma = \sqrt{\xi^2 - k^2}$$

in the region $\xi_o > k$. As was done with the acoustic pressure solution, the contribution due to complex singularities is considered small and is ignored in the radial displacement solution.

The normalized cylinder displacement field for driving frequencies of 0.1, 1, 10, and 100 is shown in Figures 5.23 through 5.26. As would be expected, they display similar behavior to the surface pressure field. Although the individual contributions due to the branch line integrals and real residues are not presented, again the residues dominate the solution below coincidence frequency while the branch line integral b_2 dominates the solution at higher frequency.

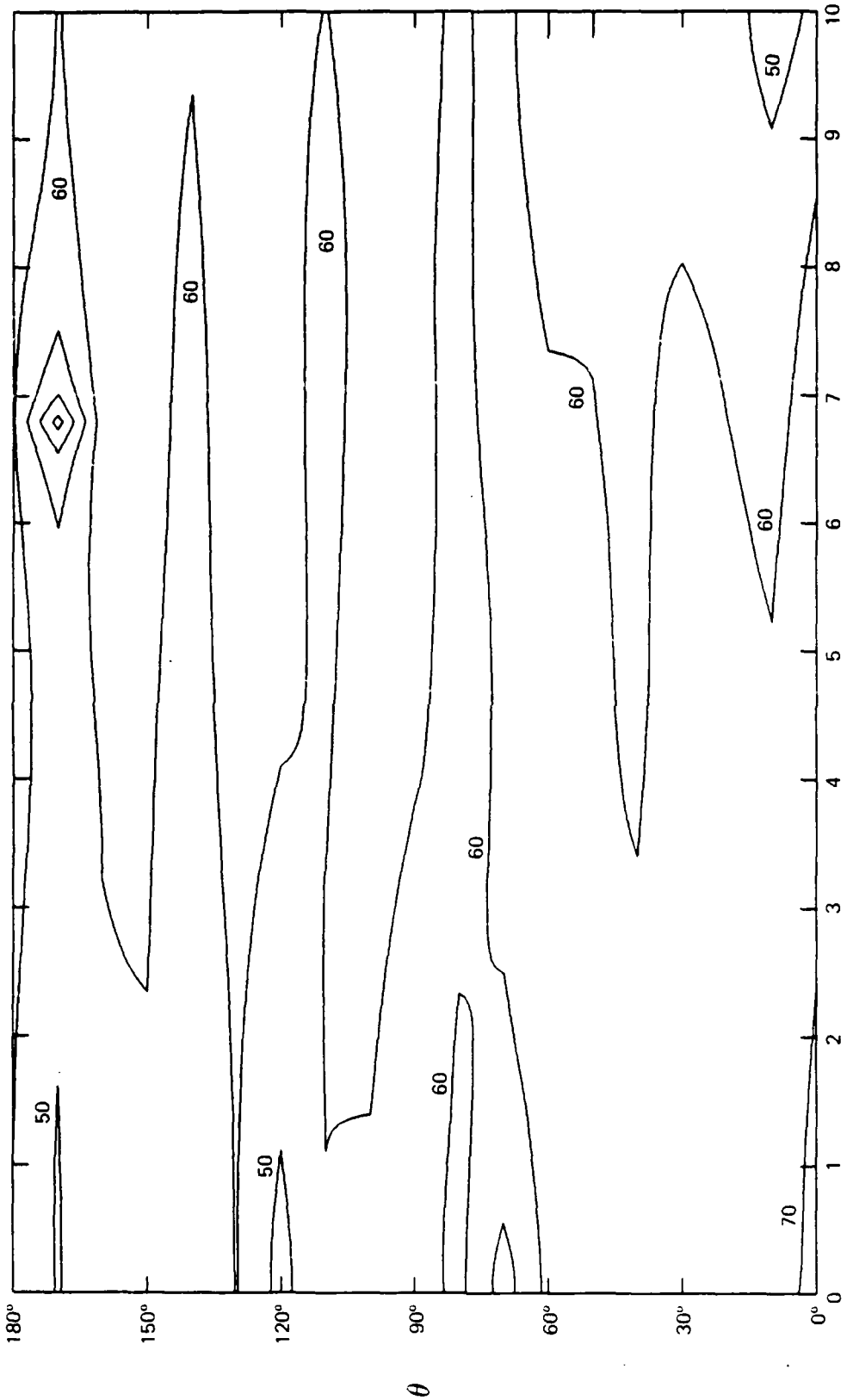

Figure 5.23. Constant magnitude contours of the shell displacement $w(\theta,x)$ expressed in dB re w_{ref} for Ω=0.1.

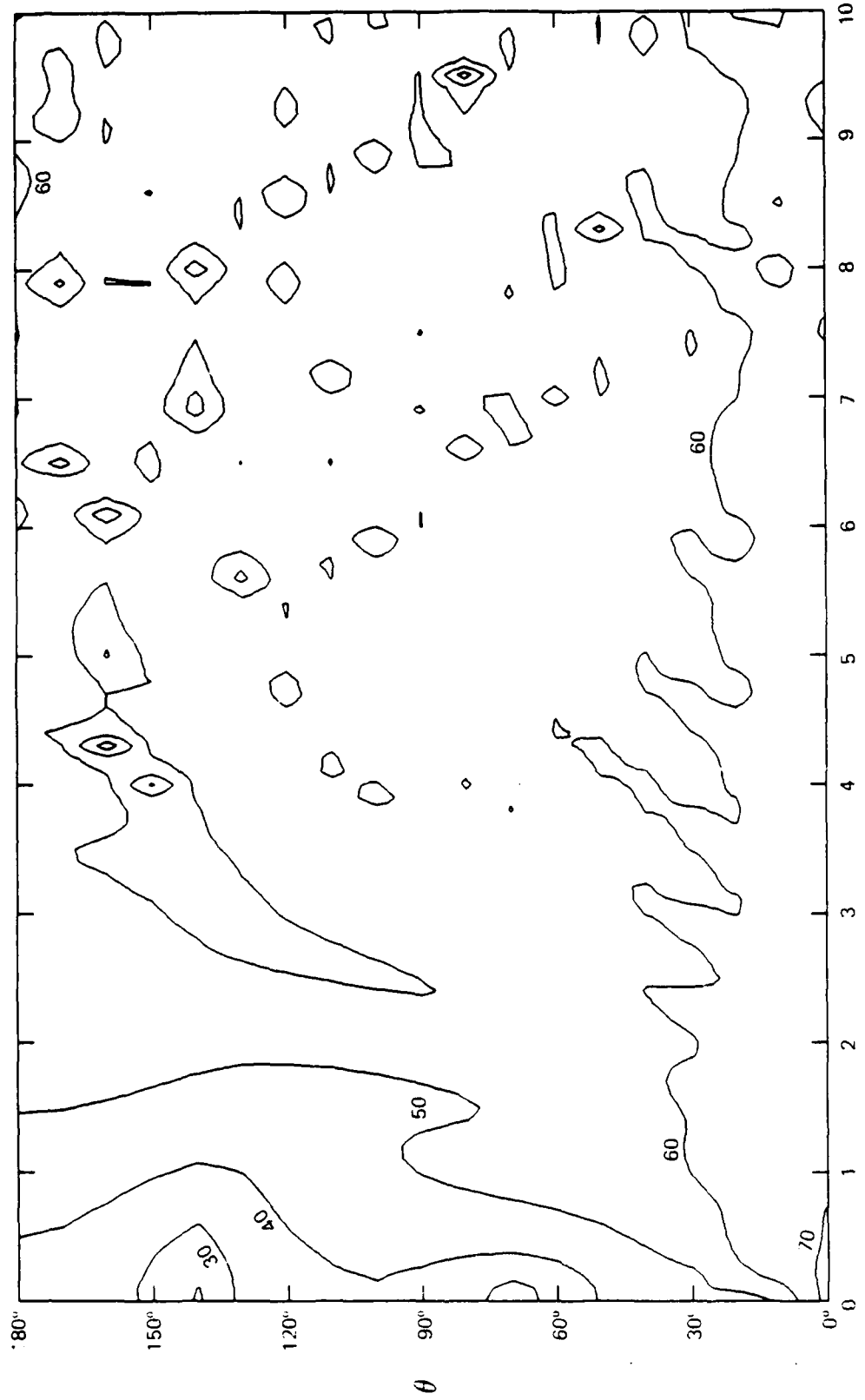

Figure 5.23. Constant magnitude contours of the shell displacement $w(\theta,x)$ expressed in dB re w_{ref} for Ω=0.1.

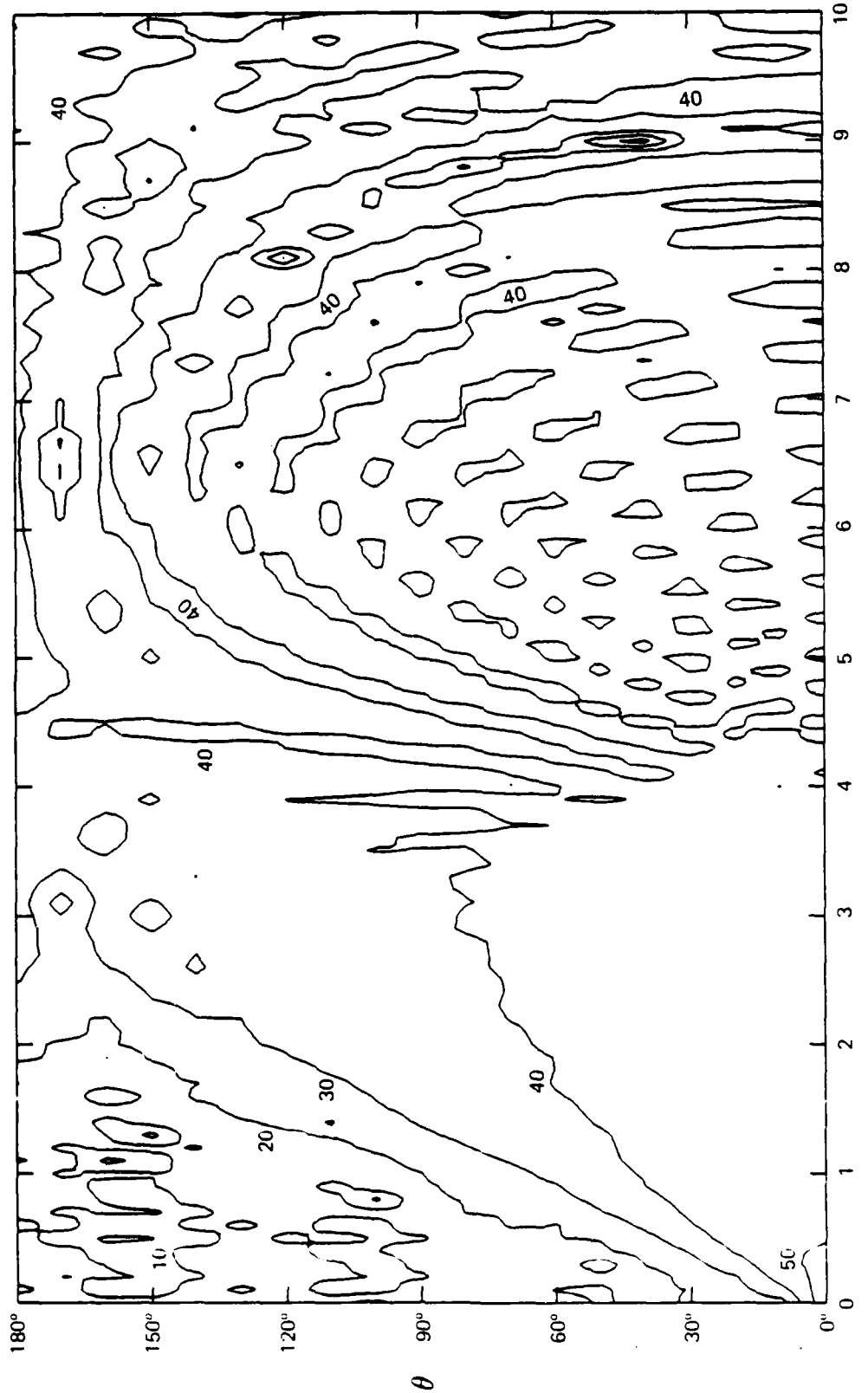

Figure 5.25. Constant magnitude contours of the shell displacement $w(\theta,x)$ expressed in dB re w_{ref} for Ω=10.

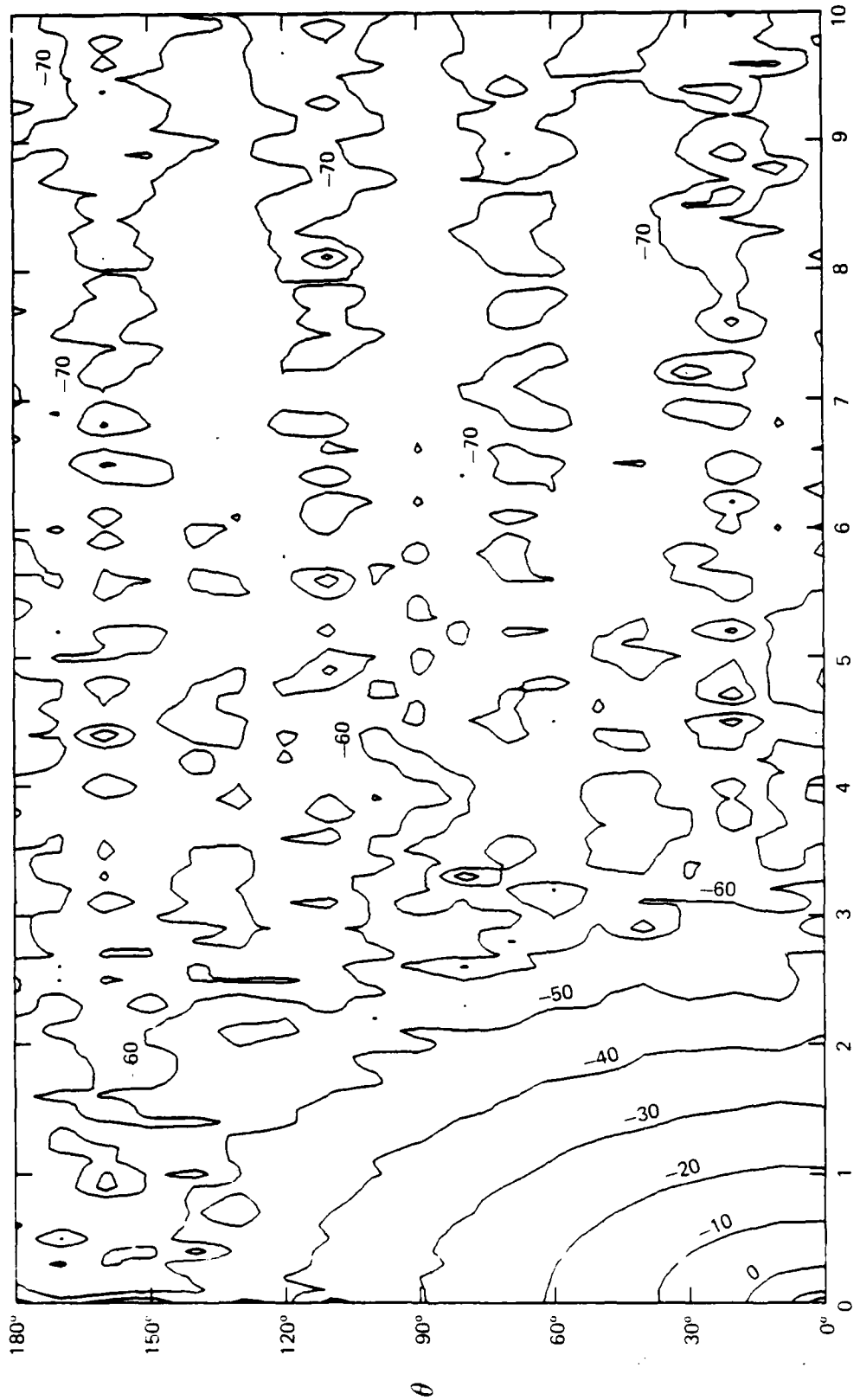

Figure 5.26. Constant magnitude contours of the shell displacement w(θ,x) expressed in dB re w_{ref} for Ω=100.

Chapter 6

SUMMARY AND CONCLUSIONS

The acoustic nearfield of a cylindrical shell of infinite axial extent has been examined. The elastic shell is loaded externally by a fluid medium and internally by an applied harmonic point force acting in the radial direction. This model is a useful approximation of finite length structures commonly found in the ocean and for which analytic solutions are not available. The acoustical and structural behavior of this simple geometry can provide insight into the mechanisms by which energy is transported and the parameters that control these mechanisms. A practical problem of interest might be the characterization of the self-noise of an acoustic sensor system that is mounted in the vicinity of an elastic structure which is being mechanically excited by internal equipment. Green's function techniques could be used to extend the results to include any type of distributed mechanical or nonharmonic loading.

The surface force exerted by water can be comparable to the inertial and damping forces found in a vibrating structure. Consequently fluid loading can alter the structural response of the elastic shell from its in vacuo state. The problem is a classical boundary value problem where boundary conditions at the shell-medium interface and in the farfield can be used to couple the elastic and acoustic response of the system. Several methods of approach have been discussed in the Introduction. The geometry of the problem suggested the use of cylindrical coordinates since the boundary surface of the cylinder would rep-

resent a constant coordinate surface. An integral transform technique was chosen to reduce the governing set of differential equations of motion into a set of algebraic equations in an axial wavenumber space. Eigenfunction analysis was used to express the acoustic pressure and surface displacement fields in terms of a Fourier series of modal contributions over a discrete circumferential wavenumber spectra. The main effort became the solution of the inverse Fourier integral and the convergence behavior of the modal sum. Various investigators have used asymptotic methods to calculate the farfield and high frequency solutions. Since the primary interest of this study has been the nearfield at *frequencies below the classical plate coincidence frequency*, Cauchy's theorem was chosen to solve the inverse Fourier integral. As was demonstrated in the last chapter, the nearfield solution can be written in terms of a finite sum of residue contributions from real singularities.

The contribution of the elastic cylinder to the fluid-loaded problem was written in terms of a spectral modal mechanical impedance. The Flugge equations were chosen to represent the shell because they represent a thin shell theory that is also conservative. This was shown by their development using variational energy methods in the Appendix. Differences were discussed between thin shell theories, thick shell theories that account for shear deformation and rotary inertia, and elastic theories based upon the equations of elasticity. A comparison between the Flugge theory and an elastic theory due to Gazis indicates that the Flugge theory is an adequate representation of the shell's in vacuo middle-surface deformation for frequencies up to several times the plate coincidence frequency. At higher frequency, either a thick shell or thick plate theory would be more appropriate. If fluid loading is included, Flugge theory would be expected to give reasonable results to

higher frequency than expected for the in vacuo problem since the shell impedance would represent only a portion of the characteristic equation.

The in vacuo modes of vibration were investigated and shown to consist of three orthogonal branches that represent coupled motion of the middle-surface deformation of the shell. Since the eigenvalues, or singularities of the inverse Fourier integral, control the surface deformation and acoustic field at low frequency when fluid loading is negligible, their values and behavior were calculated and discussed. Although neither the longitudinal nor torsional branches are sensitive to shell thickness, the flexural branch which has a large radial deformation component was found to be highly sensitive. Therefore, for negligible fluid loading, both the radial displacement field and the acoustic field would be expected to be sensitive to shell thickness. At high frequency, the in vacuo branches were shown to behave like simpler systems such as plates and circular bars. The addition of fluid loading restricts the free modes of vibration to at most a single mode for each circumferential mode order. This fluid-loaded branch is a modified version of the in vacuo flexural branch and therefore its frequency spectra is also sensitive to shell thickness.

For in vacuo free vibration, at each circumferential mode order a cutoff frequency was shown to exist that represents the transition between axially propagating and nonpropagating waves. At the cutoff frequency the phase velocity is infinite while the group velocity is zero, thus indicating that at lower frequency energy cannot propagate axially. A zero cutoff frequency was shown to represent rigid body motion. As shown in Figure 3.1, the cutoff frequency is higher for increasing mode order. At low frequency the displacement and acoustic fields will be

influenced by only a small number of modes while at high frequency a large number of modes would contribute.

The addition of fluid loading increases these cutoff frequencies and introduces a second, higher cutoff frequency. At frequencies above this upper cutoff frequency, axially propagating waves cannot exist. Consequently, each circumferential mode order has an associated free mode of vibration only over a limited frequency bandwidth in the fluid-loaded case. As was shown in Figure 4.14, for mode orders above some critical mode order, axially propagating waves are no longer possible at any frequency. Unlike the in vacuo case, at high frequency the number of mode orders at which free waves are possible decreases. As expected, the fluid-loaded cutoff frequencies are sensitive to shell thickness with thinner shells contributing more circumferential modes to the shell's displacement and acoustic fields than do thicker shells.

The in vacuo frequency spectra, dispersion curves, and group velocity behavior are extensively presented in Chapter 3. At frequencies above the ring frequency, the longitudinal branch of a cylindrical shell looks much like the longitudinal branch of a plate or bar at all mode orders. Similarly, the torsional and flexural branches of a cylindrical shell behave like the torsional branch of a bar or the flexural branch of a classical plate above the ring frequency. At frequencies below the plate coincidence frequency, the classical plate theory and Timoshenko-Mindlin plate theory yield similar results. Below the ring frequency, both the axisymmetric and first beam mode of the flexural branch can be modeled by membrane theory. Above the ring frequency and at higher mode orders at all frequencies, bending effects dominate the frequency spectra of the flexural branch.

The addition of fluid loading and the spectral formulation of the acoustic pressure field were discussed in Chapter 4. Both physical and mathematical reasons were given for the choice of the Sommerfeld branch lines to specify the radial wavenumber as a single-valued function in the region of interest. The behavior of the normalized spectral modal acoustic radiation impedance $Z_{an}(\gamma)$ was shown by Figures 4.3-4.5 to consist of two characteristic regions. In one of these regions the function is monotonic, possesses no poles, and is zero only at infinity. In the other region, the function contains an infinite number of alternating poles and zeroes, although it is also zero at infinity. The spectral modal specific acoustic impedance $Z_{fn}(\gamma r)$ has a similar behavior except that it becomes infinite in this second region at infinite range. The Sommerfeld branch lines are the boundary between these two regions.

Existence properties of the singularities were derived. Since the characteristic equation with fluid loading is Hermitian only for $|\xi|>k$ on the top Riemann sheet, then the real branch must be confined to this region. Furthermore, real singularities cannot exist at all on the bottom Riemann sheet and imaginary singularities cannot exist anywhere. This means that singularities cannot exist on the Sommerfeld branch lines. Consequently, the transformed displacement or pressure integrand would be analytic on a contour of integration along the Sommerfeld branch lines. On the top Riemann sheet, singularities were shown to exist in sets that are symmetric about both the real and imaginary axes. Two real singularities would comprise a set while a set of complex singularities would consist of four. Consequently, any one quadrant of the complex axial wavenumber domain would yield the location of all of the singularities. On the bottom Riemann sheet, singularities are only conjugate symmetric about the imaginary axis, and therefore two quadrants

of the axial wavenumber domain would be required to find the location of all the singularities.

Fluid loading was shown to reduce the number of real branches from three to one. This single real branch can be associated with the in vacuo flexural branch, except it must exist only between the lower and upper cutoff frequencies and at a higher axial wavenumber than the in vacuo flexural branch. At each cutoff frequency, the real flexural branch splits into two complex branches with a behavior described by Figures 4.16 and 4.17. The counterpart of the in vacuo longitudinal branch is a complex branch that is characterized by having a large radial wavenumber as shown in Figure 4.15. No counterpart of the in vacuo torsional branch has been found.

The behavior of the fluid-loaded real branch was discussed and compared to the in vacuo flexural branch. Expressions were developed that characterize its behavior over various regions of interest and specify the cutoff frequencies. It was shown that at a cutoff frequency fluid loading decreases the phase velocity from the in vacuo value and limits it to finite values. The maximium fluid-loaded phase velocity at any frequency is the acoustic velocity. Similarly, fluid loading also decreases the group velocity over its in vacuo values. This can be interpreted as decreasing the rate at which energy is transported along the cylinder which would be expected when an additional impedance is added to a system.

Cauchy's theorem and integral formula were used to evaluate both the radial displacement of the shell and the acoustic nearfield. The solution was shown to consist of two branch line integrals and the residue contribution from the real and complex singularities. The residue from each symmetric pair of complex singularities enclosed by the con-

tour of integration was shown to decay both axially and radially such that its contribution to the solution could be ignored except very near the excitation point. For frequencies below the plate coincidence frequency, the nearfield contribution of the branch line integrals was found to be at least 15 dB below the contribution from the residue of the real singularity. Consequently the shell radial displacement and nearfield pressure can be written as a finite sum of residue contributions. Since the real singularities are not dependent upon field point, a finite set will serve to calculate the field at any desired r, θ, or x resolution desired. This is seen as a considerable computational advantage over performing a separate numerical integration of the original inverse Fourier integral at each field point. Above the plate coincidence frequency, the solution entirely consists of the branch line integrals. The well known high frequency acoustic beaming effect that occurs at the coincidence angle was shown to be due to branch integral B_2.

The characteristics of the branch line integrals and the residues were also discussed in Chapter 5. The modal contributions to both B_2 and B_1 were shown to be uniformly convergent with a mode convergence approximately equal to $\gamma a+10$. Since the convergence behavior is primarily due to the denominator terms of the modal contributions, modal convergence is only weakly dependent upon radial distance. An analytic solution, Equation (5.24), was derived for branch line integral B_1 using Laplace's method. Comparison with numerically generated data indicates that Equation (5.24) is a good approximation whenever $x>a$. For each mode order, the residue of the real singularity was shown to represent a wave that propagates axially and decays radially. Above the plate coincidence frequency, the total residue contribution behaves like an axial standing wave that contributes little to the solution.

Calculations of the acoustic nearfield were presented for $\Theta=0$ in Figures 5.14-5.16 with $\Omega=0.1$, 1, and 10 and in Figure 5.18 with $\Omega=100$. The nearfield was defined based upon practical size considerations of typical structures rather than on the basis of acoustic wavelength. Since most structures of interest have a length-to-radius ratio of about ten and sensing equipment is generally found within one radius of the structure or else in the farfield, then a reasonable definition of the nearfield would be $x<10a$ and $a<r<2a$. Below the plate coincidence frequency, good coupling between the drive point pressure and the acoustic nearfield is seen to exist. This indicates that structural vibration could be an important component of the self noise of a sonar array at these frequencies. If the reciprocal problem of an acoustic point source near an elastic cylindrical shell is considered, these results indicate that large amounts of acoustic energy would couple into the structure and thus decrease the power radiated directly into the farfield. Above the plate coincidence frequency, the acoustic field is similar to that of a point-excited plate and poor coupling is observed between the drive point pressure and most of the acoustic nearfield. Both the surface pressure field and the shell radial displacement field were calculated for $\Omega=0.1$, 1, 10, and 100. As expected, they display similar behavior. Again strong coupling between the drive point and points within 10a of the drive point is seen for frequencies below the plate coincidence frequency. Above this frequency, the response is confined close to the drive point and resembles the response of a point-excited plate.

APPENDIX

DERIVATION OF THE FLUGGE SHELL EQUATIONS BY APPLICATION OF HAMILTON'S VARIATIONAL PRINCIPLE

For a conservative mechanical system, Hamilton's variational principle states that the motion of the system from time t_1 to time t_2 is such that the line integral

$$J = \int_{t_1}^{t_2} L \, dt \tag{A.1}$$

has a stationary value for the correct path of motion. The functional L is the Lagrange functional, which represents the difference between the kinetic and potential energies of the system at any instant. Of all the possible paths by which the system could move, it will actually follow the path by which the value of J is either a minimum, a maximum, or an inflection point. That is, the path will be such that the derivative of J with respect to some variable will be zero. In terms of variational calculus, Hamilton's principle can be written as

$$\delta J = \delta \int_{t_1}^{t_2} L \, dt = 0 \tag{A.2}$$

where δ stands for "the variation of" and will be defined later. This principle is a manifestation of the impulse-momentum theorem, and application of the principle results in equations commonly called the

Lagrange-Euler, or simply, the Euler equations. They represent the governing equations of motion for the system. They can also be independently developed by using D'Alembert's principle, which is based upon the consideration of small virtual displacements from some instantaneous state. The Lagrange functional L has been shown by Weinstock (1974) to yield the conservation of energy law E=T+V when introduced into the Euler equations. General reference is made to Weinstock, Morse and Feshbach (1953), Goldstein (1981), and Sechler (1968) for material developed in this appendix.

Development of Hamilton's principle for a general problem can be very concise, as in the case of Morse and Feshbach's treatment, but at the possible sacrifice of clarity. On the other hand, a more informative approach by examples, such as that presented by Weinstock, can become very lengthy. Here, we will try to strike a middle ground by developing the method based upon the kinetic energy term of the Lagrange functional and then by developing the potential energy term in a more concise manner with emphasis only upon points not adequately discussed in the initial development. In general, we will be dealing with energy densities, such that

$$J = \int_{t_1}^{t_2} \iiint_V L_V \, dV \, dt = \int_{t_1}^{t_2} \iint_S L_S \, dS \, dt \qquad (A.3)$$

is the integral to be made stationary, and L_V is the Lagrange volume density. Since the radial dependence of the problem is known, the problem can be reduced to a three-dimensional one in x, θ, and t by calculating the Lagrange surface density $L_S=T_S-V_S$ and the elemental volume $dV=rR^3 \, d\rho \, dx \, d\theta$. The variable ρ represents a radial coordinate measured from the shell's middle surface that is related to the radial coordinate

r by $r=1+\rho$. The R^3 factor is due to the normalization of r, ρ, and x with respect to the middle-surface radius of the shell.

The instantaneous kinetic energy per unit volume at any point in the shell is given by

$$T_V = \frac{1}{2}\rho_s R^2 \left[\left(\frac{\partial u_r}{\partial t}\right)^2 + \left(\frac{\partial u_\theta}{\partial t}\right)^2 + \left(\frac{\partial u_x}{\partial t}\right)^2\right] . \tag{A.4}$$

In terms of the middle surface deformations, Equations (2.5), this is

$$T_V = \frac{1}{2}\rho_s R^2 \left[\dot{u}^2 + r^2\dot{v}^2 + \dot{w}^2 - 2\rho\dot{u}\dot{w}_{,x} - 2r\rho\dot{v}\dot{w}_{,\theta} + \rho^2\dot{w}^2_{,\theta} + \rho^2\dot{w}^2_{,x}\right] \tag{A.5}$$

where the dot notation represents differentiation with respect to time, and the differentiation notion

$$y_{,x} = \frac{\partial y}{\partial x} \qquad \text{and} \qquad y_{,\theta x} = \frac{\partial^2 y}{\partial\theta\partial x}$$

has been introduced. Since u, v, and w are functions of x, θ, and t only, the radial dependence of T_V is known, and the surface kinetic density can easily be calculated.

$$\begin{aligned} T_S &= R\int_{-h/2}^{h/2} T_V\, r\, d\rho = R\int_{-h/2}^{h/2} (1+\rho)\, T_V\, d\rho \\ &= \frac{1}{2}\rho_s h R^3 \left[\dot{u}^2 + \dot{v}^2 + \dot{w}^2 + \beta(3\dot{v}^2 - 4\dot{v}\dot{w}_{,\theta} + \dot{w}^2_{,\theta} - 2\dot{u}\dot{w}_{,x} + \dot{w}^2_{,x})\right] \end{aligned} \tag{A.6}$$

where the normalized thickness ratio $\beta = h^2/12$ has been introduced.

If the potential energy of the system was zero, then the problem would be to find u, v, and w for which

$$J = R^2 \int_{t_1}^{t_2}\iint_S L_S(\dot{u},\dot{v},\dot{w},\dot{w}_{,\theta},\dot{w}_{,x})\, dS\, dt \tag{A.7}$$

is stationary. Let us now introduce some comparision functions u^*, v^*, and w^* which are close to the exact solutions and are defined by

$$\begin{aligned} u^*(x,\theta,t,\alpha) &= u(x,\theta,t) + \alpha\, \xi(x,\theta,t) \\ v^*(x,\theta,t,\alpha) &= v(x,\theta,t) + \alpha\, \eta(x,\theta,t) \\ w^*(x,\theta,t,\alpha) &= w(x,\theta,t) + \alpha\, \zeta(x,\theta,t) \end{aligned} \tag{A.8}$$

where α is a small non-dimensional constant. The perturbation functions ξ, η, and ζ are restricted only in that they must be at least twice differentiable in any variable x, θ, or t, and they must be zero at all boundaries (including t_1 and t_2). This last condition assures that the boundary conditions yield the exact solutions. If we introduce the comparison functions into Equation (A.7) and group terms according to powers of the arbitrarily small constant α, we yield a new integral

$$\bar{J} = J + \alpha\, J_1 + \tfrac{1}{2}\, \alpha^2\, J_2 \tag{A.9}$$

where

$$\begin{aligned} J_1 = \rho_s h R^5 \int_{t_1}^{t_2} \iint_S \Big[&(u - \beta w_{,x})\xi + (v + 3\beta v - 2\beta w_{,\theta})\eta + w\,\zeta \\ &+ \beta(\dot{w}_{,\theta} - 2\dot{v})\dot{\zeta}_{,\theta} + \beta(\dot{w}_{,x} - \dot{u})\dot{\zeta}_{,x}\Big]\, dS\, dt \end{aligned} \tag{A.10}$$

is defined as the first variation integral, and

$$\begin{aligned} J_2 = \rho_s h R^5 \int_{t_1}^{t_2} \iint_S \Big[&\dot{\xi}^2 + (1+3\beta)\dot{\eta}^2 + \dot{\zeta}^2 - 4\beta\, \dot{\eta}\dot{\zeta}_{,\theta} + \beta\, \dot{\zeta}^2_{,\theta} \\ &+ \beta\, \dot{\zeta}^2_{,x} - 2\beta\, \dot{\xi}\dot{\zeta}_{,x}\Big]\, dS\, dt \end{aligned} \tag{A.11}$$

is called the second variational integral. Since α is an arbitrarily small constant, this last term can be disgarded, and for a stationary condition

$$\frac{\partial \bar{J}}{\partial \alpha} = \delta J = J_1 = 0 \tag{A.12}$$

must be true, since the limits of integration are constant with respect to α. This process serves to define the meaning of the variation of J.

The first variational integral contains terms of the form

$$\int_{t_1}^{t_2} f(x,\theta,t)\dot{\xi}\, dt = f\,\xi\Big|_{t_1}^{t_2} - \int_{t_1}^{t_2} \frac{\partial f}{\partial t}\,\xi\, dt \tag{A.13}$$

when integrated by parts. Since $\xi(t_2)=\xi(t_1)=0$ was a requirement on ξ, the first term vanishes, leaving only the second term. Other terms containing mixed derivatives also exist in the integrand of the form

$$\int_{t_1}^{t_2}\int_{0}^{2\pi} f(x,\theta,t)\dot{\zeta}_{,\theta}\, d\theta\, dt = f\,\dot{\zeta}\Big|_{0}^{2\pi} - \frac{\partial f}{\partial \theta}\,\zeta\Big|_{t_1}^{t_2} + \int_{t_1}^{t_2}\int_{0}^{2\pi} \frac{\partial^2 f}{\partial\theta\partial t}\,\zeta\, d\theta\, dt \tag{A.14}$$

after twice integrating by parts. Continuity of the solution in the circumferential direction (or a free boundary condition in the axial direction for derivatives with respect to x) eliminates the first term on the right hand side, while the requirement $\zeta(t_1)=\zeta(t_2)=0$ eliminates the second term, again leaving only the last term. The constant terms which result from integration by parts that are not eliminated due to forced constraints and continuity conditions will form the natural boundary conditions of the system. Following this process the first variational integral becomes

$$J_1 = -\rho_s h R^5 \int_{t_1}^{t_2} \iint_S \left[(\ddot{U} - \beta \dot{W}_{,x})\xi + (\ddot{V} + 3\beta\dot{V} - 2\beta\dot{W}_{,\theta})\eta + \ddot{W}\zeta \right.$$

$$\left. + \beta(\ddot{U}_{,x} + 2\ddot{V}_{,\theta} - \ddot{W}_{,\theta\theta} - \ddot{W}_{,xx})\zeta \right] dS\, dt \quad . \tag{A.15}$$

For the stationary condition to apply, J_1 must be zero. It is argued and proven by Weinstock that for arbitrary functions ξ, η, and ζ, the only way J_1 can be zero is if the functional coefficients of ξ, η, and ζ are identically zero for all values of x, θ, and t within the range of integration. This would yield a set of three differential equations governing the behavior of the shell (if potential energy was neglected).

Examining the variation of the kinetic energy δT, we find many terms which are proportional to β. These terms are related to rotary inertia and are generally small except at high frequency. In keeping with our earlier assumptions concerning zero-thickness shear strain, which reduced the theory to a zero-order theory, this contribution will be assumed negligible, leaving

$$\delta T = J_1 = -\rho_s h R^5 \int_{t_1}^{t_2} \iint_S (\ddot{U}\xi + \ddot{V}\eta + \ddot{W}\zeta)\, dS\, dt \quad . \tag{A.16}$$

Natural boundary conditions were not imposed deriving Equation (A-15).

Before considering the potential energy some comments are in order. Relation (A.9) gives the appearance of a Taylor's series expansion about the exact solution in which the first variational integral J_1 acts as a first derivative, J_2 acts as a second derivative, and higher order derivatives are zero. This is the approach presented by Morse and Feshbach. When forming the Taylor's series expansion, it must be remem-

bered that L_s is, in this case, a function not of u, v, and w, but of the functions $\dot{u}$, $\dot{v}$, $\dot{w}$, $\dot{w}_{,\theta}$, and $\dot{w}_{,x}$ which can be thought of as generalized coordinates q_m. However, the Morse and Feshbach perturbation functions η_m associated with these generalized coordinates are related to the perturbation functions ξ, η, and ζ in the same way that the generalized coordinates are related to the functions u, v, and w. That is, the perturbation function associated with $\dot{w}_{,x}$ would be $\zeta_{,x}$. The Taylor series expansion would be

$$\bar{J}(q_1^*,q_2^*,q_3^*,q_4^*,q_5^*) = J(q_1,q_2,q_3,q_4,q_5) + \left[\sum_{m=1}^{5}\alpha\,\eta_m\frac{\partial}{\partial q_m^*}\right] J(q_1^*,q_2^*,q_3^*,q_4^*,q_5^*)\Big|_{\alpha=0}$$

$$+\frac{1}{2!}\left[\sum_{m=1}^{5}\alpha\,\eta_m\frac{\partial}{\partial q_m^*}\right]^2 J(q_1^*,q_2^*,q_3^*,q_4^*,q_5^*)\Big|_{\alpha=0} + \text{higher order terms,} \qquad (A.17)$$

and δJ would be the second term of the expansion with the α removed by differentiation. Once those perturbation functions that are derivatives of ξ, η, and ζ are removed by integration by parts, the resulting form is often called the Euler equations. Often overlooked in the development to this point is that the integration by parts may have introduced natural boundary conditions upon the system.

Another point of note is that the stationary condition $\delta J=0$ does not necessarily guarantee a minimum. Often, it is obvious from the problem at hand that the stationary point must be a minimum, such as for the problem of the shortest distance between two points. However, this is not always apparent. In such cases where doubt exists, the second variational integral can be examined over the surface of stationarity in much the same way the second derivative serves to determine whether a point is a maximum, minimum, or inflection for a simple function. Such techniques are extremely complex and beyond the scope of this work.

The potential energy of the system arises from two sources. The first is from the instantaneous elastic strain associated with the stress distribution in the shell of the deformed motion. This strain energy density is defined as

$$U_V = \frac{1}{2} (\varepsilon_{xx}\sigma_{xx} + \varepsilon_{\theta\theta}\sigma_{\theta\theta} + \varepsilon_{\theta x}\sigma_{\theta x}) \quad , \tag{A.18}$$

and the total strain energy of the shell would be given by

$$U = R^3 \iiint_V U_V \, r \, d\rho \, d\theta \, dx \quad . \tag{A.19}$$

The factor of 1/2 in the strain energy density arises from the elastic relationship between stress and strain. Since the force on an elemental volume varies linearly from zero at some initial state to a value proportional to σ at some final state, the average force moving through some distance proportional to ε is $\sigma/2$, and therefore, the strain energy is proportional to $\varepsilon\sigma/2$.

Another source of potential energy is due to the applied loading on the shell. For this problem, this includes the pressure loading on the shell given by $p_a(x,\theta,t)$ and the distributed driving forces denoted by $f_d(x,\theta,t)$. The driving forces will be restricted to only radial forces, and therefore, the potential energy associated with p_a and f_d will arise due to the deformation w and be in the form of work, where

$$W = R^3 \iint_S (f_d - p_a) \, w \, d\theta \, dx \quad . \tag{A.20}$$

Forces which act in the direction of the displacement are considered to do positive work.

From Equation (2.10) relating stress and strain, the strain energy density can be written as

$$U_V = \frac{E}{2(1-\mu^2)} \left[\varepsilon_{xx}^2 + \varepsilon_{\theta\theta}^2 + 2\mu\ \varepsilon_{xx}\varepsilon_{\theta\theta} + \left(\frac{1-\mu}{2}\right)\ \varepsilon_{\theta x}^2\right] \quad . \tag{A.21}$$

If the strains are expressed in terms of the membrane strains and the curvature terms, as given by Equations (2.8) and (2.9), then the strain energy surface density U_S can be determined by integrating over the thickness, yielding

$$U_S = R \int_{-h/2}^{h/2} (1+\rho)\ U_V\ d\rho$$

$$= \frac{EhR}{2(1-\mu^2)} \left\{\left[e_{xx}^2 + e_{\theta\theta}^2 + 2\mu\ e_{xx}e_{\theta\theta} + \left(\frac{1-\mu}{2}\right)\ e_{\theta x}^2\right]\right. \tag{A.22}$$

$$\left. + \beta\left[\kappa_{xx}^2 - 2(e_{xx} + \mu\ e_{\theta\theta})\kappa_{xx} + 2\mu\ \kappa_{xx}\kappa_{\theta\theta} + \kappa_{\theta\theta}^2 + \left(\frac{1-\mu}{2}\right)(3\kappa_{x\theta}^2 + \kappa_{\theta x}^2)\right]\right\}$$

where terms of order greater than β have been neglected. The terms proportional to β are due to bending of the shell, while the remaining terms represent the strain energy due to the extension of the shell's middle surface.

The membrane strains e and the nondimensional curvature terms κ are known functions of the middle-surface deformations u, v, and w and their spatial derivatives. Hamilton's variational principle may again be applied to yield

$$\delta U = \frac{EhR^3}{(1-\mu^2)} \int_{t_1}^{t_2} \iint_S (q_u\xi + q_v\eta + q_w\zeta)\ d\theta\ dx\ dt \quad . \tag{A.23}$$

The term $q_u\xi$ represents a variation with respect to u, which is given by

$$[e_{xx} + \mu\ e_{\theta\theta} - \beta\ \kappa_{xx}]\xi_{,x} + \left(\frac{1-\mu}{2}\right)[e_{\theta x} + \beta\ \kappa_{\theta x}]\xi_{,\theta} \tag{A.24}$$

or

$$g_u = -\frac{\partial}{\partial x}[e_{xx} + \mu\, e_{\theta\theta} - \beta\, \kappa_{xx}] - (\frac{1-\mu}{2})\frac{\partial}{\partial \theta}[e_{\theta x} + \beta\, \kappa_{\theta x}] \quad . \quad (A.25)$$

The integration by parts yields constant terms that are identically zero since by definition ξ must be zero at the boundaries $x=\pm\infty$ and $\theta=0,2\pi$. In a similar manner, the variation with respect to v is derived from

$$(\frac{1-\mu}{2})[e_{\theta x} - 3\beta\, \kappa_{x\theta}]\eta_{,x} + [e_{\theta\theta} + \mu\, e_{xx} - \beta\mu\, \kappa_{xx}]\eta_{,\theta} \quad (A.26)$$

or

$$g_v = -(\frac{1-\mu}{2})\frac{\partial}{\partial x}[e_{\theta x} - 3\beta\, \kappa_{x\theta}] - \frac{\partial}{\partial \theta}[e_{\theta\theta} + \mu\, e_{xx} - \beta\mu\, \kappa_{xx}] \quad . \quad (A.27)$$

Again, integration by parts yields constant terms that are zero.

The variation with respect to the radial deformation w is not quite as simple as the others and is derived from

$$[e_{\theta\theta} + \mu\, e_{xx} + \beta\, \kappa_{\theta\theta}]\zeta + \beta(\frac{1-\mu}{2})[\kappa_{\theta x} + 3\, \kappa_{x\theta}]\zeta_{,\theta x}$$

$$+ \beta[\kappa_{\theta\theta} + \mu\, \kappa_{xx}]\zeta_{,\theta\theta} + \beta[\kappa_{xx} + \mu\, \kappa_{\theta\theta} - e_{xx} - \mu\, e_{\theta\theta}]\zeta_{,xx} \quad . \quad (A.28)$$

From the above,

$$g_w = [e_{\theta\theta} + \mu\, e_{xx} + \beta\, \kappa_{\theta\theta}] + \beta(\frac{1-\mu}{2})\frac{\partial^2}{\partial\theta\partial x}[\kappa_{\theta x} + 3\, \kappa_{x\theta}]$$

$$+ \beta\frac{\partial^2}{\partial\theta^2}[\kappa_{\theta\theta} + \mu\, \kappa_{xx}] + \beta\frac{\partial^2}{\partial x^2}[\kappa_{xx} + \mu\, \kappa_{\theta\theta} - e_{xx} - \mu\, e_{\theta\theta}] \quad . \quad (A.29)$$

The constants associated with the integration by parts are identically zero, zero due to continuity conditions at $\theta=0$ and 2π, or require that

$$\zeta_{,x}(x=\pm\infty,\theta,t) = 0 \quad .$$

This condition is met for a free boundary condition.

The work due to the applied forces and the acoustic pressure is dependent only upon the radial deformation w and has a variation

$$\delta W = R^3 \int_{t_1}^{t_2} \iint_S (f_d - p_a)\, \zeta \, d\theta \, dx \, dt \quad . \tag{A.30}$$

The total variation is therefore

$$\delta J = \int_{t_1}^{t_2} \iint_S L_S \, d\theta \, dx \, dt = \int_{t_1}^{t_2} \iint_S (T_S - U_S + W_S) \, d\theta \, dx \, dt = 0 \tag{A.31}$$

which for arbitrary ξ, η, and ζ can only be satisfied if the coefficients of ξ, η, and ζ are each separately and identically zero. The positive sign associated with the work of the external forces is due to the general definition of potential energy for a conservative system. This states that the difference in potential energy between a final and initial state is equal to the negative of the work done by the forces on the system when the system goes from the initial to the final state. Positive work is defined as increasing the kinetic energy of the system. These equations are given by

$$\begin{aligned} q_u + \frac{R^2}{c_p^2} \ddot{u} &= 0 \\ q_v + \frac{R^2}{c_p^2} \ddot{v} &= 0 \\ q_w + \frac{R^2}{c_p^2} \ddot{w} - \frac{1}{D} (f_d - p_a) &= 0 \end{aligned} \tag{A.32}$$

where the low frequency phase velocity of compressional waves in a plate

$$c_p^2 = \frac{E}{\rho_s(1-\mu^2)}$$

and the normalized extensional rigidity of the shell

$$D = \frac{Eh}{(1-\mu^2)}$$

have been introduced. By introducing the definitions of g_u, g_v, and g_w given by Equations (A.25), (A.27), and (A.29) along with the definitions of the dimensionless curvatures given by Equation (2.9) and the membrane strain Equations (2.8), the differential equations of motion governing the shell can be written in terms of the middle surface displacements as

$$u_{,xx} + (\tfrac{1-\mu}{2})(1+\beta)u_{,\theta\theta} + (\tfrac{1+\mu}{2})v_{,\theta x} + \mu w_{,x} + \beta(\tfrac{1-\mu}{2})w_{,\theta\theta x} - \beta w_{,xxx} = \frac{R^2}{c_p^2}\ddot{u} \qquad \text{(A.33a)}$$

$$(\tfrac{1+\mu}{2})u_{,\theta x} + (\tfrac{1-\mu}{2})(1+3\beta)v_{,xx} + v_{,\theta\theta} + w_{,\theta} - \beta(\tfrac{3-\mu}{2})w_{,\theta xx} = \frac{R^2}{c_p^2}\ddot{v} \qquad \text{(A.33b)}$$

$$\mu u_{,x} + \beta(\tfrac{1-\mu}{2})u_{,\theta\theta x} - \beta u_{,xxx} + v_{,\theta} - \beta(\tfrac{3-\mu}{2})v_{,\theta xx} + (1+\beta)w + 2\beta w_{,\theta\theta} + 2\beta w_{,\theta\theta xx} + \beta w_{,\theta\theta\theta\theta} + \beta w_{,xxxx} = -\frac{R^2}{c_p^2}\ddot{w} + \frac{1}{D}(f_d - p_a) \quad . \qquad \text{(A.33c)}$$

REFERENCES

Abramowitz, M., and Stegun, I. A., eds. (1972). Handbook of Mathematical Functions (National Bureau of Standards, Washington, D.C.).

Baron, M. L., and Bleich, H. H. (1954). "Tables for frequencies and modes of free vibration of infinitely long thin cylindrical shells," J. Appl. Mech. 21, 178-84.

Bleich, H. H. (1954). "Sound radiation form an elastic cylindrical shell submerged in an infinite medium," Proc. 2nd U. S. Natl. Cong. Appl. Mech. (ASME, New York) p. 213.

Bleich, H. H., and Baron, M. L. (1954). "Free and forced vibrations of an infinitely long cylindrical shell in an infinite medium," J. Appl. Mech. 21, 167-77.

Brillouin, L. (1960). Wave Propagation and Group Velocity (Academic Press, New York), pp. 99-100.

Bromwitch, T. J. (1959). An Introduction to the Theory of Infinite Series, 2nd ed. (Macmillan, New York), pp. 130-32.

Burroughs, C. B. (1984). "Acoustic radiation from fluid-loaded infinite circular cylinders with doubly periodic ring supports," J. Acoust. Soc. Am. 75(3), 715-22.

Carrier, G. F., Krook, M., and Pearson, C. E. (1966). Functions of a Complex Variable (McGraw-Hill, New York), pp. 59-60.

Chertock, G. (1964). "Sound radiation from a vibrating surface," J. Acoust. Soc. Am. 36(7), 1305-13.

Chree, C. (1886). "Longitudinal waves of a solid bar," Quart. J. Math. 21, 287.

Cohen, L. H., and Schwiekert, D. G. (1963). "Sound radiation from an arbitrary body," J. Acoust. Soc. Am. 35(10), 1626-32.

Copley, L. G. (1968). "Fundamental results concerning integral representations in acoustic radiation," J. Acoust. Soc. Am. 44(1), 28-32.

Crighton, D. G. (1972). "Force and moment admittance of plates under arbitrary fluid loading," J. Sound Vib. 20(2), 209-18.

Crighton, D. G. (1977). "Point admittance of an infinite thin elastic plate under fluid loading," J. Sound Vib. 54(3), 389-91.

Crighton, D. G. (1979). "The free and forced waves on a fluid-loaded elastic plate," J. Sound Vib. 63(2), 225-35.

Crighton, D. G., and Innes, D. (1983). "Low frequency acoustic radiation and vibration response of locally excited fluid-loaded structures," J. Sound Vib. 91(2), 293-314.

Crighton, D. G., and Innes, D. (1984). "The modes, resonances and forced response of elastic structures under heavy fluid loading," Phil. Trans. R. Soc. Lond. A312, 295-341.

Doolittle, R. D., and Uberall, H. (1968). "Sound scattering by elastic cylinders," J. Acoust. Soc. Am. 43(1), 1-14.

Dubbeldey, P. S. (1983). "Application of a new complex root-finding technique to the dispersion relations for the elastic waves in a fluid-loaded plate," SIAM J. Appl. Math 43(5), 1127-39.

Feit, D. (1966). "Pressure radiated by a point-excited elastic plate," J. Acoust. Soc. Am. 40(6), 1489-94.

Feit, D. (1970). "Sound radiation from orthotropic plates," J. Acoust. Soc. Am. 47(1), 388.

Flugge, W. (1973). Stresses in Shells, 2nd ed. (Springer-Verlag, Berlin).

Forsythe, G. E., Malcom, M. A., and Moler, C. B. (1977). Computer Methods of Mathematical Computations (Prentice-Hall, Englewood Cliffs, N.J.).

Frymoyer, E. M. (1967). "Vibration and wave propagation in cylindrical shells," Ph.D. dissertation, Pennsylvania State University.

Gazis, D. C. (1959). "Three-dimensional investigation of the propagation of waves in hollow circular cylinders. I: Analytic Foundation. II: Numerical results," J. Acoust. Soc. Am. 31(5), 568-78.

Geers, T. L. (1978). "Doubly asymptotic approximations for transient motions of submerged structures," J. Acoust. Soc. Am. 64(5), 1500-1508.

Geers, T. L., and Felippa, C. A. (1983). "Doubly asymptotic approximations for vibration analysis of submerged structures," J. Acoust. Soc. Am. 73(4), 1152-59.

Goldstein, H. (1981). Classical Mechanics, 2nd ed. (Addison-Wesley, Reading, Mass.).

Graff, K. F. (1975). Wave Motion in Elastic Solids (Ohio State University Press, Columbus, Ohio).

Greenspon, J. E. (1960). "Vibrations of a thick-walled cylindrical shell: Comparison of the exact theory with approximate theories," J. Acoust. Soc. Am. 32(5), 571-78.

Gutin, L. Y. (1965). "Sound radiation from an infinite plate excited by a normal point force," Sov. Phys. Acoust. 10, 369-71.

Harari, A., and Sandman, B. E. (1976). "Vibratory response of laminated cylindrical shells embedded in an acoustic fluid," J. Acoust. Soc. Am. 60(1), 117-28.

Hayek, S. I. (1980). Notes on Mathematical Methods in Engineering (class notes printed by the Pennsylvania State University).

Horton, C. W., King, W. R., and Diercks, K. J. (1962). "Theoretical Analysis of the scattering of short acoustic pulses by a thin-walled metalic cylinder in water," J. Acoust. Soc. Am. 34(12), 1929-32.

IMSL Incorporated (1982). IMSL Library, 9th ed. (IMSL, Houston, Texas).

Junger, M. C. (1952a). "Radiation loading of cylindrical and spherical surfaces," J. Acoust. Soc. Am. 24, 288.

Junger, M. C. (1952b). "Vibrations of elastic shells in a fluid medium and the associated radiation of sound," J. Appl. Mech. 19, 439-45.

Junger, M. C. (1953a). "The concept of radiation scattering and its application to reinforced cylindrical shells," J. Acoust. Soc. Am. 25(5), 899-903.

Junger, M. C. (1953b). "The physical interpetation of the expression for an outgoing wave in cylindrical coordinates," J. Acoust. Soc. Am. 25(1), 40-47.

Junger, M. C. (1954). "Dynamic behavior of reinforced cylindrical shells in a vacuum and in a fluid," J. Appl. Mech. 21(1), 35-41.

Junger, M. C. (1975). "Radiation and scattering by submerged elastic structures," J. Acoust. Soc. Am. 57(6), 1318-26.

Junger, M. C. (1978). "Discussion of 'Point admittance of an infinite thin elastic plate under fluid loading,'" J. Sound Vib. 61(1), 141-42.

Junger, M. C., and Feit, D. (1972). Sound Structures and Their Interaction (MIT Press, Cambridge, Mass.).

Junger, M. C., and Garrelick, J. M. (1984). "Multiple modal resonances of thin cylindrical shells vibrating in an acoustic medium," J. Acoust. Soc. Am. 75(5), 1380-82.

Kalotikhina, Z. V. (1958). "On the vibrations of a cylindrical shell in water and the complex spectrum of its radiation," Sov. Phys. Acoust. 4, 349-51.

Leissa, A. W. (1969). Vibration of Plates (National Aeronautics and Space Administration, Washington, D.C.).

Leissa, A. W. (1973). Vibration of Shells (National Aeronautics and Space Administration, Washington, D.C.).

Liu, Y. N., and Tucker, A. J. (1984a). "The distribution of radiated and vibratory powers of a point-driven infinite cylindrical shell. Part I: Uncoated structure," DTNSRDC Report No. 84/043 (Dec. 1984).

Liu, Y. N., and Tucker, A. J. (1984b). "The distribution of radiated and vibratory powers of a point-driven infinite cylindrical shell. Part II: Structures with compliant coatings," DTNSRDC Report No. 84/044 (Dec. 1984).

Love, A. E. H. (1927). A Treatise on the Mathematical Theory of Elasticity, 4th ed. (Dover, New York), pp. 173-74.

Maidanik, G. (1966). "The influence of fluid loading on the radiation from orthotropic plates," J. Sound Vib. 3(3), 288-99.

Maidanik, G., and Kerwin, E. M. Jr. (1966). "Influence of fluid loading on the radiation from infinite plates below the critical frequency," J. Acoust. Soc. Am. 40(5), 1034-38.

Mason, J. P. (1983). "Cylindrical Bessel functions for a large range of complex arguments," Naval Research Laboratory Report No. 8687 (April 29,1983).

Mindlin, R. D. (1951). "Influence of rotatory inertia and shear on flexural motions of isotropic, elastic plates," J. Appl. Mech. 18, 31-38.

Mirsky, I., and Herrmann, G. (1956). "Three-dimensional and shell theory analysis of axially symmetric motions," J. Appl. Mech. 23, 563-68.

Mirsky, I., and Herrmann, G. (1957). "Nonaxially symmetric motions of cylindrical shells," J. Acoust. Soc. Am. 29, 1116-23.

Mirsky, I., and Herrmann, G. (1958). "Axially symmetric motions of thick cylindrical shells," J. Appl. Mech. 25, 97-102.

Mirsky, I., and Herrmann, G. (1959). "Nonaxially symmetric motions of cylindrical shells," J. Acoust. Soc. Am. 31, 250.

Morse, P. M., and Feshbach, H. (1953). Methods of Theoretical Physics, Vol. I and II (McGraw-Hill, New York).

Morse, P. M., and Ingard, K. U. (1968). Theoretical Acoustics (McGraw-Hill, New York), pp. 356-66.

Muller, D. E. (1956). "A method for solving algebraic equations using an automatic computer," Mathematical Tables and Aids to Computation 10, 208-15.

Pierucci, M. (1979). "The matched asymptotic expansion (MAE) technique applied to acoustic radiation from vibrating surfaces," J. Sound Vib. 66(2), 199-217.

Pierucci, M. (1981). "Additional solutions to the free bending waves of a fluid loaded thick plate," J. Acoust. Soc. Am. 70(3), 866-69.

Pierucci, M., and Graham, T. (1979). "A study of bending waves in fluid-loaded thick plates," J. Acoust. Soc. Am. 65(5), 1190-97.

Pochhammer, L. (1876). "Uber die Fortpflanzungsgesch-windigkeiten von Schwingungen in einem unbegrenzten isotropen kreiscylinder," Z. Math. 81, 324-26.

Rayleigh, Lord (J. W. Strutt) (1887). "On waves propagating along the surface of an elastic solid," Proc. Math. Soc. London 17, 4.

Rayleigh, Lord (J. W. Strutt) (1945). The Theory of Sound, 2nd ed. (Dover, New York), Vol. 2, p. 109

Sandman, B. E. (1976). "Fluid loaded influence coefficients for a finite cylindrical shell," J. Acoust. Soc. Am. 60(6), 1256-64.

Schenck, H. A. (1968). "Improved integral formulation for acoustic radiation problems," J. Acoust. Soc. Am. 44(1), 41-58.

Sechler, E. E. (1968). Elasticity in Engineering (Dover, New York).

Skudrzyk, E. J. (1958). "Sound radiation of a system with a finite or infinite number of resonances," J. Acoust. Soc. Am. 30, 1140-52.

Skudrzyk, E. J. (1968). Simple and Complex Vibrating Systems (Pennsylvania State University Press, University Park, Penna.).

Skudrzyk, E. J. (1971). The Foundations of Acoustics (Springer-Verlag, New York).

Smith, P. W. Jr. (1959). "Sound radiation from a cylindrical shell excited by concentrated forces," Cambridge Acoustical Associates Report (June 26, 1959).

Smith, P. W. Jr. (1978). "The imaginary part of input admittance: A physical explanation of fluid-loading effects on plates," J. Sound Vib. 60(2), 213-16.

Stephanishen, P. R. (1978). "Radiated power and radiation loading of cylindrical surfaces with nonuniform velocity distributions," J. Acoust. Soc. Am. 63(2), 328-38.

Stephanishen, P. R. (1982). "Modal coupling in the vibration of fluid-loaded cylindrical shells," J. Acout. Soc. Am. 71(4), 813-23.

Stephanishen, P. R., and Benjamin, K. C. (1982). "Forward and backward projection of acoustic fields using FFT methods," J. Acoust. Soc. Am. 71(4), 803-12.

Stephanishen, P. R., and Chen, H. (1984). "Nearfield pressures and surface intensity for cylindrical vibrators," J. Acoust. Soc. Am. 76(3), 942-47.

Stokes, G. G. (1868). "On the communication of Vibrations from a vibrating body to a surrounding gas," Phil. Trans. 158, 447.

Stoneley, R. (1924). "Elastic waves at the surface of separation of two solids," Proc. R. Soc. A106, 416-28.

Strawderman, W. A., Ko, S. H., and Nuttall, A. H. (1979). "The real roots of the fluid-loaded plate," J. Acoust. Soc. Am. 66(2), 579-85.

Stuart, A. D. (1972). "Acoustic radiation from a point excited infinite elastic plate," Ph.D. dissertation, the Pennsylvania State University.

Stuart, A. D. (1976a). "Acoustic radiation from submerged plates. I. Influence of leaky wave poles," J. Acoust. Soc. Am. 59(5), 1160-69.

Stuart, A. D. (1976b). "Acoustic radiation from submerged plates. II. Radiated power and damping," J. Acoust. Soc. Am. 59(5), 1170-74.

Timoshenko, S. (1940). The Theory of Plates and Shells (McGraw-Hill, New York), p. 439.

Thompson, W. Jr., and Rattaya, J. V. (1964). "Acoustic power radiated by an infinite plate excited by a concentrated moment," J. Acoust. Soc. Am. 36(8), 1488-90.

Uberall, H., Dragonette, L. R., and Flax, L. (1977). "Relation between creeping waves and normal modes of vibration of a curved body," J. Acoust. Soc. Am. 61(3), 711-15.

Ugincius, P., and Uberall, H. (1968). "Creeping wave analysis of acoustic scattering by elastic cylindrical shells," J. Acoust. Soc. Am. 43(5), 1025-35.

Viktorov, I. A. (1967). Rayleigh and Lamb Waves: Physical Theory and Applications (Plenum Press, New York).

Vogel, W., and Feit, D. (1980). "Response of a point excited infinitely long cylindrical shell immersed in an acoustic medium," DTNSRDC Report No. 80/061 (Nov. 1980).

Walter, J. L. (1979). "Coincidence of higher order modes: A mechanism of the excitation of cylindrical shell vibrations via internal sound," Ph.D. dissertation, the Pennsylvania State University.

Weinstock, R. (1974). Calculus of Variations (Dover, New York).

Wilf, H. S. (1962). Mathematics for the Physical Sciences (John Wiley and Sons, New York), p. 29.

Williams, E. G., and Maynard, J. D. (1982). "Numerical Evaluation of the Rayleigh integral for planar radiators using the FFT," J. Acoust. Soc. Am. 72(6), 2020-30.

INITIAL DISTRIBUTION LIST

Addressee	No. of Copies
DTIC	2
DARPA	1
NAVSEASYSCOM (SEA-55N, -56W)	2
NRL	1
ONR (Dr. A. Tucker)	1
DTNSRDC, Bethesda (Code 1905.4: Dr. David Feit, Dr. W. Vogel; Code 1902: Dr. G. Maidanik; Dr. Y. Liu)	4
DTNSRDC, Annapolis (Code 2740.1: D. Maxwell)	1
NADC (Dr. A. Horbach, Dr. T. Gabrielson, J. McEachern)	3
APL/JOHNS HOPKINS	1
APL/U. WASHINGTON	1
ARL/U. TEXAS	1
URI (Prof. Peter Stephanishen)	1
ARL/PENN STATE (Dr. Alan Stuart)	1
Cambridge Acoustical Associates (Dr. M. Junger)	1
BBN (Dr. R. Haberman)	1
San Diego State University (Dr. Mauro Pierucci)	1

END

DATE

FILMED

DTIC

9-88